Doctoral theses at NTNU, 2022:202

Jonas Blomberg Ghini

Transient Heat Transfer to Confined Superfluid Helium

Doctoral thesis

NTNU
Norwegian University of Science and Technology
Thesis for the Degree of
Philosophiae Doctor
Faculty of Natural Sciences
Department of Physics

NTNU
Norwegian University of
Science and Technology

Jonas Blomberg Ghini

Transient Heat Transfer to Confined Superfluid Helium

Thesis for the Degree of Philosophiae Doctor

Trondheim, June 2022

Norwegian University of Science and Technology
Faculty of Natural Sciences
Department of Physics

NTNU
Norwegian University of
Science and Technology

NTNU
Norwegian University of Science and Technology

Thesis for the Degree of Philosophiae Doctor

Faculty of Natural Sciences
Department of Physics

ISBN 978-82-326-5302-7 (printed ver.)
ISBN 978-82-326-6765-9 (electronic ver.)
ISSN 1503-8181 (printed ver.)
ISSN 2703-8084 (online ver.)

Doctoral theses at NTNU, 2022:202

Printed by NTNU Grafisk senter

ABSTRACT

To investigate how the Large Hadron Collider at CERN can survive UFO attacks much larger than expected, we build and perform an experiment designed to measure the transient temperature evolution of both a stainless steel heater subjected to millisecond time–scale losses and the confined helium cooling this heater.

In Paper [1] we focus on a configuration where the heater is cooled by an open bath of superfluid helium. Setup validation is done by fitting the Kapitza heat transfer expression $Q = a_\mathrm{K}\ ({T_\mathrm{s}}^{n_\mathrm{K}} - {T_\mathrm{b}}^{n_\mathrm{K}})$ to steady state measurements, finding fit parameters within the expected range; $a_\mathrm{K} = 1316.8 \pm 10\%$ $\mathrm{W\,m^{-2}\,K^{-n_K}}$, $n_\mathrm{K} = 2.528 \pm 10\%$. We do not find conclusive evidence of an orientation dependence of the Kapitza heat transfer mechanism, nor heat transfer differences that can be attributed to local surface variations along the same heater. The setup shows critical heat flux in line with estimates from literature, and the time between a step in heating and the onset of film boiling follows the expected $\propto Q^{-4}$ dependence.

During the first millisecond after a step in applied heating power density our measurements show a slower thermal rise time than that found by a time–dependent one–dimensional model of our setup using the steady state Kapitza heat transfer expression as the cooling boundary condition. After the first millisecond, agreement between measurement and model is excellent.

In Paper [2] we confine the helium near the heater to a channel of 120 µm depth. The helium is isolated from the external bath with the exception of two pin–holes that, on the time–scale of tens of milliseconds, allow only negligible heat exchange with the external bath.

We measure the temperatures of both the heater strip and the channel helium during slow–pulse heating that reaches peak power after 9 ms, fast–pulse heating that reaches peak power after 100 µs, and step heating that reaches steady power after 100 µs.

Using the steady state Kapitza heat transfer expression at the interface between heater and helium, and the Gorter–Mellink heat transfer regime in the helium channel, we obtain excellent agreement between simulation and measurement during the first 5 ms of slow–pulse tests. Using instead the measured helium temperature in the Kapitza expression, we obtain excellent agreement between the simulated and measured heater response during the first 150 ms of slow–pulse tests.

The same model fails to explain the fast–pulse transient response of the heater and helium, while it can only explain the helium response to a step in applied power. The steady state Kapitza expression may therefore not be applicable to heating events that are over within a single millisecond.

ABBREVIATIONS

AFM	Atomic Force Microscopy
AM	Acoustic Mismatch
BLM	Beam Loss Monitor
CEA	Commissariat A L’energie Atomique
DAQ	Data Acquisition
LHC	Large Hadron Collider
MB	Main Bending
MQ	Main Quadrupole
MQED	Minimum Quench Energy Density
NIST	National Institute Of Standards And Technology
PEEK	Polyether Ether Ketone
PID	Proportional-Integral-Derivative
PRL	Phonon Radiation Limit
PTFE	Polytetrafluoroethylene
QPS	Quench Protection System
RMS	Root Mean Square
RRR	Residual Resistivity Ratio
SMU	Source Measure Unit
UFO	Unidentified Falling Object

PREFACE

This thesis is submitted in partial fulfilment of the requirements to obtain the degree Philosophiae Doctor (PhD) at the Norwegian University of Science and Technology (NTNU), in Trondheim, Norway.

The work culminating in this thesis began in September 2015, and ended in March 2022, at the Department of Physics. The work has hinged upon the involvement of three institutions; Asle Sudbø, at NTNU's Center for Quantum Spintronics, was the main supervisor; Bernhard Auchmann, at Paul Scherrer Institut and CERN's Performance Evaluation section, was the first co–supervisor; and Bertrand Baudouy, at CEA's Fundamental Research Division, was the second co–supervisor.

During this time, one semester's worth of physics courses (30 ECTS) were completed, and one year of administrative duties were performed, both at NTNU. Three years were spent at CERN, and about half a year of accumulated time was spent in the cryogenics laboratory at CEA.

ACKNOWLEDGEMENTS

Here, finally, at the end of a gruelling and seemingly insurmountable task, I feel genuine pride in the work I have done. While I didn't answer every lofty question I posed at the start, I exhausted every avenue I was able to identify, and have reached conclusions I stand by. What I have done is good enough. Better than enough, even.

The road to get here winds its way through some of the darkest days of my life, and some of the brightest. Realising that a single disregarded component in the temperature sensor circuitry made all my transient measurements useless was a dark day. Realising I knew how to compensate for it was a bright one.

Along this road I have had an incredible amount of help and support, and I would not have made it through any of this without these helping hands and minds.

It started when Bernhard Auchmann pitched a cool helium–related problem in the cafeteria of Building 30 the summer of 2015. Since then you stood by my side, providing your supervision unerringly and with a steadfast sense of calm during my many swings in and out of dread and despair at the state of my progress and work. At no point did I ever feel I was an afterthought, and at no point did I feel you were giving up on me.

To bolster my theoretical understanding of superfluid helium it was soon clear I needed expert help, and Asle Sudbø picked me and my project up, despite my electrical power engineering background not at all preparing me for hard–core applied physics research. Your trust and patience during times when I needed space, and your daring to place real and meaningful deadlines on me when I needed to be pushed, were instrumental in putting me in the frame of mind to actually wrap up my work.

To round out the team, I was lucky to engage Bertrand Baudouy as my third supervisor, bringing invaluable experimental experience to my fledgling endeavour. In exemplary fashion you navigated me through design decisions, cryostat operating procedures, and the order in which those damned pumping valves must open and close. Despite forgiveness, I still feel bad for frying that heating element in the cryostat you let me use for my experiments.

Bernhard and Bertrand, your repeated reviews, comments, weekend guidance, and perpetual presence within arms reach ensured my efforts to condense my work actually led to this final form, contained within my thesis. Beyond the efforts you put into my research, the references you provided during hiring all but guaranteed I got hired by my current employer. Thank you both, for everything.

While my extraordinary supervisors represent a necessary condition, the list of critical supporting cast has grown long over the years.

Lorenzo, Marco, and Michał, the STEAM team, I will forever cherish our discussions and stand–up meetings, and our trip, Lorenzo and Michał, to Berlin, despite EasyJet's best efforts to keep us in Geneva. And Björn, my long time office mate, may your one millibitcoin forever appreciate in value! Emmanuele, you gave me my first taste of real scientific work, and together with Arjan, you took me in under the PE section. Daniel, Rüdiger, Scott, Alejandro, Vera, Vivien, Zinour, and Edvard, you all helped make my time at CERN wonderful.

Karolina Kulesz, while our time in Building 30 did not overlap for all that long, our friendship persists, and will certainly continue till either of us think the other is too shitty or too dead to bother any longer. Thank you for taking me skiing and climbing that time I really needed it. You will get through it too.

Diego Berdeja, we were $(MDJ)^2$ for but a short time. The two of us, though, formed a friendship made of stronger stuff after the summer searching for secret temples and radiation doses that probably shaved a year or two off our life expectancy. I managed to visit you once, and I will again! Also you too will make it through. If I can, being just a monkey, someone of your calibre will surely succeed.

Laura, Pan, and Agnieszka, my work and my person has impacted you in many, largely painful ways. Life happens and mistakes are made, not just in the laboratory, but also at home. You have all played a part in forming my ideas of relationships, and even though you did not sign up as teachers, I cannot help but learn, so I can do better and cause less pain next time.

Among those that began their PhD's at the Center for Quantum Spintronics at NTNU around the same time as I, I hold especially dear the time shared with Even, Fredrik Nicolai, and Therese. You always showed the slow experimentalist that I too had a place in real science. Atousa, Lina, Marion, Jeroen, Sol, Payel, Jonas, Karen–Elisabeth, Alireza, Eirik, Matthias, Bjørnulf, Håvard, Tancredi, Frode, Anna Cecilie, Niels Henrik, Håkon, Christian, Verena; it takes a large Quspin village to raise a PhD.

Arnau Sala, had you not pointed out my mistake in the exponent of the Monte–Carlo energy criterion during my exam I would, with certainty, have failed the exam, for the third time, and likely given up on the whole PhD.

My family has always supported me, for which I am deeply grateful; Fred, I would not have had the skills and confidence in my practical abilities had you not become a part of my life, bringing with you an infinite source of knowledge and love of teaching the practical arts. Nina, my mother, you never doubted I would make it, and you always reminded me that failure in a project does not mean failure in life. Ingeborg and Daniel, I love you both with all my heart, and you have given me more strength through this than you might realise. Frida, my cousin, on your recommendation I sought therapy, in hindsight clearly necessary, during a turbulent time at the start of my PhD. This ensured I navigated the turbulent waters I was facing.

Luca, my father; one should not speak ill of the dead, but damn, bad timing. I will miss you till its my time to go. I loved our trip to Teknisk Museum. You did good. I wish you were here to celebrate this achievement.

Matteo Blomberg Ghini, my oldest brother; this would have been impossible without you. I will never make financial decisions as wise as yours, but had you made decisions as poor as mine, I would have had to call it quits in 2020.

Adriana Bronfield, knowing I would be happy, even if I failed, gave me the chance to succeed. I am so excited to get going with our life I can barely wait! Thank you, for your patience, space, closeness, and support during my last and heaviest lifting.

PAPERS

Paper I:
Jonas Blomberg Ghini, Bernhard Auchmann, and Bertrand Baudouy
Millisecond Time–Scale Measurements of Heat Transfer to an Open Bath of He II
ArXiv:2203.04626 [1]

Paper II:
Jonas Blomberg Ghini, Bernhard Auchmann, and Bertrand Baudouy
Millisecond Time–Scale Measurements of Heat Transfer to Confined He II
ArXiv:2203.04701 [2]

CONTENTS

CHAPTER 1

INTRODUCTION AND MOTIVATION

Chapter content:

This chapter will introduce the two main observations that shows our understanding of millisecond time–scale heat transfer to superfluid helium is incomplete. It will also explain why this lacking knowledge is a problem for the reliable operation of the LHC. The story involves UFOs attacking the large superconducting magnets at CERN; what's not to love?

The endless question "why?" led from stories around the firepit to lectures on the standard model of particle physics. It will never cease to provoke and motivate the incessant drive towards more answers and, inevitably, even more questions. Among the tools developed as means of illuminating the universe we live in is the Large Hadron Collider (LHC); a circular particle collider, the largest ever built, both in physical size and collision energy, meant to reach the frontier of the standard model. One of the machine's stated purposes was to prove the existence of the elusive Higgs boson. While the particle was found in 2012 [3, 4], knowledge, of course, remains incomplete [5]. As such, the LHC has not yet outlived its usefulness, with several planned upgrades, chief among which are; 1) the high–luminosity upgrade [6] which will increase the number of particle collisions with respect to the baseline design, and 2) the high–energy upgrade [7] to make each collision more energetic.

The LHC consists of an enormous set of complicated interlocking parts, all contributing to the end goal of detecting as many collisions at the interaction points (where the two counter–rotating beams collide) as possible. Most of the LHC is made up of superconducting dipole magnets used to bend the particle beam trajectories into a closed loop. These magnets are all permeated with superfluid helium, tasked with both the initial cooldown from room temperature, and improving the thermal stability of the magnet, maintaining their operating temperature of 1.9 K.

1.1 Unidentified Falling Objects in the LHC

Thermal stability of a superconducting magnet is crucial because during normal operation, the magnet will be subject to various local energy depositions that will increase the temperature, threatening a quench [8, p. 593–594]. A quench occurs when the superconductor locally transitions to normal–conducting. As a matter of definition, a quench is often considered irreversible [9, p. 656]. However, superconductivity will recover once the material cools back down to normal operating temperature.

Quenches can be caused by myriad reasons, and Bottura proposed the order–of–magnitude classification scheme shown in Figure 1.1 [10]. Examples include the AC losses associated with the current–ramp–rate, which induce losses as the field strength of an LHC magnet is brought up to operating energy. Or when the strong Lorenz forces of the magnetic field cause Wire motion as the conductors in a magnet physically move, releasing energy by friction. Or beam losses where energy from the particle beam is deposited in the magnets by Particle showers. If the energy deposition from any such cause exceeds a threshold depending on magnet type, location, and time–scale of energy deposition, it will cause a quench.

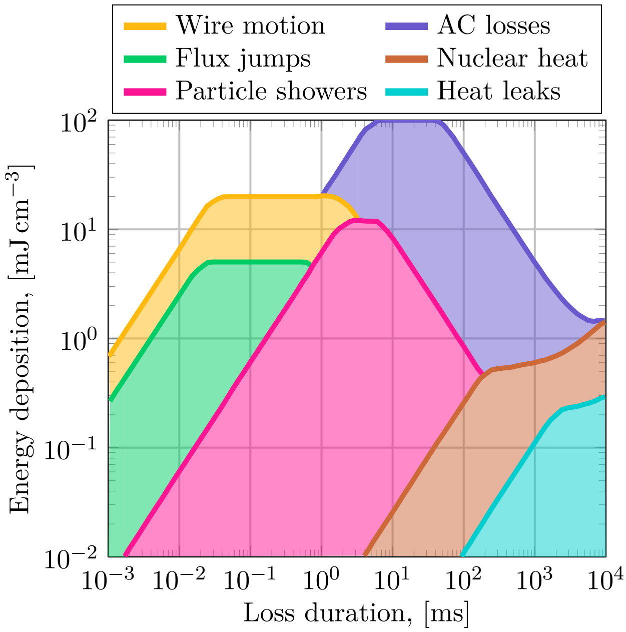

Figure 1.1: Approximate classification of the loss mechanisms that can deposit energy in a magnet during normal operation [10, Recreated from Fig. 5]. Classification is according to characteristic loss duration and energy density of the deposition. Particle showers are especially relevant to this thesis, as beam losses fall into this category. Note that direct impact of the particle beam on the magnet falls under Nuclear heat.

Beam losses and beam–loss induced quenches have several different sources and characteristics [11–15], and an unidentified falling object (UFO) [16] is a particular kind that has been used to guide the design process of the experimental work presented herein. UFOs fall under the Particle showers class of losses in Figure 1.1.

The two particle beams circulate in individual beam pipes, and are surrounded by the superconducting magnets that produce the magnetic fields maintaining the beam trajectories. A UFO event is the interaction between matter originating from within the machine itself, typically considered to be dust particles falling from the top of the beam pipe, and the particles in the beam. This interaction results in a shower of secondary particles that locally heat up the magnet. They are important because of the desire to keep increasing both the luminosity and the energy of the LHC. The more particles there are in the beam, the more collisions will happen during a UFO event [17], and the more energy individual beam particles possess, the more energy is released when it collides with the UFO [18, Fig. 5.11].

In particle accelerators the beam loss monitor (BLM) is used to ensure beam losses remain below safe limits to keep equipment from being damaged [8, Sec. 7.4.16]. Many such devices are located around the machine (2–3 BLMs per large superconducting magnet), allowing for real–time monitoring of the local rate of ionization, which relates to the energy deposition in the magnets, with a time–resolution down to some tens of microseconds. Figure 1.2 shows a representative plot of a UFO event as measured by a BLM. The data in the plot is interpreted as the product of two factors [19, Eq. 5.2]; 1) a time–dependent number of inelastic beam particle collisions with a dust particle happening within a given time–interval, here: 40 µs, and 2) a scaling factor, called the BLM response, that relates each such inelastic collision to a local ionization (measured by the BLM). The BLM response is estimated from Monte–Carlo simulations of beam–UFO interactions and the resulting particle shower using FLUKA (a general purpose particle interaction simulation tool developed at CERN).

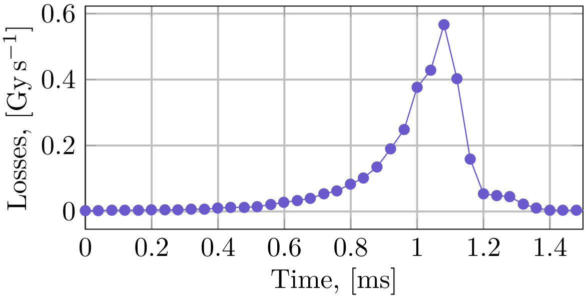

Figure 1.2: Representative example of BLM signal during a UFO event, detected 17 September 2015. Data provided by Bernhard Auchmann from the BLM `BLMBI.28R2.B0T20_MBB-MBA` [20].

For the experimental design described in Chapter 3, the most important feature of a UFO event is the time–scale; a UFO event is characterised by the roughly Gaussian loss profile seen in Figure 1.2, with a duration on the order of a half to a whole millisecond. While the energy deposition from a UFO event is clearly of critical importance for the operation of the LHC, for the experimental work presented in this thesis, it is less important; the materials used to build the experimental samples are different from those used to build LHC magnets (meaning thermal conductivity and heat capacity are different), and because experiments are carried out for a large range of energy values to investigate both weak and strong losses.

1.2 Why Look at Helium Cooling?

The thermal stability of a superconducting magnet with respect to transient energy depositions, such as those from beam losses, is expressed as the minimum quench energy density (MQED), typically given in units of mJ cm^{-3}. A superconductor has three critical parameters; temperature, current density, and magnetic field. Before any disturbance, when operating in steady state, only the magnetic field varies across the magnet cross section. Near the aperture/beam pipe, the field seen by an individual cable strand is strong (around 8.3 T at nominal particle beam energy), while a strand near the outside edge of the magnet sees a much weaker field (on the order of 3 T) [21, Fig. 2]. The temperature is at 1.9 K across the entire magnet, while the current density in all the cables is the same. This means the energy density necessary to cause a quench varies like the field; high field means only a small amount of energy is necessary to quench, while in a low–field region the opposite is true. The MQED, then, is not only tied to an energy density necessary to initiate a quench; it is also specific to the location in the magnet where the quench originates.

With regards to beam losses, the resulting energy deposition will almost exclusively be limited to the horizontal midplane region of the magnet, nearest the beam pipe, roughly coincident with the place the magnet has the lowest margin to quench[21, Fig. 4]. Figure 1.3 shows the MQED for the main dipole magnets of the LHC as it varies depending on the duration of the energy disturbance [22, Fig. 2]. The plot illustrates the compounding problem with UFOs that at higher beam energies, not only will each UFO cause more energy to be released, but less energy is needed to quench a given magnet.

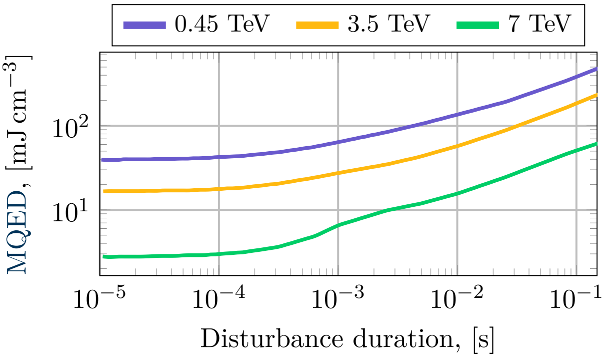

Figure 1.3: MQED at three LHC beam energies for the main dipole magnets as it varies with the duration of an energy deposition [22, recreated from Fig. 2].

The MQED curves in Figure 1.3 are not measured in the machine. The plot shows the result of modelling efforts that take energy disturbances at a variety of durations as input (UFOs, of course, but also both much faster and much slower disturbances), and then runs an electro–thermal simulation to determine whether or not a superconductor quenches when subject to this disturbance. The modelling software used to obtain the results in Figure 1.3 is QP3 [23]. QP3 models a single strand in the superconductor cable as a longitudinally discretised one–dimensional electrical and thermal conductor. Current and heat flows along the conductor, with additional heat flows/sources/sinks related to joule heating within a section of the strand, cooling across the insulation between the strand and the large helium bath surrounding the entire superconductor, and cooling directly from the surface of the strand to the helium that permeates the magnet cables. There is no thermal contact between adjacent helium volumes within the strand, nor between the strand volumes and the bath.

It has proven difficult to generate controlled beam losses with characteristics like that of a UFO. As such, comprehensive measurements of the MQED in the real LHC magnets are not available. However, an orbit–bump quench test was done in 2011 which roughly represents the UFO–like loss pattern [24]. The test was done by "bumping" a small part of the beam in order to make a specific number of particles crash directly into the beam pipe of one of the main quadrupoles in the LHC[1]. This gave rise to an energy deposition lasting about 10 ms, consisting of a series of fast loss peaks roughly a third of a millisecond apart. Two different total particle loss numbers were tested; $4 \cdot 10^8$ protons and $8.2 \cdot 10^8$ protons. The larger number of particles impacting the beam pipe lead to more energy deposited in the magnet itself. For the smaller number/energy, no quench was observed, while for the larger, the magnet quenched about half–way through the disturbance.

Auchmann *et al.* analysed the orbit–bump quench tests, finding from simulations of the energy depositions from the two tests that for the test where no quench was seen, 198 $\mathrm{mJ\,cm^{-3}}$ was deposited locally in the magnet, while for the test that saw a quench, a total of 405 $\mathrm{mJ\,cm^{-3}}$ was deposited [22, Sec. V B]. The estimated time of quench was 5 ms after the start of losses, and 265 $\mathrm{mJ\,cm^{-3}}$ had been deposited in the magnet within this time. These energy densities come from FLUKA simulations similar in nature to those used to determine the BLM response mentioned before.

The important finding is that QP3 simulations, using losses found by the FLUKA simulations, give an MQED of just 50 to 80 $\mathrm{mJ\,cm^{-3}}$. This means there is a large discrepancy between when modelling suggests a magnet would quench and when the magnet actually quenches in the LHC; taking 265 $\mathrm{mJ\,cm^{-3}}$ as the measured MQED and 65 $\mathrm{mJ\,cm^{-3}}$ as the simulated MQED gives a ratio of 4.1 in favour of the real quench energy. Auchmann *et al.* conclude that the only uncertainty within the electro–thermal model implemented in QP3 significant enough to potentially explain the discrepancy is the helium cooling. They suggest, tentatively, that an enhanced nucleate–boiling regime could be part of the explanation.

1.3 Large and Numerous UFOs

Some of the early work done in preparation for the large experimental effort presented herein was to look at all the UFO events recorded by the BLM system over the course of LHC operation between June 2015 and June 2016. While this work was only used internally at CERN and never prepared for publication, it finds evidence in line with the orbit–bump quench test.

By using FLUKA estimates for how much energy an individual UFO event deposits in a magnet ($3.29 \cdot 10^{-7}$ $\mathrm{mJ\,cm^{-3}}$ per lost proton), then comparing it with the estimated MQED for losses around 1 ms (8 $\mathrm{mJ\,cm^{-3}}$ from Figure 1.3 at 7 TeV), a total of 45 UFOs were found to deposit *more* energy in the magnets than the MQED. However, only the four largest UFOs actually caused a quench. The smallest energy deposition that did cause a quench was 28 $\mathrm{mJ\,cm^{-3}}$, 3.5 times larger than the estimated MQED, while the largest deposition that did *not* cause a quench was 24 $\mathrm{mJ\,cm^{-3}}$, 3 times the MQED. This is quite in line with the factor 4 found from the orbit–bump quench test.

---

[1] The parts of the LHC that actually bend the beam into a circular orbit are composed of long strings of dipole and quadrupole magnets. A "cell" is composed of three dipoles followed by a quadrupole followed by another three dipoles and then a second quadrupole.

1.3.1 Machine Protection and Availability

The magnetic energy stored in an LHC main bending (MB) dipole magnet during normal operation, combined with the enormous current flowing in the cables (on the order of 10 kA [25, Tab. 7.5]) mean that once a quench occurs, and a normal–conducting zone forms in the magnet, considerable heat can be generated by resistive joule heating [26], which could damage a magnet [9, Sec. 8.1.4]. A quench protection system (QPS) is implemented in the LHC in order to ensure the magnets take no damage during a quench [25, Sec. 9.4]. When it detects the start of a quench, it rapidly heats the entire quenching magnet above its critical temperature in order to reduce the energy density developed as the magnet current decays to zero. In tandem with the quench protection trigger there is also a beam dump, since the quenching magnet can no longer maintain the beam trajectory, and the beam must therefore be dumped safely to avoid equipment damage [25, Chap. 17].

After a quench happens, with the QPS triggering rapid heating of the affected magnet(s), as well as a beam dump, about 12 hours of LHC availability are lost, mostly due to the cryogenic system turn–around time [27]. A beam dump on its own, however, where no quench happened, leads to 3 hours lost.

Since several different beam–induced losses can quench magnets, the BLM system is connected to the QPS; if the beam can be dumped *before* the losses are so large they cause a quench, several hours of LHC availability can be saved. UFOs, while originally expected to cause several quenches have, as described, turned out to not actually do. Therefore, in the LHC today, a compromise has been struck; set the BLM thresholds sufficiently high so that even large UFOs will not trigger a beam dump [17], while still keeping thresholds for other kinds of losses tuned to trigger beam dumps.

The drive for higher LHC luminosity will increase the rate of UFO events, and the drive for higher LHC collision energy will both lower the MQED and lead each individual UFO to deposit more energy. As these LHC upgrades are implemented it becomes ever more important to tune the protection systems more accurately to balance the desire to prevent the long downtime associated with a full–on UFO–induced quench against the desire to also prevent the shorter downtime of a premature beam dump when no quench was really about to happen.

1.4 The Work Herein

This is the backdrop; some unknown mechanism, not accounted for in the usual electro–thermal simulations of LHC superconducting magnets, acting in the millisecond time–range, prevents the rapid superconductor temperature rise otherwise expected. To investigate this mechanism, the core of the work herein is the design and construction of an experimental sample meant to approximate the environment around a single superconducting strand of an LHC main dipole magnet, and then subjecting this sample to energy depositions either in the form of steps in applied heating power density, or pulses, both fast and slow, while submerged in superfluid helium.

The work culminates in the two papers appended to this thesis; the first paper details the sample used in an open bath configuration, subject to steps in applied heating power density, while the second paper investigates the sample upon confining the superfluid helium to a small channel, subject to steps and pulses in applied heating power density.

Chapter 2 looks at the theoretical knowledge of heat transfer to and in superfluid helium, as well as historical experimental work. Chapter 3 lays out the design of the experimental sample, while Chapter 4 details the temperature measurements in terms of calibration, uncertainty, and post processing of signals. Finally, Chapter 5 explains the numerical modelling framework developed to analyse the results. The work culminates in the two papers appended at the end of the thesis; Paper [1] detailing open bath, and Paper [2] detailing closed channel measurement results.

CHAPTER 2

THEORY AND BACKGROUND

Chapter content:

This chapter is written as an exposition of the various aspects of heat transfer to and in superfluid helium that were in one way or another investigated when designing and then making sense of the experimental work presented in papers [1] and [2]. It chronicles the winding path taken through some of the vast theoretical and experimental developments between the Keesoms's observation of a strange peak in the helium heat capacity roughly 90 years ago, and the experiments that are part of this thesis.

The chapter is roughly divided in three; sections 1, 2, and 3 discuss heat transfer *to* helium, governed by the Kapitza conductance. Section 4 then describes heat transfer *in* helium, with exclusive emphasis on the Gorter–Mellink regime. Finally, sections 5 and 6 join the two aspects of heat transfer, discussing time–dependent and confinement effects.

Figure 2.1 shows the P–T phase diagram of helium around the region where it is liquid. While four regions are indicated, the region of most relevance to this thesis, and also the region with the most fascinating physics, is the Superfluid region.

There are also three curves in the figure, separating the regions; the Melting curve describes the boundary between fluid and solid, and has no bearing on the work herein. The λ–line curve separates the normal and superfluid regions, and represents the temperature at which the strange superfluid properties of helium arise. This curve is of critical importance. The last curve is the Saturation curve, which describes the conditions where vapour and liquid coexists in stable forms that can be easily differentiated, and this curve is important for the pumped–cryostat used in experiments herein.

All substances, be it water, hydrogen, carbon, or iron, will have a P–T diagram that looks something like the one for helium, save for one crucial difference. All other substances solidify below some temperature, even at low pressures. Every other substance will have a P–T diagram where the Solid region fills all regions of the diagram that are not Normal fluid or Vapour. No other known substance has anything resembling the Superfluid region, with the exception of ^{3}He, the rarer isotope of regular ^{4}He, and the hypothetical dense neutron fluid in neutron stars.

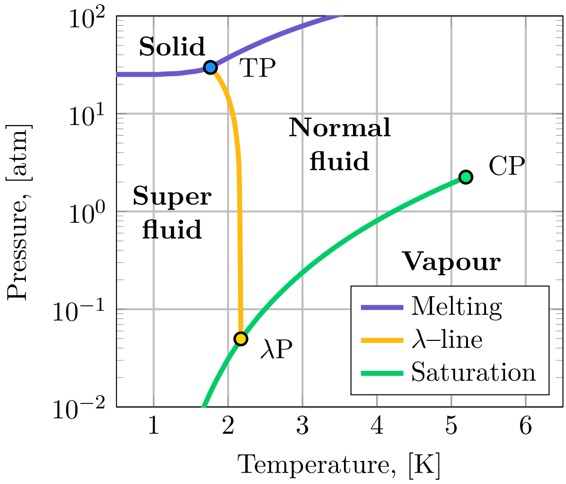

Figure 2.1: Phase diagram of helium around the λ–line. Above 1.8 K, the melting line is taken from McCarty [28, Eq. 38]. Below 1.8 K, the melting line in taken from Driessen *et al.* [29, Fig. 1, bcc region]. Note that Driessen *et al.*'s data starts at 1 K. In this figure, the value at 1 K is considered constant down to 0 K. The λ–line is taken from McCarty [28, Table 15]. The saturation line is taken from Van Sciver [30, Appendix A 2.1]. λP refers to the λ point, CP, the critical point, and TP the triple point.

The experiments done as part of this thesis explore two main aspects of the Superfluid region; heat transfer into helium from a heater, and heat transfer within helium. Heat transfer *to* helium will be interpreted in terms of the Kapitza conductance at the heater–helium interface, while heat transfer *in* helium by the Gorter–Mellink mutual friction heat transfer mechanism.

2.1 Kapitza Resistance and Heat Transfer

When a large copper block is cooled by an open bath of superfluid helium from one side and heated from the other, a peculiar temperature distribution arises. On the liquid side of the heater–helium interface, the thermal gradient is nearly imperceptible, while at the interface itself there is a discontinuous temperature drop, confined to a layer no more than a few atoms thick [31, Fig. 8].

The archetypal experimental observation is shown in Figure 2.2. Under the heat flux Q_{in}, there is a jump ΔT_{s} in temperature at the interface between the solid heater and the superfluid helium. While the figure indicates a large distance between the interface and the nearest sensors, various experimental techniques have been used to make sure the temperature profile is really discontinuous. Already in Kapitza's original paper the distance across which ΔT_{s} falls was given an upper bound of 10 µm [32].

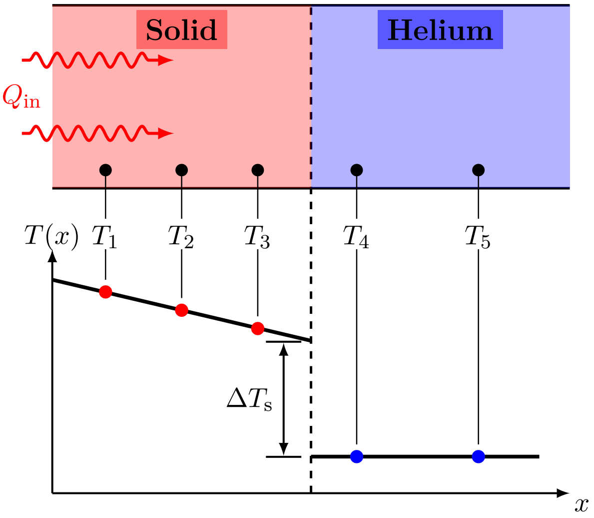

Figure 2.2: Archetypal measurement showing presence of the Kapitza resistance [30, recreated from Fig. 7.32]. Thermometers 1—5 give the discrete temperature distribution along the measurement sample. In the solid, there is a heat flux dependent gradient towards the interface, while in the helium, the effective thermal conductivity is so large, no discernible gradient is visible. ΔT_{s} is the temperature jump at the interface attributed to the Kapitza resistance.

The Kapitza resistance is *not* a unique feature of the interface between a solid and superfluid helium. The resistance exists across all interfaces, at all temperatures, so long as the acoustic impedances of the two media in contact are different. Mismatched impedances mean an incident sound wave has a high likelihood of being reflected rather than transmitted, seen as a resistance at the interface. For most interfaces between a solid and a fluid, the thermal boundary layer, with fluid atoms near the interface being nearly stationary, completely dominates the effective heat transfer coefficient, especially at temperatures above a few kelvin. For interfaces between solids, the acoustic properties tend to be similar enough that the Kapitza resistance is negligible, though there are exceptions, such as lead interfacing with diamond. The interface of importance to this work is that between stainless steel and superfluid helium, for which the Kapitza resistance plays the decisive role.

In literature the terms Kapitza conductance and Kapitza resistance tend to be used interchangeably. The Kapitza conductance is the inverse of the resistance, analogous to electrical circuit resistance. The terms are used interchangeably herein as well, depending on convenience.

In principle, the Kapitza conductance h_{K} is found in the limit of small heat flux and small temperature discontinuity;

$$h_{\text{K}} = \frac{\mathrm{d}Q}{\mathrm{d}T_{\text{s}}}, \tag{2.1}$$

where $\mathrm{d}Q$ is the infinitesimal heat flux crossing the interface, giving rise to the infinitesimal temperature discontinuity $\mathrm{d}T_{\text{s}}$. In practice, this kind of relationship cannot be used when ascertaining the conductance from measurements, since there is no practical way to measure infinitesimal temperature discontinuities for infinitesimal heat flux. So, a more pragmatic definition is used;

$$h_{\text{K}} = \frac{Q_{\text{in}}}{\Delta T_{\text{s}}}. \tag{2.2}$$

2.1.1 Phonon Radiation Limit

Figure 2.3 shows the first physical picture used to describe heat transfer across the temperature discontinuity between a hot metal surface and cool superfluid helium [30, Sec. 7.5.1]; the phonon radiation limit (PRL).

Let a phonon C_{in}, within the metal, be incident upon an area $\mathrm{d}A$ at the interface. The phonon's angle of incidence with respect to the perpendicular is α, so its velocity components are $v_{\text{parallel}} = v \sin\alpha$, and $v_{\text{perpendicular}} = v\cos\alpha$, where v is the speed of sound in the material. Only the perpendicular component may transfer energy across the interface, but the PRL assumes *all* the energy of this perpendicular component is transferred.

An approximation to the low–temperature phonon energy density is that from the Debye model [33, p. 108];

$$E_{\text{ph}} = \frac{3}{5}\pi^4 \frac{N}{V}\frac{k_{\text{B}}}{\theta^3}T^4, \tag{2.3}$$

where N/V is the number density of particles in the material, and θ is its Debye temperature. In this context, low temperature means $T \ll \theta$, which is usually fulfilled for liquid helium temperatures.

The incident heat flux upon $\mathrm{d}A$ becomes $v\cos\alpha E_{\text{ph}}$, where v is the speed of sound in the solid.

The total heat flux is then the contribution from all such phonons within the hemisphere $\alpha \in [0, \pi/2]$ and $\psi \in [0, 2\pi]$, and is given by [34, Eq. 8];

$$q = \frac{1}{4}vE_{\text{ph}}, \tag{2.4}$$

The factor $v/4$ comes from looking at how many phonons at position (r, α, ψ) would strike the area $\mathrm{d}A$ per second [35, p. 39].

From the definition of the Debye temperature [33, p. 106, Eq. 28], the speed of sound in a solid is given as,

$$v = \frac{k_{\text{B}}\theta}{\hbar}\left(\frac{6\pi^2 N}{V}\right)^{-1/3}, \tag{2.5}$$

which, together with the phonon energy density from Equation (2.3), gives the total heat flux as,

$$q = \frac{\pi^4}{10\hbar}\left(\frac{k_{\text{B}}}{\theta}\right)^2\left(\frac{3N}{4\pi V}\right)^{2/3} T^4 = \sigma_{\text{PRL}}T^4. \tag{2.6}$$

This is analogous to the Stefan–Boltzmann law of radiative power from a black body, with σ_{PRL} denoting the constant of proportionality for the PRL.

Viewing the interface between a solid and superfluid helium in light of the phonon radiation expression in Equation (2.6) yields a net radiation balance across the interface;

$$q_{\text{net}}^{\text{PRL}} = \sigma_{\text{PRL}}(T + \Delta T)^4 - \sigma_{\text{PRL}}T^4, \tag{2.7}$$

where ΔT is the temperature discontinuity at the interface. Note that this radiation balance assumes the size of the interface, namely the distance across which ΔT falls, is small compared with the phonon mean free path and dominant phonon wavelength.

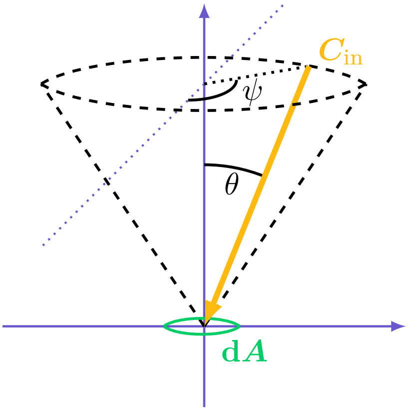

Figure 2.3: Phonon C_{in}, incident on the surface element dA on the interface between some material below and some other material above the horizontal axis [30, Fig. 7.33].

In real materials, this condition might be only partially fulfilled. For stainless steel, of interest herein, a rough estimate of the mean free path comes from the relationship between thermal conductivity and heat capacity; $k = (1/3)Cvl$ [33, p. 116, Eq. 42]. Using $k \simeq 0.2\ \mathrm{W\,m^{-1}\,K^{-1}}$ and $C \simeq 10^4\ \mathrm{J\,m^{-3}\,K^{-1}}$ (see Section 3.4 on page 95) at $T \simeq 2$ K, with the speed of sound $v \simeq 3100\ \mathrm{m\,s^{-1}}$ [36], gives the phonon mean free path $l \simeq 20$ nm. Using instead the relationship between the Debye temperature and the Debye frequency [33, p. 106, Eq. 27], converting to wavelength by the speed of sound, with the Debye temperature of 304 stainless steel $\theta_{\text{steel}} \simeq 400$ K [37, Table 4.2], gives the Debye wavelength $\lambda_D = hv/\theta k_{\text{B}} \simeq 0.4$ nm. The practical interface between the steel and superfluid helium would be no smoother than the steel surface, which, even after electropolishing or the best abrasive smoothing techniques only reach surface roughness levels of about 100 nm [38]. So, the interface size may not be small enough to guarantee the phonons see a flat interface.

From the radiation balance in Equation (2.7), by expanding $(T + \Delta T)^4$ and factoring out $4T^3\Delta T$, a form of the net heat flux is found;

$$q_{\text{net}}^{\text{PRL}} = 4\sigma_{\text{PRL}} T^3 \Delta T \left[1 + \frac{3}{2}\frac{\Delta T}{T} + \left(\frac{\Delta T}{T}\right)^2 + \frac{1}{4}\left(\frac{\Delta T}{T}\right)^3 \right]. \tag{2.8}$$

In the low–ΔT limit, Equation (2.2) gives an expression for the Kapitza conductance;

$$h_{\text{K}}^{\text{PRL}} = 4\sigma_{\text{PRL}} T^3. \tag{2.9}$$

There are several problems with the PRL, and it is considered an upper bound for the heat flux that would cross the interface in reality. These problems include the fact that all phonon modes have been considered, even though the helium, being a liquid, can only sustain longitudinal modes. In fact, no characteristics of helium are considered at all, since the tacit assumption of the PRL is that the solid is the only limiting factor for the heat flux across the interface. There is also no account of the finite reflection coefficient of incident phonons at the interface; in reality, some fraction of phonons would be reflected rather than transmitted.

The key success of the PRL is that it predicts the right temperature dependence of the heat flux, firmly establishing that at the very least, phonon mediated energy transport across the interface plays a large role.

2.1.2 Acoustic Mismatch Theory

Khalatnikov's acoustic mismatch (AM) theory was the first improvement on the PRL [30, Sec. 7.5.2]. The key advance is in accounting for the finite reflection and transmission coefficients at the interface. Figure 2.4 shows a drawing of the interface between a solid and superfluid helium. Some phonon within the solid is incident upon the interface at an angle θ_{in}. In the AM picture, only incident phonons of angle such that the scattered phonon on the helium side ends up *inside* a cone swept out by the critical angle θ_{crit} may be transmitted. All phonons outside this scattering criterion are completely reflected at the interface. This critical angle is determined by the ratio of the speed of sound in the solid and the helium [30, Eq. 7.97],

$$\theta_{\mathrm{crit}} = \arcsin\left(\frac{v_{\mathrm{He\,II}}}{v_{\mathrm{solid}}}\right), \tag{2.10}$$

where $v_{\mathrm{He\,II}}$ is the speed of (first) sound in superfluid helium and v_{solid} that in the solid. Due to the large difference in speed of sound, the critical cone is very narrow. Using $v_{\mathrm{solid}} = 3100\ \mathrm{m\,s^{-1}}$, and $v_{\mathrm{He\,II}} \simeq 230\ \mathrm{m\,s^{-1}}$ [39] around 1.9 K, θ_{crit} is on the order of 4°. The critical cone arises because only longitudinal phonons may propagate in the liquid, since a liquid cannot sustain the shear forces necessary for transversal modes.

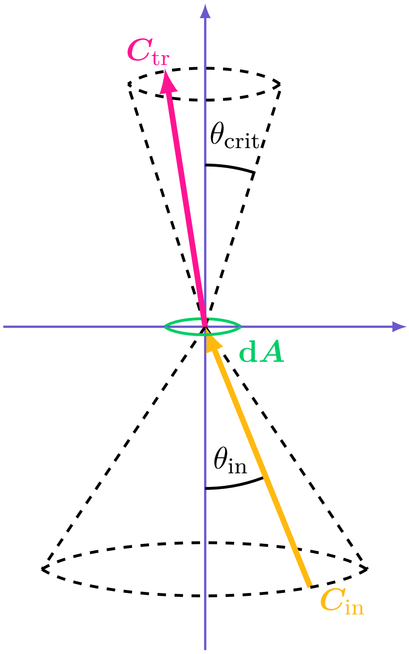

Figure 2.4: Phonon C_{in}, incident on the surface element $\mathrm{d}A$ on the interface between a solid below and superfluid helium above the horizontal axis [30, Fig. 7.35]. C_{tr} is the transmitted phonon. θ_{crit} is the critical angle that sweeps out the cone outside of which no phonons can scatter into.

In the PRL, the total heat flux was made up of all phonons from all angles. AM has a similar expression as that in Equation (2.4), but it is modified by the critical cone restriction [30, Eq. 7.98];

$$q_{\text{possible}} = \frac{1}{4} v_{\text{solid}} E_{\text{ph}} \left(\frac{v_{\text{He}}}{v_{\text{solid}}} \right)^3 . \tag{2.11}$$

This accounts for all phonons that would scatter into the critical cone.

However, not all such phonons are transmitted. The significant impedance mismatch between the solid and the superfluid helium results in a low transmission coefficient. At the interface this is defined as [40, Eq. 5][1]

$$t = 4 \frac{Z_{\text{solid}} Z_{\text{He}}}{\left(Z_{\text{solid}} + Z_{\text{He}}\right)^2}, \tag{2.12}$$

where the impedance of a medium $Z = \rho v$ with ρ its density and v the speed of sound in the medium.

For the case of any practical solid and superfluid helium, where $Z_{\text{solid}} \gg Z_{\text{He}}$, this transmission coefficient simplifies to,

$$t = 4 \frac{Z_{\text{He}}}{Z_{\text{solid}}} = 4 \frac{\rho_{\text{He}} v_{\text{He}}}{\rho_{\text{solid}} v_{\text{solid}}}. \tag{2.13}$$

With this, the transmitted heat flux is found,

$$q_{\text{transmitted}} = 4 \frac{\rho_{\text{He}}\, v_{\text{He}}}{\rho_{\text{solid}}\, v_{\text{solid}}} \cdot \frac{1}{4} v_{\text{solid}} E_{\text{ph}} \left(\frac{v_{\text{He}}}{v_{\text{solid}}} \right)^3 = \left(\frac{\rho_{\text{He}}\, {v_{\text{He}}}^4}{\rho_{\text{solid}}\, {v_{\text{solid}}}^4} \right) v_{\text{solid}} E_{\text{ph}}. \tag{2.14}$$

A different phonon energy density must be used here, as compared with the PRL; only the longitudinal phonons in the superfluid helium matter, so E_{ph} is a third of that in Equation (2.3) [30, Eq. 7.102],

$$E_{\text{ph}} = \frac{4}{15} \frac{\pi^5 k_{\text{B}}^4}{h^3\, {v_{\text{He}}}^3} T^4, \tag{2.15}$$

which, with Equation (2.14), gives,

$$q_{\text{tr}} = \frac{4}{15} \frac{\pi^5 k_{\text{B}}^4}{h^3} \frac{\rho_{\text{He}}}{\rho_{\text{solid}}} \frac{v_{\text{He}}}{{v_{\text{solid}}}^3} T^4 = \sigma_{\text{AM}} T^4. \tag{2.16}$$

This is, again, just like the black–body radiation expression, and the PRL result in Equation (2.6), with a different proportionality factor.

Compared with σ_{PRL}, σ_{AM} is much smaller, being dominated by the ratio between densities and the inverse cube dependence on the speed of sound in the solid.

The Kapitza conductance in the low–ΔT limit of the acoustic mismatch theory is found in the same was as for PRL in equations (2.8) and (2.9);

$$h_{\text{K}}^{\text{AM}} = 4 \sigma_{\text{AM}} T^3. \tag{2.17}$$

---

[1] Note that Challis includes a factor $1/\cos\theta$ in the expressions for impedance of mediums. These relate to the angle of incidence and refraction, and are accounted for by the factor $(v_{\text{He}}/v_{\text{solid}})^3$ in Equation (2.11).

After considering the excitation of surface waves at the interface by transverse phonons, Khalatnikov includes a factor $F \simeq 1.5$ in the expression for the Kapitza conductance [41, Eq. 23–33];

$$h_{\mathrm{K}}^{\mathrm{AM}} = 4\sigma_{\mathrm{AM}} F T^3. \tag{2.18}$$

2.1.3 Comparison With Measurements

Cheeke compiled a large comparison of the highest observed values of the Kapitza conductance with the predictions from both PRL and AM [34, Table III]. Some of the results are shown in Table 2.1. Cheeke's acoustic mismatch calculations use $F = 1.5$.

Two features of these results stand out; 1) for materials with large Debye temperatures, the phonon radiation limit is in good agreement with measurement, and 2) with the exception of Al_2O_3 (sapphire), the phonon radiation limit is always above the measured result and the acoustic mismatch is always below.

As pointed out by Snyder [42, p. 7], a high Debye temperature roughly corresponds to a lattice of light–weight, strongly interacting atoms, meaning phonons are easily excited. A high Debye temperature is reflected in relatively high speed of sound, seen in sapphire with $v \simeq 10$ km s^{-1} [43] or LiF with $v \simeq 6$ km s^{-1} [44]. The large acoustic mismatch between superfluid helium and these high–θ materials meansAM theory should do well, but some process permits nearly all phonons incident upon the interface to couple with the longitudinal modes in the helium. Note that although the transmission coefficient is high, the Kapitza conductance itself is low for these materials.

Note also that for higher Debye temperature, the Debye model for phonon energy density is more closely followed by the real material, and so, the poorer fit to the phonon radiation limit could be related also to the model assumptions not being fulfilled for low–θ materials.

Relevant for this thesis Using that the particle density of 304 stainless steel is approximately $8.7 \cdot 10^{28}$ m^{-3} (from density 7955 kg m^{-3}, and approximate molar mass 55.035 g mol^{-1}), and the Debye temperature and speed of sound are as before, 400 K and 3100 m s^{-1}, equations (2.9) and (2.18) (using $F = 1.5$ for the acoustic mismatch calculation) yields bounds for the Kapitza conductance of stainless steel;

$$\begin{aligned} h_{\mathrm{K}}^{\mathrm{PRL}} &= 23 \ \mathrm{kW\,m^{-2}\,K^{-1}} \\ h_{\mathrm{K}}^{\mathrm{AM}} &= 0.06 \ \mathrm{kW\,m^{-2}\,K^{-1}} \end{aligned} \tag{2.19}$$

2.2 Building on the Acoustic Mismatch Theory

The AM approach is considered physically correct in the sense that it improves upon PRL by accounting for both there being only longitudinal modes in the superfluid helium and there being a finite chance of phonon reflection at the interface. Despite this, there is obviously something missing in the description, seeing as the model results underestimate the observed Kapitza conductances by about the same factor PRL overestimates them.

Table 2.1: Selected results from Cheeke's compilation, showing the discrepancy between measured Kapitza conductance and those calculated in the phonon radiation limit and acoustic mismatch pictures at 1.9 K [34, Table III].

Solid	θ [K]	$h_\mathrm{K}^\mathrm{PRL}$ $\left[\mathrm{kW\,m^{-2}\,K^{-1}}\right]$	$h_\mathrm{K}^\mathrm{obs}$ $\left[\mathrm{kW\,m^{-2}\,K^{-1}}\right]$	h_K^AM $\left[\mathrm{kW\,m^{-2}\,K^{-1}}\right]$
Hg	72	440	30	4.6
Pb	100	190	32	1.7
Sn	195	54	12.5	0.39
Cu	343	30	7.5	0.14
Al	433	15	7.6	0.02
Ni	440	19	4	0.07
Non–metals				
KCl	230	22	6.9	0.38
Quartz	290	19	5.7	0.23
Si	636	6.4	4.2	0.05
LiF	750	5.1	4.5	0.03
Al_2O_3	1000	1.5	1.6	0.0035

Upon finding these large discrepancies between observed and predicted (both PRL and AM) conductances, a large, and still ongoing, research effort was launched to try and understand more complex properties of the Kapitza heat transfer mechanism. Most approaches have centred around ways to improve the poor acoustic matching predicted by AM, though completely separate channels of heat transfer have also been considered.

The efforts roughly fall into three main categories; 1) the presence of a dense layer of adsorbed helium atoms on the heater surface that improves the acoustic match between helium and heater [45–47]; 2) the existence of additional heat transfer channels, typically involving some means for electrons to contribute to heat transfer, or a way for evanescent phonon modes to transfer energy across the interface [34, 48–50]; and 3) the rough surface of the heater–helium interface either providing new heat transfer channels for phonon mediation or simply increasing the effective heat transfer area [32, 51–53]. These approaches are not mutually exclusive, in particular the idea of a rough surface capped by a dense layer of helium has been investigated [54]. Also, many of the rough–surface attempts include the effect of Rayleigh surface modes.

Due to the recent experimental work by Ramiere *et al.* [55], it is worth looking in a bit more detail at the rough–surface model by Adamenko and Fuks [56];

2.2.1 Surface Roughness Inclination

Adamenko and Fuks extend Little's work (Ref. [52]) by accounting for the local inclination of the rough surface [56]. They start with a smooth surface $z = 0$ on which there is a random roughness described by $\zeta(x, y)$. They describe this surface by the statistical properties σ, the amplitude variance $\sqrt{\langle\zeta^2\rangle}$, where $\langle\ldots\rangle$ denotes the ensemble average over many realisations of $\zeta(x, y)$, and l, the correlation length between peaks on the rough surface. The two properties characterise the surface inclination as,

$$\gamma = \frac{2\sigma}{l}. \tag{2.20}$$

What they find is that the ratio between the enhanced heat flux and the heat flux of the AM result is the ratio between the rough and smooth surface areas (so long as $\gamma^2 \ll 1$);

$$\frac{S}{S_0} \simeq 1 + \frac{\gamma^2}{2}, \tag{2.21}$$

where S is the surface area including the contribution from roughness and S_0 is the smooth surface area. So the heat flux becomes,

$$Q(T) = Q_0(T)\frac{S}{S_0} \simeq Q_0(T)\left(1 + \frac{\gamma^2}{2}\right), \tag{2.22}$$

where Q_0 is the AM result. From this, for the Kapitza conductance (which they refer to as $\dot{Q}$) they find,

$$\frac{h_\mathrm{K}}{h_\mathrm{K}^{AM}} = 1 + \frac{1}{2}\gamma^2 f(\Theta), \tag{2.23}$$

where $\Theta = lk_\mathrm{B}T/2\hbar v_\mathrm{He} = l/\lambda$ is a dimensionless temperature (using T in kelvin) with $\lambda = 2\hbar v_\mathrm{He}/k_\mathrm{B}T$ the dominant phonon wavelength in helium, and $f(\Theta)$ is a function which has its maximum around $\Theta \simeq 0.3$, where the phonons in the helium have wavelengths similar to the roughness correlation length. They ascribe this to a spatial resonance between the phonons and traps set up by the valleys in the rough surface. In the limit of high and low temperature f becomes,

$$f(\Theta \ll 1) \simeq 169\Theta^2, \qquad f(\Theta \gg 1) \simeq 1 + 0.0635\Theta^{-2}. \tag{2.24}$$

2.2.2 Known Surface Roughness

In 2016 Ramiere *et al.* made Kapitza resistance measurements on a Si single crystal at several temperatures and pressures up to above the solidification pressure of superfluid helium [55]. The heat transfer interface between the Si crystal and the helium was fully characterised by atomic force microscopy. They use Adamenko and Fuks's theoretical model of Kapitza resistance, and find remarkable agreement between measurements and theory.

Ramiere *et al.* use

$$\lambda(P, T) = \frac{hv_\mathrm{He}(P)}{3.83k_\mathrm{B}T} \tag{2.25}$$

as an estimate for the pressure and temperature dependent dominant thermal phonon wavelength in helium, where $v_\mathrm{He}(P)$ is the pressure dependent speed of sound in helium. This is yet another expression, different from both Shiren's and Adamenko and Fuks's. Importantly, all the expressions are of about the same order, so ultimately, it does not matter much that they differ by a factor π or π^{-1}.

The Si crystal surface is assumed to have correlation length smaller than λ under all conditions measured during experiments. This means Adamenko and Fuks's reduced temperature $\Theta = l/\lambda$ is always < 1, which in turn means they can express the Kapitza conductance enhancement ratio according to the low–temperature limit (see equations (2.23) and (2.24));

$$\frac{h_\mathrm{K}}{h_\mathrm{K}^\mathrm{AM}} = 1 + 2 \cdot \left(\frac{\sigma}{\lambda}\right)^2 \cdot 115.5\Theta^2 = 1 + 231\left(\frac{\sigma}{\lambda}\right)^2 \tag{2.26}$$

where σ is the root mean square (RMS) value of the roughness amplitudes on the surface, and they substitute $\Theta = l/\lambda$ at the last equality.

An important note here is that Adamenko and Fuks get a different factor in the Θ^2 term. They find 169, while Ramiere *et al.* use 115.5. It is not clear how this factor comes about. Adamenko and Fuks's integral function $f(\Theta)$, under the $\Theta \ll 1$ assumption, evaluates to 169.

With the σ–dependent conductance ratio, they can now calculate what σ would need to be in order to bridge the gap between their measured Kapitza resistances for the rough Si crystal surface and the AM result (which is roughly that seen for Si in Table 2.1). They present σ as a function of the dominant thermal wavelength in helium, and find a very good match to the relationship $\sigma \simeq 0.3\lambda$. For the temperature range they investigate, phonon wavelengths vary between 2 and 10 nm, meaning the necessary σ span is from around 0.5 to 3.5 nm.

The crucial step is that they show the Si crystal surface actually *is* dominated by roughnesses of these characteristics. Their atomic force microscopy (AFM) measurements of the Si crystal surface reveal that at lengths below $d \simeq 4$ nm, the roughness distribution is described by the left half of a Gaussian bell $\sigma_\mathrm{RMS}{}^2 l^2/4\pi \exp -l^2/4d^2$, where d is the scale length. When performing an AFM measurement, one asks, "how large are the bumps and how many bumps are there on this surface at the scale d". They find $\sigma_\mathrm{RMS} = 4.7$ nm, and $l = 1.5$ nm. So, for one, the σ range they determined from measurements is the range of the roughness on the surface, and the roughness correlation length fulfils the requirement that $\Theta = l/\lambda < 1$ for all temperatures measured.

Their setup permitted a secondary measurement; by looking at the Kapitza resistance at pressures just below and then just above that necessary for solidification of helium, they could tell if the solidified layer of helium discussed previously actually exists. If the layer is there, Ramiere *et al.* posit that no change in the resistance should be seen, because even if the bulk helium solidifies, the helium at the interface was solid already, and would experience no change in properties. What they find is that the resistance drops by about a factor 2. According to AM theory, the resistance should drop, since the solid helium matches the acoustic properties of silicon better than the liquid helium does. Dropping by a factor 2 is roughly in line with there suddenly being transverse phonon transmission channels in addition to the longitudinal[2]. Their conclusion is that if there was a solidified layer present before the bulk helium solidified,

---

[2] Recall, there are a total of three phonon channels, two transverse and one longitudinal, and in the AM result, there is already a factor ~1.5 accounting for partial coupling of the transverse phonons. When the two transverse channels open fully, they suppress the Rayleigh surface modes, turning off the factor 1.5, and replacing it with a factor 3, for an effective factor 2 compared to that before solidification.

then that layer could not have been part of some acoustic matching mechanism, since otherwise there would be no clearly visible phase change in the resistance.

This conclusion depends on a few assumptions. For one, it assumes the structure of the solidified layer remains the same after the bulk behind it completely changes character. Second, it assumes that the layer, as proposed by, for instance, Challis *et al.*, gives rise to exactly as good an acoustic match as what bulk solidified helium would do. It is not clear how they explain the weak pressure dependence of the Kapitza resistance at pressures below solidification. Their measurements are in line with Challis *et al.*'s old ones (Ref. [45]), so there is clearly some effect that suppresses the pressure dependence predicted by AM theory. In their supplementary, they provide the pressure dependent functions for helium density and speed of sound, which is substituted in the expression for Kapitza conductance in Equation (2.18) on page 16. Since the density and speed of sound are considered independent of temperature below the lambda transition, the ratio between the AM Kapitza conductance at 1 bar to that at 25 bar is also independent of temperature. At 1 bar (and 1.9 K), the AM result is $h_\mathrm{K}^\mathrm{AM} = 0.042\ \mathrm{kW\,m^{-2}\,K^{-1}}$, which is very close to the calculation of Cheeke in Table 2.1, while at 25 bar (and 1.9 K), the AM result is $h_\mathrm{K}^\mathrm{AM} = 0.073\ \mathrm{kW\,m^{-2}\,K^{-1}}$. So, an increase of about 75% which in AM theory is ascribed to the improved acoustic matching between the solid and helium as the density and speed of sound increase to get slightly more similar to that of a solid. In Ramiere *et al.*'s resistance plots, which should see a 75% drop, the pressure has nearly no impact on results, up until the first–order phase transition as helium solidifies. They do not suggest any mechanism that may explain this behaviour. That a dense layer of adsorbed helium can exist is supported by there being van der Waals forces tightly binding the nearest helium atoms to the surface [30, Sec. 10.2.1]. Experimental evidence of such adsorbed layers is also found, for example for graphite substrates [57, Sec. 7.1.1].

2.3 Kapitza Resistance Under Large Heat Fluxes

Equation (2.8) on page 13 expresses the net heat flux across an interface between two media with a temperature jump ΔT at the interface. Disregarding the various possible non–phonon related channels discussed in the previous section, the expression is expected to be generally valid;

$$q_\mathrm{net} = 4\sigma T^3 \Delta T \left[1 + \frac{3}{2}\frac{\Delta T}{T} + \left(\frac{\Delta T}{T}\right)^2 + \frac{1}{4}\left(\frac{\Delta T}{T}\right)^3 \right], \tag{2.27}$$

where σ describes the phonon radiation coefficient (which can be determined from PRL, AM, or more exotic approaches).

For the definition of the Kapitza conductance, it is necessary to assume ΔT small in order to then arrive at the form of Equation (2.27) as used before: $q_\mathrm{net} = h_\mathrm{K}\Delta T$, with the T^3 dependence contained in h_K. However, relevant heat transfer scenarios exist where the heat flux is not small enough that ΔT is small. The most relevant scenario for this thesis is that of a superconducting magnet being cooled by superfluid helium.

Take, for instance, the observed Kapitza conductance of copper from Table 2.1 on page 17: $h_\mathrm{K} \simeq 7.5\ \mathrm{kW\,m^{-2}\,K^{-1}}$. For a modest heat flux of just $10\ \mathrm{kW\,m^{-2}}$, ΔT would be ~1.3 K, which is certainly not small considering typical operating conditions of 1.9 K for the helium bath into which this heat must flow.

A note about Equation (2.27) is that it assumes σ is independent of temperature, and that the temperature dependence of the resulting effective h_K remains T^3. However, as found by Clement and Frederking on silver [58, Fig. 4], although at small ΔT the full expression from Equation (2.27) works well, by the time heat fluxes have risen to cause $\Delta T \gtrsim 1$ K, the deviation from measurement is quite clear with Equation (2.27) predicting a higher heat flux for a given ΔT than what is measured. Van Sciver [59, Fig. 4] finds, when working with aluminium, that the Kapitza conductance, expressed as h_0/T^3, with h_0 being the conductance in the low–ΔT limit, drops with increasing ΔT, when a constant value is expected had the T^3 dependence been true also at higher heat fluxes. Finally, Mittag finds for copper, niobium, and aluminium temperature dependencies ranging from T^3 to $T^{4.65}$ [60, Table 1], much stronger than the low–ΔT assumption indicates.

In light of the difficulties with using Equation (2.27), Claudet and Seyfert suggest a fit function [61];

$$q_\mathrm{net} = a_\mathrm{K}\left({T_\mathrm{s}}^{n_\mathrm{K}} - {T_\mathrm{b}}^{n_\mathrm{K}}\right), \tag{2.28}$$

where a_K will be called the Kapitza coefficient, of units $\mathrm{W\,m^{-2}\,K^{-n_K}}$, and n_K will be called the Kapitza exponent. T_s is the surface temperature of the heater, and T_b is the bath temperature. The two parameters a_K and n_K are determined experimentally, and they cannot be considered material parameters, but rather local surface parameters of the heater. It is also worth nothing that several different pairs of a_K and n_K will give very similar numerical results from Equation (2.28) within relatively large surface temperature ranges.

In the work presented herein, any reference to the “Kapitza model” will always refer to Equation (2.28), as a matter of convenience, despite no relationship with Kapitza the scientist.

The form of the Kapitza model looks very much like that of the phonon radiation balance in Equation (2.7) on page 12, just with a free exponent, as opposed to the theoretical value fixed at 4. Claudet and Seyfert do not give any physical explanation nor any derivation of their proposed expression. It appears the function simply does a good job of fitting the data. Note that in a paper a few years later, Kashani and Van Sciver propose a form of Equation (2.28) that has the same form as Equation (2.27) [62], by expanding it as a binomial series[3]. This still does not establish a physical connection between the phonon radiation balance and the Kapitza model as suggested by Claudet and Seyfert, however, since the binomial expansion is a mathematical property of the polynomial, not a physical one. An early precursor to the Kapitza

---

[3]

$$\begin{aligned} q_\mathrm{net} &= a\left({T_\mathrm{s}}^n - {T_\mathrm{b}}^n\right) = a\left([T_\mathrm{b} + \Delta T]^n - {T_\mathrm{b}}^n\right) = a\left(\left[\sum_{k=0}^{n}\binom{n}{k}{T_\mathrm{b}}^{n-k}\Delta T^k\right] - {T_\mathrm{b}}^n\right) \\ &= an{T_\mathrm{b}}^{n-1}\Delta T\left[1 + \frac{n(n-1)}{2!}\left(\frac{\Delta T}{T_\mathrm{b}}\right) + \frac{n(n-1)(n-2)}{3!}\left(\frac{\Delta T}{T_\mathrm{b}}\right)^2 + \frac{n(n-1)(n-2)(n-3)}{4!}\left(\frac{\Delta T}{T_\mathrm{b}}\right)^3 + \dots\right] \end{aligned}$$

model could be by Goodling and Irey [63, Eq. 1], which relates the bath temperature to the Kapitza conductance by a variable exponent, rather than the theoretical 3;

$$h_{\mathrm{K}} = AT^{B}, \tag{2.29}$$

where A and B are fit parameters found from measurements.

In light of this, there are no obvious bounds on the parameters. Seeing as the observed temperature dependence of the Kapitza conductance has been found at least as high as $T^{4.5}$, this could be considered an upper limit for n_{K}.

Jones and van der Sluijs measure the Kapitza conductance between a large number of copper samples and superfluid helium at several bath temperatures, fitting their result to the same expression as Goodling and Irey [64]. They find one sample of machined copper whose Kapitza conductance shows a temperature dependence of $T^{6.4}$, and several on the order of T^{6} after coating the copper with thin layers of silver. Most of their samples are fitted with exponents below 4.5, though.

Figure 2.5 shows Kapitza model fits to data from several sources. Cu, 1.8 K and Cu, 2.14 K show the fit to Goodling and Irey's data for a copper cylinder at the indicated bath temperatures, while Pt, 1.8 K and Pt, 2.14 K show fits to their data for a platinum cylinder [63]. The two Cu – polished curves show the fit to data by Kashani and Van Sciver's measurements of a mechanically polished copper surface in a 2 K bath [62]. S1 and S2 refer to Sample 1 and Sample 2 which went through the same surface preparation steps. Cu – solder refer to two different samples also by Kashani and Van Sciver, where the copper surface was coated with a thin layer of solder (50%Pb–50%Sn). Ag, 1.8 K and Ag, 2.1 K show fits to data from a silver surface measured by Clement and Frederking [58]. Au–Mn 2.0 K shows the fit to data from a thin gold–manganese wire measured by Shiotsu *et al.* [65][4]. Taneda, 1.8 K shows the fit to data from a copper heater measured by Taneda *et al.* [67]. Note, they also give measurements on stainless steel, relevant to this thesis, but it seems their measurements of steel failed to account for the very low thermal conductivity when calculating the heater surface temperature. They test an unspecified epoxy resin as well, and conclude their method of calculating the heater surface temperature does not work for the epoxy. The thermal conductivity of stainless steel is much closer to that of polymers than that of pure copper (see Figure 3.36 on page 104), meaning that there will be a very large gradient between the hot back of the heater sample and the helium cooled surface, leading to a surface temperature calculation that is very sensitive to the exact temperature dependent thermal conductivity of the material.

Claudet, high and Claudet, low are the proposed upper and lower bounds for copper suggested by Claudet and Seyfert from their measurements on copper heaters with various surface treatments at 1.9 K [61]. Obviously, there are copper samples both above and below these limits, further reinforcing the fact the fit parameters are not really anchored in the material itself.

Symbols indicate the data points from sources. The Kapitza parameters for all curves are given in Table 2.2. They are found by using the Python package **`lmfit`** which

---

[4] It is not clear in Shiotsu *et al.* what the material of the wire is. However, their group had earlier done work on liquid helium, and describe that setup with a 0.08 mm heater wire of Au–Mn (0.25 weight percent)[66], and it seems likely Shiotsu *et al.* refer to the same setup.

implements the Levenberg–Marquardt algorithm [68] to optimise, in a least–squares error sense, the free parameters a_K and n_K in the Kapitza model (Equation (2.28)), to the given data. The table also contains rough uncertainty estimates. Figure 2.6 illustrate how these approximate uncertainty ranges are determined. The ranges are not meant as statements about measurement accuracy, but as illustrations of how sensitive the Kapitza model fitting is to even small temperature variations in data.

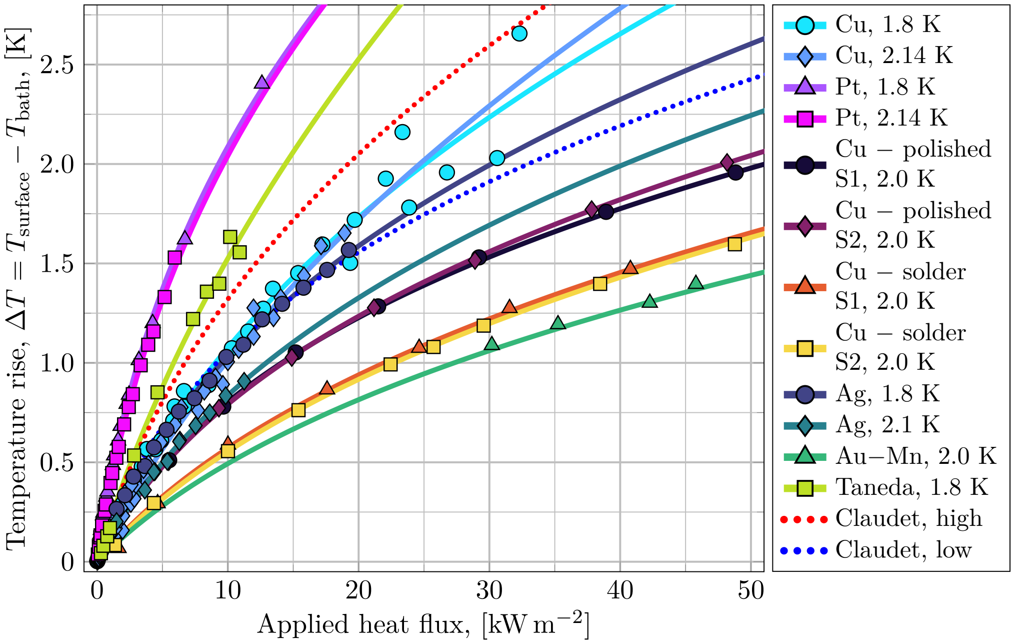

Figure 2.5: Measured data, and Kapitza model fits to the data, from several sources. Inspired by Van Sciver [30, Fig. 7.38]. The measured temperature ranges tend to be quite similar, with $\Delta T_{\max}$ ~2 K, but the necessary heat flux to reach this heater surface temperature varies greatly from sample to sample. Table 2.2 gives the Kapitza model fit parameters to the data.

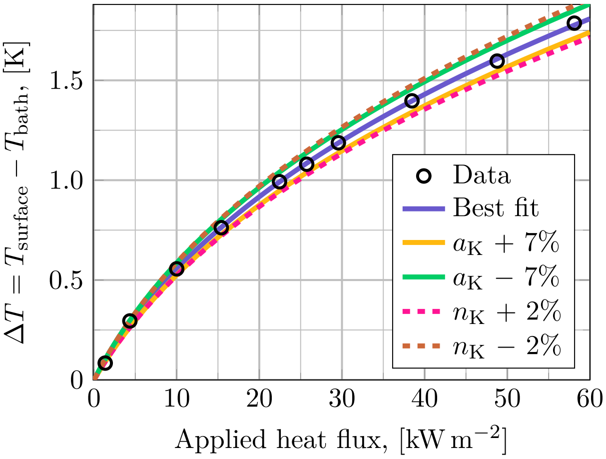

Figure 2.6: Illustration of what the uncertainty ranges in Table 2.2 mean. Data is that by Kashani and Van Sciver for their solder–coated Sample 2 [62]. Best fit is the curve shown in Figure 2.5. The remaining four curves alter the indicated parameter while keeping the other constant. The resulting range on the two parameters are such that they cover all data–points.

Table 2.2: Kapitza model fit parameters for all curves in Figure 2.5. The errors indicated on fit parameters represent the approximate range in the parameter that still gives a ΔT–curve that captures the data while the other parameter remains fixed.

Curve	Heat flux range, $[\mathrm{kW\,m^{-2}}]$	a_K, $[\mathrm{W\,m^{-2}\,K^{-n_K}}]$	n_K
Cu, 1.8 K	0 — 32.3	913.2 ±21%	2.597 ±6%
Cu, 2.14 K	0 — 18.9	1254.8 ±19%	2.274 ±6%
Pt, 1.8 K	0.2 — 12.6	215.6 ±6%	2.909 ±2%
Pt, 2.14 K	0 — 5.9	170.0 ±8%	2.952 ±2%
Cu - polished S1, 2.0 K	5.5 — 58.7	241.0 ±4%	3.913 ±1%
Cu - polished S2, 2.0 K	5.5 — 57.6	352.3 ±6%	3.606 ±1%
Cu - solder S1, 2.0 K	1.6 — 54.6	702.9 ±6%	3.397 ±2%
Cu - solder S2, 2.0 K	1.4 — 58.1	787.8 ±7%	3.333 ±2%
Ag, 1.8 K	1.5 — 19.3	481.6 ±10%	3.172 ±3%
Ag, 2.1 K	1.1 — 11.2	406.5 ±17%	3.339 ±4%
Au-Mn, 2.0 K	30.2 — 203.3	671.2 ±8%	3.612 ±1%
Taneda, Cu, 1.8 K	0.3 — 10.2	1191.4 ±13%	2.049 ±5%
Claudet, high	0 — 90	490	2.8
Claudet, low	0 — 90	200	3.8

One of the main conclusions from Figure 2.5 is that making general recommendations on what Kapitza parameters to use, for example when designing a cooling system for magnets, is hard. At $Q_\mathrm{applied} = 25\ \mathrm{kW\,m^{-2}}$, various uncoated copper samples show ΔT range from about 1.4 to 2.4 K, which could certainly be the difference between a superconducting magnet quenching or remaining superconducting. As was mentioned earlier, the Kapitza parameters do not give unique curves when allowing for small deviations; take, for instance, the two Cu – polished curves. They are nearly identical, but their fit parameters are quite different. This means that if accurate knowledge of the heat transfer characteristics of an object cooled by superfluid helium is needed, dedicated measurements must be made. It is also hard to conclude about the importance of bath temperature; for Cu, 1.8 K and Cu, 2.14 K results are similar enough the difference would not matter in practice, but Ag, 1.8 K and Ag, 2.1 K differ by about 0.3 K around $Q_\mathrm{applied} = 25\ \mathrm{kW\,m^{-2}}$, which could be important in some applications. Finally, note that none of the Kapitza exponents in Table 2.2 go above 4. While not conclusive, it strengthens the idea that the Kapitza model suggested by Claudet and Seyfert represent a sort of non–ideal radiation balance with an upper limit of $n_\mathrm{K} = 4$, as for black–body radiation. Kashani and Van Sciver's own fit to the Cu – polished S1, 2.0 K data gives $a_\mathrm{K} = 270$ and $n_\mathrm{K} = 3.995$, which results in a curve practically indistinguishable from the one made by the parameters in Table 2.2. It seems wrong, then, to take the Kapitza exponent to represent how close a surface is to ideal by how close it is to 4; the surface of Cu – polished S2, 2.0 K, prepared in the same way, deviates much further from 4, without obvious reason.

Why not just say there exists an upper limit of $n_\mathrm{K} = 4$? Going back to Section 2.1.1 on page 12, discussing the phonon radiation limit, everything starts off by assuming the Debye model is valid, giving an estimate for the phonon energy distribution in the solid. This gives the heat flux its T^4–dependence. This assumption is very good at low temperatures, but it is not exact, meaning $n_\mathrm{K} \leq 4$ is not firmly established. Now, the point still stands; while the Kapitza parameters do not appear to have upper bounds determined on theoretical grounds, it seems, from the subset of available data shown here, that a_K tops out around 1200 $\mathrm{W\,m^{-2}\,K^{-n_K}}$, and n_K respects an upper bound of 4.

2.4 Some Properties of Superfluid Helium

So far, the properties of helium itself have not mattered beyond the acoustic impedance and its impact on heat transfer at the heater–helium interface. However, something must obviously happen with the heat after it has crossed this interface into helium. Furthermore, what happens when the applied heat flux goes even higher than that discussed in the previous section? A heater submerged in an everyday liquid like water eventually starts to display nucleate boiling at the heater surface (and even film boiling if the heating power density significantly surpasses those typically encountered in the kitchen). This section discusses heat transfer properties within superfluid helium, and lead into the transient phenomena around onset of film boiling discussed in the following section.

2.4.1 Lambda Transition and Zero Viscosity

In the early 1930's, Keesom and Keesom found a peak in the heat capacity of helium around 2.17 K [69] (see Figure 2.7), and some time before that, Onnes had noted a peak in the helium density around the same temperature [70, p. 25] (see Figure 2.8). In 1936, Keesom and Keesom found that while helium above T_λ had thermal conductivity "of the order of magnitude of the heat conductivity of gases at ordinary temperatures", the apparent thermal conductivity became too large for their apparatus to measure upon dropping below T_λ [71]. They ascribed this to helium being "superheat–conductive" below the lambda transition. In 1938, both Kapitza [72], and Allen and Misener [73] (in the same issue of Nature), published measurements showing that helium below T_λ has extremely low viscosity. Kapitza coins the term "superfluid" as a qualitative descriptor of the observed behaviour. Then, in 1941, Kapitza publishes the seminal paper firmly establishing that the large effective thermal conductivity of superfluid helium observed by Keesom and Keesom is due to its low viscosity, not a particularly large thermal conductivity in and of itself, and also showing the existence of the thermal interface resistance now known as Kapitza resistance [32].

Concurrent with the experimental work in the mid to late 1930's was the theoretical effort of explaining the observations. Keesom and Keesom, in their measurements on the heat capacity, expected to find a latent heat associated with the transition, but found none. London proposed that the lambda transition was essentially like that of a Bose gas condensing into a Bose–Einstein condensate [75]. Importantly, this helps explain why there is no latent heat associated with the lambda transition; the heat capacity of a Bose gas is continuous through condensation, but the first derivative of the heat capacity is not. A month later, Tisza proposed the precursor to the two–fluid model (see Section 2.4.2), explaining many of the observations, though not explaining

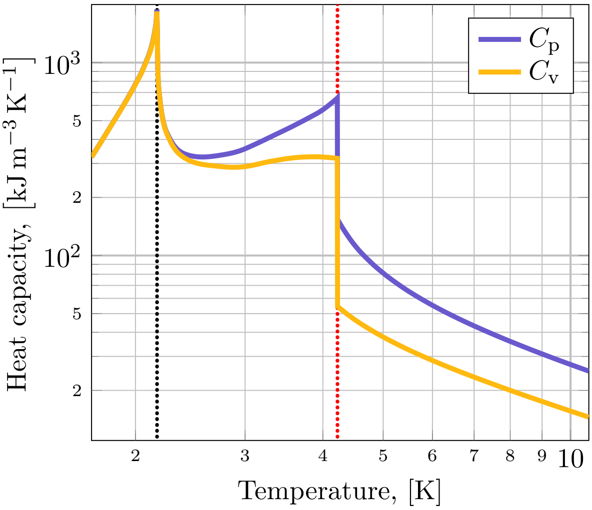

Figure 2.7: Temperature dependent volumetric heat capacity of helium between 1.7 and 10 K. Data is taken from Arp *et al.* [74]. The black dotted line indicates the lambda temperature, T_λ ~2.166 K at 1 atm. The red dotted line indicates the boiling temperature, T_{boil} ~4.222 K at 1 atm.

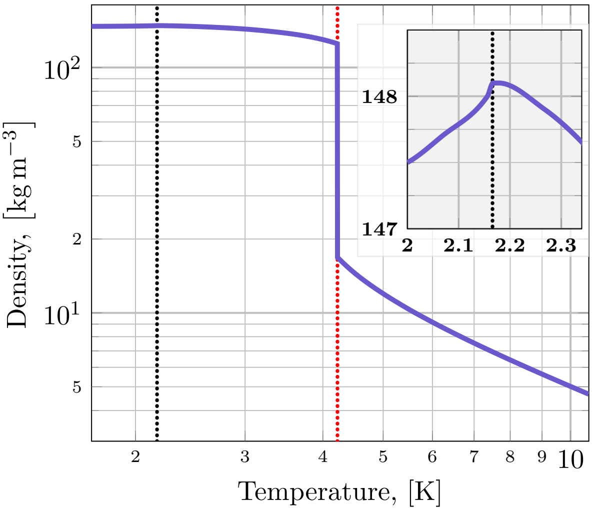

Figure 2.8: Temperature dependent density of helium between 1.7 and 10 K. Data is taken from Arp *et al.* [74]. The black dotted line indicates the lambda temperature, T_λ ~2.166 K at 1 atm. The red dotted line indicates the boiling temperature, T_{boil} ~4.222 K at 1 atm. The inset highlights, in linear scale, the density around T_λ.

why the heat capacity measured by Keesom and Keesom had a much sharper peak than that predicted by London [76].

Landau realised that the excitation spectrum of the Bose–Einstein condensate would not give rise to the observed heat capacity nor the superfluid behaviour [77]. Landau's intuition provides a simple and elegant explanation of how the viscosity of helium vanishes below T_λ; picture a volume of liquid into which a heavy projectile is launched [70, Sec. 1.5.1]. The projectile, of mass M, velocity $\mathbf{v}$, and speed v has initially the kinetic energy $E_{\text{in}} = \frac{1}{2}Mv^2$. It then interacts with the fluid, which saps some of the projectile's kinetic energy by way of an excitation that carries off an energy ϵ, with momentum $\mathbf{p}$. The projectile's new velocity and speed is $\mathbf{v}'$ and v'.

Conservation of energy and momentum demand,

$$\begin{aligned}\frac{1}{2}Mv^2 &= \frac{1}{2}Mv'^2 + \epsilon \\ M\mathbf{v} &= M\mathbf{v}' + \mathbf{p}.\end{aligned} \tag{2.30}$$

If the kinetic energy of the projectile is much larger than the energy of the excitation, one can approximate the energy balance as (and baking the factor 1/2 into ϵ for convenience),

$$M\left(v^2 - v'^2\right) \simeq Mv\left(v - v'\right) = \epsilon \quad \Rightarrow \quad M\left(v - v'\right) = \frac{\epsilon}{v}. \tag{2.31}$$

The momentum balance is,

$$M(\mathbf{v} - \mathbf{v}') = \mathbf{p}. \tag{2.32}$$

Of course, $|\mathbf{v} - \mathbf{v}'| \geq (v - v')$, which means $M(v - v') \geq p$, which, using the energy balance, gives,

$$p \leq \frac{\epsilon}{v} \quad \Rightarrow \quad v \geq \frac{\epsilon}{p}. \tag{2.33}$$

This means that only if the projectile has a velocity larger than some minimum $v_\mathrm{c} = (\epsilon(\mathbf{p})/p)_\mathrm{min}$, where $\epsilon(\mathbf{p})$ is the excitation spectrum of the liquid, is an excitation created. Otherwise, the liquid poses no resistance to the passing of the projectile. In the case of a liquid flowing around an object, or in a pipe with walls that are not ideally smooth, the same picture holds, it's just the liquid atoms moving, instead of the projectile/wall.

So, what are the excitation spectra relevant to liquids? The ideal non–interacting Bose–Einstein condensate only has single–particle excitations of the form $\epsilon(\mathbf{p}) = p^2/2m$ (kinetic energy of a single particle), while a normal liquid also has collective excitations (longitudinal phonons), with spectrum $\epsilon(\mathbf{p}) = v_\mathrm{sound}p$.

In a liquid with single particle excitations of the form $\epsilon(\mathbf{p}) = p^2/2m$, any velocity is large enough to satisfy the condition of Equation (2.33), since $p = mv$, so even for $v = 0$, there exists an accessible excitation momentum at least that small.

Landau's idea is to postulate that in the superfluid state, instead of the single particle excitation of the Bose–Einstein condensate, there is a collective behaviour whose excitations are called rotons[5] with a spectrum of the form[6],

$$\epsilon(\mathbf{p}) = \Delta + \frac{(p - p_0)^2}{2\mu}, \tag{2.34}$$

where Δ is the energy needed to excite a single roton, and p_0 and μ are empirically determined quantities. The values for these parameters are [81, p. 37],

$$\frac{\Delta}{k_\mathrm{B}} = 8.65\ \mathrm{K} \quad \frac{p_0}{\hbar} = 1.92\ \text{Å}^{-1} \quad \mu = 0.16m_4 \tag{2.35}$$

---

[5] They have this name from early considerations picturing them as helium atoms rotating around each other in a sort of backflow, where a central atom moves forwards, while neighbours flow around it [78, Fig. 2.17]. Feynman pictured them as smoke rings [79, Fig. 11.21].

[6] Note that in Landau's first paper, the proposed spectrum was not shifted upwards by p_0. The spectrum with local maxima and an minima, which leads to the correct heat capacity, was only suggested by Landau in 1947 [80].

where m_4 is the atomic mass of one helium atom. The energy gap Δ depends weakly on both pressure and temperature. In particular, as Khalatnikov notes, closer to T_λ, the it is no longer accurate to disregard interactions in the gas of excitations (dominated by rotons) [41, p. 6]. Figure 2.9 shows Landau's proposed excitation spectrum, together with recent measured values. Note that Landau's proposal only pertains to the region up to about 0.5 $Å^{-1}$, and around the roton minimum near 2 $Å^{-1}$. Between these, they did not rigorously define the spectrum.

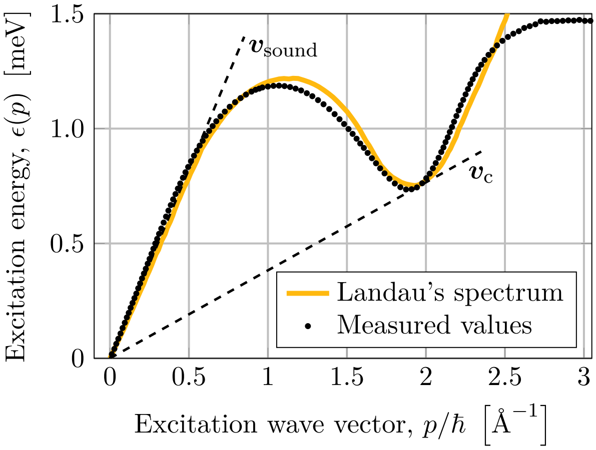

Figure 2.9: Excitation spectrum [78, recreated from Fig. 2.16]. Measured values are those by Godfrin *et al.* at saturation pressure and 0.1 K [82]. The slope v_{sound} indicates that for low momentum excitations, the spectrum matches that of phonons with speed of sound v_{sound}. The slope v_{c} indicates the critical speed below which no excitations can exist at all, in accordance with the condition in Equation (2.33).

With this kind of excitation spectrum, at fluid speeds below v_{c}, no excitations exist, and the fluid exhibits zero viscosity.

2.4.2 Two–Fluid Model

Helium below T_λ is superfluid, and Landau's excitation spectrum explains why. The spectrum does not, however, explain the transport properties of superfluid helium (for instance the effective thermal conductivity)[7].

To date, the best explanation is the phenomenological idea of the two–fluid model,

---

[7] It is worth noting that there appears to be some irregularities in the chronology of the development of the theory of He II related to much of the early work having happened right around the Second World War. In fact, Tisza held on to their trust in London's Bose–Einstein condensate idea, and developed hydrodynamics from that starting point already in 1940 [83, 84], relying on a condensate wave–function, which succeeded in predicting the fountain effect, and in interpreting second sound waves as entropy mediated temperature waves (unlike Landau, who gave no interpretation of the second kind of sound wave they found as a result of their hydrodynamic equations). Tisza's equivalent to Landau's rotons is atomic excitations in the Bose–Einstein condensate. After developing their theory further [85], Tisza to find better agreement with second sound speed measurements than what Lifshitz did from Landau's theory, though this has since been ascribed to Tisza only considering the temperature range between 1 K and T_λ [86, Fig. 2]. Landau's improved excitation spectrum was published around the same time as Tisza's developed theory. Of course, Landau had a measure of vindication by the measured excitation spectrum being essentially identical to their postulated one. Also, Landau's explanation of zero viscosity by way of the postulated roton excitation spectrum is a little more satisfying than Tisza's postulate that He II has vanishing shear modulus (which is equivalent to having zero viscosity), since Landau's approach leads *from* theory *to* observations, while Tisza's approach relies on proving from observations that the theory is correct.

first conceived by Tisza and developed by Landau. The idea is to consider helium below T_λ as a mix of two fluids, one normal–fluid component, and one superfluid component. The normal–fluid component carries all the usual properties of a normal liquid, like viscosity and entropy, as well as the excitations discussed earlier (phonons and rotons), while the superfluid component has none of these properties. The superfluid component doesn't even have a temperature seeing as it has no entropy.

Kapitza's "superfluid" term had already percolated through the relatively small superfluid research community at the time, and in hindsight, the inevitable confusion between Kapitza's superfluid and Tisza/Landau's superfluid component is unfortunate. The remedy has been to talk of helium below T_λ as He II, and above T_λ as He I, and then keeping Landau's component–wise nomenclature for He II. The key drawback to this convention is that it lends the two–fluid model more veracity than it deserves. The picture of two fluids sometimes interacting and sometimes not works to explain some of the properties of He II, but fails for others, ultimately because the picture itself is wrong; there is only helium, and one cannot pick all the blue superfluid–component atoms out of a container, leaving only the red normal–fluid–component atoms behind.

From here, the convention of calling helium below T_λ He II, and calling the two–fluid model's components normal–fluid and superfluid is followed.

He II has a density, ρ, and in the two–fluid picture, this is the sum of contributions from the two components;

$$\rho_{He\,II} = \rho = \rho_{\mathrm{n}} + \rho_{\mathrm{s}}, \tag{2.36}$$

where (as will be the case going forwards) subscript "n" refers to the normal–fluid component, and subscript "s" the superfluid component.

The He II entropy is contained exclusively in the normal–fluid component, and so,

$$\rho S_{\mathrm{He\,II}} = \rho_{\mathrm{n}} S_{\mathrm{n}}, \tag{2.37}$$

where S_x refers to the total entropy $= s\,N\,m_4$ where N is the number of particles and m_4 is the mass of one helium atom, and s is the specific entropy.

In the two–fluid model, it is assumed that the entropy of the normal–fluid component is fixed at the value it had just as the He II passed below T_λ; $S_{\mathrm{n}} = S_\lambda$. Clearly, the entropy of He II is not constant, so the idea is to let $\rho_{\mathrm{n}}(T)$ take care of the temperature dependence. The ratio ρ_{n}/ρ is approximately [30, Eq. 6.43] (and plotted in Figure 2.10),

$$\frac{\rho_{\mathrm{n}}(T)}{\rho(T)} = \frac{S(T)}{S_{\mathrm{n}}} = \left(\frac{T}{T_\lambda}\right)^{5.6}. \tag{2.38}$$

Landau pointed out in their original paper that a measurement of the normal–fluid component density could be done by measuring the change in moment of inertia of a vessel filled with He II as it oscillates under changing temperature, since the superfluid component has no viscosity, meaning the average resistance to motion would drop as the superfluid component fraction grows [77]. Andronikashvili performed this experiment by constructing a closed vessel within which they placed a stack of 100 thin aluminium plates separated along the z–axis by about 200 µm. They then twisted this vessel around the z–axis by pulling on a lever acting on the axis with a magnet, and measured the rate of damping of the oscillations, relating this rate of damping to the change in inertia of the vessel [87]. Another example of such measurements is that by Hussey *et al.* where they measure similar damping of an open vessel where the drag is on two parallel rods [88].

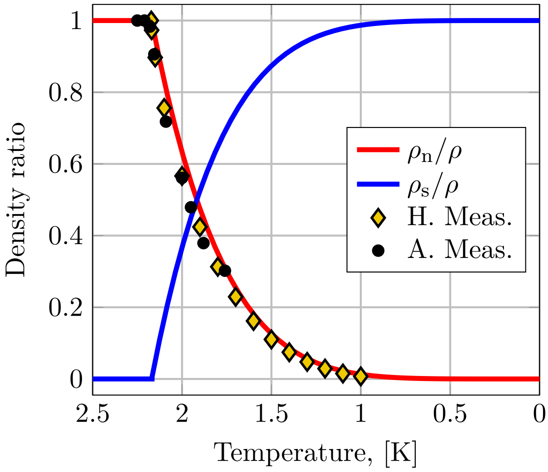

Figure 2.10: He II component ratios, calculated from Equation (2.38), as they change with temperature, plotted so as to evoke the path from above to below T_λ. H. Meas are the measurements by Hussey *et al.* where they measure viscous drag on two parallel cylinders oscillating around the axis halfway between them [88]. A. Meas. are the measurements by Andronikashvili where they measure viscous drag on a stack of parallel plates oscillating around their common axis [87].

The modelling effort done as part of this thesis does not rely on the full two–fluid model itself, but rather the much simpler mutual friction heat transfer regime described by Gorter and Mellink. As such, a more comprehensive description of the two–fluid model is not given here.

2.4.3 Not–So Sudden Phase Change

A short note about the phase transition is in order here. From the density fraction experiments, the phase transition from He I to He II essentially comes upon the fluid all the sudden. Just above T_λ, the superfluid component density fraction is zero, and it only starts growing from zero at T_λ. So, in the two–fluid model picture, all properties that hinge upon there being a superfluid component present, such as the large effective thermal conductivity, will behave as those of the pure normal–fluid component all the way down to exactly T_λ. This is in line with the ideal gas picture that initially motivated London's Bose–Einstein condensate proposition. The fluid consists of non–interacting particles, and they have properties described by Landau's two–fluid model. However, clearly, the heat capacity anomaly that first indicated helium does not behave like a regular fluid starts *before* T_λ, not *at* T_λ. As Guenault puts it "it is as if the system sees the transition coming" [70, p. 31]. The effect of this is easily observed in experiments; in a cryostat slowly cooled down from above to below T_λ, the time at which the super–heat–conductivity of helium starts precedes the time at which the heat capacity reaches its maximum by up to several seconds depending on the rate of cooling (see Section 4.5.1 on page 133 for relevant results from the work presented herein, or Capsi's measurements at the Lawrence Berkeley Laboratory [89]). This is all because He II is not really an ideal non–interacting system, which the two–fluid model essentially supposes. It is rather a system with significant inter–particle interactions; around the transition temperature the growing long–range order that, eventually, far below T_λ, is captured by the two–fluid model, is not properly described by the simplified picture of two independent fluid components.

Another experimental observation that illuminates the shortcomings of the two–fluid model is that measuring the actual fraction of helium atoms that occupy the zero–momentum ground state near $T = 0$ is not 100% as the two–fluid model indicates, but rather on the order of 10–15% [90]. This is qualitatively in line with what is found for an interacting Bose gas [78, Sec. 2.6][91, Sec. 3.7].

2.4.4 Mutual Friction Between the Two Components

Gorter and Mellink, upon reviewing measurements of steady state heat flux through and pressure gradient in capillaries filled with He II find that at high temperature gradients, the relationship $\nabla P = \rho s \nabla T$, called the London Equation or fountain pressure [30, Eq. 6.33], does not hold [92]; at high temperature gradients, the pressure gradient is lower than it ought to be. From the observation that heat flux in a capillary of He II tends to be proportional with the cube root of the temperature gradient, they postulate that an internal friction between the normal–fluid and superfluid components is responsible for the lower pressure. They propose the following expression for this force per unit volume of He II;

$$f = A\rho_\mathrm{n}\rho_\mathrm{s}(v_\mathrm{s} - v_\mathrm{n})^3, \tag{2.39}$$

where A is now called the Gorter–Mellink mutual friction coefficient A_GM, which is temperature dependent, and on the order of 1200 $\mathrm{m\,s\,kg^{-1}}$ at 1.9 K [30, Fig. 6.32], while $\mathbf{v}_\mathrm{n}$ and $\mathbf{v}_\mathrm{s}$ are the velocities of the two fluid components. This form of the force ensures that the largest interaction force happens when the two components are present at equal fractions. This force is taken to act on both fluid components, and in steady state, starting from the hydrodynamic equations for the two component velocities, they find,

$$\nabla T = \frac{\mu_\mathrm{n}}{\rho s}\nabla^2 \mathbf{v}_\mathrm{n} + A_\mathrm{GM}\frac{\rho_\mathrm{n}}{s}\left|\mathbf{v}_\mathrm{s} - \mathbf{v}_\mathrm{n}\right|^2(\mathbf{v}_\mathrm{s} - \mathbf{v}_\mathrm{n}), \tag{2.40}$$

where μ_n is the normal–component viscosity. These two terms, then, represent laminar and turbulent heat flow.

For simplicity, consider the heat flow to be along a one–dimensional circular pipe of diameter d. Assume further that the two contributing terms in Equation (2.40) can be considered independent of each other, meaning that the transition from laminar to turbulent (mutual friction) heat transfer is continuous and that the turbulence associated with the superfluid component does not influence the laminar normal–fluid component flow. Now, the laminar flow contribution to the temperature gradient $\mathrm{d}T/\mathrm{d}x$ is found by rearranging the solution to the Hagen–Poiseuille equation[8], leading to,

$$\frac{\mathrm{d}T}{\mathrm{d}x} = -\frac{32\mu_\mathrm{n}}{\rho s d^2}v_\mathrm{n} - \frac{A_\mathrm{GM}\rho_\mathrm{n}}{s}\left|v_\mathrm{n} - v_\mathrm{s}\right|^3, \tag{2.41}$$

---

[8] The Hagen–Poiseuille equation for steady state laminar flow is extensively described in any introductory fluid mechanics textbook, for instance that by White [93, Sec. 4.10].

In order to finally relate the temperature gradient and heat flux, they use the relationship $Q = \rho s T v_\mathrm{n}$, first proposed by London and Zilsel when they looked at laminar heat flow in He II [94];

$$\frac{\mathrm{d}T}{\mathrm{d}x} = -\frac{32\mu_\mathrm{n}}{(\rho s d)^2 T} Q - \frac{A_\mathrm{GM}\rho_\mathrm{n}}{\rho_\mathrm{s}^3 s^4 T^3} Q^3. \tag{2.42}$$

Note that in Gorter and Mellink's derivation they assume the flow is between parallel plates, which leads to a factor 12, rather than 32, in the Hagen–Poiseuille solution. This factor is often referred to as β [30, Eq. 6.71]. Furthermore, for non–circular channel cross sections, the parameter d no longer denotes diameter, but rather a characteristic channel size depending on the width and height of the channel (not to be confused with the hydraulic diameter of a duct) [95][96, Eq. 5.3].

Since there is no diameter dependence in the mutual friction term, in wide channels, heat fluxes of relevance to cooling of large equipment are completely dominated by the friction term. Figure 2.11 shows the contributions to the thermal gradient from the two terms for three pipe diameters. Already around 100 to 150 $\mathrm{W\,m^{-2}}$ the mutual friction term starts to dominate for wide channels, and by 1 $\mathrm{kW\,m^{-2}}$, the laminar contribution can be neglected entirely for channels on the scale of 1 mm. For this estimate, a normal–fluid component viscosity $\mu_\mathrm{n} = 1.3 \cdot 10^{-6}$ Pa s has been used [30, Appendix A4].

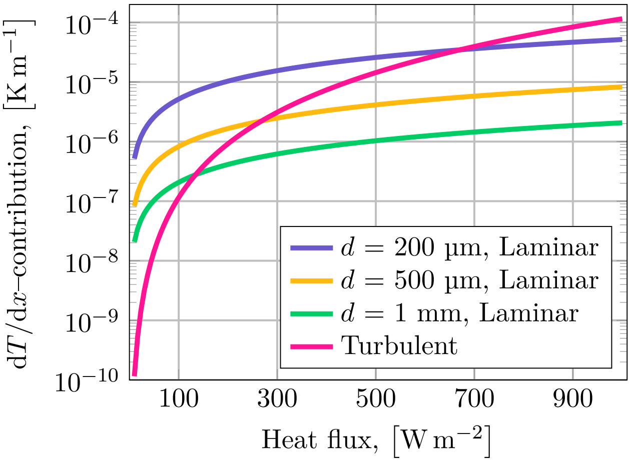

Figure 2.11: Contribution to thermal gradient from laminar flow and turbulent flow as a function of heat flux, in 200 µm, 500 µm, and 1 mm diameter pipes filled with He II at 1.9 K and 1 bar.

Mutual friction was given theoretical basis initially by Onsager [97, p. 693] as a form of superfluid turbulence, also developed by Feynman [98]. The idea is that the superfluid component of He II behaves analogously to the vortex state of a superconductor, where the density of the superfluid component is not uniform in space, allowing for continuous vortex lines of normal–fluid helium to exist in equilibrium within the bulk He II. All these vortex lines make up a random tangle that gives rise to the mutual friction between the two components. Vinen, bulding on this picture of a mass of uniformly distributed vortex lines, explains Gorter and Mellink's observations by making a phenomenological argument for how the normal–fluid component interacts with the mass of vortices [99]. The approach is to first divide the problem of finding

Gorter and Mellink's mutual friction term into two; 1) find an expression for the total length of vortex lines in a unit volume of He II, and 2) find an expression for the force per until length of vortex line acting on the tangled mass of vortices. The total force, proposed and measured by Gorter and Mellink, will then be the total vortex line length multiplied by the force per unit length of a vortex line. As part of the work in developing the phenomenological model of mutual friction, Vinen did comprehensive experiments measuring the onset time of turbulence [100]. Their measurements were done on two rectangular channels subject to steps in applied heating power density. The delay time τ is that between the time at which power is applied and the time at which turbulence is detected (using the attenuation of second sound heat pulses as a measure of the level of turbulence[9]), and a power law is found to describe the relationship between delay time and applied heating power density [100, Eq. 1];

$$\tau = a\,Q^{-3/2}, \tag{2.43}$$

where a is an experimentally determined fit parameter of units $\mathrm{s\,W^{3/2}\,m^{-3}}$. A plot of Vinen's delay time measurements is shown in Figure 2.12. The curve is the power law fitted to data with $a = 37\ \mathrm{s\,W^{3/2}\,m^{-3}}$.

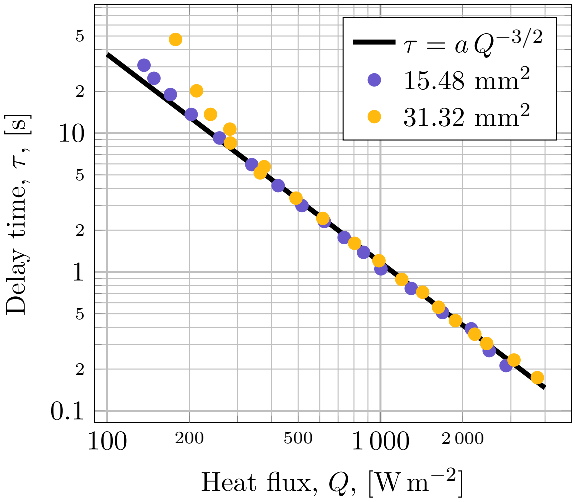

Figure 2.12: Time before onset of turbulence in a rectangular channel of indicated cross section, filled with He II at 1.41 K, upon switching on a step in heating. Before power is turned on, the helium is left undisturbed for a long time [100, Fig. 3]. The fit parameter a is $37\ \mathrm{ks\,W^{3/2}\,m^{-3}}$.

Chase conducted comprehensive studies of the fit parameter a in Vinen's turbulence onset time power law [101], and of Gorter and Mellink's temperature gradient Q^3–dependence [102].

Chase's results from measurements to find a in various geometries are shown in Figure 2.13, together with the results Vinen obtained by fitting Equation (2.43) to their temperature dependent data, as well as the results of Wang's turbulence onset measurements in open bath [103]. Note that it is unclear to what cross section Vinen's data pertains. All of Chase's geometries are essentially circular, though several of them have various kinds of obstructions along the axis of heat flow. Chase does not draw

---

[9] See, for instance, Section 6.5.6 in [30] for a description of second sound attenuation in the presence of mutual friction.

firm conclusions from the data, though notes that a is smaller for channels of irregular cross section, and larger for smooth circular cross sections, indicating that turbulence sets in faster for irregular geometries.

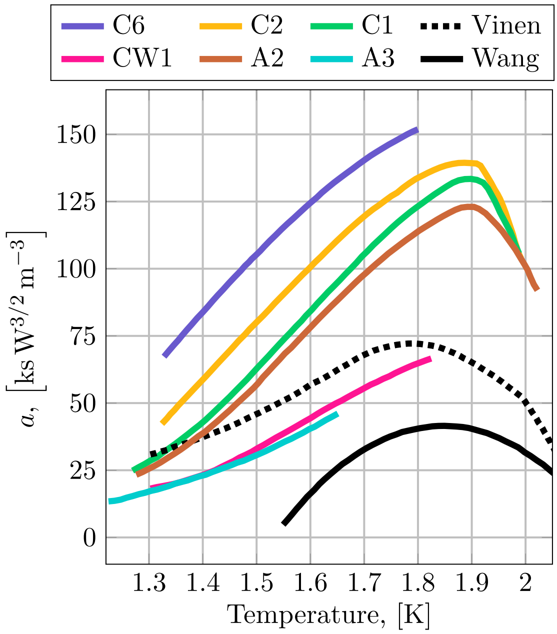

Figure 2.13: Chase's fit for parameter a in Equation (2.43), found for several circular geometries [101, Fig. 2], together with Vinen's results for a rectangular channel [100, Fig. 4], as well as Wang's data for a wire heater in an open bath at 1 bar [103, Fig. 4].
C6 : nine parallel pipes $d = 800$ µm;
C2 : pipe $d = 4.04$ mm;
C1 : pipe $d = 2.62$ mm;
CW1 : same as C1 , but filled with 70 steel wires $d = 250$ µm;
A2 : same as C2 , but steel rod $d = 1.59$ mm along axis;
A3 : same as C2 , but steel rod $d = 3.2$ mm along axis;
Vinen : rectangular channel either 2.4 mm by 6.45 mm, or 4 mm by 7.83 mm.
Wang : open bath at 1 bar.

Chase's tests of the Gorter–Mellink Q^3–dependence starts with the assumption that the thermal gradient in their one–dimensional geometries follows,

$$\left|\frac{\mathrm{d}T}{\mathrm{d}x}\right| = D(T)Q^3, \tag{2.44}$$

where $D(T)$ is the temperature dependent function made up of all the parameters in front of the heat flux factor in the Gorter–Mellink mutual friction term in Equation (2.42). The value for the thermal gradient Chase compares with this expression is the measured gradient minus the contribution from the laminar flow term.

Their measurements span a large range, from $Q_{\mathrm{app}} = 0.3$ to $20\ \mathrm{kW\,m^{-2}}$, and bath temperatures from 1.15 to 2.162 K. Their conclusion is that the measured thermal gradient departs from that predicted by the Gorter–Mellink cube law, and that an expression with a variable exponent fits the data better;

$$\left|\frac{\mathrm{d}T}{\mathrm{d}x}\right| = D(T)Q^m. \tag{2.45}$$

Between 1.2 and 1.7 K, m grows from 3 to about 3.4, and above 1.7 K, it remains steady at 3.4. In their review on quantum turbulence, Donnelly and Swanson summarise experimental results from the two decades after Chase, finding that m can range from 3 almost all the way up to 4 [104, Fig. 17].

2.4.5 He II Thermal Conductivity Function

Neglecting the laminar flow contribution to the thermal gradient, and looking at a one–dimensional channel, Gorter and Mellink's expression can be written (allowing for the exponent being variable),

$$\frac{\mathrm{d}T}{\mathrm{d}x} = -f(T,P)Q^m, \tag{2.46}$$

where for $m = 3$, $f(T,P) = A_{\mathrm{GM}}\rho_{\mathrm{n}} \,/\, \rho_{\mathrm{s}}^3 s^4 T^3$. Using instead the thermal gradient to express the heat flux,

$$Q = \left[-f^{-1}(T,P)\frac{\mathrm{d}T}{\mathrm{d}x}\right]^{1/m}, \tag{2.47}$$

where $f^{-1}(T,P)$ is called the thermal conductivity function of He II.

Building on the observation that an exponent m larger than 3 seems to better fit data, Sato *et al.* propose a different empirical fit for the thermal conductivity function [105], and that an average exponent of $m = 3.4$ fits data better than 3 (with their thermal conductivity function) across a wide range of temperatures and pressures [106];

$$f^{-1}(T,P) = h(t)g_{\mathrm{peak}}(P), \tag{2.48}$$

with $t = T/T_\lambda$, and,

$$g_{\mathrm{peak}}(P) = e^{a+bP+cP^2}, \tag{2.49}$$

where P is the pressure in MPa, and

$$h(t) = 1 + (t-0.882)^2 \sum_{k=0}^{9} \alpha_k (t-1)^k, \tag{2.50}$$

with coefficients a, b, c, and α_k given in Table 2.3.

Table 2.3: Coefficients for the pressure dependent and temperature dependent factors of Sato *et al.*'s fit in Equation (2.48).

a = 34.20842 b = -0.85979 c = 0.041388

α_0 = -$(0.118)^{-2}$ α_1 = $1.2172617 \cdot 10^3$ α_2 = -$1.4992321 \cdot 10^4$
α_3 = -$3.9491398 \cdot 10^5$ α_4 = -$2.9716249 \cdot 10^6$ α_5 = -$1.2716045 \cdot 10^7$
α_6 = -$3.8519949 \cdot 10^7$ α_7 = -$8.6644230 \cdot 10^7$ α_8 = -$1.2501488 \cdot 10^8$
α_9 = -$8.1273591 \cdot 10^7$

Vitrano *et al.* recently measured the time–dependent temperature development along the length of a rectangular channel 50 mm wide, 1 mm deep, and 140 mm long, and using the fit by Sato *et al.*, they find excellent steady state agreement between measurements and simulations of the setup, while with the theoretical fit to the thermal conductivity function, using $m = 3$, the agreement is not nearly as good [107, 108]. Note that they implement a time–dependent expression allowing for comparison also with measurements in their channel at times before the steady state temperature distribution is established. Also during this transient the thermal conductivity function fit by Sato *et al.* provides a better match between the measured temperature distribution and simulations.

2.4.6 Critical Heat Flux in He II

Let a channel of length L be filled with He II at a bath temperature of T_b. Heat flowing through the channel will cause a thermal gradient, and the peak heat flux allowable at the hot end of the channel becomes,

$$\frac{\mathrm{d}T}{\mathrm{d}x} = f(T,P)Q^m \quad \Rightarrow \quad \frac{1}{f(T,P)}\mathrm{d}T = Q^m \mathrm{d}x \quad \Rightarrow \quad \int_{T_\mathrm{b}}^{T_\lambda} \frac{1}{f(T,P)}\mathrm{d}T = {Q_\mathrm{peak}}^m \int_0^L \mathrm{d}x, \tag{2.51}$$

where it is assumed there is no spatial dependence (importantly, that the channel cross section is fixed).

This relation between Q_peak and the temperature–integrated thermal conductivity function is often expressed as [30, Eq. 7.7],

$$Q_\mathrm{peak} L^{1/m} = Z(T_\mathrm{b}) = \left[\int_{T_\mathrm{b}}^{T_\lambda} \frac{1}{f(T,P)}\mathrm{d}T\right]^{1/m} \tag{2.52}$$

and it depends mostly on the bath temperature, and shows that it is the channel length that limits the peak heat flux by the fact that He II at the hot end of the channel may not go above T_λ. Note that since the thermal conductivity function is lower for higher pressures, the peak heat flux falls with pressure.

Equation (2.52) hides the dependence on variable channel geometry. As described in a review by Van Sciver [109], an experiment in saturated He II was done by Gentile and François where a vertical channel of He II had a conical constriction a little above the heater, with a wide base, which then tapered down to a pipe of smaller cross section. This meant that the cross section of He II shrunk from a maximum near the heater to a minimum at the start of the pipe. In this experiment, it was seen that gas bubbles formed first at the constriction, not next to the heater. It is important to keep in mind that the temperature was still highest near the heater. In saturated helium, the relevant point determining the maximum heat flux is not T_λ, but $T_\mathrm{sat}(P)$, meaning the saturation line in Figure 2.1 on page 10. It also means that, such as in Gentile and François's experiment, boiling in the channel can happen before onset of film boiling at the heater surface.

In a channel of uniform cross section, filled with pressurised He II (meaning a pressure higher than the λ–point in Figure 2.1), Q_peak is also the critical heat flux that marks the onset of film boiling. The remained of this section deals only with pressurised He II, and will therefore speak of Q_crit, rather than Q_peak.

Critical Heat Flux from Wires in Open Baths

There is also a difference in the critical heat flux expression depending on the geometry of the heater itself. Equation (2.52) pertains to a heater at one end of a channel open to a large bath at the other end.

For cylindrical geometries, such as thin wires, submerged in He II, the critical heat flux is found as (based on a theoretical fit of the thermal conductivity function with exponent $m = 3$) [30, Eq. 7.13],

$$Q_\mathrm{crit} = \left[\frac{2\Psi}{r_0}\int_{T_\mathrm{b}}^{T'} \frac{1}{f(T,P)}\mathrm{d}T\right]^{1/3}, \tag{2.53}$$

where Ψ is a fit parameter, r_0 is the radius of the wire/cylinder, and $T' \simeq T_\mathrm{b} + 0.01$ K. This means that the critical heat flux only depends on the radius of the heater and the bath temperature, which makes sense; a thicker wire has more surface area across which to convert the applied heating power to a heat flux into the He II bath.

Starting from this expression, Sakurai *et al.* propose their own fit to the thermal conductivity function, allowing them to also change the integration limits, arriving at (neglecting the pressure dependence of $f^{-1}(T,P)$) [110, Eq. 3],

$$Q_\mathrm{crit} = K \left[\frac{2}{r_0} \int_{T_\mathrm{b}}^{T_\lambda} \frac{1}{f(T)} \mathrm{d}T \right]^{1/3}, \tag{2.54}$$

with K a fit parameter they determine to be 0.58, and the fit to the thermal conductivity function,

$$f^{-1}(T) = g(T_\lambda) \left[t^{6.8} \left(1 - t^{6.8}\right) \right]^3, \tag{2.55}$$

with $t = T/T_\lambda$, and $g(T_\lambda) = \rho^2 {s_\lambda}^4 {T_\lambda}^3 \,/\, A_\mathrm{GM}(T_\lambda)$, with $s_\lambda = 1559\ \mathrm{J\,kg^{-1}\,K^{-1}}$ and $A_\mathrm{GM}(T_\lambda) \simeq 1150\ \mathrm{m\,s\,kg^{-1}}$. Note that T_λ in the upper bound is still considered pressure dependent.

With this expression for the critical heat flux, Sakurai *et al.* find good agreement with their own measurements in saturated helium, and relatively good agreement with a data set by Lemieux and Leonard who used a slightly thinner wire [111]. Note that Sakurai *et al.* used $K = 0.5$ to fit Lemieux and Leonard's data.

Shiotsu *et al.* (same group as Sakurai *et al.*) finds excellent agreement between measured critical heat flux and that found by Equation (2.54) in subcooled He II [112]. When they measure the critical heat flux as a function also of wire diameter [113], Equation (2.54) still agrees with measurements for wire diameters up to 1.2 mm, though the agreement is poor for all diameters at bath temperatures above 2.14 K.

Critical Heat Flux from Flat Plates in Open Baths

Tatsumoto *et al.* conducted critical heat flux measurements for thin flat heater strips/plates that were insulated on one side, and exposed to subcooled He II on the other [114]. With the same thermal conductivity function as proposed by Sakurai *et al.*, they use,

$$Q_\mathrm{crit} = K \left[\frac{2}{\frac{Lw}{2(L+w)}} \int_{T_\mathrm{b}}^{T_\lambda} \frac{1}{f(T)} \mathrm{d}T \right]^{1/3}, \tag{2.56}$$

where K is still 0.58, L is the length of the heater, and w is the width of the heater. This is akin to replacing r_0 in Equation (2.54) by $Lw \,/\, 2(L+w)$. This expression is in good agreement with their measurements on heaters with $w = 10.5$ mm and $L =$ 10.5, 15.6, and 40 mm. Note that the data they show in their main result (Figure 5) has some data points not accounted for in their experimental setup. At least some of the data is from an earlier study they did on narrower heater strips [115].

2.5 Transient Heat Transfer

So far in this chapter, the heat transfer has essentially been considered steady state; a heater is supplied energy from some kind of source, it heats up, helium cools it from the surface, and eventually a steady state is established, and one can determine the Kapitza conductance h_K, or the Kapitza fit parameters a_K and n_K.

However, as discussed in the previous section, eventually, the heating is strong enough that a maximum, or critical heat flux is reached. The critical heat flux, as discussed in the previous section, is a steady state property of the heater–helium system. During steady state heating that exceeds the critical heat flux, fully developed film boiling governs the heat transfer from the heater surface into He II. The onset of film boiling, and whether or not it even happens for a particular Q_app that exceeds the critical heat flux, is inherently a question of transient behaviour.

Since the Kapitza conductance relies on transmission of phonons across the interface between heater and He II, and since even on the helium side, these phonons move at velocities on the order of hundreds of metres per second, it is assumed that the Kapitza conductance behaves essentially the same under transient conditions as it does in steady state. This was confirmed experimentally by Katerberg and Anderson by measuring the Kapitza resistance by two separate techniques on the same sample: 1) the “DC” technique where they simply measure the interfacial temperature discontinuity under some applied heat flux, and 2) the “AC” technique where they have two second sound resonance cavities on either side of a thin copper foil, and let one cavity resonate by applying an oscillating current to a heater in the cavity, and then tune the other cavity to resonate at the same frequency. The Kapitza resistance is then measured by looking at half the temperature amplitude drop in the second resonator compared with the first [116].

This means that also for transient heating the Kapitza model from Equation (2.28) on page 21 is expected to describe the interfacial heat transfer.

During transient heating, the Kapitza regime, namely the region of applicability of the Kapitza model, persists in a quasi–steady state, allowing for temporarily much higher heat fluxes than the steady state critical heat flux. This was first observed by Kobayashi *et al.* in the mid 1970’s, though their original publication contains only a brief note about the effect near the end [117].

Figure 2.14 shows the results of Shiotsu *et al.* measuring the critical heat flux from an 80 µm diameter wire of gold–manganese submerged in a bath of He II at 2 K, under atmospheric pressure [112]. They find that with lifetimes generally on the sub–millisecond time scale, the Kapitza heat transfer regime persists also for applied heat fluxes Q_app above the steady state critical heat flux Q_crit. Once the heat–flux–dependent lifetime is exceeded, they see the onset of film boiling, with a characteristic large increase in heater surface temperature. Gradt *et al.* found the same result, where the temperature of a 51 µm diameter rhodium–iron wire remains stable for a short time, with the heat flux and measured heater temperature related by the Kapitza model, before then seeing the heater temperature shoot up, marking the onset of film boiling [118]. Van Sciver and Lee made measurements on a large cylindrical heater in He II subject to steps in heating power, and also found there is a lifetime within which the heat flux at the heater surface can go above the steady state critical value before then observing the temeprature rise associated with onset of film boiling [119].

By Kapitza regime, then, is meant both the steady state situation where the Kapitza model applies, as well as the transient time before the onset of film boiling. Breakdown of the Kapitza regime refers to the transition out of the Kapitza and

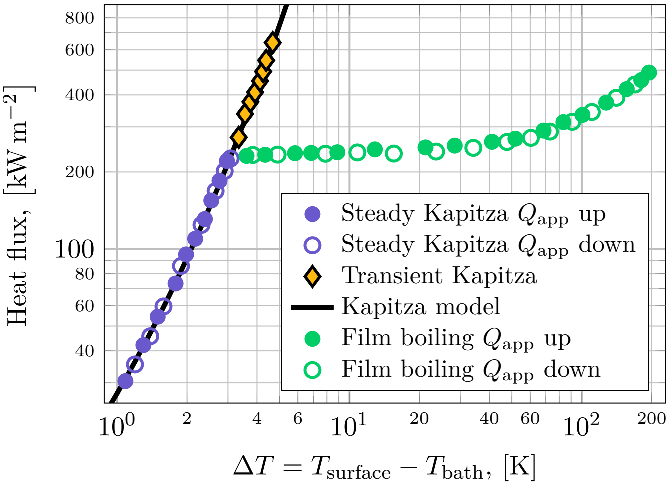

Figure 2.14: Heat flux to a bath of He II as a function of the heater surface temperature of a 80 µm Au–Mn wire in a bath of 2 K under atmospheric pressure [112, recreated from Figure 2]. The plot also shows the transient Kapitza regime, and how the Kapitza model fits data with $a_{\text{K}} = 671.2\ \text{W}\,\text{m}^{-2}\,\text{K}^{-n_{\text{K}}}$, and $n_{\text{K}} = 3.612$ (from Table 2.2 on page 24).

into the film boiling regime (which is typically considered the onset of film boiling). In confined geometries, the Kapitza breakdown does not entail quite so clear a transition into film boiling, and this will be discussed in Section 2.6 on page 45.

Other liquids, including He I, also have a meaningful critical heat flux associated with the onset of film boiling. Making, for such a non–He II liquid, a heat transfer curve similar to that in Figure 2.14 (without the Transient Kapitza part) would invariably show a hysteresis feature related to the onset and termination of film boiling. To start film boiling the applied heat flux must be (slightly) above the critical heat flux, while to end film boiling, the applied heat flux must be lowered considerably below the critical heat flux [30, Sec. 5.1]. This is because it takes more energy to activate a nucleation site to start forming the vapour film than it takes to maintain the film once established. For He II, however, this hysteresis is not consistently observed [30, Sec. 7.6]. No appreciable hysteresis is seen in Shiotsu *et al.*'s data in Figure 2.14, while close to saturation conditions, Shiotsu *et al.* do find it [112, Fig. 5]. Caspi and Frederking observe hysteresis even at temperatures some ways below T_λ and at pressures far above saturation [120]. As such, the film boiling regime in He II is not completely understood [30, Sec. 7.6].

2.5.1 Kapitza Regime Lifetime

Van Sciver measured transient temperature distributions along a long cylindrical pipe, and found a relationship between the Kapitza regime lifetime Δt^* and the applied heat flux Q_{app} (for $Q_{\text{app}} > Q_{\text{crit}}$) as [121],

$$\Delta t^* = \frac{K}{{Q_{\text{app}}}^4}, \tag{2.57}$$

where K is a function of the bath temperature, and the heat transfer conditions at the end of the pipe (whether or not the pipe was open).

As part of these measurements, Van Sciver found that the temperature distribution along the pipe followed an exponential curve: $\Delta T(x) \simeq \Delta T_0 \exp(-x/l)$, where ΔT_0 is the temperature of the helium immediately adjacent the heater, and l is the penetration length[10]. With this temperature profile, and assuming that heat transfer was dominated by mutual friction in counterflow, meaning the laminar term in Equation (2.42) on page 32 can be neglected, they found an expression for the lifetime $\propto {Q_{\mathrm{app}}}^{-4}$, just like the phenomenological fit [121, Eq. 18];

$$\Delta t^* \simeq \frac{3\rho\overline{C}\Delta T_0}{{Q_{\mathrm{app}}}^4} \int_{T_{\mathrm{b}}}^{T_{\mathrm{b}}+\Delta T_0} f^{-1}(T)\,\mathrm{d}T, \tag{2.58}$$

where $\overline{C}$ is the average heat capacity between T_{b} and $T_{\mathrm{b}} + \Delta T_0$.

The proportionality constant K from this expression is in the same range as those found by fitting Equation (2.57) to data.

After Van Sciver, several measurements were made on other geometries, notably effectively shorter ones, where the peak steady state heat flux is higher. Figure 2.15 summarises a few such measurements. Note that measurements showing a longer time to film boiling onset used lower–amplitude applied heating power; the total amount of energy supplied from the heater at the time of film boiling onset is $E = \Delta t^* Q_{\mathrm{app}}$, which is ultimately what causes the boiling to start.

Van Sciver open/closed refers to the data by Van Sciver that lead to Equation (2.57). Seyfert *et al.* refers to measurements Seyfert *et al.* made on a channel where He II was kept within a gap of 1 or 2 mm between two concentric cylinders. Around the midpoint of the outer cylinder, they placed a 10 mm wide heater, leaving 40 mm of unheated/bare cylinder wall to either side. At either end, the He II was in contact with a bath regulated so the channel ends always had the same temperature. Aside from the bath contact at the channel ends, the setup was placed in a vacuum [123]. Wang *et al.* refers to the measurements by Wang *et al.* on a wire heater in an open bath subject to very short and very strong rectangular heating pules [124]. Shiotsu duct/open bath refers to measurements made by Shiotsu *et al.* where they placed a rectangular heater in a He II bath. The heater, 10 mm wide and 40 mm long, was insulated on one side, and cooled by the helium bath on the other [125]. duct are results where the heater was at the end of an open, 100 mm long vertical duct of the same cross section as the heater itself, while open bath are results for the heater with no constraints on the helium at all. Shiotsu wire refers to Shiotsu *et al.*'s measurements on a 0.2 mm diameter wire submerged in He II [126].

The straight lines in the figure are not fits to data, but rather show power laws of the kind Van Sciver found (Equation (2.57)), with different exponential dependencies on the boiling onset time Δt^*. The expected power law is $\propto {Q_{\mathrm{app}}}^{-4}$, represented by the red line, and much of the data does follow such a power law. However, for higher

---

[10] Note that this observation was later generalised to the "infinite channel" approximation, for which Dresner found a general time–dependent solution which amounts to scaling of a fixed temperature distribution in space, temperature amplitude, and time [30, Sec. 7.2.2]. This solution assumes the thermal conductivity function is constant, and equal to its value at the initial temperature, meaning the solution only strictly speaking holds for small temperature gradients. Baudouy then extended the infinite channel model further to also account for temperature the temperature dependence [122].

heat flux and lower heating duration, it appears the slope slackens, towards $\propto Q_{\text{app}}{}^{-2}$. Both Wang and Shiotsu *et al.* attribute this to the fact it takes time to build up a steady state vortex line density (recall Equation (2.43) on page 33), meaning the mutual friction force needs time to grow. When Van Sciver derived Equation (2.58), they assumed fully developed Gorter–Mellink heat transfer, with the associated Q^3–dependence of the thermal gradient. However, if the Gorter–Mellink/mutual friction regime is not dominant yet, the laminar regime is still important, which is linear in Q, which means similar arguments to Van Sciver's leads to a slope $\propto Q_{\text{app}}{}^{-2}$.

With the exception of Van Sciver's data, all the other data slopes upwards for the lowest applied heat fluxes. For an applied heat flux equal to the steady state critical heat flux it will take an infinite amount of time to reach film boiling onset, and that initial steep slope at the start of each data set is associated with the departure from this. Note that all the Shiotsu wire data follow slopes steeper than both the fully turbulent $\propto Q_{\text{app}}{}^{-4}$ and the laminar $\propto Q_{\text{app}}{}^{-2}$, indicating they did not make measurements sufficiently far above the steady state critical heat flux to see the establishment of the Van Sciver power law. They propose their own fit to data that depends on the heater wire radius, but otherwise does not seem to represent any physically derived relationship.

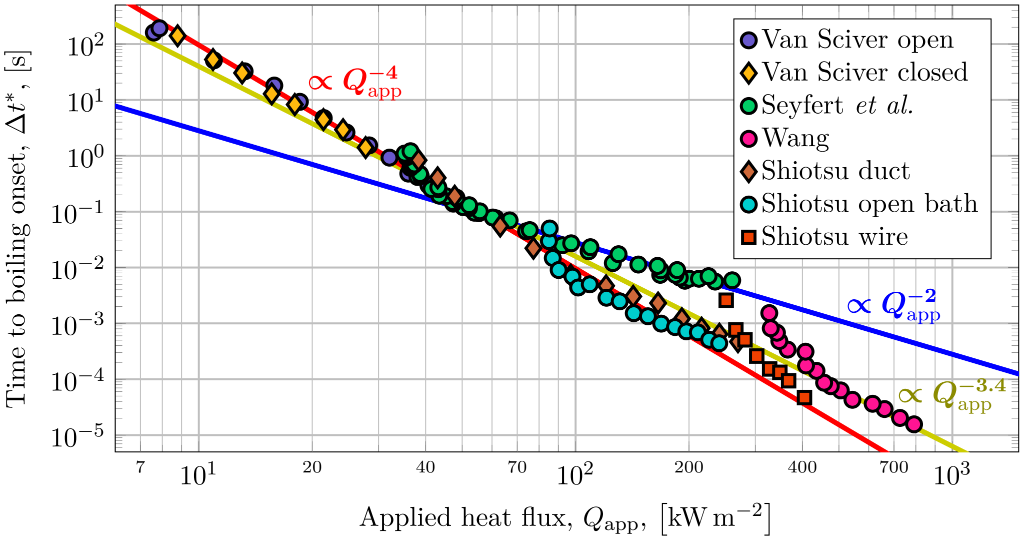

Figure 2.15: Various boiling onset measurements for a large range of applied heat fluxes and heating durations. Van Sciver takes data from figures 2 and 6 in [121]. Seyfert *et al.* takes data from Figure 3 in [123]. Wang *et al.* takes data from Figure 3 in [124]. Shiotsu duct/open bath takes data from figures 3 and 6 in [125]. Shiotsu wire takes data from Figure 3 in [126]. All data is for heat transfer at 1.8 K. The straight lines are not strict fits to data, but simply follow the indicated proportionality.

2.5.2 Transient He II Heat Transfer Regimes

Nemirovskii and Tsoi reviewed a large number of transient heat transfer measurements made up till the late 1980's and proposed the approximate classification scheme shown in Figure 2.16 [127]. An important note is that the boundaries between regions are accurate to within an order of magnitude at best, especially when it comes to the boiling boundary (red and orange lines).

For very low heat fluxes, regardless of the duration of heating, the laminar counterflow regime completely dominates. This regime is to the left of the green vertical bar in the figure. The two blue dotted lines are relationships of the kind Vinen found during their transient measurements: $\tau = a(T)Q^{-3/2}$, with τ being the time needed to establish the steady state vortex line density. The upper of the two lines is for $a = 150\ \mathrm{ks\,W^{3/2}\,m^{-3}}$, associated with development of turbulence in smooth circular channels at 1.9 K (see Figure 2.13 on page 34), while the lower is for $a = 40\ \mathrm{ks\,W^{3/2}\,m^{-3}}$, associated with development of turbulence in irregular circular and rectangular channels, and open baths, also at 1.9 K.

The regions **D** and **F** refer to either “developing” or “fully developed” turbulence. Vinen’s experiments with small steps in applied heat flux were in the upper region of **D**, crossing into **F**.

The region **S**, associated with very strong, short heat pulses, is the second–sound–wave heat transfer regime. Fiszdon *et al.* studied this regime for successive, moderate heat pulses in the millisecond regime [128], while Shimazaki *et al.* have studied this region in the limit of single, strong, fast pulses [129]. Summarily, the regime is characterised by three sub–regions; 1) for heat pulses up to about $50\ \mathrm{kW\,m^{-2}}$, independent of exact duration (within the single–digit millisecond range), a second–sound–wave forms, and propagates from the heater, carrying all the energy supplied by the heater. 2) if this second–sound–wave passes through a region where there is already a high density of vortex lines, such as that left in the wake of a previous pulse, *or* if the amplitude of the pulse is large enough to generate its own high–density field of vortex lines immediately behind the wave–front, the pulse reaches a limiting heat transfer capability, and excess energy transfer happens by a diffusion–like process, significantly slowed down by the dense vortex tangle. 3) for heat pulses on the order of a few hundred $\mathrm{kW\,m^{-2}}$, most of the energy from the heater goes into creating the dense vortex tangle (with heat diffusing through it), as well as evaporating helium (boiling), with only a very small fraction of heat transported by second sound. Note that this diffusion–like process is essentially the Gorter–Mellink regime already discussed. The orange line at the end of the second–sound–wave regime is that associated with heat transfer exclusively happening by film boiling, which Nemirovskii and Tsoi suggest follow a relationship $\tau = (C/Q)^2$, where C is a constant ranging from 50 to 5000 $\mathrm{s^{1/2}\,W\,m^{-2}}$. $C = 5000$ in the figure.

The region **B** is that of film boiling, with the red limiting line being that described by Van Sciver; $\tau = K(T)Q^{-4}$, with $K = 9.6 \cdot 10^5\ \mathrm{s\,W^4\,m^{-8}}$ in the figure.

According this this classification of regimes, the experiments done as part of the work presented herein are mostly in the **D** and **F** regions, though heat fluxes reach as high as $100\ \mathrm{kW\,m^{-2}}$ with pulses as short as 0.5 ms. The effect of confinement of helium plays a large part in a more accurate classification of regimes, as well as the bath temperature and pressure, which is some of the reason why Figure 2.16 on the next page can only be taken as a guide.

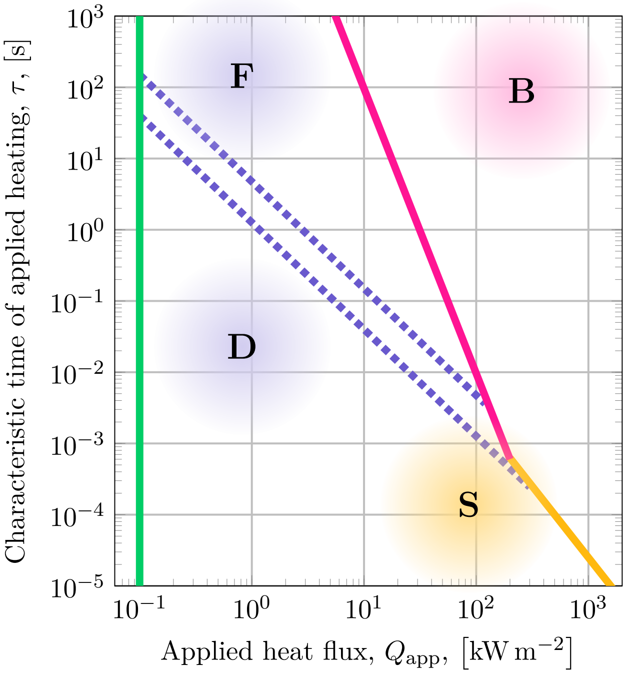

Figure 2.16: Rough classification of transient heat transfer regimes in He II [127, recreated from Fig. 1]. Left of green line: laminar flow regime. **D** and **F**: developing and fully developed Gorter–Mellink regimes. **S**: second–sound–wave heat transfer regime. **B**: boiling heat transfer regime.

2.5.3 Numerical Modelling

Numerical modelling of transient heat transfer to and in He II is dominated by two main branches. On the one hand are simulations working with some version of the two–fluid hydrodynamic equations, on the other are simulations approximating heat transfer as a purely diffusive process with a modified classical heat equation.

Modelling the complete two–fluid hydrodynamics is beyond the scope of this work, so only the second, simplified approach, used herein is discussed.

Modified heat equation Assume that the fully developed mutual friction regime is always realised, and that all heat transfer happens by way of perfect counterflow of the two fluid components[11]. Then assume the regular Fourier law of thermal conduction applies to He II, and use the steady state heat flux expression (Equation (2.47) on page 35) to define an effective thermal conductivity (neglecting the pressure dependence of the thermal conductivity function);

$$\begin{aligned} Q = -k_{\text{eff}}\nabla T &= \left[-f^{-1}(T)\nabla T\right]^{1/m} \\ &= \left[-f^{-1}(T)\frac{|\nabla T|^{m-1}}{|\nabla T|^{m-1}}\nabla T\right]^{1/m} = \left[-f^{-1}(T)\frac{1}{|\nabla T|^{m-1}}\right]^{1/m}\nabla T. \end{aligned} \tag{2.59}$$

---

[11] If forced flow of He II is considered, the assumption is rather that heat transfer by convection and heat transfer by counterflow are independent.

This essentially leads to the same energy balance equation as that used by, for instance, Kitamura *et al.*;

$$\rho(T)C(T)\frac{\partial T}{\partial t} = \nabla\left\{\left[-f^{-1}(T)\frac{1}{|\nabla T|^{m-1}}\right]^{1/m}\nabla T\right\}, \tag{2.60}$$

where C is the specific heat capacity (C_v in a closed volume of He II, or C_p in an open).

This is the approach used for simulations done as part of interpretation of results herein, and a complete discussion of the implementation is given in Chapter 5. Some brief remarks about how this model has been used in the past will be made here.

This was the earliest approach to transient numerical modelling of He II, proposed initially by Seyfert *et al.* during their experiments, already discussed in Section 2.5.1 on page 39, investigating the time before film boiling onset in channels [123]. They do not show any transient simulation results as such, but rather present their modelling results in terms of how much energy is predicted to enter the helium in the channel during the time to film boiling onset versus how much energy the model can account for in the helium. What they find is that both for open and closed channels, including the case for Van Sciver's long–pipe measurement [121], the transient model based on Equation (2.60) gets close to the measured values. The agreement between model and measurement is worse for larger heat pulses, because the model must approximate ever faster heat transfer, which means, eventually, the assumptions of fully developed mutual friction and counterflow fail. For the strongest heating, meaning the fastest time–scales, they consider the model to be a good order–of–magnitude estimate, but not necessarily more.

Okamura *et al.* used the same model to interpret their measurements made on a heater/He II setup in which a 2.5 m long 6 mm diameter tube filled with He II under atmospheric pressure is heated from the bottom by a copper surface [130]. The tube is coiled so that the region where the heater and He II touch is horizontal. The heater temperature is measured by sensors embedded within, and a sensor 5 mm from the heater surface measures the He II temperature. They apply a sinusoidal heat flux with a fixed offset, of peak amplitude on the order of 1 $\mathrm{kW\,m^{-2}}$, and find that the model underestimates the helium temperature by about 5 mK for applied heat flux frequencies in the range of 0 to 11 Hz. Note that the error grows over time. Furthermore, their results are presented on the order of seconds, and no mention is made about the millisecond time–scale.

Fuzier and Van Sciver, measuring transient temperature development in a 860 mm long and 10 mm diameter pipe subject to forced flow of He II and rectangular heat pulses on the order of 1 to 20 ms duration and 100 $\mathrm{kW\,m^{-2}}$ amplitude, modified Equation (2.60) to account for the flow of helium, and find excellent agreement between measurements and simulation in the limiting cases of high and low flow velocity [131]. Of relevance to the work presented herein is the situation with no flow of He II at all, and Fuzier and Van Sciver's modelling suggests Equation (2.60) ought to serve as a good approximation, even for fast transients.

2.6 Heat Transfer in Confined Geometries

Some aspects of helium confinement have already been considered by way of open or closed channels of various dimensions. There are, however, a few remaining cases worth briefly reviewing, of relevance to the work presented herein.

2.6.1 Heating Across Narrow Gaps

When heat supplied to He II cannot directly escape the bath along the same axis as it was supplied, the helium can be considered confined. Two experiments will be discussed here, both relying on Caspi and Frederking's observations of multi–phase phenomena in superfluid helium [120] to explain their results. By multi–phase phenomena is meant the heat transfer state that can arise when strong heating is applied to He II such that either 1) He I exists, in more or less stable form near the heater, while the rest of the bath remains He II, or 2) gaseous helium is nearest the heater, then a layer of He I above/around it, and finally the bulk He II.

Circular Heater, Open on All Sides

Warren and Caspi measured the heater temperature as a function of applied heat flux and the gap between the heater surface and an opposing adiabatic wall [132]. In their setup, a cylindrical heater is insulated on all sides except for one, where it is cooled by He II. In the horizontal orientation, the heat flux faces downwards. They confine the He II by placing an adiabatic cylinder of the same radius as the heater, with their axes coincident, forming a gap δ between the heater surface and the flat top of the adiabatic cylinder. Figure 2.17 shows both their measurement data, and a simple diagram of the setup in the horizontal orientation. For vertical orientation, they turn the setup sideways, so the gap is along the x–axis.

At a bath temperature of 2.107 K, and a gap of 250 µm, in the vertical orientation (black dots in the figure), they identify four distinct heat transfer regions; 1) $Q_\text{app} \lesssim 5\ \text{kW}\,\text{m}^{-2}$, heat flows out of the gap region according to the Gorter–Mellink regime. 2) $5\ \text{kW}\,\text{m}^{-2} \lesssim Q_\text{app} \lesssim 7.5\ \text{kW}\,\text{m}^{-2}$, along the dashed grey line in the figure, a stationary He I layer is formed at the heater surface. 3) $7.5\ \text{kW}\,\text{m}^{-2} \lesssim Q_\text{app} \lesssim 12.5\ \text{kW}\,\text{m}^{-2}$, the He I layer has become hot enough that nucleate boiling starts, and since the gap is vertical, the bubbles very effectively remove heat as they flow out of the gap. However, as Q_app approaches $12.5\ \text{kW}\,\text{m}^{-2}$, the vaporised He I blankets the entire heater surface, marking the onset of film boiling, which is the fourth and last heat transfer regime; 4) $Q_\text{app} \gtrsim 12.5\ \text{kW}\,\text{m}^{-2}$, film boiling has begun.

They did not mark their data points according to whether they were taken for growing or shrinking applied heat flux, but they do note that the black–ringed yellow point in the figure is the first data point they gather *after* reducing the heat flux from the highest value. This point is slightly below the heat flux at which film boiling started, indicating a small level of hysteresis. It is interesting to note that when lowering the applied heat flux, Warren and Caspi find that recovery from film boiling goes back into nucleate boiling, rather than needing to drop all the way down to the dashed grey line indicating a stable He I layer.

For the horizontal orientation, with a narrower gap, and slightly higher bath temperature (blue squares in the figure), they find a similar behaviour, though the heat fluxes necessary to transition from one regime to another are much lower. This is due to three effects together; 1) because the gap is smaller, the heat transfer cross section out of the gap is smaller, so the gradient becomes larger for the same heat flux. 2) The bath temperature is slightly closer to T_λ, and above the temperature for which the thermal conductivity function has its peak (around 1.92 K (see Section 2.4.5 on page 35)), meaning the effective thermal conductivity of the He II in the gap is lower. And, 3) the heater is oriented downwards, so the convection of He I, and eventual bubbles in the nucleate boiling regime, have a harder time bringing heat out of the gap.

For lower bath temperatures, regardless of orientation and gap size, the distinctive nucleate boiling regime vanishes, as seen in the figure. They do not offer a full explanation for this. In fact, it is evidence of confusing behaviour; the He I layer forms just as before (identified by the linear region highlighted by dashed grey lines), but unlike in the near–T_λ cases, as this layer heats up, it goes straight into film boiling, rather than transitioning through nucleate boiling. Furthermore, the film boiling regime is now not as violent as for the higher bath temperatures, seen as the relatively shallow departure from the linear regime. The 2.107 K data, once film boiling sets in, sees a very rapid surface temperature growth as the heat flux is increased.

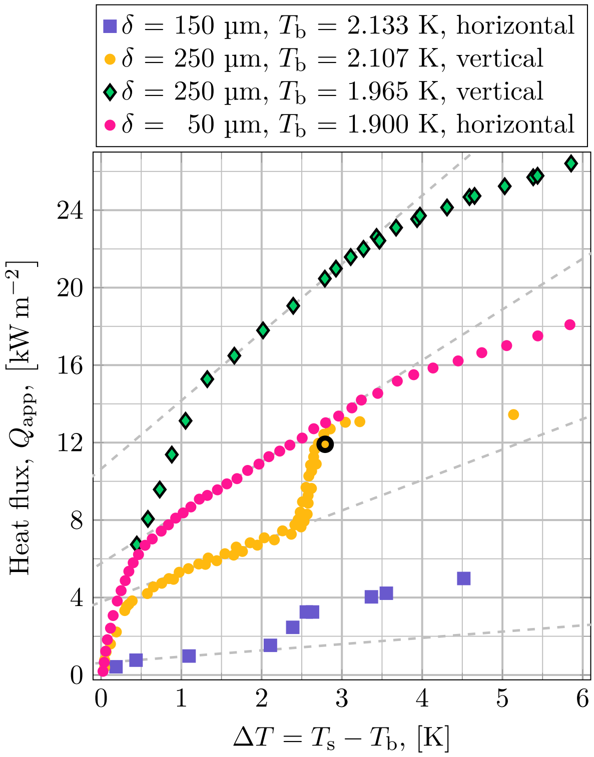

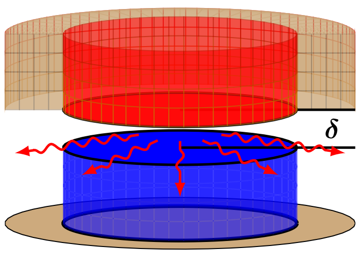

Figure 2.17: The data from Warren and Caspi's measurements on heat transfer to He II in the narrow gap δ between a heater and an adiabatic wall [132, figures 2 and 3]. The dashed grey lines indicate the heat transfer regions associated with a film of He I covering some fraction of the heater surface. Above: simple diagram of the He II gap. In the horizontal orientation, heat flows from the bottom of the red cylinder (heater), downwards, across the gap, towards the adiabatic blue cylinder.

Rectangular Channel, Open at Either End

Kobayashi *et al.* did experiments on a short channel open at either end, for varying channel depths [133]. Their setup, as shown in Figure 2.18, viewing the channel from the side. The red rectangle is a copper block into which they placed several temperature sensors. The zigzag line behind the copper block is the heating element. They extrapolate the surface temperature of the copper block using T_1' and T_1. In the results figure legend, T_1 refers to the extrapolated surface temperature. T_s is a sensor in the channel helium itself, measuring the temperature immediately adjacent to the heater. T_2 and T_3 are embedded in surface of the insulating material confining of the helium to the gap d. T_e measures the helium temperature at the channel exit, and T_b the bath temperature. The channel length L is 22 mm, while in the plane of the paper, the channel extends 16 mm. The channel helium communicates with the bath only through the top and bottom of the channel as shown in the figure.

Just like Warren and Caspi, they find four distinct heat transfer regions, or regimes, indicated in the figure. In Regime 1, which they call the “Kapitza region”, heat effectively moves out of the channel by the Gorter–Mellink regime; while the heater surface temperature steadily grows, the temperature of both the helium adjacent to the surface, and the helium on the other side of the channel, stay at the same temperature. Their temperatures only start increasing above $Q_\mathrm{app} \gtrsim 6\ \mathrm{kW\,m^{-2}}$. Note also that there is nor significant temperature gradient across the channel, as is expected. Also worth noting is that fitting the Kapitza model (Equation (2.28) on page 21) to the data below 7 $\mathrm{kW\,m^{-2}}$ (not accounting for the change in helium temperature) finds $a_\mathrm{K} = 2419.9\ \mathrm{W\,m^{-2}\,K^{-n_K}}$, and $n_\mathrm{K} = 2.1129$. The resulting fit is within about 5% in the region $Q_\mathrm{app} \in [1.6, 7.5]$. At $Q_\mathrm{app} \simeq 7.9\ \mathrm{kW\,m^{-2}}$, there is a transition from Regime 1 to Regime 2. The helium in the channel is now uniformly at T_λ. From here, like Warren and Caspi, they find a more rapid temperature increase with applied heat flux, and see that the helium adjacent to the heater keeps heating up until it reaches the boiling point around 4.22 K. This marks the transition to Regime 3, where nucleate boiling heat transfer ensures the heater surface temperature and the temperature of helium adjacent to the heater surface remains mostly constant. Regime 4 marks the point where film boiling starts. Note that in Regimes 3 and 4, the temperature of the helium on the insulated side of the channel behaves quite erratically, even going down for growing heat flux once film boiling sets in. Breon and Van Sciver measured boiling heat transfer in He II confined to a vertical circular channel, including in their study the capture of high–speed images, and found that very complicated fluid flow patters arise once boiling starts [134] (as is also the case for boiling of water on a stove top). This means, strictly speaking, Kobayashi *et al.* do not have a well–defined steady state in the channel opposite the heater, since, at times, cool helium from the bath will rush in to fill the void of a departing bubble, while at other times, hot bubbles might reach all the way across the channel.

Kobayashi *et al.* define four critical heat fluxes; Q_λ = the heat flux necessary to heat up the helium adjacent to the heater to T_λ, marking the entry into Regime 2. Q_n = the heat flux necessary to start nucleate boiling, and thus transition into Regime 3. Q_max = the heat flux necessary to start film boiling. These three are indicated in the figure. Then they define Q_min = the level they need to lower the applied heat flux

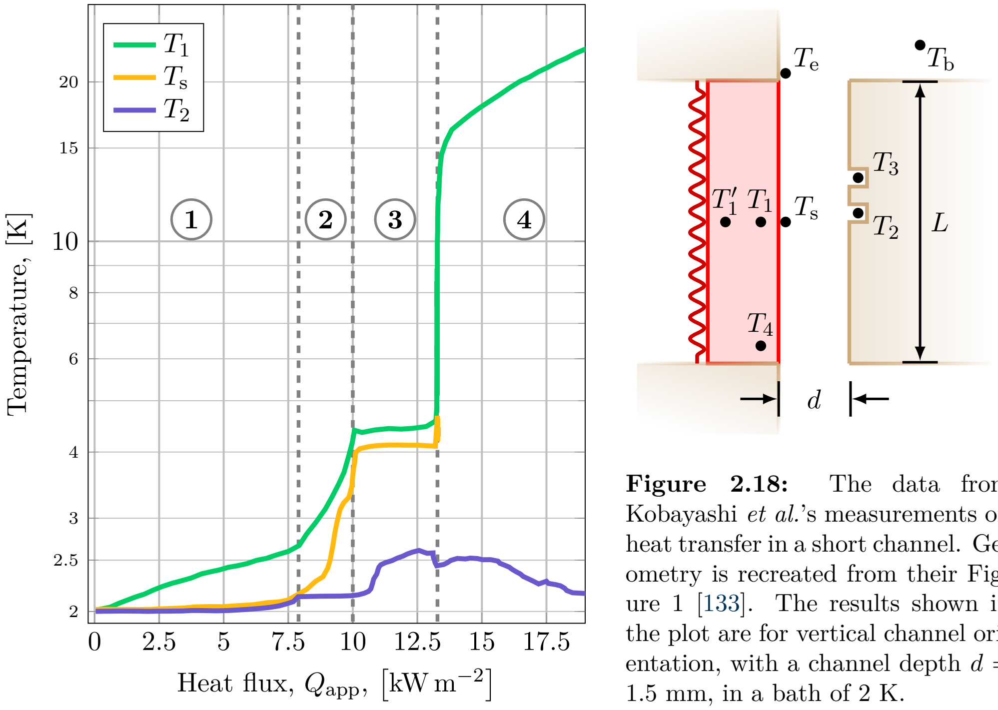

Figure 2.18: The data from Kobayashi *et al.*'s measurements on heat transfer in a short channel. Geometry is recreated from their Figure 1 [133]. The results shown in the plot are for vertical channel orientation, with a channel depth $d =$ 1.5 mm, in a bath of 2 K.

to after film boiling before returning to either Regime 3 or Regime 2.

They find that Q_λ is independent of channel orientation, since so long as all the helium is He II, the Gorter–Mellink mutual friction regime determines the heat transfer out of the channel, and this regime does not have any dependence on gravity. Q_λ grows with channel depth as the heat transfer cross section of the channel increases.

They also find Q_n to be independent of orientation and that it goes up with larger channel depth. Their explanation for this appears to rely on two assumptions;

Assumption 1: Above Q_λ a bubble/region of subcooled He I forms at the heater surface, and it remains local to the middle of it, rather than spreading outwards to cover the entire heater surface, even though the heat flux from the surface is uniform (see Figure 2.19).

Assumption 2: Above Q_λ, between the He I region and the wall on the opposite side of the channel, He II still exists, and all this He II remains steady at T_λ. To the sides of this column of coexisting He I and He II, towards the channel ends, the high–effective thermal conductivity Gorter–Mellink regime keeps cooling the heater, meaning the orientation of the channel remains irrelevant. This is also used to explain how Q_n goes up with channel depth; deeper channel means larger cross section of He II.

Q_max depends on both orientation and channel depth; in a deeper channel, the nucleate boiling heat transfer cross section is larger, and so, it takes more to saturate it, and trigger film boiling onset. For a vertical channel, buoyancy propels the nucleated bubbles out of the channel faster than when bubbles have to slide along either the insulated channel wall (horizontal upwards orientation) or along the heater itself (horizontal downwards orientation). In fact, for the horizontal downwards orientation, they find the lowest Q_{max}, since coating the heater surface completely with gas is easier when buoyancy tends to keep the bubbles in place, rather than lift them away. For this reason, the equivalent plot for the horizontal downwards orientation does not show nearly as prominent a nucleate boiling regime as that seen in Figure 2.18; essentially, Regime 3 is very narrow, or completely gone, so transition from Regime 2 is directly into Regime 4.

Kobayashi *et al.*'s key observation is the existence of Regime 2. Here, the coexistence of He I near the heater and He II near the far wall, with an interface some distance δ from the heater surface, allows a larger heat transfer to take place along the He II gap $d-\delta$ than what is expected from the presence of He I. Figure 2.19 shows how they picture the coexistence to look in their channel. Since the temperature at the middle of the heater surface does not show signs of nucleate boiling onset so long as Q_{n} is not reached, the bubble of subcooled He I at the middle of the heater must possess some form of high–effective thermal conductivity regime of its own; if the He I reverted to natural convection cooling of the heater, the heater temperature would have shot up immediately upon reaching Q_{λ}, since power keeps being supplied on the copper side of the interface, while the helium side has become, essentially, a thermal insulator. Eventually, either the heater is too hot for the helium to remain liquid, *or* the helium across the channel depth all turns to He I, marking the entry into nucleate boiling/Regime 3.

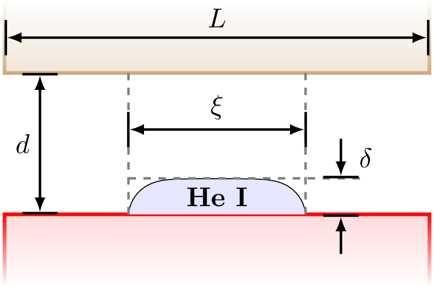

Figure 2.19: For applied heat fluxes above Q_{λ}, a region of He I forms near the middle of the heater surface, and this region grows with increasing heat flux [133, recreated from Figure 4a]. The He I bubble has width ξ and thickness δ. Above the He I, He II exists as usual, letting heat flow according to the Gorter–Mellink regime. In their short channel ($L = 22$ mm), they see no orientation dependence, and as such, this picture is general.

2.6.2 Steady State Heat Transfer in Rutherford Cables

To assess the steady state heat transfer characteristics of both existing Rutherford cables in the LHC, and those intended for the High–Luminosity LHC upgrade, Granieri conducted comprehensive experimental work in the late 2000's/early 2010's [96]. In the LHC, both the MB dipole magnets and the main quadrupole (MQ) focusing magnets use a cable insulation scheme which leaves only very narrow and relatively tortuous channels leading from cable edges to the cooling He II bath. While not geometrically uniform, the channels have characteristic cross sectional dimensions on the order of 5 to 15 µm [96, p. 88], while their lengths are on the order of 6 to 12 mm. Thermal measurements were done on replicas of the inner–layer MB Rutherford cable where the strands were made by copper–nickel (rather than superconducting niobium–titanium, which would be harder to heat). The replica cable is a section about 150 mm long. Instrumentation of one such resistive cable replica was done by machining grooves along some of the strands, and placing thermocouples at a few locations. A total of six cable replicas, with the instrumented one near the middle, were stacked on top of each other, and placed under compression. Heating the cable stack was done by running current through the instrumented cable (or also in adjacent cables for certain tests).

Results obtained when running current through the instrumented cable as well as the two adjacent cables are shown in Figure 2.20. The bath temperature is 1.9 K. Note that the heating power is represented as an absolute power per cable, not as an equivalent heat flux. Furthermore, since there is He II present in the region near the sensors, the temperature readings are not measurements of any particular surface temperature. Also, heat transfer in this kind of geometry is not solely determined by helium; a significant amount of heat also flows by conduction through the solids.

That said, results for Sensor $C1$ and Sensor $C2$ clearly fall into the same regimes as identified by Kobayashi *et al.*; below $P_{\text{app}} \lesssim 90$ mW, there is practically no temperature difference within the cable due to the efficient heat transfer through the He II that permeates the cable (laminar regime for lower, and Gorter–Mellink regime for higher powers). This is Regime 1 as per Kobayashi *et al.*'s classification.

Between 90 mW $\lesssim P_{\text{app}} \lesssim$ 200 mW, the temperature rises more quickly with growing power, until it plateaus, which looks similar to Regime 2, where He I is formed near the heated surfaces. However, Granieri ascribes this to heat conduction through the solids rather than through helium, which is reasonable, given the growth is here nearly linear, evoking the typical Fourier law where $\nabla T \propto Q$. Regime 3 starts around $P_{\text{app}} \simeq 200$ mW, and now helium cooling again dominates as nucleate boiling within the cable stack takes place. Then film boiling starts around 300 mW, meaning the helium no longer effectively cools the cable stack, and the curve reverts back to the nearly linear solid–conduction state. When plotting the temperature rise above bath temperature, $\Delta T = T_{\text{sensor}} - T_{\text{bath}}$, Granieri finds $\Delta T \propto P^{2.7}$ below $P_{\text{app}} \lesssim 60$ mW, and $\Delta T \propto P^2$ between 60 mW $\lesssim P_{\text{app}} \lesssim$ 125 mW, indicating that, indeed, for the lowest heat fluxes, something very similar to a fully developed turbulent Gorter–Mellink regime dominates, while above that, the linear P–dependence of solid–conduction starts to take over (until the brief respite of nucleate boiling).

For the edge sensor, Sensor $E1$, the evolution is different. Regime 1 is the same as for the other two sensors, again because He II keeps the temperature equal across the cable stack. However, Region 2 does not look the same here; between 90 mW $\lesssim P_{\text{app}} \lesssim$ 125 mW, the sensor readings are nearly flat at T_λ, very similar to the way Kobayashi *et al.*'s readings in Region 2 looked for the helium sensor on the wall opposite the heater in their experiment. This indicates that near the cable edges, helium cooling dominates, at least until the critical heat flux of the cooling channels is surpassed. It also suggests the temperature sensor is in better thermal contact with the helium than the cable stack itself, since the copper–nickel definitely keeps heating up. Eventually, though, He II heats up enough to turn into He I, and the same solid–conduction as is seen in the centre–sensors dominates. Granieri ascribes the lack of the clear nucleate boiling plateau expected from Regime 3 to potential presence of an unintended helium pocket near the sensor, or that there could be a larger thermal resistance between this sensor and the helium than that of the other two sensors.

Granieri then prepared a new setup with the key difference being an insulation scheme that left wider channels for helium cooling [96, Fig. 5.20]. The measurement

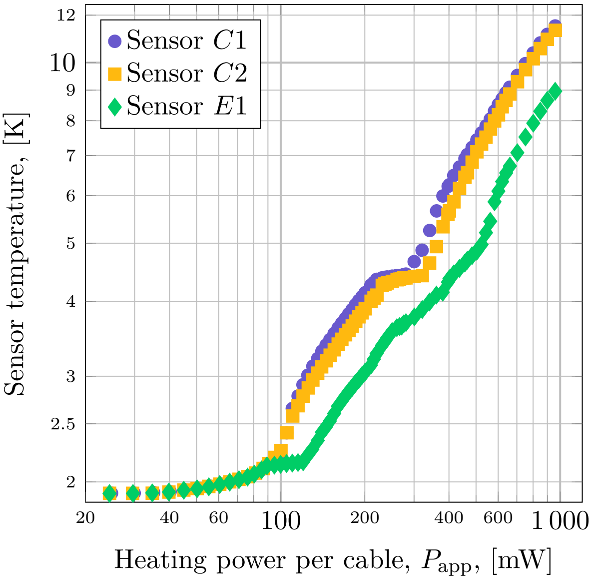

Figure 2.20: Steady state measurements by Granieri where the instrumented cable replica and the two adjacent cables were powered [96, recreated from Figure 3.17]. Sensor $C1$ and Sensor $C2$ lie along the centre–line of the cable, approximately 35 mm apart, while Sensor $E1$ lies near the edge of the cable, closer to the He II bath. In Granieri's thesis, $C1$ = "TCJ 5", $C2$ = "TCJ 7", and $E1$ = "TCJ 6".

results from this setup are qualitatively similar to those shown in Figure 2.20 (see figures 4.4 and 4.5 in [96]), but the improved helium cooling means temperatures for the same applied power are lower. Furthermore, in the low–applied–power region, which for the better insulation scheme is $P_{\text{app}} \lesssim 400$ mW, $\Delta T \propto P^{3.15}$, nicely in line with the Gorter–Mellink regime.

Finally, they prepared a setup to investigate heat transfer through channels of characteristic dimension ~15 to 20 µm [96, Chap. 6]. They etched microchannels into a Pyrex® substrate, and characterised them by photo–microscopy to confirm their dimensions. Arrays of up to a thousand parallel channels were then used as the helium path between a heated chamber and an external bath. Their results show that even for such small channels, the Gorter–Mellink regime is present.

2.6.3 Longer Channels Heated Along Their Entire Length

Since the work presented herein relies on experiments done on a channel of He II 150 mm long, heated from below along its entire length, it serves to review two older experiments of similar setups. One has already been mentioned; Okamura *et al.*'s work in the early 1990's, which included two–fluid modelling (discussed in Section 2.5.3 on page 43). The other is work by Chen and Van Sciver in the mid 1980's.

Steady State and Orientation Dependence

Chen and Van Sciver measured the steady state temperatures of the helium in a channel 127 mm long, 12.7 mm wide, and of depth between 0.5 and 3 mm, heated by a thin stainless steel foil along the entire length of the channel [135]. Along the centre–line of the channel, they placed six temperature sensors; on the surface of the heater, they placed a sensor in the middle and two sensors 24.5 mm from either end.

On the opposite side, across the helium channel, they placed sensors at corresponding locations. The channel could be oriented continuously between vertical and horizontal, where the horizontal orientation had the heater face upwards. Figure 2.21 shows the steady state temperature of the helium in the middle of the channel as it varies with applied heating and channel orientation. The bath temperature outside the channel was 1.9 K, and the channel depth was 500 µm. Chen and Van Sciver note that during the testing the bath temperature grew by about 50 mK as power was slowly increased by passing a growing current through the heater. This small offset is not accounted for in the figure, which has been recreated from Chen and Van Sciver's relative temperature readings with absolute temperature assuming $T_{\text{bath}} = 1.9$ K.

The first inflection point, around 0.6 $\text{kW}\,\text{m}^{-2}$, marks the heat flux where the helium in the middle of the channel reaches T_λ. This heat flux is defined with respect to the heater cross sectional area, not the channel cross sectional area. The way up to this heat flux is like Regime 1 in Kobayashi *et al.*'s results back in Figure 2.18 on page 48, where heat transfer is dominated by counterflow in the Gorter–Mellink regime. Above this first critical heat flux, called Q_λ, Regime 2 should begin. However, Chen and Van Sciver's channel is shallower, at 500 µm against Kobayashi *et al.*'s 1.5 mm, and Chen and Van Sciver's bath temperature is 0.1 K lower. Keeping up the comparison with Figure 2.18, the temperature rise measured by Chen and Van Sciver is more rapid than in Kobayashi *et al.*'s case. Kobayashi *et al.* see a temperature gradient across the 1.5 mm depth of the channel, where the helium far from the heater stays just below T_λ for a while, ensuring they actually observe Regime 2. In Chen and Van Sciver's channel, all the helium heats up more uniformly across the mere 500 µm depth, and so there isn't any He II left in the middle region of the channel by the time the sensor reads T_λ. So there is no prolongation of the Gorter–Mellink heat transfer regime, since there is no He II above/next to He I that can carry heat away, preventing the onset of nucleate boiling. So, then, above 0.8 $\text{kW}\,\text{m}^{-2}$, the nucleate boiling regime is clearly identifiable, with a helium channel temperature reading right around 4.4 K. This is Regime 3 by Kobayashi *et al.*. The effectiveness of this regime is highly dependent on orientation, as was already noted in the previous section; in the horizontal orientation, the bubbles of gaseous helium aren't helped out of the channel by buoyancy, so the heater is completely coated by gas much sooner than when there is a tilt to the channel.

Note that Chen and Van Sciver say the data in Figure 2.21 is characteristic of their results, even in the case where the channel depth is 3 mm, which is larger than the gaps used by Kobayashi *et al.* This indicates that channel depth alone does not predict the existence of Regime 2. Channel length must certainly also play a role, since a longer channel has a lower critical heat flux (in the Gorter–Mellink regime), as described by Equation (2.52) on page 36.

The heat flux where boiling starts, which they call Q^*, is a function of channel orientation, depth, and location in the channel. Looking first at the vertical orientation, Q^* is lowest at the top of the channel, for the shallowest depth. Making the channel deeper, or looking at a point further down the channel, Q^* goes up. The depth–dependence is straight forward; a larger channel cross section (deeper channel) means the same heat flux from the heater spreads out over a larger channel cross section. The orientation dependence is also clear; at the lower end of the channel, the only heat is that locally supplied by the heater, while going upwards, heat rising from below adds

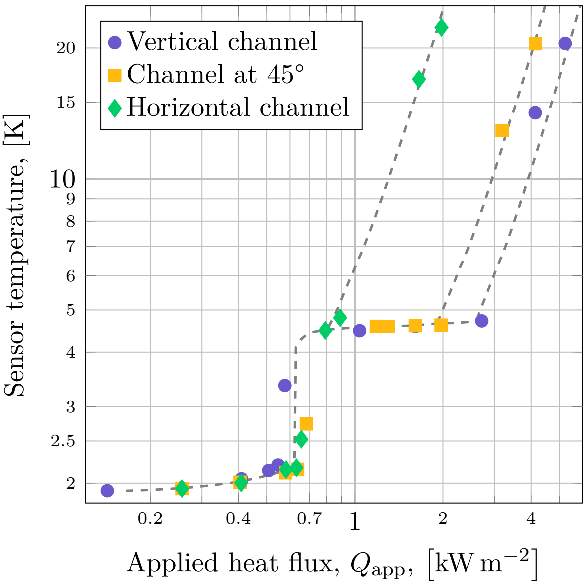

Figure 2.21: Steady state temperature of the middle sensor on the helium side of the channel as it varies with applied heating and channel orientation [135, Fig. 2]. Channel depth w = 500 µm, and bath temperature is 1.9 K. The dashed grey curves are guides proposed by Chen and Van Sciver, not fits to data.

to that supplied by the heater, eventually breaching the heat flux necessary to start film boiling. The combined effect of orientation and channel depth is a little more complicated. Nucleate boiling most effectively removes heat from the heater surface when bubbles can depart at an angle perpendicular to the surface, because this way there is the least amount of interference between the recently departed bubble from one nucleation site and the soon–to–depart bubble growing at another. This process is most effective for a horizontal heater. Buoyancy of bubbles give them a velocity component parallel to the surface, which means a hot gas bubble will travel up the channel, causing this interference with the conditions seen further up. In a shallow channel there is no space for the nucleated bubbles to move far from the heater, so more heat is removed when the channel is vertical (which is optimal for the buoyancy process). In a deep channel, the bubbles *can* move away from the heater surface, and so, an optimal angle exists, depending on channel depth, where a maximum nucleate boiling heat flux occurs. By Chen and Van Sciver's results, this appears to be around 45 to 60° channel tilt away from vertical.

For the heat flux necessary to break out of Regime 1, Q_λ, there is also location, depth, and angle dependence. Depth dependence is obvious, by the same argument as for the boiling heat flux. Location dependence is also clear; a shorter channel can carry more heat, so the middle of the channel has the lowest Q_λ, since from this point, the effective channel length is the longest. What is strange, though, is the clear angle dependence. In perfect counterflow, there should be no dependence on orientation because there is not supposed to be any net mass flow, and because there should not be any buoyancy effect to speak of for the very small temperature differences involved. In fact, they find, for the middle and top locations in the channel, no angle dependence. It is only seen for the lowest location. Also, when horizontal, Q_λ behaves as expected; lowest for the middle of the channel, and higher towards the ends. The suggested explanation for why the lower location sees such a large angle dependence is that the heating induces a flow of helium after all. It is worth keeping in mind that Q_λ represents the heat flux necessary to bring He II up to the transition temperature. As such, the helium will be in a thermodynamic state not very well described by the two–fluid model, and the classical–fluid natural convection may very well be present. This, then, should be seen, to some extent, at all locations along the channel, which they don't. The explanation for this is that only at the bottom of the channel is there ample supply of cool He II which depresses the local temperature, permitting the abnormally high Q_λ.

Note that Lottin and Van Sciver had already observed something essentially like natural convection in a long cooling loop filled with He II when a low–lying region of the loop was heated sufficiently to bring the helium locally above T_λ [136].

Time–Dependent Measurements

Okamura *et al.* made transient measurements on a channel similar to that used by Chen and Van Sciver [137]; 170 mm long, 7 mm wide, and depth of 0.5, 1, or 1.5 mm. A nichrome foil heater is placed along the channel, so the entire length of the channel is heated. They place five temperature sensors on the helium channel side, and three on the heater itself. Edge sensors are 25 mm from the ends, and helium sensors are 30 mm apart.

Their steady state results are reasonably in line with Chen and Van Sciver's results, including evidence of the enhanced Q_λ when their channel was vertical (Okamura *et al.* only test vertical and horizontal orientation, with no angles in between). Note that Okamura *et al.* do not explicitly comment on this observation, but their data (their Figure 2a) certainly suggest the same behaviour as that described by Chen and Van Sciver.

Their transient results for helium channel temperature development during three applied heat fluxes around Q_λ are shown in Figure 2.22. Q_λ here, in a bath of 1.92 K, and for a channel depth of 1.5 mm, is around 0.9 $\mathrm{kW\,m^{-2}}$. Several observations are of note. Most obvious is that establishing a steady state takes a very long time. Going back to Vinen's expression for how long it takes to develop turbulence $\tau = aQ^{-3/2}$ (Equation (2.43) on page 33), Okamura *et al.*'s rectangular channel is relatively similar to those used by Vinen in the original turbulence onset experiments, meaning $a \simeq$ 60 $\mathrm{ks\,W^{3/2}\,m^{-3}}$ (see Figure 2.13 on page 34). With $Q_{\mathrm{app}} = 0.8\ \mathrm{kW\,m^{-2}}$, $\tau \simeq 2.5$ seconds. However, the heat flux is represented by the cross section of the heater surface, not the helium channel cross section. The relevant heat flux for development of turbulence (after which the Gorter–Mellink regime dominates) is the heat flux in the channel itself. Since the heater covers the entire underside of the channel, the local heat flux in the helium changes with location, from a minimum near the middle to a maximum near the ends. For simplicity, look at the heater area for the left half of the channel; 85 mm by 7 mm, and the cross section of the channel; 7 mm by 1.5 mm. The heat flux at the channel end is thus the applied heat flux multiplied by the ratio between these two areas; $Q_{\mathrm{He\,end}} \simeq 45\ \mathrm{kW\,m^{-2}}$. This assumes heat flow is symmetric to either side of the midpoint. Using this in Vinen's expression gives $\tau \simeq 6.3$ ms. This means it might only take a few tens of milliseconds before most of the channel is dominated by turbulent mutual friction, with the Gorter–Mellink expression for heat

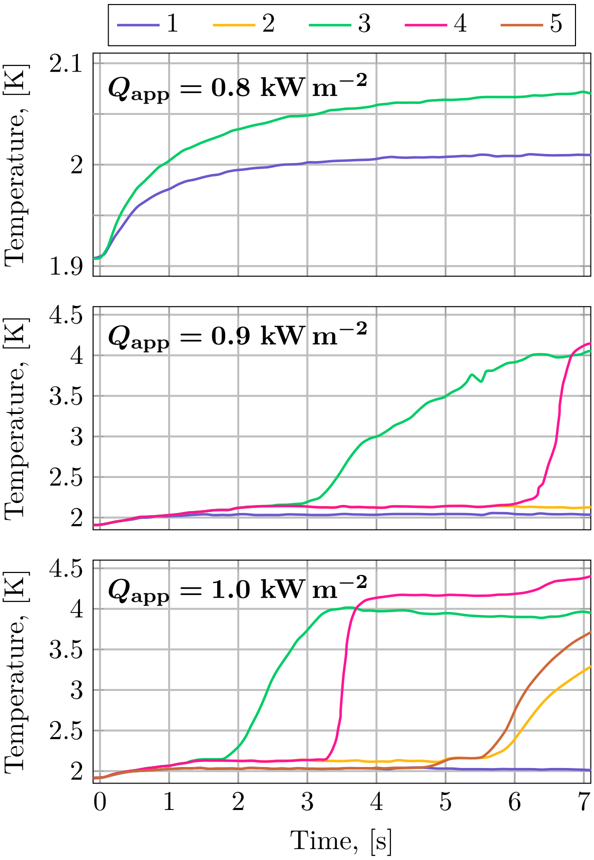

Figure 2.22: Okamura *et al.*'s transient measurements of helium channel temperatures in the horizontal orientation for a bath temperature of 1.92 K and a channel depth of 1.5 mm [137, recreated from Figure 6b]. Sensor 1 is nearest the left end of the channel, Sensor 3 is in the middle, and Sensor 5 is nearest the right end of the channel. For $Q_{\text{app}} = 0.8\,\text{kW}\,\text{m}^{-2}$, results for sensors 2, 3 and 4 are indistinguishable. The same for sensors 1 and 5. For $Q_{\text{app}} = 0.9\,\text{kW}\,\text{m}^{-2}$, results for the edge sensors (1 and 5) are indistinguishable.

transfer accurately describing the time–development. This is a simplified picture; it is not clear how fast turbulence that develops near the channel ends propagates towards the middle, or even if it does at all, given that the channel heat flux near the middle is very low compared with that near the end. Further complicating this is the measurement by Awschalom and Schwarz that finds there is practically always some small remanent density of vortex lines in the helium [138], meaning that turbulence does not develop from a completely pure laminar state.

For higher heat flux, He I forms in the channel, seen as first Sensor 3 and then Sensor 4 shooting up towards 4 K for $Q_{\text{app}} = 0.9\,\text{kW}\,\text{m}^{-2}$. For $Q_{\text{app}} = 1.0\,\text{kW}\,\text{m}^{-2}$, the picture becomes increasingly complicated, notably because Sensor 4, which is halfway between the midpoint at Sensor 1 and the edge region at Sensor 5, reads the highest temperature. The temperature appears to eventually go above the boiling temperature around 4.22 K, but the results were not plotted for sufficiently long times to tell if the sensor data then started to display the characteristic chaotic behaviour associated with boiling (note that time–dependent heater temperatures would remain stable in the nucleate boiling regime, but the departing bubbles would significantly disturb the time–dependent helium temperatures). Okamura *et al.* do not comment on this symmetry violation, though an important point stands; the middle region of the channel is warmer than the edges, which makes intuitive sense, seeing as heat transfer, and thus thermal gradient, must be from the middle towards the ends.

Figure 2.23 shows Oakmura *et al.*'s transient measurements in a 1 mm deep channel for a bath temperature of 1.8 K, with $Q_{\text{app}} = 0.8$ kW m^{-2}. For this configuration, $Q_\lambda \simeq 0.65$ kW m^{-2}, so these results show a situation where the applied heating is further above Q_λ than what was shown in Figure 2.22. The picture is even more chaotic now than before; although the middle sensor does rise above T_λ first, both the adjacent sensors follow very soon after, and reach higher temperatures. Sensor 4, which was hottest before, actually cools back down after some time, while Sensor 2 keeps growing, and shows the sort of jagged behaviour that could be associated with boiling.

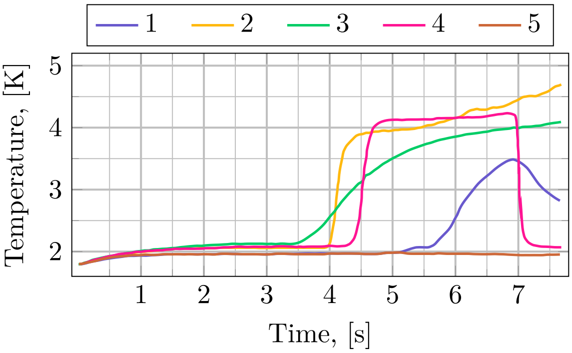

Figure 2.23: Okamura *et al.*'s transient measurements of helium channel temperatures in the horizontal orientation for a bath temperature of 1.8 K and a channel depth of 1 mm, with $Q_{\text{app}} = 0.8$ kW m^{-2} [137, recreated from Figure 11b].

Ultimately, the time–dependent heat transfer in a channel like this is extremely complicated, and certain unintuitive behaviours appear when the heat flux goes above Q_λ, where a single heat transfer mechanism no longer dominates, and then again once boiling begins.

Chapter 3

Experimental Design

Chapter content:

The core of the work presented in this thesis is the experimental setup; a heater exposed to helium, instrumented with temperature sensors to measure time–dependent and steady state temperatures.

This chapter covers, in extensive detail, the design of the setup, choices made, and how data is collected. Beyond proving to experienced readers that confidence in the setup is warranted, it is also meant to give budding scientists about to design their own setups a review of some of the many issues that inevitably crop up during such work.

The chapter is divided in four; Section 1 describes the conceptual design, while Section 2 follows with a description of what was actually placed in the cryostat. Section 3 details the instrumentation and data acquisition systems. Section 4 reviews the relevant properties of the materials used to build the setup.

3.1 Design of Experiment

As laid out in Chapter 1, the heat transfer experiment that forms the backbone of this thesis needs to approximate the conditions experienced by a strand in the LHC MB magnets during a UFO event. These conditions are described by the following qualitative characteristics:

- A volume of metal is heated by a transient source of energy that has, roughly, a Gaussian time–profile, where zero energy is delivered after about 1 ms;
- The metal volume has a surface in direct contact with He II, and this helium cools the surface during the transient energy deposition;

- The helium touching the surface of the metal is confined to a small channel with only limited thermal contact to a larger external bath into which the deposited energy drains on long time–scales.

An additional need is that in order to validate the experimental results, the sample must be operational also in an open bath configuration in order for open bath steady state measurements to be made, since, as discussed in Section 2.1 on page 10, while it expected to work also during transient heating, the only regime where the Kapitza model (Equation (2.28) on page 21) is *known* to provide a reliable description of heat transfer is in steady state when the heater is submerged in a large volume of stationary He II.

Figure 3.1 shows a schematic representation of what immediately surrounds a single strand in the Rutherford cable of an LHC MB magnet. Labels are as follows;

(1) Representative strand on which the design is based;
(2) The part of the inter–strand helium assigned to the strand in question;
(3) Crossing strands in the second layer of the Rutherford cable;
(4) Adjacent strands in the same layer of the Rutherford cable;
(5) Insulation wrapped around the outside of the Rutherford cable;
(6) The part of the inter–strand helium assigned to the surrounding strands;
(7) External helium bath. The thermal path from inter–strand helium to the bath is typically much more complicated than indicated here; an actual magnet is made up of stacks of several Rutherford cables, and there are also micro–metre channels along gaps in insulation layers leading to the bath.

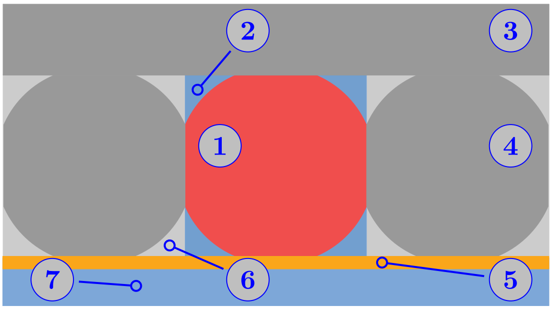

Figure 3.1: Schematic representation of what surrounds a single strand within the Rutherford cable of a main dipole LHC magnet [139, Recreated from Figure 11].

The strands of an inner layer LHC MB magnet cable are 1.065 mm in diameter [25, Sec. 7.2.1], giving a circumference of 3.35 mm. Approximating a strand will be done by using a narrow metal heater strip. As indicated in Figure 3.1, the strands in the cable are not completely circular. This is due to large external pressure applied to the magnet cables from a collar around the magnet, which causes the relatively ductile strand material to deform. This also means that only a part of the strand perimeter is in contact with He II. As described, for instance, by Bottura *et al.* in their computer model of an entire cable, the wetted perimeter of a strand could be, on average, as small as 4% [140].

3.1.1 The Physical Sample

Two main practical reasons lead to using a heater strip width of 3 mm; 1) assembly of the sample is done by hand, and a wider strip is easier to handle than a narrower one; and 2) the temperature sensors used for instrumentation of the sample are 1 mm wide, while the pressure sensors intended for use in the closed channel configuration are 1.7 mm wide, giving a practical lower limit on the width of the heater. 3 mm is still on the order of the strand perimeter, and makes assembly and handling less error–prone.

The length of the heater strip is constrained by two factors; 1) it must be longer than a single strand twist pitch in the Rutherford cable (115 mm), and 2) it cannot exceed the diameter of the cryostat into which the sample is placed (250 mm). To make sure there is ample room for wiring, the heater strip has a design length of 150 mm. This is also the length of the channel. Note that the real heater strip must extend further than this; there must both be some spare length of steel onto which a layer of copper can be sputtered in order to provide a good surface for soldering of power leads. The real heater strip has 158 mm of exposed stainless steel, 150 mm of which is inside the channel during closed channel tests.

Choosing the thickness of the heater strip is a question of desired electrical resistance and the material used. This is discussed in detail in Section 3.1.2 on page 62. For now, it suffices that the heater strip material is stainless steel 304, and the strip's thickness is 50 µm.

The heater strip is supported in a bottom plate made of glass–fibre reinforced polyether ether ketone (PEEK) (throughout this work, PEEK is always referring to GF PEEK). PEEKis chosen because it has a thermal contraction similar to that of metals, meaning that after mating the heater strip to the bottom plate with Eccobond® glue, the chance of delamination during cooldown is lower. Note that during liquid nitrogen testing it became clear that thermal shock still causes delamination; the PEEK contracts slightly more than the metal, so the metal strip buckles, tearing free of the Eccobond®. For cooling rates slower than about $-20\ \mathrm{K\,s^{-1}}$, no delamination was seen.

Eccobond®, as used herein, refers to the two–component epoxy resin Eccobond® 286 A/B. Eccobond® is used in all places where larger objects are adhesively joined, and for leak proofing/sealing the final closed channel assembly. An earlier design used 3M DP–190 instead, but cracks seemed to form in the cured epoxy. A report by Perin *et al.* finds that Eccobond® 286 A/B shows the best leak resistance from among several usual epoxy adhesives in use for cryogenic applications[141].

Figure 3.2 shows a drawing of the final assembly of top and bottom plates, together with the heater strip. The rectangular detail in the drawing highlights the groove into which the heater strip is glued with Eccobond®. The groove is 3.1 mm wide to account for manufacturing tolerances on the bottom plate and the heater strip. The groove is 190 µm deep to fit the heater strip with some margin. The circular detail highlights the laminate that makes up the heater strip; the orange base layer is 100 µm thick, and is made of Kapton; the yellow mid–layer is around 30 µm thick, and is a glue that holds the Kapton and stainless steel together; the red top layer is 50 µm thick, and is the stainless steel heater strip itself. The reason for using a layered structure like this is to make sure there is an insulating material covering the whole underside of the stainless steel heater strip. This helps avoid helium touching the underside of the heater in case the assembly leaves some small gaps or holes between the Eccobond® and the heater. Resting on the bottom plate, is the top plate, with a groove of its own, aligned with the groove in the bottom plate. The top plate groove is also 3.1 mm wide, and it makes the necessary space for the confined helium used in closed channel experiments. In open bath experiments, the bottom plate (with heater) is used alone, so the heater is exposed to the open bath directly.

Label (1) in the drawing points to the two recessed holes right above the heater strip used to mount pressure probes in the channel. No such holes exist in the bottom plate, since the channel area is completely covered by the heater strip. Label (2) points to two of the five temperature sensor lead holes in the top plate. There are five such holes in the bottom plate too. Label (3) points to a hole right above the heater strip used to mount a capacitance measurement probe. Label (4) points to two of the 16 bolt holes used to hold the top and bottom plates together during closed channel experiments.

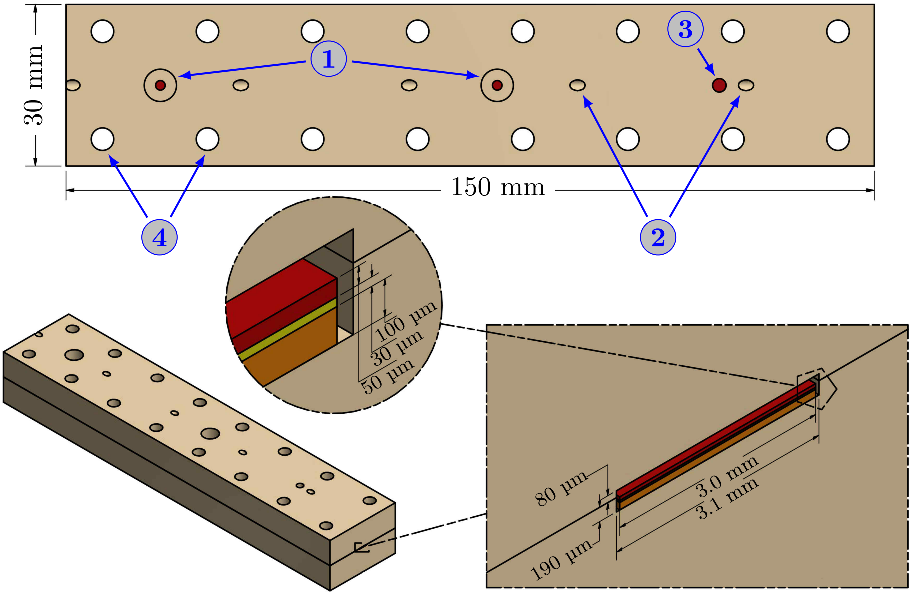

Figure 3.2: Drawing of top and bottom PEEK plate assembly, with heater strip. (1): pressure probe holes, (2): temperature sensor lead holes, (3): capacitance measurement probe hole, and (4): bolt holes, . Bolt holes and temperature sensor lead holes have equivalent holes in both top and bottom plates.

The design depth of the channel is decided as such; around a single strand of an inner layer LHC MB magnet cable there is a cross sectional area of helium approximately equal to the area of a square of 1.065 mm sides minus the area of a circle of 1.065 mm diameter; $\left(1.065\cdot 10^{-3}\right)^2 - \pi/4\left(1.065\cdot 10^{-3}\right)^2 = 2.43\cdot 10^{-7}\ \mathrm{m}^2$. The width of the heater is 3 mm, so the height of the channel should be $2.43\cdot 10^{-7}\ /\ 3\cdot 10^{-3} =$ 81 µm, leading to a design depth of 80 µm.

Figure 3.3 shows the cross sectional views of the top and bottom plates, clarifying the geometry of the temperature sensor lead holes, pressure probe holes, and capacitance measurement hole. It also highlights the dimple in the top and bottom plates where the temperature sensors are placed. The temperature sensor lead holes are angled 45° in order to ensure a as large a bending radius of the temperature sensor leads as practically possible. In a previous design, the mounting approach for the temperature sensors had the sensor leads following approximately 180° of an arc with $r \lesssim 200$ µm. During cooldown to cryogenic temperature of this older design, about half the sensors lost electrical contact. Only one sensor broke during cooldown of the design presented here.

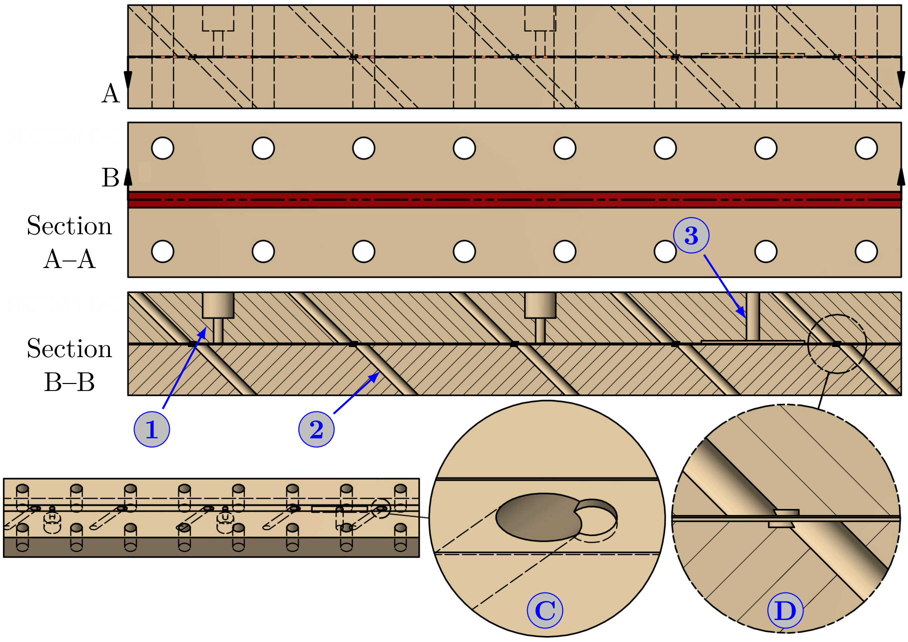

Figure 3.3: Drawing of Top and Bottom PEEK plates, with heater strip. (1): pressure probe hole, (2): sensor lead hole, and (3): lead hole for capacitance measurement probe. Section *A–A* is the top–down view of the bottom plate. *B–B* is the cross section of the top and bottom plates along the centre–line of the assembly, viewed from the side. Detail (C): dimple in the PEEK to fit the Cernox® sensors mounted to the heater strip, and (D): equivalent sensor dimples are also present in the top plate.

After the heater strip is seated in its groove, Eccobond® is injected by a syringe down into the angled sensor lead holes in order to prevent helium from the back of the sample to cool the sensors directly. Figure 3.4 shows the top and bottom plates after injection of Eccobond® into the sensor lead holes. The fragile sensor leads are soldered to metal pads glued to the surface of the plates in order to facilitate the connection of more robust wires onto which the leads that go out of the cryostat are connected. Note that the top plate in the photograph (the lower of the two plates) has the capacitive measurement probe inserted and its hole filled with Eccobond®, while the two pressure probe holes are not yet filled[1].

---

[1] The capacitive measurement lead wire extends from its probe hole midway between the second to left–most pair of bolt holes in the lower of the plates in the photograph.

Figure 3.4: Top Plate and Bottom Plate 1 after installation of heater strip, Eccobond® filling of sensor lead holes, and attachment of sensor leads and sensor lead extensions to soldering pads.

For the experimental work, two identical bottom plates were prepared, referred to Bottom Plate 1 and Bottom Plate 2, and a single top plate was prepared, referred to as the Top Plate.

3.1.2 Applied Heating Power Density

To heat the heater strip, current is passed through it from a source outside the cryostat. For practical reasons (limitations in wiring and power supply), sustaining currents above about 10 A is not desirable. The three main heating events experiments aim to recreate are, 1) steady state heating for the sake of having measurement validation of open bath results against the Kapitza model (Equation (2.28) on page 21), 2) fast sub–1 ms pulses to investigate the UFO beam loss events, and 3) slow pulses that deliver peak power after around 10 ms lasting about 500 ms to help ascertain the validity of using the Kapitza model during a transient heating event. The constraints of the fast pulses guided the design of the external circuitry, while the steady state current constraints decided the thickness of the strip.

Heat flowing from surface to helium To effectively describe the heating events of the experiment, a way to quantify the heat flux flowing into the helium is necessary. The externally applied power leads to a volumetric heating of the heater strip, while it is more practical to express data by something like a heat flux. The applied heating power density, Q_{app}, then, is defined as;

$$Q_{\mathrm{app}} = \frac{\rho L_{\mathrm{strip}}}{W_{\mathrm{strip}} d_{\mathrm{strip}}} I^2 \frac{1}{L_{\mathrm{strip}} W_{\mathrm{strip}}}, \tag{3.1}$$

where ρ is the resistivity, which is around 45 $\mu\Omega\,\mathrm{cm}$, L_{strip} is the length of the strip = 158 mm, W_{strip} is the width of the strip = 3 mm, d_{strip} is the unknown thickness of the strip, I is the current passing through the strip.

At cryogenic temperatures the resistivity of stainless steel changes only negligibly for temperature up to at least 10 K, so Q_{app} is considered temperature independent.

There are a few constraints that together determine the chosen heater strip thickness. For one, 50 µm stainless steel sheets were readily available from the CERN workshop. Then Table 2.2 on page 24 shows that representative heater–to–helium heat fluxes from prior steady state experiments against which validation will be done tend to be somewhere between 50 and 90 $\mathrm{kW\,m^{-2}}$. Finally, there is a practical limit of about 10 A for the current that can be sustained at steady state without risking damage to the power leads that enter the cryostat used for experiments. With $d_{\mathrm{strip}} =$ 50 µm and $I = 10$ A in Equation (3.1) gives $Q_{\mathrm{app}} = 100\ \mathrm{kW\,m^{-2}}$. 50 µm is therefore acceptable.

The main alternative material considered was copper, but in order to get a thickness of copper thin enough to give the desired applied heating power densities under the current constraints, the copper would have to be on the order of 20 nm thick, which would have lead to a much more complicated and expensive heater production probably involving sputtering onto a substrate which would need to be carefully chosen for its material properties. Furthermore, copper has electrical resistivity highly dependent on temperature below 10 K, which would complicate analysis.

For the analysis of data, after the real resistance, R_{strip}, of the heater strip is known, from measurements of the real strips used, the resistivity of the material is no longer directly used to determine the applied heating power density. Also, as will be explained in Section 3.3.1 on page 69, what is actually measured is the voltage across the heater strip, and only after accounting for R_{strip} is the current available. Equation (3.1) therefore becomes;

$$Q_{\mathrm{app}} = \frac{V_{\mathrm{S}}^2}{R_{\mathrm{strip}}} \frac{1}{L_{\mathrm{strip}} W_{\mathrm{strip}}}, \tag{3.2}$$

where V_{S} is the measured voltage across a heater strip. This is the expression that will be used when determining the applied heating power density from measurement data.

Since Q_{app} is a representation of the volumetric applied heating power, it does not directly translate to the heat flux across the heater–helium interface. Nor does it change depending on the open–bath or closed–channel configurations of the setup. It is a function of the resistance of the heater strip, regardless of how much of the heater length is exposed to He II.

RLC circuit for pulses In order to generate fast pulses with sufficient power, an approach using the discharge of a capacitor into a resistive–inductive circuit, with the heater strip included, is used. There are two important benefits to this; 1) the circuit is simple, and made with readily available components, and 2) the circuit is flexible, so more than one time–scale can easily be tried by changing components.

Figure 3.5 shows the circuit used to generate the pulses delivered to the heater strip. R_{pulse}, L, and C are chosen to get the desired pulse shape, and V_0 is chosen to get the desired total energy delivery.

To charge C, $T1/G_1$ and $T2/G_2$ are both off, so current flows into the capacitor, but not onward to the terminal. Once the desired charging level is reached, $T1/G_1$ turns on. This bypasses the capacitor because voltage across the open $T1$ transistor is much lower than the threshold voltage of the diode. Having the diode and $T1$ transistor in the circuit means the voltage source does not need to be turned off during pulse firing. A bypass resistor in series with the voltage source is needed to limit the current.

To fire the pulse, $T2/G_2$ is turned on. This lets current flow from C to ground, through the heater strip.

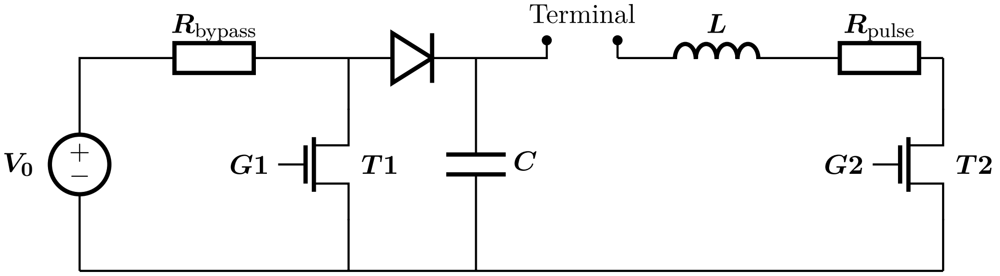

Figure 3.5: Pulse generation circuit. V_0 is a DC voltage source that charges the capacitor C. The diode ensures energy from C only passes to ground through the heater strip. R_{bypass} is used to limit the charging and bypass currents. "Terminal" denotes the connectors where the heater strip power leads are attached (everything behind the terminals is at room temperature). L and R_{pulse} are used to shape the pulse. G_1 and G_2 are the gates to the two power transistors $T1$ and $T2$ that are both off when charging C and on during pulse firing. Turning on G_1 happens when C has charged to the desired level. Then G_2 turns on at some later time to fire the pulse.

A discussion of the circuit elements and the analytical model used to describe the circuit is relegated to Appendix A on page 163, seeing as these parameters are not critical for the project as such. The important part is the resulting time–dependent current pulses, which are discussed in Section 3.3.1 in relation to the data acquisition (DAQ) system for the heater strip(s).

Steps in Applied Heating Power Density When applying a step in current, used for steady state measurements, a much simpler circuit is used than that for RLC pulses. Figure 3.6 shows a diagram of the circuit configuration when applying stepped heating. The source is set to the desired current value, and left "on". The transistor T is then turned on by G when the step is to begin. The reason for using the transistor to control when the current starts to flow is that the transistor turns on much faster than the internal switch in the current supply, and it turns on in a smoother way than what is possible with a manually operated switch.

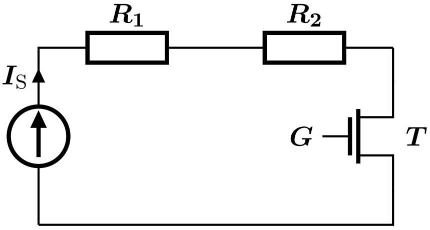

Figure 3.6: Simple diagram of the circuit used for stepped heating. I_S is the set current on the source. R_1 and R_2 represent the heater strips (stepped heating in closed channel uses only R_2). T is the same transistor as $T2$ in Figure 3.5. G is the gate signal to start the current flow.

3.2 Real Samples in the Cryostat

Figure 3.7 shows a diagram of the double bath cryostat used for experiments. The experimental sample is placed within the inner, pressurised He II vessel (Label (9) in

Figure 3.7: Diagram of the cryostat used for experiments [142, Recreated from Figure 1b].
(1): Vacuum vessel
(2): Foam insulation
(3): Liquid helium vessel
(4): Thermal radiation shields on insert
(5): Lambda plate supports
(6): Liquid helium bath with surface at atmospheric pressure and 4.2 K
(7): Lambda valve; closed during operation
(8): Lambda plate
(9): Pressurised He II vessel; the experimental sample is placed here
(10): Saturated He II vessel
(11): Joule–Thomson valve
(12): Heat exchanger
(13): Inner thermal radiation shield
(14): Outer thermal radiation shield
(A): Instrumentation lead port
(B): Helium transfer port
(C): Saturated bath pumping port.

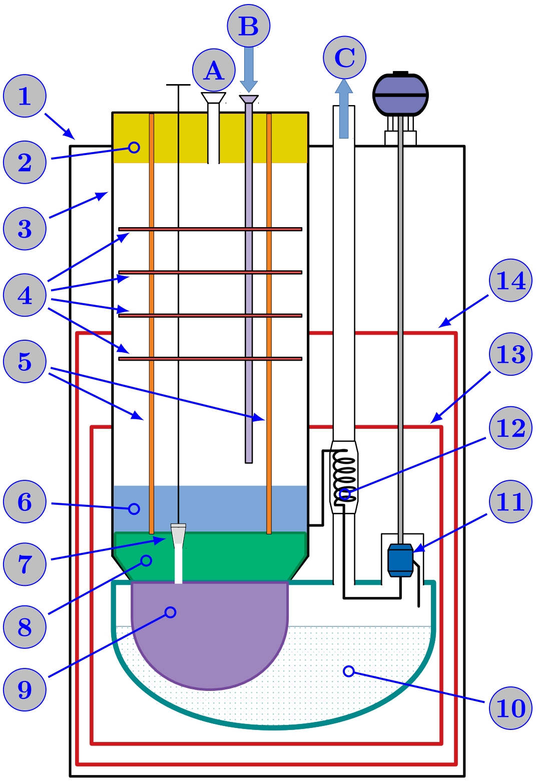

figure). The helium in this inner bath is regulated to a desired set–temperature, for instance 1.9 K, by two processes working together;

1. The saturated bath is kept at some temperature a few millikelvin below the desired set–temperature of the inner bath by controlling the pressure at the surface of the saturated bath. This is done using a pressure controller that acts on a butterfly valve sitting between the pumping port (Label (C) in the figure) and the vacuum pumps.
   Increasing the pumping (opening the butterfly valve) means the pressure on the saturated bath falls. The temperature of the bath then falls as the slightly–too–hot helium molecules that escape the saturated surface are pumped away.
   This means the bath keeps losing helium to pumping, and the Joule–Thomson valve (Label (11) in the figure) is used to regulate the rate of helium replenishment to the cryostat. The helium that fills the saturated bath passes through a heat exchanger (Label (12) in the figure) in order to lower the temperature of the new helium coming in.
2. The inner bath is regulated by using a heating element within the bath to maintain the temperature at the set–temperature. The thermal gradient within the bath is negligible so long as the experimental sample is at least a few centimetres from the heating element and the helium is He II.

These two regulation methods are operating independently. This means some care must be taken when setting the inner bath temperature and the saturated bath pressure. If the saturated bath pressure is low enough compared to the inner bath set–temperature, the inner bath heater will keep adding heat that then passes out into the saturated bath, which will then evaporate unnecessarily large amounts of helium. There is a helium recovery system connected to the vacuum pumps that pump on the saturated bath, so the helium used is not lost to the atmosphere, but it is still desirable to not waste expensive helium.

Figure 3.8 shows a photograph of the cryostat insert, from a little above the Lambda plate and down, shortly before the insert is lowered into the liquid helium vessel (Label (3) in Figure 3.7) for open bath measurements. The wires around the two plates mostly pertain to instrumentation, which will be discussed in Section 3.3, and some are for applying current to the heaters.

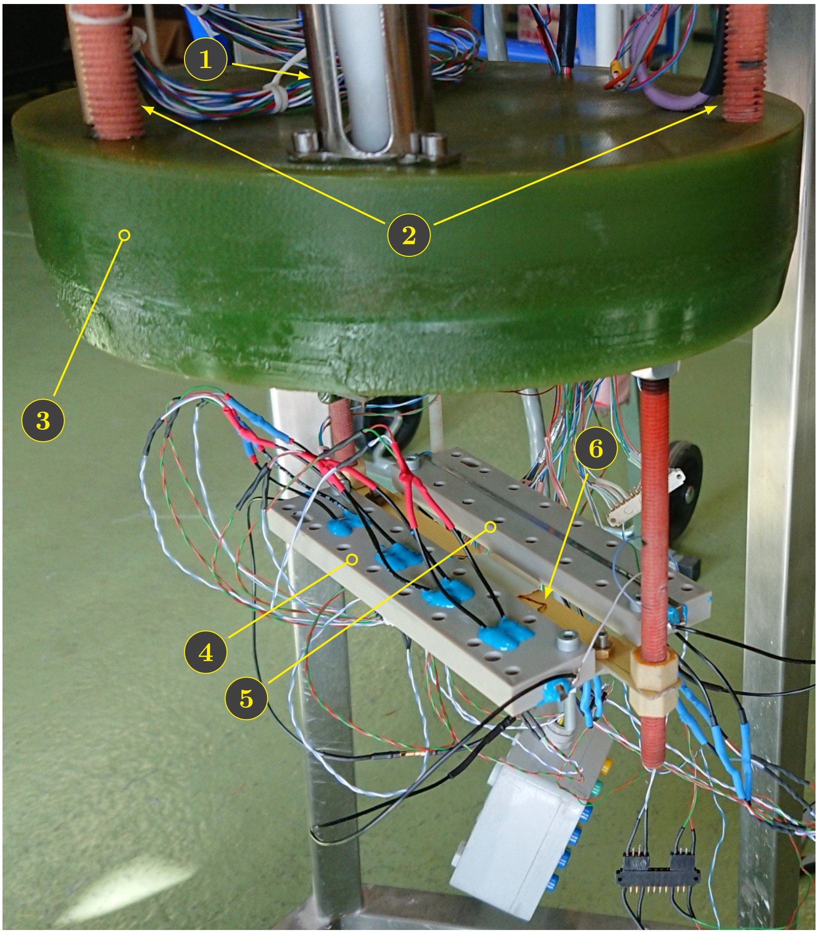

Figure 3.8: Photograph of the bottom of the cryostat insert set up for open bath measurements. (1): Lambda valve (Label (7) in Figure 3.7). (2): Lambda plate supports (Label (5) in Figure 3.7). (3): Lambda plate (Label (8) in Figure 3.7). (4): Bottom Plate 2. (5): Bottom Plate 1. (6): Reference temperature probe, used for temperature control and calibration.

Figure 3.9 shows a photograph of the cryostat insert, from just below the Lambda plate and down, shortly before the insert is lowered into the liquid helium vessel for closed channel measurements.

In order to ensure there were no continuous thermal paths through superfluid helium, leading from the helium channel to the bulk bath outside the sample, the entire perimeter of the interface between the two PEEK plates was sealed with Eccobond® (seen as the blue band running along the middle of the sample). To the same end, Eccobond® was applied around the heads and nuts of all the aluminium bolts used to press the two plates together. This measure proved successful at isolating the channel helium from the bulk bath, but has the drawback that it is not possible to gain non–destructive entry into the channel after the Eccobond® has cured.

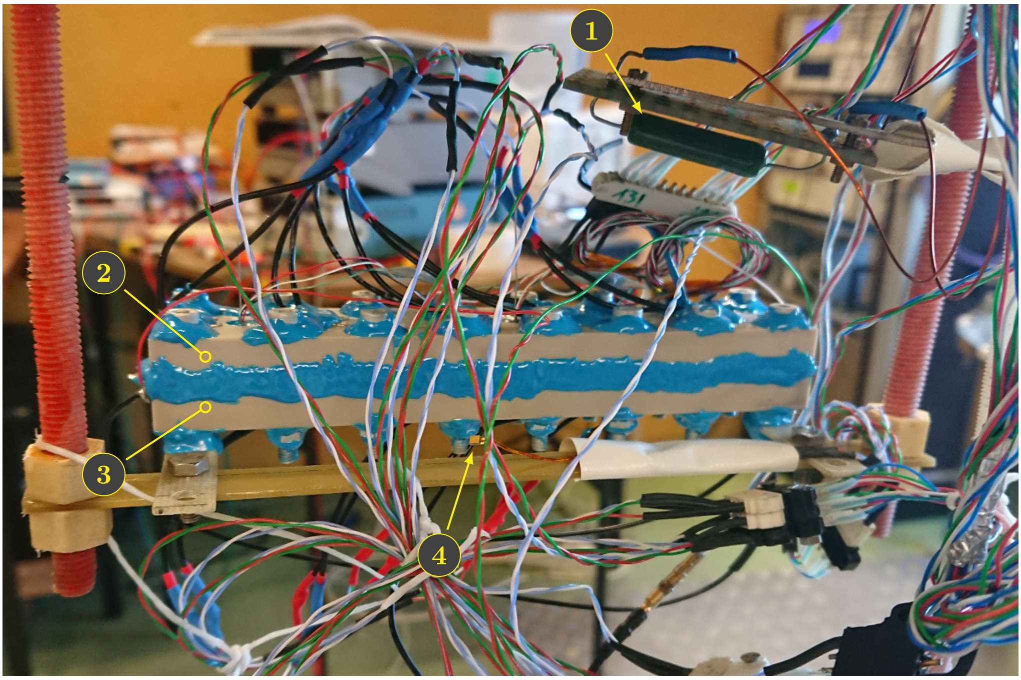

Figure 3.9: Photograph of the bottom of the cryostat insert set up for closed channel measurements. (1): Heating element used to control the temperature in the pressurised He II bath. (2): the Top Plate. (3): Bottom Plate 2. (4): Reference temperature probe, used for temperature control and calibration.

About channel depth and pin–holes After first assembly of the closed channel, bolting together the Top Plate and Bottom Plate 2 (before sealing with Eccobond®), the resulting channel depth turned out to be about 50 µm at both ends of the channel. This error stems from some manufacturing issues that required resurfacing the PEEK plates. The resurfacing left a shallower groove in the Top Plate than intended, but otherwise saved the features necessary for heater strip attachment in the two bottom plates, as well as the sensor dimples in the Top Plate.

To approach the design depth of 80 µm, and reduce the importance of a 25 µm flatness deviation along the channel (found by a dedicated flatness measurement of all

PEEK plates after resurfacing), a layer of 70 µm Kapton tape was placed on either side of the heater strip of Bottom Plate 2 before closing the channel. The resulting channel depth, at both ends of the channel, became 120 µm. Figure 3.10 shows a photograph of Bottom Plate 2 with Kapton tape. Note that during open bath measurements, no tape was present.

Figure 3.10: Bottom Plate 2 with Kapton tape. The two pegs at either end are for alignment of top and bottom plates. Image is rotated 90° clockwise from photograph.

Since helium must be obviously be allowed to enter the sample in order to fill the channel, pin–holes are needed on either side of the channel. Figure 3.11 shows the assembled closed channel sample, seen from the channel end furthest away from labels (1) and (2) in Figure 3.9. On the other side of the sample, there is an identical pin–hole. Before the Eccobond® covering the end of the channel was applied, the tip of a syringe needle was lodged in the channel end. After curing, the needle was pulled out of the Eccobond®.

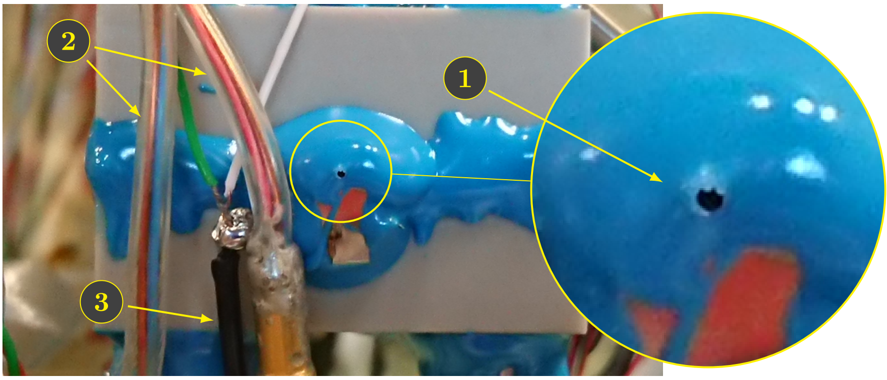

Figure 3.11: Photograph of the assembled Top Plate 1 and Bottom Plate 2, showing the channel end covered by Eccobond®. (1): Pin–hole. (2): Power leads coming from the powering circuit outside the cryostat. (3): Power lead soldered to the heater strip itself, which attaches through a connector to the blue power lead of Label (2). The thin green lead is the grounding–point for measuring the voltage across the heater strip. The thin white wire is the grounding–point for measuring the capacitance across the helium channel. The two grounding–points are the same, but connect to two different DAQ systems.

Figure 3.12 shows the approximate geometry of a pin–hole. The figure is not to scale. The dotted area on the right–hand side of the figure is the cross sectional area of the pin–hole at the interface between pin–hole and channel. Its area[2] is $3.405 \cdot 10^{-8}$ m^2.

---

[2] The area is found in two steps; 1) take the area of the circle sector of angle 2θ in Figure 3.12, and 2) subtract from this area the triangle of angle 2θ and height 105 µm.

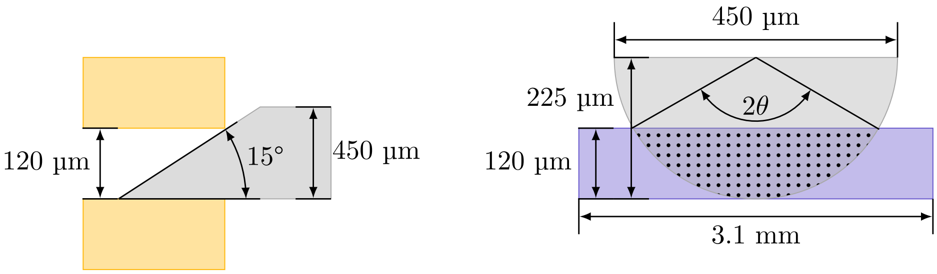

Figure 3.12: Diagram showing the geometry of the pin–hole. The left–hand side of figure shows the needle (grey wedge) lodged between the Top and Bottom plates (yellow rectangles), seen from the side, akin to the orientation in Figure 3.9. The right–hand side shows the channel helium cross section (blue rectangle) with the needle in front of it (grey half–circle), akin to the orientation in Figure 3.11. The dotted area represents the cross section of the pin–hole at the interface between pin–hole and channel.

3.3 Instrumentation

The previous sections laid out the physical sample, with the core part being the stainless steel heater strip and the external circuitry used to generate current pulses that heat the strip, which, then, in turn, heat the helium in contact with the heater. For steady state measurements, the heater strip is still used, but the current is now a step directly from a power supply.

The next step is to explain the way measurements are done. The two most important ones are 1) the voltage across the heater strip, in order to get access to the real resistive heating power density developed in the strip, and 2) the temperature of the heater strip (in both open bath and closed channel measurements) and of the helium in the channel (only relevant for closed channel measurements).

In addition, there are sensors to measure the pressure in the helium channel during closed channel measurements, and a capacitance measurement used to detect the change in helium permittivity when it transitions from liquid to gas.

The final sensor used in experiments is the factory–calibrated reference probe used to calibrate the temperature sensors. This probe, and the calibration itself, is discussed in Section 4.1 on page 109.

3.3.1 Data Acquisition: Heater Strip Voltage

To explain the instrumentation for measuring the voltage across the heater strip(s) during experiments, it serves to look at Figure 3.13 showing a photograph of the setup used for open bath measurements. The closed channel measurements use only a single heater strip, and, as seen in Figure 3.9, the entire sample is sealed in Eccobond® making it harder to see where the voltage probes are attached.

In the open bath setup the two plates are arranged with Bottom Plate 1 (lower plate in Figure 3.13) facing upward, and Bottom Plate 2 (upper plate in the figure) facing downward.

In the figure, labels (5) and (6) point to the measuring leads used to measure the voltage across the heater strips. The set of leads labelled (5) measures the voltage across both heater strips (they are in series), while the leads labelled (6) only measure the voltage across the upwards facing heater.

During closed channel measurements, where only a single heater strip is used, the leads labelled (6) are reused for heater strip voltage measurements, while those labelled (5) are repurposed for the capacitance measurement discussed in Section 3.3.5 on page 92.

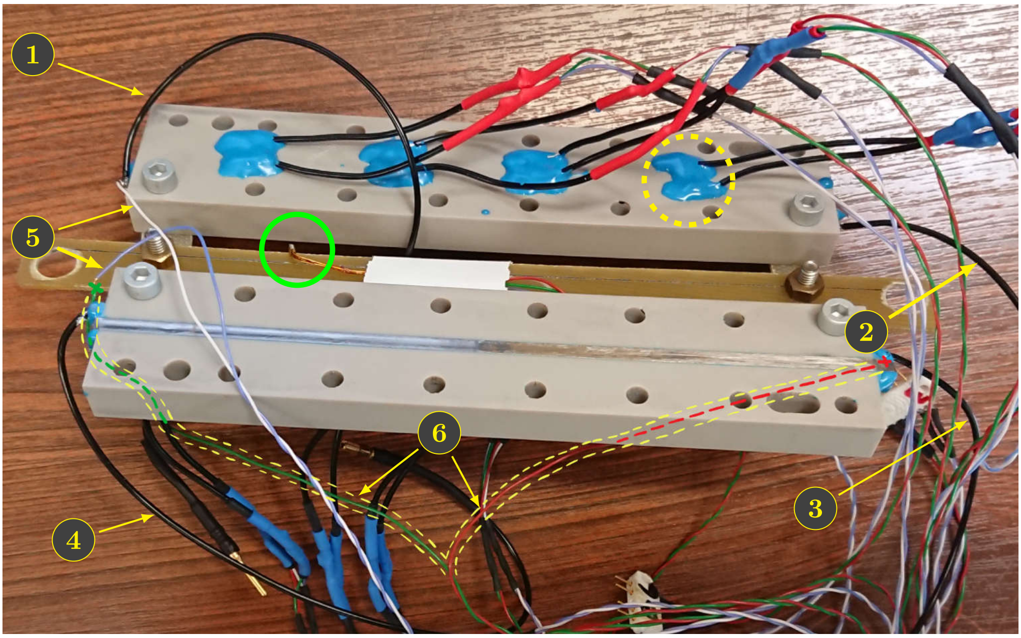

Figure 3.13: Photograph of Bottom Plate 1 (lower in photograph) and Bottom Plate 2 (upper in photograph). The dashed yellow circle towards the upper right highlights the Eccobond® seal placed on all the soldering pads seen in Figure 3.4 on page 62. The green circle near the middle left highlights the reference temperature probe.
(1), (2), (3), and (4): Connector leads on either end of heater strips in their corresponding bottom plates. Current flows from the powering circuit outside the cryostat, into connector lead (1), through the heater strip in Bottom Plate 2, into connector lead (2), then connector lead (3), then into the heater strip of Bottom Plate 1, then to connector (4), and out of the cryostat.
(5): Leads (white and blue wires) that connect to measuring tabs for measuring the voltage across both heater strips in series. (6): The two yellow dashed paths that follow the two leads (green and red wires) that connect to the measuring tabs for measuring the voltage across only the heater strip in Bottom Plate 1.

The measurement itself is done by connecting the terminals of the measurement probes to channels in a National Instruments SCB–68 connection box, which in turn is connected to an NI PCI–6251 multifunction I/O device in a computer running a NI LabView interface. The sampling frequency is 500 kHz. Raw data from the PCI–card is written to TDMS files[3], which are transferred to a separate computer for analysis in Python using the **`npTDMS`** package. The same PCI–card also sends the signals that turn on the two transistors $T1$ and $T2$ in Figure 3.5 on page 64.

Three different power supplies are used during measurements; for low power steady state measurements in the open bath configuration, an Aim–TTi EL155R source is used; for transient step measurements in the open bath configuration, an Agilent Technologies/Keysight N8735A source is used; and for transient step measurements in the closed channel configuration, a Keithley 2400 source measure unit (SMU) source is used.

Charging of capacitors for pulsed measurements in the closed channel configuration is done with the Aim–TTi source, though for those measurements, the heating circuit is independent of the source, since energy during pulses is supplied by the capacitor.

Two heater strips, one measurement Once an external circuit that can generate the desired pulse shape and amplitude is found, the critical step for analysis is knowing the resistance of the heater strip(s). The voltage across one heater strip is measured, and knowing its resistance means knowing the current, which in turn means knowing the heating power density developed in the steel according to Equation (3.2) on page 63.

From Figure 3.13, there are two possible heater strip voltage measurements; V_1, the voltage across the heater strip in Bottom Plate 1, and V_{both}, the voltage across both heater strips. Running a steady 1 A current, independently measured by a Keithley 2400 SourceMeter® SMU to 0.9995 A, with a current sensing accuracy of $\pm 0.22\% + 560\ \mu\text{A}$ [143], with the two heater strips at 1.9 K, yields 0.923 V across both heater strips, and 0.465 V across Heater Strip 1. This means the voltage across Heater Strip 2 is 0.458 V. This means R_1, the resistance of Heater Strip 1, is $0.465 \pm 0.001\ \Omega$, while R_2, the resistance of Heater Strip 2, is $0.458 \pm 0.001\ \Omega$.

During the open bath measurements, only the voltage across Heater Strip 1 was measured, and the voltage across Heater Strip 2 is obtained by the ratio of their resistance values;

$$V_2 = \frac{R_2}{R_1} V_1 = 0.985 V_1. \tag{3.3}$$

The reason for choosing to measure only Heater Strip 1 is three–fold; 1) the heater strips have different resistance, so a single measurement across both would give the wrong applied heating power density value for the open bath measurements. 2) the PCI–6251 card has a maximum range of ±10 V, meaning that for a total strip resistance of almost 1 Ω, a current of 10 A would exceed the rated voltage, causing clipping of the measured value, so some form of voltage divider would be necessary. And 3) for closed channel measurements, only a single strip is used, so by using a workflow that has only a single heater strip measurement regardless of configuration, the circuit setup and data analysis become less error prone.

---

[3] The TDMS (Technical Data Management Streaming) file format is a proprietary binary file format created by National Instruments that facilitates the streaming of high frequency data capture directly to disk. Reading such files requires special software, though many commonly used applications have easily available or built–in access, such as Microsoft Excel, OpenOffice Calc, or the **`npTDMS`** package in Python.

Representative Voltage Measurements

Figure 3.14 shows representative measurements of the voltage across the heater strip during steps in the open bath (3.14a) and closed channel (3.14b) configurations.

The open bath step–heating (Figure 3.14a) shows that the time from power–on till a steady applied current is actually achieved is on the order of 2 to 3 ms. This delay stems from the current source (the Agilent Technologies/Keysight N8735A power supply) needing time to go from zero current to the DC current it is set to. Within 200 µs, the value is 95% of the steady state value. By 500 µs, 98% of set current is reached. The data sheet quotes a load transient recovery time of less than 1 millisecond [144]. This is “Time for output voltage to recover within 0.5% of its rated output for a load change 10–90% of rated output current, local sense”. Going from zero to 100% of rated output current in a total of 3 ms is in line with the specification.

For closed channel step–heating (Figure 3.14b), the smaller and faster Keithley 2400 SMU power supply is used, which reaches the desired output current after only 100 µs. Using the large Agilent/Keysight source for open bath steps, despite its slower rise time, is due to the need for much larger currents in open bath transient steps than in the closed channel.

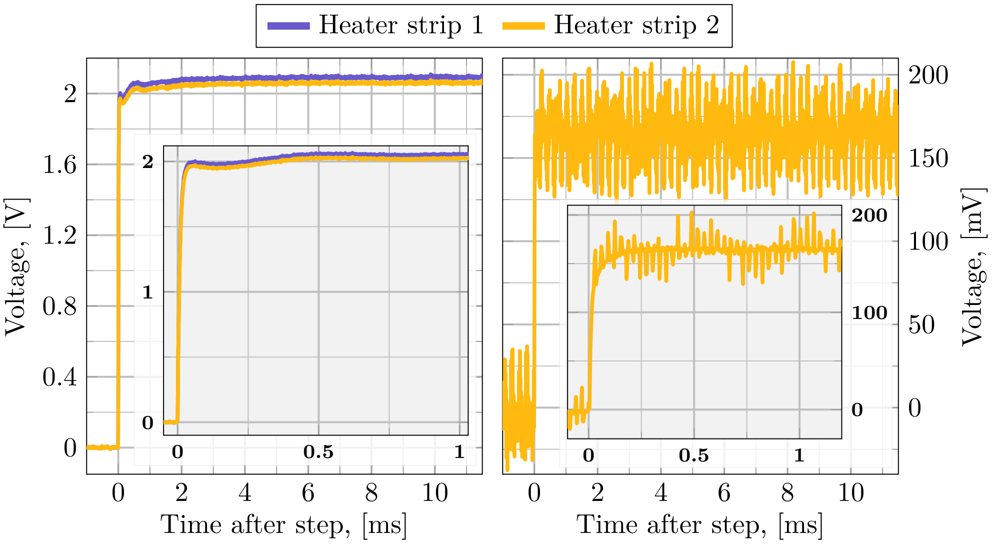

(a) Step–heating in open bath. **(b)** Step–heating in closed channel.

Figure 3.14: Representative heater voltage measurements from a step in open bath (a), and a step in closed channel (b). Recall, only Heater Strip 2 is used in closed channel tests. The inserts highlight the initial parts of the measurements, in the same axis units as the parent figure.

The amplitude of the noise seen on the open bath measurement (Figure 3.14a) is on the order of ±10 mV. This amplitude is seen across all applied power levels. At the lowest heating powers, it translates to an uncertainty in the measurement of less than 5%, while for the measurement shown here, it is only 0.5%.

The noise in the heater strip voltage for the closed channel configuration (Figure 3.14b) is clearly worse than in the open bath case. The amplitude is on the order of

±35 mV. The insert in the figure, which highlights the first 750 µs of the power–on transient, shows that the noise is not very dense; although severe, with amplitude around 20% of the measured value, a simple median filtering of the data is enough to clean up the signal. The noise also displays a structure. In the open bath measurement (Figure 3.14a), the noise is random. In the closed channel, however, there is clearly some form of a modulating oscillation present; there is a peak about every 14 µs, with a modulating envelope of frequency around 4.0 kHz (found by the approximate period between peaks of the envelope). There is no clear source of this noise, but since it can be filtered out so easily, it does not impact the measurements.

Figure 3.15 shows representative measurements of the voltage across the heater strip during a fast pulse (3.14a) and a slow pulse (3.14b) in the closed channel configuration.

The pulsed heating plots include the result of a least–squares fitting of data to an analytical expression of a series–RLC circuit response. The RLC model is discussed in Appendix A on page 163. To find the RLC fit curve, the Python package **`lmfit`** is used. It includes an implementation of the Levenberg—Marquardt algorithm, which minimises the least squares error between a model result and data by making guesses at free model parameters within provided constraints. In the RLC model used here, the free parameters are: the initial voltage, V_0, across the capacitor; the resistance of circuit elements that are *not* the heater strip across which the voltage is measured (R_{total} in the figure captions is the sum of this external resistance and 0.465 Ω, the resistance of Heater Strip 1); the inductance, L, and the capacitance C. Note that this fitting does not equate to a measurement of the circuit parameters. The fitting algorithm is essentially a Monte–Carlo method seeking to minimise the least–squares error between the RLC model result and the measurement by adjusting the free parameters of the model. Several configurations of circuit parameters will give curves that are indistinguishable, even if their fit–suggested parameter values differ significantly[4].

In the fast–pulse plot (Figure 3.15a), visible from around 1.5 ms, there is a small oscillating error in the measurement. The value at this time is expected to be zero, plus random noise, but instead, there is a structured oscillatory signal visible, just as was the case for the closed channel step–heating (Figure 3.14b). There is about 15 µs between each little peak, while the frequency of the modulation envelope is about 1.25 kHz. This modulation frequency is very close to the natural frequency of the circuit; taking the RLC fit values[5] of $C = 179.0$ µF and $L = 92.7$ µH gives $f = (1/2\pi)\sqrt{(LC)^{-1}} = 1.236$ kHz. In the closed channel step–heating measurement, the frequency of the oscillation (4 kHz) is not clearly tied to any circuit components, seeing as the powering circuit (shown in Figure 3.6 on page 64) does not contain any capacitances or inductances of sizes needed for oscillations as slow as the kilo hertz range, so the fast–pulse error oscillations being so near the natural frequency of the

---

[4] Quantifying the range is hard, but as an example, capacitance values between 140 µF and 180 µF can all give good fits when variation in the other parameters is permitted. The range of values, then, is at least on the order of ±10%.

[5] Even though the fit values are not a real measurement of the component values, they are in the range of what is correct, and since several pairs of C and L values will give similar frequency, the RLC fit values are useful to assess the circuit behaviour.

circuit could be a coincidence[6]. Since the amplitude of the structured component of the noise is low, though, and does not reflect actual current flowing in the heater strip, which is clear seeing as the oscillations are also present *before* any power flows at all and the temperature measurements do not show low–powered continuous oscillatory energy input (see Section 4.5.4 on page 137), it will be filtered out and disregarded.

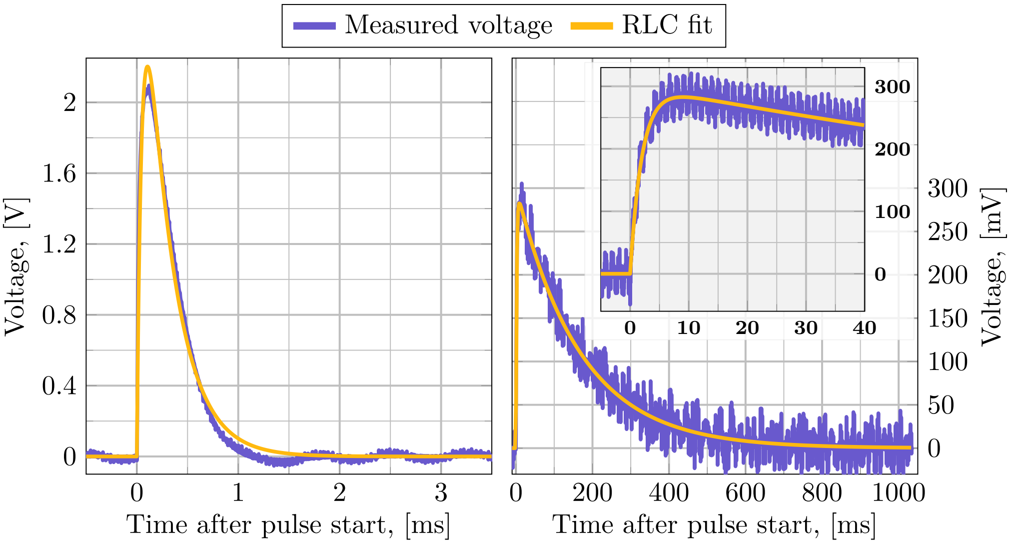

(a) Fast heating pulse in closed channel, with least squares RLC fit. Parameters: V_0 = 10.575 V, R_{total} = 1.795 Ω, L = 92.7 µH, C = 179.0 µF.

(b) Slow heating pulse in closed channel, with least squares RLC fit. Parameters: $V_0 = 2.708$ V, $R_{\text{total}} = 4.273$ Ω, $L = 8.5$ mH, C = 39.5 mF.

Figure 3.15: Representative heater voltage measurements from a fast heating pulse in closed channel (a), and a slow heating pulse in closed channel (b). The inserts highlight the initial parts of the measurements, in the same axis units as the parent figure. Note: the slow–pulse plots show only every 130 measured points for the long–time–scale plot, and every 5 for the insert.

There is also a constant voltage offset in the measurement, on the order of 35 mV, not shown in the plots. It only appears *after* applying the gate voltage signal to transistor $T2$ in Figure 3.5 on page 64, and disappears again immediately after the gate signal is returned to zero. Cross–talk between the output channel used for the transistor gates and the input channels for measurement of voltages is a potential cause. When looking at the temperature data, there is no evidence of any small constant heating that then disappears towards the end of the measurement. As such, the offset is compensated in plots and analysis, and assumed to have no impact on temperature measurements.

In the slow–pulse plot (Figure 3.15b), there is also a large scale, structured measurement error, like in the fast–pulse plot, but the frequency is about 760 Hz. The

---

[6] Parasitic capacitances of instruments are on the order of pico and nano farad at most, so an inductance not accounted for in design would need to be on the order of 1 to 10 H, which is closer to values relevant for large electrical motors, not what could reasonably arise from a few metres of wire in this experiment.

natural frequency of the circuit with $C = 39.5$ mF and $L = 8.5$ mH is only 8.7 Hz. The input capacitance of the transistor is on the order of a few nanofarad at most, while the input capacitance of the PCI–card is quoted as 100 pF [145], so neither of those sources give resonant frequencies near 760 Hz with the circuit inductance. What was true for the fast–pulse measurements is also true for slow pulses, however; when looking at the temperature measurements (see Section 4.5.5 on page 138), there is no evidence of the 760 Hz oscillation. So it will be filtered out and disregarded. The same voltage offset seen in the fast–pulse heater voltage data when the transistor gate signal is on is also seen for slow pulses, and is compensated in the same way.

Offset voltage in stepped heating measurements Since both the fast–pulse and slow–pulse heater strip voltages show an offset voltage associated with the transistor signals used to control the current in the circuit, it must be assumed that also the step–heating measurements have such an offset. In the pulse data, the offset is measured directly, and so, is easily compensated. For stepped heating, however, it is not straight forward; the circuit (Figure 3.6 on page 64) is never in a state where the transistor is in its *on* state while the current is *off* during regular measurements. This means there is no discontinuity in the voltage data just as the transistor is switched off.

For low power steady state open bath measurements, the power supply (Aim–TTi, mentioned on page 71) has a reliable output current measurement, being only about ±0.5% ±3 mA away from the set current [146]. The accuracy of the power supply current measurement is confirmed using the current sensing mode of the Keithley 2400 SMU (which is also used for step tests in the closed channel configuration). This means an expected heater strip voltage value can be calculated from the known strip resistance. This gives an offset voltage of no more than 2.5 mV across measurements at every 100 mA from 0.1 to 5 A, which translates to about 0.25% of the measured voltage value for each test. This small an error is, in practice, not important.

The closed channel step measurements use the Keithley 2400 SMU as a current source directly, which has an output current measurement accuracy of ±0.27% + 900 µA [143]. The current range is from 50 to 1000 mA, so the typical current error will be $^{+2}_{-1}$ mA. This means also for these tests a reliable expected heater voltage value is available; there is, in fact, a significant offset found to be about 42 mV in all measurements. The offset is calculated and compensated for each test. The key difference in the measurement setup between the low power open bath step measurements, that show no significant voltage offset, and the low power closed channel step measurements, that do show such an offset, is that the closed channel measurements includes a measurement of the gate control signal on transistor $T2$ in Figure 3.5 on page 64. The offset likely arises due to cross talk between the output channel and the measurement channel.

High power open bath step measurements use the Agilent/Keysight current source, which has a much poorer internal current measurement and current setting accuracy than the smaller Aim–TTi or Keithley sources, especially at lower currents. Its documentation specifies the current measurement accuracy to ±0.1% + 330 mA [144]. This means estimating the offset voltage based on the set current is not reliable. A dedicated measurement where the current supply was on, but not feeding any current, yields a measured value of 56 mV. This is the offset voltage. However, as seen with the lower power measurements, the offset voltage is not constant from one measurement to another. From the calculated offset voltages in the closed channel step measurements, the observed variation in offset voltage is on the order of ±10% of the offset value. So, for the high power open bath step measurements, the offset voltage will be taken as 56±6 mV.

Note that in Figure 3.14, the offset voltage is *not* accounted for in the plot. The offset voltage is subtracted from the measured signal only during filtering for analysis when converting to applied heating power density (for instance when making the plots in Section 4.5 on page 133).

Skin–effect and current distribution in the heater An obvious question regarding the applied heating power density is if the current flowing in the heater strip is distributed evenly across the heater strip cross section. The fast pulses and steps deliver current with relatively high frequency components; the fast pulses the highest, at around 10 kHz. An oscillating current flowing in a conductor will tend to confine itself to a thin layer near the outer surfaces of the conductor. The thickness of this layer is called the skin depth δ [147, Sec. 8–3.2];

$$\delta = \sqrt{\frac{\rho}{\pi f \mu}}, \tag{3.4}$$

where ρ is the resistivity of the conductor, f is the applied frequency, and μ is the permeability of the conductor material.

For 304 stainless steel, the permeability is that of vacuum; 304 steel is austenitic, and does not exhibit significant ferro magnetism. Wilson and Bunch found that various treatments, like cold–working did not alter the permeability of 304L stainless steel (which differs from 304 steel by having about 0.05% less carbon, the balance made up with iron), while welding increased it by a factor of 2 [148]. No welding or other high–temperature work was done on the heater strips after receiving them.

For the 10 kHz frequency component, with the estimated resistivity of the two heater strips used (around 0.44 $\mu\Omega\,\mathrm{m}$), the skin depth becomes 3.3 mm. If the permeability were twice as high, it would still be 2.4 mm. Both these depths are one and a half orders magnitude larger than the heater strip thickness. This means during all tests, the current is always distributed uniformly over the cross section of the strip.

3.3.2 Data Acquisition: Temperature Sensors

The temperature sensors mounted in the samples are uncalibrated Cernox® bare chip 1050 sensors, with a temperature measurement range from 1.4 K to 420 K, though their sensitivity drops sharply above about 10 K.

Figure 3.16a shows a drawing of the bare chip. It consists of a sapphire substrate (blue in figure) onto which a zirconium oxynitride is photolithographically patterned (red in figure). A gold layer is then sputtered onto the surface and photolithographically patterned to create contacts [149]. The zirconium oxynitride is the sensing element of the sensor.

Figure 3.16b shows a photograph of a Cernox® sensor after first applying a strengthening Eccobond® bead at the attachment points of the leads, and then applying GE 7031 varnish to the leads for electrical insulation. The leads are then twisted, in order to mitigate the mutual inductance coupling between the heater strip and the sensor leads that would otherwise skew transient measurements[7]. Sensor characteristics and operation will be discussed in Section 4.1 on page 109, related to the calibration and translation from measured voltage signal to temperature.

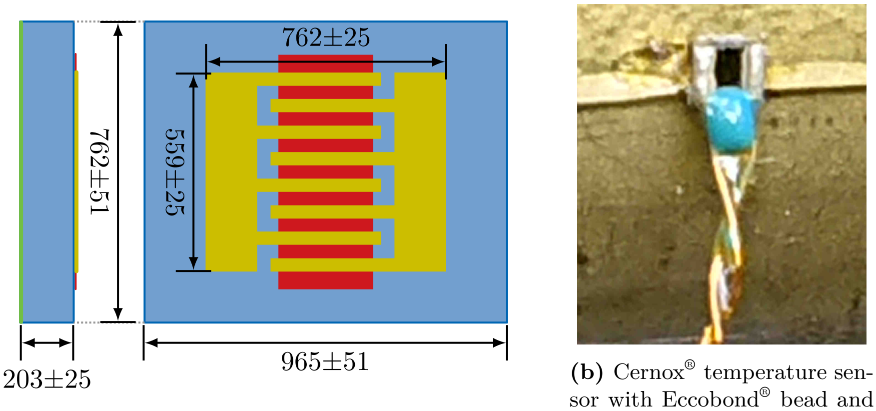

(a) Drawing of Cernox® bare chip [150, Recreation of CX–BR figure]. All dimensions are in micrometres.

(b) Cernox® temperature sensor with Eccobond® bead and twisted GE 7031 varnish covered leads.

Figure 3.16: Drawing of Cernox® bare chip (a), and photograph of Cernox® bare chip (b). In the drawing; blue rectangles are the sapphire substrate (from above or the side). Green line under substrate: Au–Pt–Mo alloy backing sheet. Red rectangle: zirconium oxynitride sensing element. Yellow pattern: gold contacts for sensor lead attachment.

Mounting them is done in two ways; for the two bottom plates, the sensors are mounted directly on the underside of the heater strip, while for the one Top Plate, they are mounted in the small dimples seen Detail (D) in Figure 3.3 on page 61.

Figure 3.17 shows a photograph taken during testing of the temperature sensor attachment procedure, using dummy sensors (without Eccobond® bead). The heater strip laminate has 1.5 mm diameter cutouts every 31.25 mm (starting 12.5 mm from the edge of the Kapton tape), where the stainless steel is exposed. The cutouts align with the mounting dimples in the PEEK plates seen back in Figure 3.3. The temperature sensors are attached to the bottom of the stainless steel heater using GE 7031 varnish. Two such instrumented heater strips are then mounted in their groove in Bottom Plate 1 and 2, such that the protruding temperature sensors slot into the sensor dimples. The sensor leads are threaded through the angled holes, and attached to soldering pads near the sensor lead holes (as seen in Figure 3.4).

---

[7] During transient heating events, the current in the heater strip sees large current changes in time, which causes a strong magnetic field to arise around the heater strip, which in turn couples to the sensor lead loop unless the leads are tightly twisted.

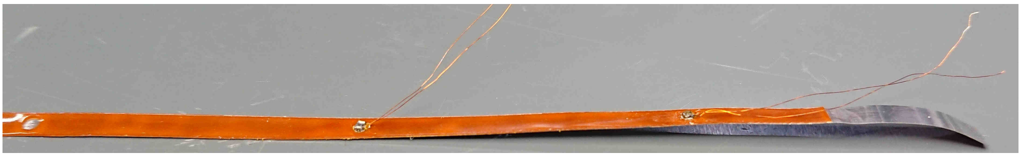

Figure 3.17: Underside of a trial heater strip, testing the temperature sensor attachment procedure with dummy sensors.

Open Bath and Closed Channel Diagrams

Figure 3.18 shows a diagram of the sample configuration used for open bath measurements. The upwards facing plate is Bottom Plate 1, and the downwards facing plate is Bottom Plate 2. Sensor labelling refers to Upwards or Downwards heater orientation and the indexed position relative to the middle sensor in each PEEK plate. There are two sensors missing; `U+1` and `D+2`. `D+2` short–circuited after assembly[8], and `U+1` broke during cooldown[9]. `T_bath` represents the reference probe used both for calibration of the other sensors, and to provide a temperature reference for control of the helium bath.

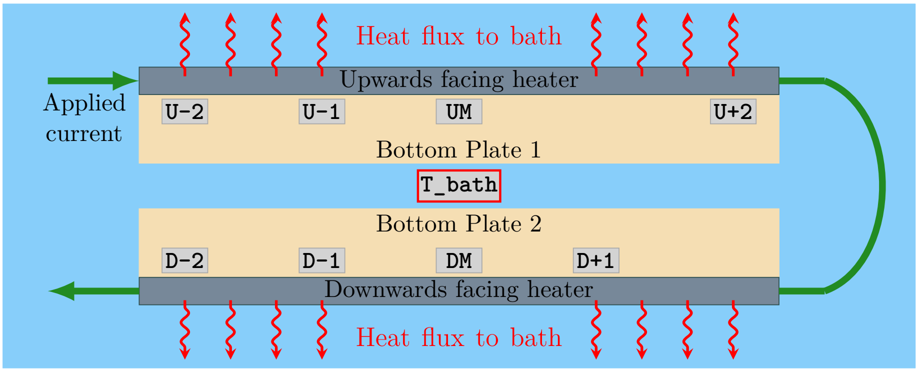

Figure 3.18: Diagram of the configuration used for open bath measurements. The light blue outer rectangle represents the helium bath. Light grey rectangles represent the Cernox® sensors. `D` labels downwards facing heater sensors, and `U` upwards facing heater sensors. The number refers to the sensor's site left (negative) or right (positive) of the middle sensor (`UM` or `DM`). The red–edged rectangle represents the reference probe.

Figure 3.19 shows a diagram of the sample configuration used for closed channel measurements. The closed channel measurements were made after the open bath measurements, and based on the analysis of the open bath results, Bottom Plate 2, the downwards facing plate in the open bath experiments, was chosen for the closed channel experiments. The sensor labelling follows the same indexing convention as

---

[8] The likely mechanism is that when applying the GE 7031 insulation varnish to the sensor leads, its viscosity could make it hard to cover the whole surface of the lead wire. If two bare spots align on the two leads for each sensor, the spots may touch after the leads are twisted. One such issue was discovered at room temperature, before assembly, while the issue with sensor `D+2` was only seen after assembly, when the Eccobond® had cured.

[9] The likely mechanism is that the thermal contraction made one or both of the sensor leads rip from their attachment points, despite the strengthening Eccobond® bead.

before, but the sensors are referred to either as *Channel* sensors (labels with `C`), which are those sensors that are touching the channel helium directly, and are mounted in the Top Plate, or as *Heater* sensors (labels with `H`). Sensors with labels `H-2`, `H-1`, `HM`, and `H+1`, are the same physical sensors as `D-2`, `D-1`, `DM`, and `D+1` from the open bath measurements.

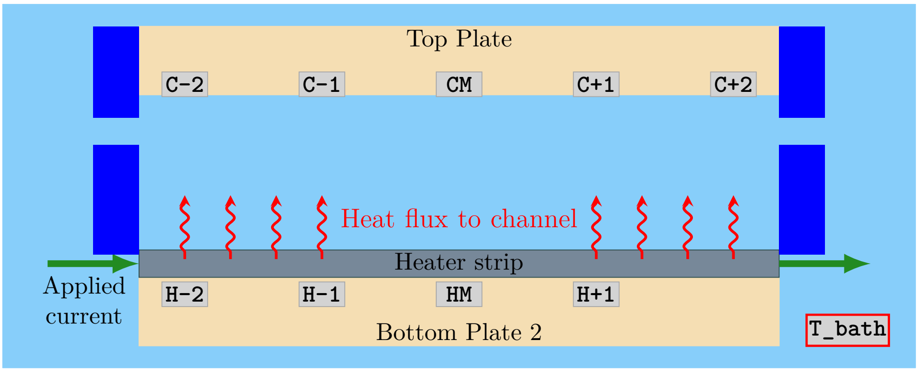

Figure 3.19: Diagram of the configuration used for open bath measurements. The light blue outer rectangle represents the helium bath. The light grey rectangles represent the Cernox® sensors. Sensor labels with `C` are helium channel sensors, and sensor labels with `H` are heater sensors. The red–edged rectangle represents the reference probe. The darker blue blocks on either side of the helium channel represent the pin–hole constriction, separating the channel helium from the bath.

Sample X–Ray Image of Sensors `UM` and `CM`

Figure 3.20 shows an X–ray image of the middle sensors on Bottom Plate 1 and Top Plate 1, as a representative example of the real environment around the temperature sensors. Dark areas in the image generally correspond to regions of high material density in the real sample. Note, though, that the silver–loaded EPO–TEK appears denser than it really is.

The dashed circle highlights small voids in the Eccobond®. The holes are isolated, and no helium enters these voids, meaning they do not interfere with the measurement in any appreciable way. The same goes for the large void highlighted by the dashed rectangle; during application of Eccobond®, the syringe was not inserted deep enough into the sensor lead holes, and a void was left. All sensors in Top Plate 1 have such a void. The void is completely sealed, however, so no helium fills the void, meaning it has no effect on measurements. The large low density region to the upper left of the image is the middle pressure probe hole. For reference, assessing various dimensions in the image is best done by considering the diameter of the sensor lead holes (seen in the dashed rectangle) to be 2 mm, and the sensor substrates to be 200 µm. The labels in the figure point to the following;

Label (1)	Heater strip;
Label (2)	Sapphire sensor substrates. The bright gap between the sapphire and the heater is filled with GE 7031 varnish;
Label (3)	Silver filled epoxy lead attachment beads;

Label (4) External sensor lead attachment wires.

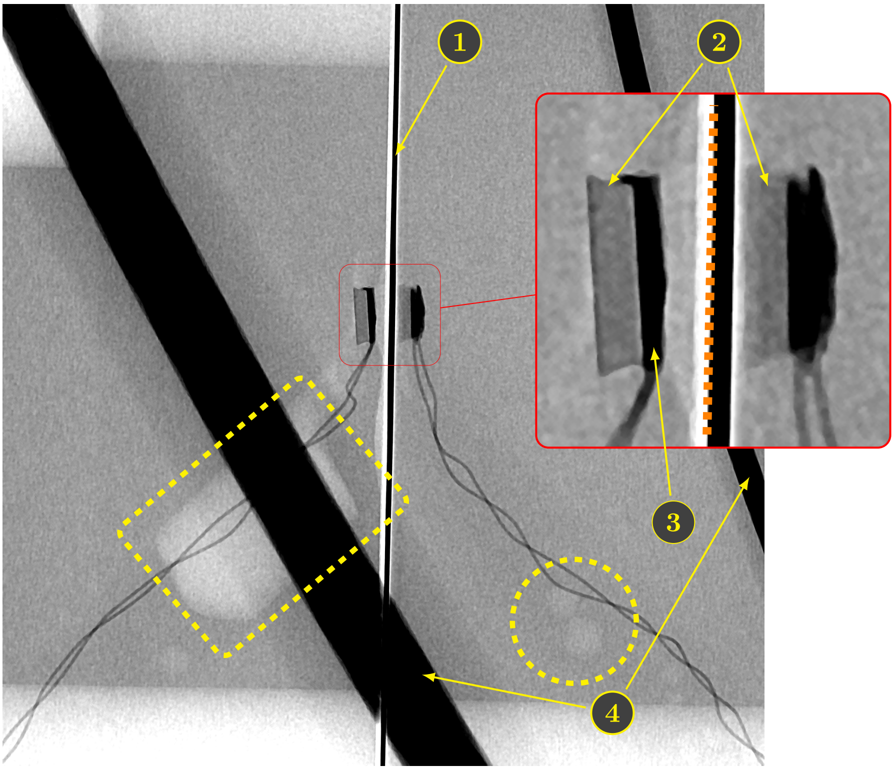

Figure 3.20: X–ray image of sensors `UM` and `CM`, taken at 6 µm resolution. Regions of high density appear darker. The central black line is the heater strip, the surface of which is indicated by the dashed orange line in the insert. Everything to the right of the orange line is the bottom plate, while everything to the left of this is the top plate (the white gap is the channel).
The dashed circle highlights small bubbles/voids in the Eccobond® along the sensor leads. The Dashed rectangle highlights the void behind the Top Plate sensor. The insert magnifies the region around the two sensors. Label (1): Heater strip. (2): Sapphire sensor substrates. (3): Silver filled epoxy for lead connection. (4): External sensor leads (their differing diameter stems from one passing in front and the other passing behind the assembly).

Note that the heater sensor (right–hand side) is oriented with the substrate facing the heater, while the channel sensor (left–hand side) is oriented with the substrate facing away from the helium channel. The heater sensor has its orientation to avoid that sensor lead attachments touch the heater strip, as this would cause a short–circuit, making the sensor useless. The channel sensor has its orientation to achieve the best possible thermal contact between the helium and the sensitive element of the sensor (the zirconium oxide used for the actual temperature sensing).

Figure 3.21 shows zoomed images of the two sensors `U-1` and `UM`, rotated to the heater strip is above them. Using the known Cernox® sensor substrate thickness of 203 µm as a scale, the distance between the heater strip and the sensors can be estimated. This gap is filled with varnish. As seen in the figure, `U-1` is about 20 µm from the heater, while `UM` is a little askew, going from 60 down to 30 µm away. Similar images for `U-1` and `U+1` indicate there is no gap between the heater and `U-2`, while `U+1` is tilted, going from 50 to 0 µm away. There cannot be zero varnish between the heater and a sensor, and since the imaging resolution is 6 µm, all zero–estimates are taken as 6 µm. This means the set of varnish layer thickness estimates is 20, 60, 30, 6, 50, and 6 µm. The RMS value of this set is about 35 µm. This leads to the standard estimated varnish layer thickness of 35 ± 6 µm which is used in the analysis of data in Paper [1] and Paper [2].

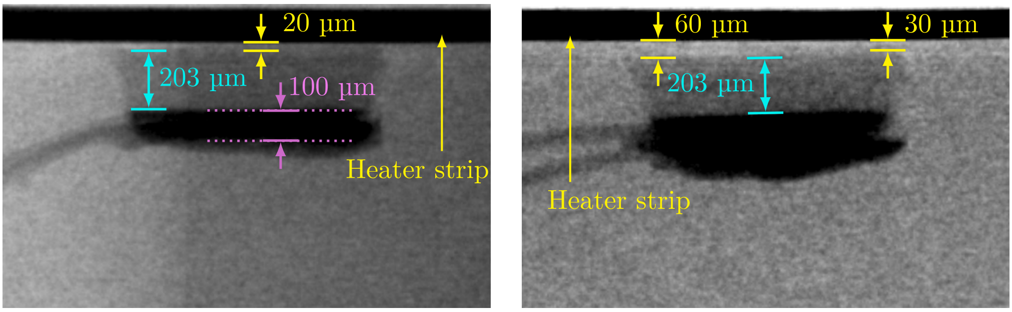

(a) X–ray image of `U-1`. Distance between heater and sensor base is about 20 µm. Purple dimensions indicate the thickness of the EPO–TEK beads.

(b) X–ray image of `UM`. Distance between heater and sensor base is goes from about 60 to 30 µm, for an average of 45 µm.

Figure 3.21: X–ray images of `U-1` and `UM`, showing approximate distances. The imaging resolution was 6 µm. Cyan dimensions are used as the scale in the images.

Measuring the Voltage Across a Cernox® Sensor

Using a Cernox® sensor to measure temperature means measuring the voltage across a material with a temperature dependent resistivity (zirconium oxynitride) subject to a known current. So, three things are necessary; 1) the sensor must be fed some excitation current, which for all the measurements done during this research was 10 µA. 2) The voltage across this resistance (Cernox® sensor) must be measured in order to calculate the instantaneous resistance by using the known excitation current. 3) A calibration must be used to translate the resistance to a temperature. This section will discuss points 1) and 2), while 3) is discussed in Section 4.1 on page 109.

The current source feeding the sensor is outside the cryostat together with all the other DAQ equipment. Figure 3.22 is a circuit diagram showing how the Cernox® sensors are wired. The sensors are connected in series, two at a time, in order to reduce the number of current sources necessary. The voltage across sensors are all measured individually, with circuits independent of the current excitation leads. This means the resistance measurement is a four–lead measurement. The main benefit of this is that the resistance measurement is not contaminated by the lead resistance $2 \times R_{\mathrm{IL}/2}$. The acceptable drawback is that several extra lengths of wire must be built into the cryostat at construction; per resistance measurement, two sets of wires for current excitation and two sets for voltage measurement.

The wires drawn in red represent the approximately 7 cm long sensor lead extension wires and the 2.5 cm long sensor leads, seen back in Figure 3.4 on page 62. The four–lead measurement only really starts at the sensor lead extension ends, where the

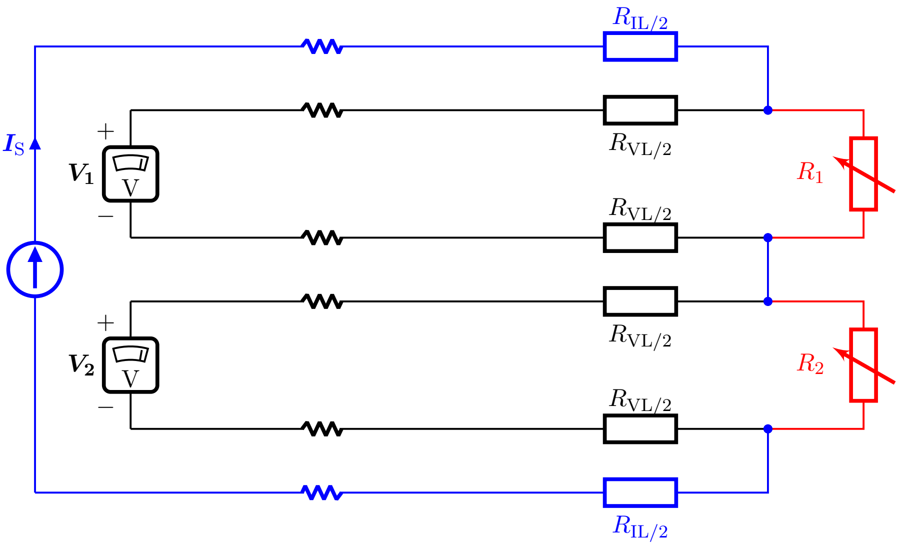

Figure 3.22: Circuit diagram of the measurement setup used for Cernox® sensors. The circuit is set up to use a four–lead resistance measurement of the two sensors while also sharing the current source.
I_S: source current, 10 µA. $R_{\mathrm{IL}/2}$: resistance of the current leads from current source down to Cernox® (the two wires, down and back up, are assumed identical). The jagged elements near the middle of all horizontal leads in the circuit represent the long distance from source/meter to sensor. $R_{\mathrm{VL}/2}$: resistance of the voltage measurement leads from volt meter down to Cernox® (the two wires, down and back up, are assumed identical). R_1 / R_2: Cernox® sensors. V_1 / V_2: voltage measured across R_1 / R_2.

excitation current and voltage measurement wires attach. Even at room temperature, the resistance of this small shared path is imperceptibly small. At cryogenic temperatures, where the sensor resistances typically range from 5 to 15 kΩ, the contribution from the shared path is zero.

The series connections of Cernox® sensors for the open bath measurements are as follows (referring to Figure 3.18): 1) `U-2` and `U-1`, 2) `UM` and `U+2`, 3) `D-2` and `D-1`, and 4) `DM` and `D+1`.

The series connections of Cernox® sensors for the closed channel measurements are as follows (referring to Figure 3.19): 1) `H-2` and `H-1`, 2) `HM` and `H+1`, 3) `C-2` and `C-1`, 4) `CM` and `C+1`, and 5) `C+2` (the last sensor is alone, since there is an odd number of Cernox® sensors in the closed channel experiment).

The voltage measurement leads of each sensor are connected to a pair of terminals in a National Instruments SCXI–1125 module. This module is slotted into an NI SCXI–1000 chassis, which routes the sensor signals to an NI PCI–6052e multifunction I/O device in a computer running a NI LabView interface (note that the heater strip DAQ and temperature sensor DAQ systems are separate and independent).

Open bath measurements As indicated in Figure 3.18, there are eight Cernox® sensors in the DAQ system. The PCI–6052e card has a total of eight differential voltage measurement channels available, and can work at a maximum total sampling frequency of 333 $\mathrm{kS\,s^{-1}}$. The card must operate in multiplexed mode, and with all channels in use, it was seen that some cross–talk between channels showed up at the highest possible measurement frequency (333 $\mathrm{kS\,s^{-1}}$ / 8 channels = 41.625 $\mathrm{kS\,s^{-1}}$ per channel), so the sampling is done at 40 $\mathrm{kS\,s^{-1}}$ per channel, where no such cross–talk was seen.

Closed channel measurements Figure 3.19 on page 79 indicates nine Cernox® sensors in the DAQ system, which, first of all, are more than the number of channels available in the PCI–6052e card. Furthermore, the two pressure probe measurements (discussed in Section 3.3.4 on page 87) are also collected here, as well as a dummy measurement and a measurement of the heater strip voltage. This makes a total of 13 measurement channels. To reach this number of channels, a second SCXI–1125 module is slotted into the SCXI chassis. The chassis itself adds an extra multiplexing layer that effectively extends the number of available channels on the PCI card.

The heater strip measurement is for synchronisation purposes; since the heater strip and temperature DAQ systems are independent, they do not have the same timing, and therefore some means of synchronising data is necessary in order to analyse it. For open bath measurements, to maximise the sampling frequency, visual synchronisation of data streams was done[10]. For the closed channel measurements, a heater strip measurement channel was added to the temperature DAQ system in order to use it as a timing reference between the heater strip DAQ and temperature DAQ systems. The data from this channel is used in a binary way; when it is above a certain noise threshold, the heating is considered *on*, and otherwise *off*.

The dummy channel is present in order to smooth out the switching transient in the SCXI chassis when it internal multiplexer goes from the first 1125–module to the second. This transient gave rise to what appeared to be a fixed voltage offset in the last Cernox® sensor channel. By introducing a dummy channel that was simply a short circuit of the channel terminals, any residual charge on the circuitry in the SCXI chassis that handles going from one slot to another is discharged. Lowering the sampling frequency would have the same effect, but in order to avoid the switching issue the sampling frequency would have to be lowered much further than the cost of adding the dummy channel.

For closed channel measurements, a sampling frequency of 20 $\mathrm{kS\,s^{-1}}$ per channel is used. Frequencies up to 25.6 $\mathrm{kS\,s^{-1}}$ per channel should be possible, but the switching issue was still present at 25 $\mathrm{kS\,s^{-1}}$ per channel, even with the dummy channel. At 22.5 $\mathrm{kS\,s^{-1}}$ per channel, the issue was gone, meaning 20 $\mathrm{kS\,s^{-1}}$ per channel is a conservative choice.

Representative Voltage Measurements

Figure 3.23 shows the raw voltage values measured across the temperature sensors during steps in open bath and closed channel configurations, and are from the same

---

[10] It is completely clear, when looking at the raw voltage data, when the heating pulse started, with accuracy matching the sampling frequency.

tests shown back in Figure 3.14. These plots, showing the Cernox® sensor voltage measurement, are not immediately useful for understanding the temperature development during the heating event; the calibration discussed in Section 4.1 on page 109 is needed for that. It is also not useful to compare the voltage drops seen on one sensor to that of another within the same plot. There are, however, a few notes worth making.

The resistivity of the zirconium oxynitride of a Cernox® sensor has a negative temperature dependency coefficient; as the sensor heats up, the resistivity drops. So, a colder sensor gives a higher voltage reading (for the same excitation current). All the sensors shown in Figure 3.23 show starting voltages on the order of 0.1 V, meaning that, with the excitation current being 10 µA, their resistances are on the order of 10 kΩ.

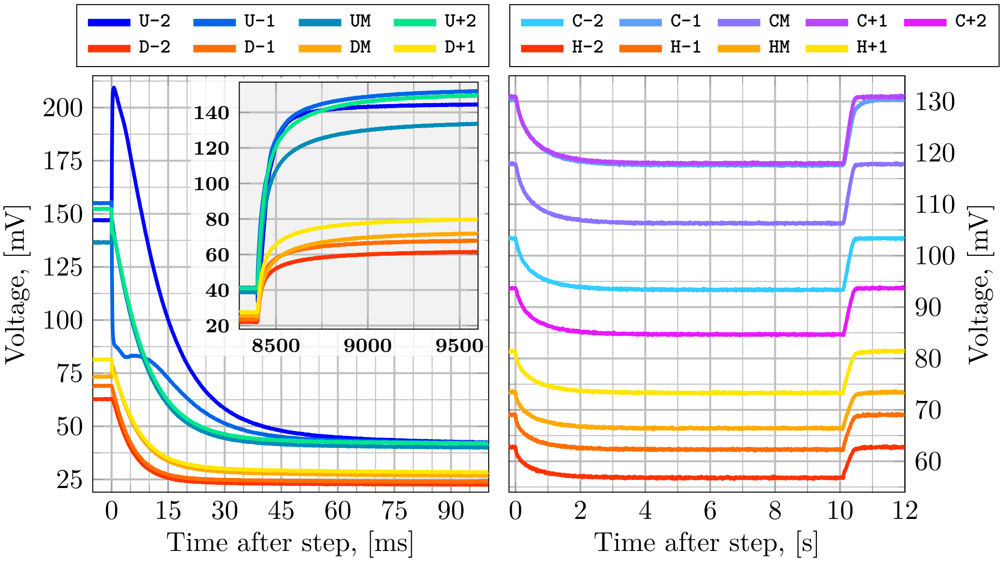

(a) Step–heating in open bath. **(b)** Step–heating in closed channel.

Figure 3.23: Representative temperature sensor voltage measurements from a step in heating applied to the open bath configuration (a), and a step in heating applied to the closed channel configuration (b). The insert in Figure 3.23a shows the relaxation back to the bath temperature after turning off the applied heating.

An important observation, and part of what lead to using Bottom Plate 2 (with Heater Strip 2) for the closed channel measurements, is the large voltage jump seen in `U-2` and `U-1` in the open bath step (Figure 3.23a) just as the heating is turned on. There is also a small jump as heating is turned off, visible for `U-2` in the insert. The jump itself does not have any direct impact on the measurement results (see Section 4.4.2 on page 132), but choosing Bottom Plate 2 leads to a lower likelihood of such a jump ever being large enough to go beyond the channel measurement range of the PCI–6052e card (a smaller range means better voltage resolution, which is clearly desirable).

Although the plots cannot be interpreted directly in terms of temperature, it is worth noting that for the closed channel step, the time constant to reach a steady state temperature is much longer than in the open bath. An important difference is that in the closed channel, the applied heating power density is much smaller than what is necessary to give a similar temperature rise in the open bath. Furthermore, in the closed channel, heat flowing out of the channel helium along various parasitic cooling paths play an important role in determining the overall time constant.

Figure 3.24 shows the raw voltage values measured across the temperature sensors during fast and slow pulses in the closed channel configuration, and are from the same tests shown back in Figure 3.15.

Like in the step–heating plot (figure 3.23a), the fast–pulse plots has clearly visible voltage jumps right as the pulse is discharged. They are much smaller, though, than in the open bath step, of course, since Bottom Plate 2 is used in the closed channel measurements. For the fast–pulse plot, only the heater strip sensors show this jump, while the helium channel sensors are unaffected.

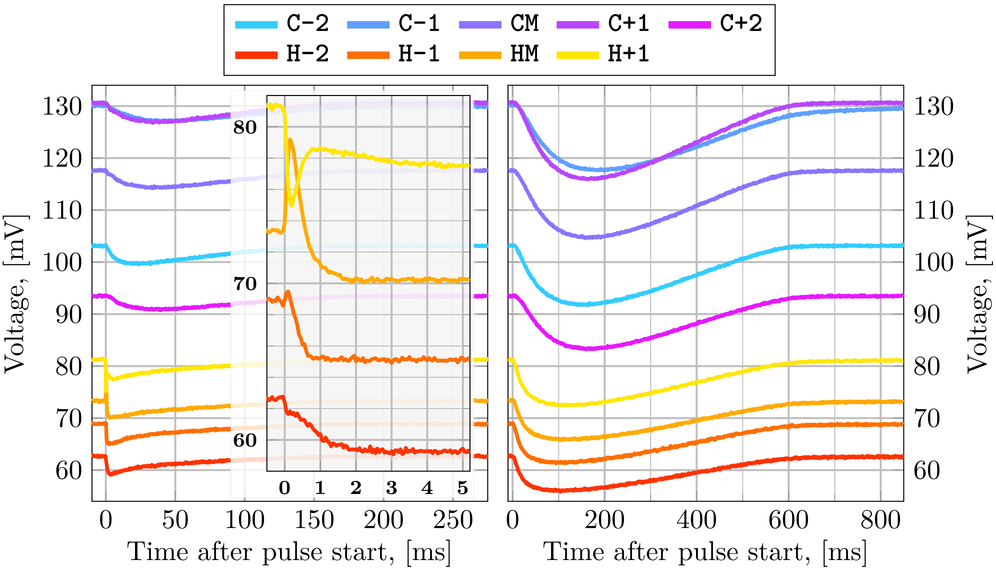

(a) Fast pulse in closed channel. **(b)** Slow pulse in closed channel.

Figure 3.24: Representative temperature sensor voltage measurements from a fast heating pulse applied to the closed channel configuration (a), and a slow heating pulse applied to the closed channel configuration (b). The insert in Figure 3.24a highlights the first 5 ms after the start of the pulse.

The apparent ordering and clustering of sensor voltage values in these four figures stems from choices made during mounting of sensors into top and bottom plates. The sensors with the highest resistances (~4.3 kΩ at 4.2 K) were placed in Bottom Plate 1. The channel helium sensors are those with medium–resistance (~3.7 kΩ at 4.2 K) values. Bottom Plate 2 was originally prepared as a replacement for Bottom Plate 1, in case Bottom Plate 1 broke, and the lowest–resistance sensors (~2.5 kΩ at 4.2 K) were mounted there. Grading the sensors like this stems from the slight increase in temperature sensitivity for a sensor with higher resistance. In practice, the difference between sensors is negligible, and this choice was mostly made as a means of organising sensors during assembly.

Measurement uncertainty is most interesting when seen in terms of actual temperatures, so that discussion is held till Section 4.2 on page 112, after the calibration method is explained. In terms of the raw voltage uncertainty, all sensors, during all measurements, show noise levels on the order of ±0.15 mV, which for the lowest–resistance sensor (`D-2`/`H-2`), translates to about ±0.7% of the voltage value during the steady state in Figure 3.23a.

3.3.3 Data Acquisition: Reference Temperature Probe

A key component of the measurement setup is the temperature reference probe which sits openly in the bath near the experimental sample(s). The photograph in, for instance, Figure 3.8 on page 66, shows the reference probe as Label (6) placed between Bottom Plate 1 and 2, at the bottom of the cryostat insert.

The probe is a Lake Shore CX–1050–SD–1.4L Cernox® sensor. The sensor comes calibrated from the manufacturer; the calibration runs from 1.4 K to 325 K. This is the only manufacturer calibrated temperature probe used in the setup, and the sensor is therefore referred to as the *reference probe* throughout.

Rather than the bare chip used for the temperature measurements in the sample(s), the reference probe is a much more rugged SD type. Its dimensions are shown in Figure 3.25. It does not need to be mounted in any particular way; helium is touching it around its entire perimeter, and along the lead wires, and the sensor will therefore be in excellent thermal contact with the bath helium. The SD packaging means the sensing element is in a vacuum, housed by a rugged alumina body, mounted on top of the same sort of sapphire substrate as the bare chip sensors.

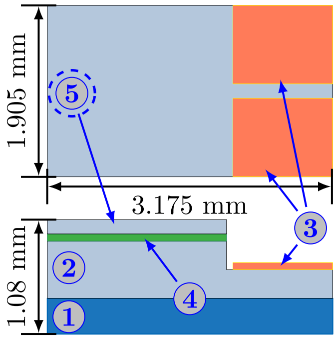

Figure 3.25: Drawing of Cernox® SD packaged sensor [150, Recreation of CX–SD figure]. All dimensions have a tolerance of ±0.127 mm. Lower region views the sensor from the side, and upper region from above.
(1): sapphire substrate.
(2): alumina sensor body, within which sits the zirconium oxynitride sensing element on the sapphire substrate in the same way as for the bare chip sensors.
(3): sensor lead soldering pads.
(4): gold–tin solder used for vacuum sealing the sensor body.
(5): sensor body lid.

Gold plated copper leads come attached to the sensor from the manufacturer, and the leads are connected to a Lake Shore 336 Temperature Controller with the same sort of four–lead measurement as was used for the bare chip Cernox® sensors. The temperature controller handles both the current excitation and the voltage measurement of the reference probe. The manufacturer calibration is provided as a data table relating measured resistance to sensor temperature, and this table is loaded into the temperature controller so the bath temperature is immediately available for temperature regulation. The controller itself is connected to the same LabView interface that is used to read and save the temperature data from the Cernox® sensors in the experimental samples. Over this connection, the reference temperature data (in kelvin) is read and saved, and regulation parameters are written to the temperature proportional-integral-derivative (PID) controller.

The controller acts on the resistive heater indicated by Label (1) back in Figure 3.9 on page 67. The reference temperature probe measurement is used for comparison against the set temperature of the PID controller. The values for the control loop are found by trial and error; open bath measurements (where large step heating is applied for several seconds at a time) need larger/more aggressive settings to react faster to the thermal load, and closed channel measurements (where short pulses and weaker steps are applied) use lower/less aggressive settings.

Figure 3.26 shows representative reference temperature measurements during the same step–tests shown back in Figure 3.23, together with the heater voltage signals. The total energy input to the bath is low enough that equivalent plots for fast– and slow–pulse tests show no information different from that seen in Figure 3.26b. The reference probe temperature data is represented by the rise above the average temperature of the bath in the seconds leading up to power–on.

The heater voltages shown are filtered versions of those in Figure 3.14 on page 72. Around the power–on/power–off points, the filtering is a moving average with a narrow window size, while the long steady region in between is a Butterworth low–pass filter with a low cutoff frequency[11]. Unless otherwise noted, this filtering approach is always used for the heater voltage.

Since any temperature change in the bath is very slow compared to the transient effects measured by the Cernox® sensors in the experimental samples, the data acquisition frequency from the reference probe can be quite low. The logging of data happens intermittently at intervals typically between 20 and 70 ms, though this is not fixed, and depends on the particular hardware state. This results in the jagged curves seen in the plots.

The closed channel curve (Figure 3.26b) shows that the translation from measured sensor voltage to calibrated temperature, done by a Lake Shore 336 Temperature Controller, has a lower accuracy limit of 0.1 mK associated with the digitisation of the voltage signal.

3.3.4 Data Acquisition: Pressure Probes

To measure the pressure during heating of the helium channel, two Kulite CCQ–062 pressure probes are mounted in the Top Plate. Figure 3.27 shows a photograph of the closed channel assembly, highlighting the pressure probes. The pressure probes themselves are not visible; the three parts that are seen are 1) the probe hole filled with Eccobond®, 2) the four probe wires used for excitation and measurement, and 3) the long thin pressure reference tubes, as the probes give differential pressure referred to the ambient. The pressure probes themselves are stainless steel cylinders, of diameter 1.7 mm and length 9.5 mm. The sensing element is at the bottom of the probe housing, behind a perforated screen. The screen sits flush with the top of the channel so it does not extend into the helium volume, nor create a hollow space for helium to fill. The

---

[11] Section 4.4.2 on page 125 discusses filtering of signals, including a simple overview of the Butterworth filter.

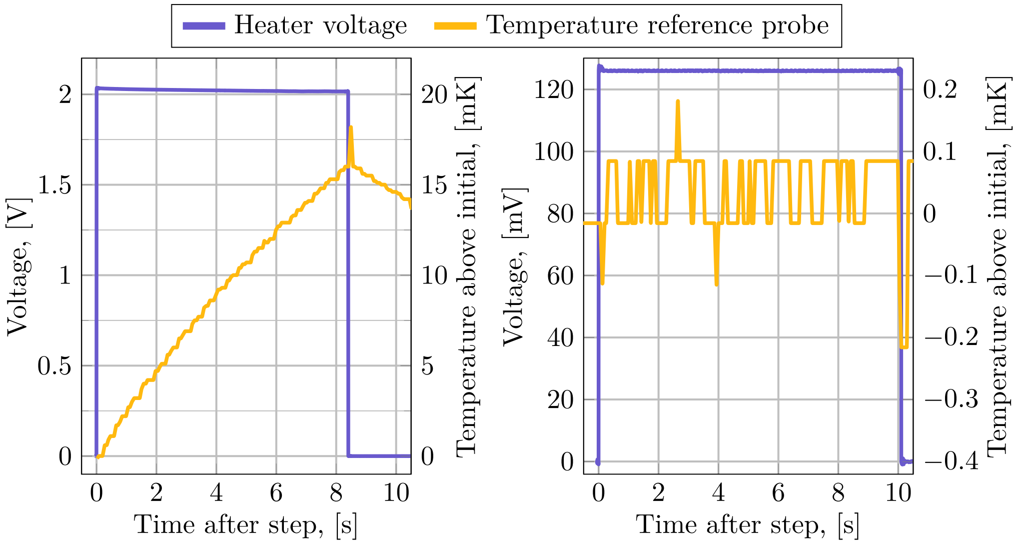

(a) Step–heating in open bath.

(b) Step–heating in closed channel.

Figure 3.26: Representative reference temperature measurements, together with the heater voltage measurement, from a step in heating applied to the open bath configuration (a), and a step in heating applied to the closed channel configuration (b). The initial temperature in the open bath plot is 1.8987 K, and for the closed channel plot it is 1.8991 K. For fast–pulse and slow–pulse heating, no appreciable bath temperature change is seen (like for closed channel steps), so the plots are not presented here. The plots show filtered heater voltage signals (and the open bath plot only shows that of one heater, not two).

probes are mounted with Eccobond®, and after the initial application cured, the back of the probe holes were filled with more Eccobond®.

Since the pressure probes are differential, the back of the probe is open to the bath outside through the reference tube (of diameter 410 µm). If the diaphragm used to measure the pressure were to burst due to an over–pressure in the channel, any subsequent measurements would now suffer from having an open thermal path going from the channel out to the bath through the helium filling the burst pressure probe. To guard against this, a conservative peak pressure rating is chosen. The ideal gas law states that pressure is proportional to temperature for a fixed density;

$$P = \rho \frac{R}{M_{\mathrm{He}}} T. \tag{3.5}$$

Assuming all the helium in the channel evaporates instantaneously and no helium escapes through the pin–holes, the density of the gas after evaporation is the same as the liquid before evaporation. So, $\rho \simeq 147$ kg m^{-3}, $M_{\mathrm{He}} \simeq 4$, and $R = 8.3145$ J K^{-1} mol^{-1}; $P = 305.6$ kPa K^{-1}T. If T is taken as 4.2 K, the boiling point at standard atmospheric pressure, $P = 1.29$ MPa. The differential pressure probes made

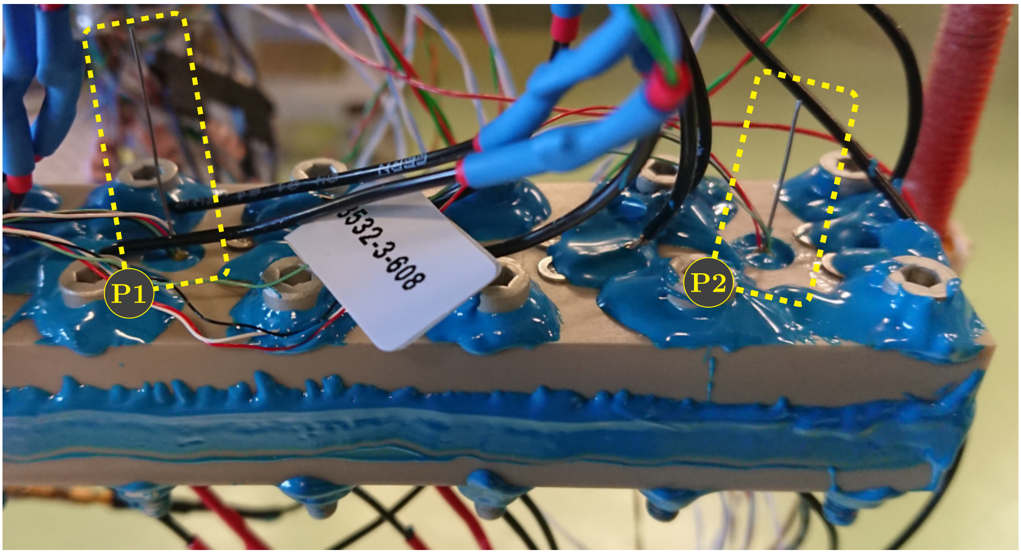

Figure 3.27: Photograph of Top Plate 1 and Bottom Plate 2 assembly, before insert is lowered into cryostat. Label (P1): Pressure Probe 1 (P1), in the middle of the channel, next to temperature sensor `CM`. (P2): Pressure Probe 2 (P2), at the edge of the channel, next to temperature sensor `C+2`.

by Kulite come in a few different pressure ratings, and with the very conservative[12] ideal gas law estimate in mind, the two that are relevant are rated for 3.5 bar (with burst pressure 1.05 MPa), or 7 bar (with burst pressure 2.1 MPa). The 7 bar rated probes are chosen to be absolutely sure the probes do not accidentally burst under strong heating powers. This does sacrifice some sensitivity, since a higher burst pressure means a stiffer diaphragm, which means less strain induced voltage for a given pressure differential.

Pressure Probes in Use

Figure 3.28 shows a circuit diagram of a single pressure probe. The probes are configured as four–arm, fully active Wheatstone bridges. The sensing element (the Wheatstone bridge proper) is a silicon diaphragm where the resistors R_1 and R_3 are placed so they stretch when the pressure in front of the diaphragm increases, while R_2 and R_4 are compressed. The compensation resistor R_{comp} is used to reduce the temperature dependence of the probe output. This resistor is chosen by the manufacturer and is included directly on the sensor lead wires. According to the sensor data sheet, the compensation works down to 88.75 K [151], meaning that for experiments at superfluid–helium temperatures, the compensation is not complete.

The working principle of this kind of probe is that when the pressure on one side of

---

[12] As the helium heats up, and pressure starts to build, the pin–holes will, of course, help keep the pressure lower. Furthermore, the helium, during such a transient, will certainly not be in thermal equilibrium, so the ideal gas law does not really apply. The main goal of this choice is to guard against accidental bursting, however, so a simple and known–to–be conservative approach is used.

the diaphragm goes up, the diaphragm deforms, bulging away from the high pressure side. This bulge stretches and compresses the resistors mounted to it. The circuit is excited by a constant current (it can also be excited by a constant voltage), and as the various resistance values change with the strain of tension or compression, the voltage distribution in the circuit changes, leading to a non–zero measurement across points (B) to (D). The probe diaphragm is made so that the deformation–induced strain depends linearly on the pressure causing the deformation, V_{meas} is proportional to the pressure as well.

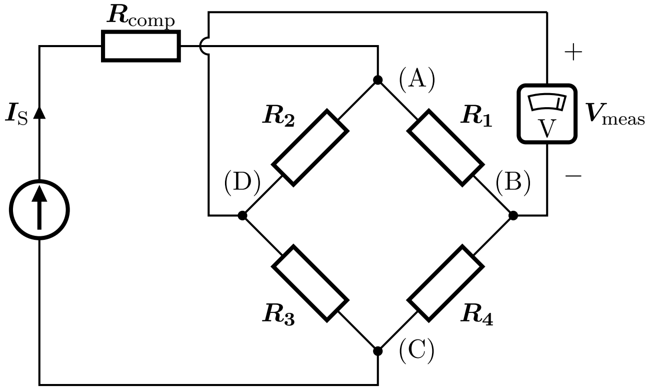

Figure 3.28: Circuit diagram of Wheatstone bridge. The resistors $R_{1,2,3,4}$ are active piezoresistive strain gauges or (ideally) equal resistance ($\simeq$ 1000 Ω). R_{comp} is a temperature compensation resistor ($\simeq$ 1000 Ω). I_{S} is the excitation current, and V_{meas} is the measured sensor output.

Self–heating of probes The real resistance values of the Wheatstone bridge are not specified by the manufacturer; however, after placing the assembled sample in the cryostat and cooling it down to 1.9 K, a Fluke 87 V multimeter is used to measure the input and output resistance of the two pressure probes used. The input resistance is that seen by the excitation current source, or the resistance between (A) and (C) plus the compensation resistor in Figure 3.28. The output resistance is that seen by the voltage measurement device, or the resistance between (B) and (D). All resistances R_1 to R_4 are made to be identical on a single probe, although small deviations are to be expected (not specified by the manufacturer). Table 3.1 lists the results of the multimeter measurement, together with the manufacturer–provided pressure sensitivity for a constant probe excitation of 10 V. A measurement made at 4.25 K yields the same resistance values.

Table 3.1: Measured resistance values of P1 and P2, and manufacturer provided pressure sensitivity under 10 V constant excitation.

	R_{input} [Ω]	R_{output} [Ω]	Sensitivity [mV bar^{-1}]
P1	1648	730	13.69
P2	1681	749	15.07

The output resistances of the two probes represent the part of each probe that is in contact with the channel helium. This means an equivalent resistor of 730 Ω for P1 and 749 Ω for P2. During testing of the system, an excitation current of 3 mA was necessary to see any signal from the probes at all. A Lake Shore Model 121 Programmable DC Current Source was used for excitation. The source (one for each sensor) is connected as shown in Figure 3.28. These sources have limited current set–values[13], and at the next lower setting, 1 mA, the excitation is too small to read the signal. For 3 mA excitation current, across an input resistance of 1650 Ω, the excitation voltage is around 5 V, which is half of what the rated excitation voltage is. This means translation from voltage measurement to pressure in Table 3.1 must be halved (one bar pressure differential across the diaphragm in the probe gives half the reading shown in the table). The voltage measurement leads of the two pressure probes are connected to two separate channels in the SCXI chassis used for the Cernox® sensors.

The self–heating of the pressure probes was found to be prohibitively large, however. 3 mA flowing in a resistance of about 750 Ω means a joule heating of 6.75 mW. For comparison, the self–heating of the Cernox® sensors, excited by 10 µA at around 10 kΩ is on the order of 1 µW. The Cernox® self–heating is negligible, even in the closed channel[14]. The self–heating of the pressure probes significantly alter the temperature of the channel helium, and since the pin–holes are so small, there is no practical way for the temperature regulation of the bulk bath outside the channel to compensate for the heating. Even at a pressure probe excitation of 1 mA, for which no useful voltage signal could be measured, the self–heating disturbs the channel temperature.

Signal amplifiers were tested to boost the probe output, but they did not help sufficiently to abate the self–heating problem. More testing and better understanding of signal conditioning of the pressure probes might have helped, but with the probe resistances and necessary excitation current it seems the application in such a small channel of helium is outside the range of what these sensors are meant for. As such, no significant effort is put into making use of the pressure probe data after making a limited number of dedicated measurements using step heating power in the range between 1 and 10 $\mathrm{kW\,m^{-2}}$. Another reason for why pressure measurements were not prioritised over pure temperature measurements is that the risk of bursting probes at high heating powers meant the pressure related tests had to be done at the very end of the measurement campaign, at which point the schedule was a constraint for how much time could be spent on tweaking the setup. Finally, for the fast–pulse tests that are of most interest to the work presented in this thesis, the pressure probes never showed any signal at all, meaning no evaporation of helium actually happened during these tests. Paper [2], dealing with closed channel results, does not discuss results of the pressure measurements.

Representative Voltage Measurements

For completeness, Figure 3.29 shows the first 300 ms of the voltage readings of the two pressure probes during step heating up to an applied heating power density of about 2.5 $\mathrm{kW\,m^{-2}}$, in the closed channel configuration. The pressure probe voltage rise starting around 50 ms coincides with when the channel helium heats above T_λ, while the pressure maximum at 100 ms coincides with the point in time where all Cernox® channel sensors reach 4.2 K, and hence the boiling point. The reason for the signals

---

[13] The current sources can be set to 13 fixed values: 100 nA, 300 nA, 1 µA, 3 µA, 10 µA, 30 µA, 100 µA, 300 µA, 1 mA, 3 mA, 10 mA, 30 mA, and 100 mA [152].

[14] Confirmed by simple testing of measuring the temperature in one set of temperature sensors while turning on the excitation current in another (no temperature change is seen).

being offset from zero is that, as mentioned, the thermal compensation resistor on the probe input does not completely balance the loss of resistivity in the Wheatstone bridge itself below about 88 K. The zero–offset would be trivial to compensate in analysis.

The peak voltage in the measurement is on the order of a single millivolt, with noise on the order of 10% of this. In absolute terms, the noise is about ±0.1 mV. This is slightly better than for the Cernox® sensors connected to the same PCI–6052e measurement device, that show voltage measurement noise on the order of ±0.15 mV.

The temperature disturbance when both pressure probes are excited is about 18 mK; the bath is at 1.929 K during the step, while the channel helium starts at 1.947 K before power is applied. This disturbance is seen as too large to use the pressure probes during regular measurements in the closed channel. As long as the pressure probes are on, the initial conditions in the channel are not those intended for study.

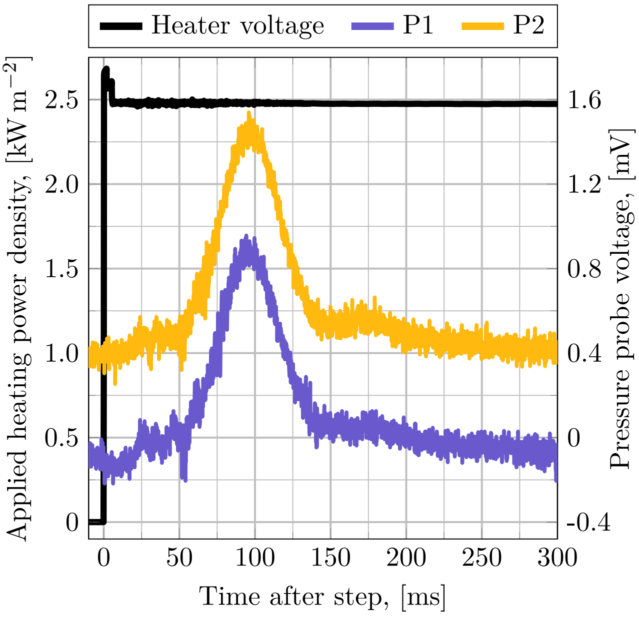

Figure 3.29: Representative pressure probe voltage data, from a step in applied heating power density to about 2.5 kW m^{-2}. The Aim–TTi current supply (otherwise only used for steady state open bath tests) is used here, which slight overshoots the target current during the initial part of the transient.

3.3.5 Data Acquisition: Capacitance Measurement

Figure 3.30 shows the temperature dependent relative permittivity of helium between 1.4 and 50 K. As the temperature of helium grows towards T_λ, its relative permittivity remains nearly constant at 1.058. Then it falls gradually towards 1.05 near boiling (at atmospheric pressure). After the phase change, the permittivity has fallen to 1.0065, and it approaches 1 as the temperature grows further towards room temperature.

With electrodes above and below some volume of helium, this ~4% drop in permittivity could be used to detect the phase transition by monitoring the capacitance between the two electrodes across the helium.

Back in Figure 3.3 on page 61, a cutout in the top plate of the assembly is shown, by Label (3). Into this cutout a copper piece is placed, with a lead soldered onto it

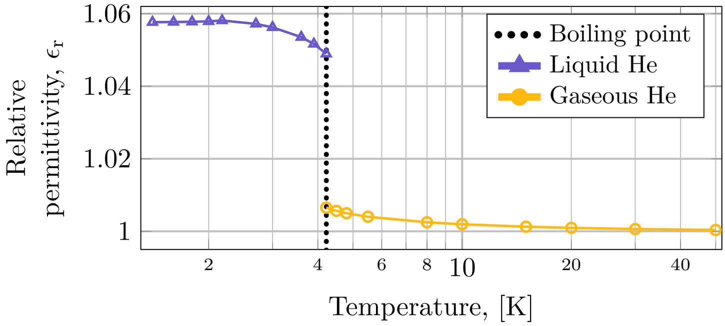

Figure 3.30: Temperature dependent relative permittivity of helium [153, p. 35].

that extends through a hole to outside the assembly, for connection to a separate DAQ system.

The copper piece is 2.9 mm wide and 20 mm long, and by using the heater strip as the other electrode, the capacitance across the channel helium can be monitored. Estimating the capacitance between the copper piece and the heater strip is done by assuming it follows the simple parallel–plate capacitor relationship. This neglects the additional capacitance from the electrical field that extends somewhat beyond the edges of the copper piece. With the channel depth of 120 µm and the relative permittivity at 1.9 K from Figure 3.30, the capacitance is,

$$C = \epsilon_0 \epsilon_\mathrm{r} \frac{A}{d} = 8.854 \cdot 10^{-12} \left[\mathrm{F\,m^{-1}}\right] \cdot 1.05783 \, \frac{2.9\,[\mathrm{mm}] \;\; 20\,[\mathrm{mm}]}{120\,[\mathrm{\mu m}]} = 4.527\,[\mathrm{pF}]\,. \quad (3.6)$$

After all the helium between the copper piece and the heater strip has evaporated, reducing the relative permittivity to around 1.00654 (using the value of gaseous helium at the boiling point, assuming no increase in pressure), the capacitance will have dropped to $C = 4.307$ pF.

Since the intention is to detect the phase change, the absolute capacitance is not important, only the change in capacitance is. What the estimate shows is that the expected change is on the order of 0.25 pF. The setup used to measure this is shown in the circuit diagram in Figure 3.31.

To carry out the measurement, a National Instruments PXI–6251 Multifunction I/O module is used as a signal generator, and a PXI–6133 is used for measuring the source and capacitor voltages. Both cards are placed in a PXI–1031 chassis, with a PXI–8108 controller running LabView.

For the measurement, the impedance of the shunt resistor should be close to the (frequency dependent) impedance of the capacitance. This is in order to have voltage measurements with similar amplitudes, as this reduces measurement noise after the real–time analysis step which relies on measuring the phase angle between the two voltages.

The voltage measurements will give the RMS value of the generator voltage, V_G, the RMS value of the voltage across the capacitor, V_C, and the phase angle α between the two. At this point, it is clear that in order to calculate the capacitance value at least one full cycle of the generated input voltage must be measured so that the phase

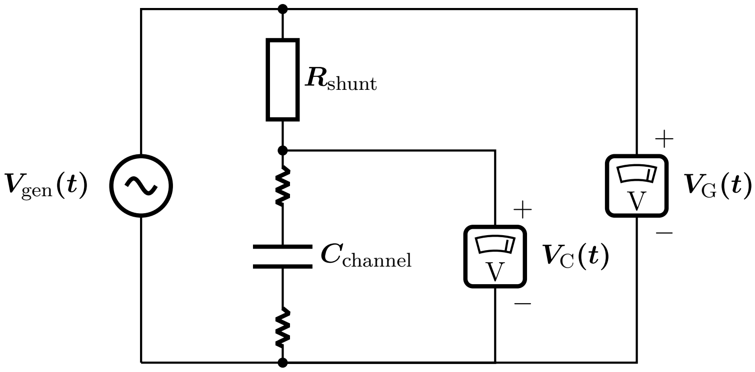

Figure 3.31: Diagram of the circuit used to measure the capacitance between the copper piece and the heater strip in the closed channel assembly. $V_{\mathrm{gen}}(t)$ is the applied AC signal. R_{shunt} is a shunt resistance used to measure the circuit current. C_{channel} is the capacitance between the copper piece and the heater strip. $\Delta C_{\mathrm{channel}}$ is found from the change in phase angle between the signal generator voltage $V_{\mathrm{G}}(t)$ and the capacitance voltage $V_{\mathrm{C}}(t)$. The shunt resistance is outside the cryostat, and the jagged elements before and after the capacitor represent the long lead wires that go down to the measurement sample.

angle can be determined with any accuracy. Using a larger number of cycles, the phase angle can be determined more accurately by averaging measurements.

With α and the two RMS values, the RMS value of the voltage across the shunt resistor, V_{R}, is found by the cosine rule: $V_{\mathrm{R}} = \left[V_{\mathrm{G}}^2 + V_{\mathrm{C}}^2 - 2V_{\mathrm{G}}V_{\mathrm{C}}\cos\alpha\right]^{1/2}$.

From this, the generator RMS current is found: $I_{\mathrm{G}} = V_{\mathrm{R}}/R_{\mathrm{shunt}}$. The shunt voltage also gives the phase angle ϕ between the generator current and the capacitor current: $\phi = \arccos\left(V_{\mathrm{G}}\sin\alpha/V_{\mathrm{R}}\right)$.

The impedance Z_{C} of the capacitor is: $Z_{\mathrm{C}} = V_{\mathrm{C}}/(I_{\mathrm{G}}\cos\phi)$. Assuming the series resistance of the capacitor is zero, the reactance, X_{C}, equals the impedance, so the capacitance value, C_{total} is: $C_{\mathrm{total}} = (2\pi f_{\mathrm{gen}} Z_{\mathrm{C}})^{-1}$.

This total capacitance includes both the interesting channel capacitance, and stray capacitances associated with the lead wires and sensing equipment. Since the change in capacitance is the only important measurement for the sake of detecting evaporation of helium, no compensation is needed at this point, based on the assumption that stray capacitances remain constant throughout the measurement.

Once measurements were done, even though the method had proven successful on larger scale systems [154, 155], the data gathered from these measurements was too noisy to be of use. The typical capacitance value measured was about 210 pF, while the expected observed capacitance change would be on the order of 0.1% of this value. Given that these measurements involve sufficiently strong heating to cause helium to evaporate, they were postponed to the end of the measurement campaign, like the pressure measurements were. The schedule did not leave sufficient room to tune the measurement setup. The measured capacitance suggests there is a large stray capacitance in the circuit that would need to be tracked down and either compensated or removed. Furthermore, the choice of shunt resistance and generator frequency have an impact on the result. Larger electrodes would have helped too, as this increases the capacitance associated with the helium permittivity. No further effort was devoted to these measurements, and Paper [2] does not include them.

3.4 Material Properties

Figure 3.32 schematically shows the region around the Cernox® sensors after mounting, indicating the various materials of relevance. For analysis of data, the thermal conductivities and heat capacities of copper, sapphire, GE 7031 varnish, silver filled epoxy, Eccobond®, glass–fibre filled PEEK, and stainless steel are needed, as these make up the thermal path between the heater strip surface and the back of the assembly. Section 5.1 on page 141 discusses the modelling of this thermal path. In addition, parameters for aluminium are needed due to the aluminium bolts used for the top and bottom plate assembly, relevant for an attempted modelling extension discussed in Appendix B.

Note that the region labelled (A), the soldering joint between thin sensor leads and thick sensor lead attachments (see Figure 3.4 on page 62), represents the thermal anchor which is considered to be at the bath temperature at all times during measurements below T_λ. This is a reasonable assumption since the thick sensor lead attachments, surrounded by He II, have a much larger cross section than the thin sensor leads, meaning whatever small amount of heat is propagated towards the anchors along the sensor leads quickly dissipates into the bath.

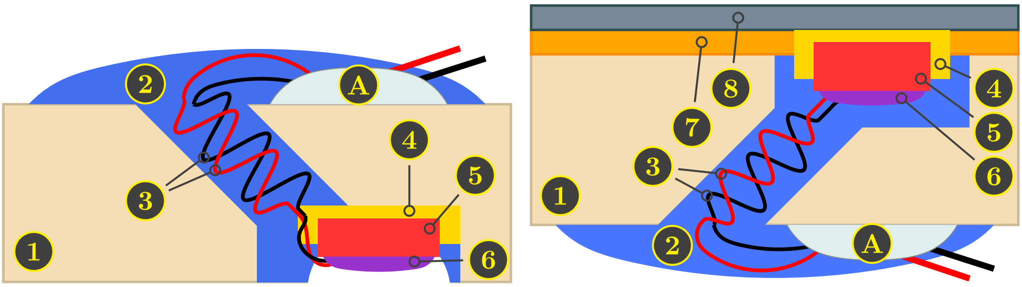

(a) Top plate. **(b)** Bottom plate.

Figure 3.32: Schematic representation of the region around the Cernox® temperature sensors as they are mounted in Top Plate 1 and Bottom Plate 1 and Bottom Plate 2. The figures are not to scale. Labels refer to the same material in both figures. (1): Glass–fibre filled PEEK. (2) Eccobond®. (3): copper sensor lead wires. (4): GE 7031 varnish. (5): sapphire sensor substrate. (6): silver–filled epoxy. (7): kapton insulation tape. (8): stainless steel heater strip. (A): Soldering point where thin sensor leads meet larger sensor lead attachments (seen in Figure 3.4 on page 62).

Nomenclature

Herein, when talking of the orientation of PEEK plates and cooled surfaces, the following convention is used;

Bottom plates The bottom plates (distinguished by the direction the heater is facing) have their *top* coincident with the heater side and their *bottom*

	coincident with the bath side, regardless of plate orientation. So the top of the downwards facing PEEK plate is the side where the heater is, and the bottom is the other side, where the helium bath cools the sample from behind.
Heater	When referring to the *heater surface* it is always meant the helium wetted surface of the heater where direct heat transfer from heater to helium takes place.
Top Plate	Similarly to the bottom plates, when talking of the *top* of the single Top Plate in the setup, it is meant the side where the sensors measure the helium channel temperature. The bottom of the Top Plate is the side facing the helium bath.

3.4.1 Fitting Curves to Material Parameter Data

The cubic spline fitting routine mostly used herein is the Python function wrapper `scipy.interpolate.CubicSpline()`. It produces a smooth function that is twice differentiable at all provided data points. For some materials, the data points are spaced such that oscillatory behaviour across several data points is seen (Runge's phenomenon [156]). For these cases, `scipy.interpolate.PchipInterpolator()` is used instead. The resulting fit function is very similar to `CubicSpline()`, but it sacrifices 2nd order differentiability at data points in order to guarantee monotonicity of the fit function between data points. This means the `PchipInterpolator()` does not oscillate across the fitted temperature range (save for whatever oscillations may be present in the data itself). The text will not make reference to whether the `CubicSpline()` or the `PchipInterpolator()` is used.

Copper The heat capacity data is found from the fit on the National Institute of Standards and Technology (NIST) material properties website [157];

$$C = \exp\left(a + b\tau + c\tau^2 + d\tau^3 + e\tau^4 + f\tau^5 + g\tau^6 + h\tau^7\right) \left[\mathrm{J\,kg^{-1}\,K^{-1}}\right], \tag{3.7}$$

where $\exp(x) = 10^x$, and $\tau = \log_{10}(T)$, where T is the temperature. The fit coefficients are given in Table 3.2.

Note that on NIST's website, the equation range is 4–300 K. However, the background sources shows that the fit is reliable from 1 K, when comparing the NIST fit values to the source below 4 K [158, p. 4.112–1].

Table 3.2: Heat capacity fit coefficients for copper, used in Equation (3.7).

a	−1.918 44	b	−0.159 73
c	8.610 13	d	−1.8996
e	21.9661	f	−12.7328
g	3.543 22	h	−0.3797

The density of copper is 8940 $\mathrm{kg\,m^{-3}}$ [159].

NIST provides a thermal conductivity fit together with the heat capacity, with the same quoted range of validity (4–300 K). Unlike for the heat capacity fit, the thermal conductivity is overestimated below 4 K. Their source provides a fit that is valid across the relevant range (1.7 to 100 K) [160, Equation 7–2][15];

$$C = (W_\mathrm{o} + W_\mathrm{i} + W_\mathrm{io})^{-1}\left[\mathrm{W\,m^{-1}\,K^{-1}}\right], \tag{3.8}$$

where

$$\begin{aligned} W_\mathrm{o} &= \frac{\beta}{T} \\ W_\mathrm{i} &= \frac{P_1 T^{P_2}}{1 + P_1 P_2 T^{P_2+P_4} \exp\Big((-P_5/T)^{P_6}\Big) + W_\mathrm{o}} \\ W_\mathrm{io} &= \frac{P_7 W_\mathrm{i} W_\mathrm{o}}{W_\mathrm{i} + W_\mathrm{o}}, \end{aligned} \tag{3.9}$$

where T is the temperature, $\beta = 0.634$ / RRR (the residual resistivity ratio (RRR) is assumed to be 100 here), and the coefficients are given in Table 3.3.

Table 3.3: Thermal conductivity fit coefficients in Equation (3.9).

P_1	$1.754 \cdot 10^{-8}$	P_2	2.763
P_3	1102	P_4	-0.165
P_5	70	P_6	1.756
P_7	$0.2178\ \beta^{-0.1661}$		

Sapphire For the heat capacity of sapphire, Viswanathan's polynomial fit is used below 20.0661 K [161], and Fugate and Swenson's polynomial fit above 20.0661 K [162]. Note that both sources quote their results on a per–atom basis, and sapphire has five atoms per unit cell (Al_2O_3). So, the heat capacity C becomes;

$$C = \begin{cases} 5 \cdot \left(4.5 \cdot 10^{-2}\,T + 1.72 \cdot 10^{-3}\,T^3\right), & T < 20.0661\ \mathrm{K} \\ 5 \cdot \left(1.755 \cdot 10^{-3}\,T^3 + 1.907 \cdot 10^{-7}\,T^5\right), & T \geq 20.0661\ \mathrm{K} \end{cases} \tag{3.10}$$

Fugate and Swenson's fit is only validated to 25 K, but comparison with measurements by Ditmars *et al.* show good agreement also above 25 K [163], so Fugate and Swenson's fit is used for convenience.

Roditi International Corporation Ltd., a manufacturer of sapphire crystals and wafers, quotes the density of sapphire as 3980 $\mathrm{kg\,m^{-3}}$ [164].

Lake Shore Cryotronics, the manufacturer of the Cernox® temperature sensors used for experiments, provide their own thermal conductivity data for sapphire [165, Figure 1], which is in good agreement with a separate source by Berman *et al.* [166, highest curve in Fig. 1]. They do not provide a fit function, so a cubic spline fit to data read from the cited figure is used. Note, the readout of data is done by the use of a free online tool called WebPlotDigitizer [167]. This tool is always used when reading data from plots in sources that do not provide fit functions or raw data directly.

---

[15] There is a misprint in the expression for W_i; W_o should be included in the denominator.

GE 7031 varnish Heat capacity data for the GE 7031 varnish is taken from a measurement by Heessels [168]. No fit function is provided, so a cubic spline fit to the data is used.

The volume density of the varnish is 890 $\mathrm{kg\,m^{-3}}$, as per the product specification by the supplier [169].

For thermal conductivity, the measurements by McTaggart and Slack are used [170]. Also they do not provide fit functions, so cubic splines are fitted to the data.

Silver filled epoxy As per communication with Lake Shore Cryotronics customer service, the silver filled epoxy used to attach sensor leads to the pads on the Cernox® sensors is EPO–TEK H20E. There is only limited availability of material parameters for this proprietary compound, but within the most relevant temperature range, both heat capacity and thermal conductivity can be found.

Heat capacity data up to 9 K is taken from Weyhe *et al.* [171]. Above 9 K, no data is found, and the Weyhe *et al.* cannot be extrapolated; the slope is too steep to feasibly capture the true behaviour at higher temperature. The solution is to combine the dataset from Weyhe *et al.* with heat capacity data for Stycast 2850FT, measured by Swenson [172, FIG. 3]. Stycast 2850FT is an epoxy which, like EPO–TEK H20E, is loaded with high conductivity particulate matter. For the Stycast 2850FT, the loading is done with alumina or silicon carbide, not silver. The two materials are not analogous, but their high–temperature heat capacity will be similar enough that using Stycast 2850FT in place of the extrapolated EPO–TEK H20E data is preferable.

The two components of EPO–TEK H20E are mixed 1:1, so the total density is the average of the two: 2550 $\mathrm{kg\,m^{-3}}$ [173]. Stycast 2850FT is made by mixing the base with a small amount of catalyst. Swenson uses Catalyst 9. The mixing ratio by mass of Stycast 2850FT and Catalyst 9 is 100 : 3.5 [174]. The density of Stycast 2850FT is 2400 $\mathrm{kg\,m^{-3}}$, and that of Catalyst 9 is 1000 $\mathrm{kg\,m^{-3}}$. This gives a combined density of 2292 $\mathrm{kg\,m^{-3}}$.

The curve for the silver filled epoxy heat capacity is made by making a fifth degree polynomial fit to the logarithm of the Weyhe *et al.* data up to 8 K, and the Swenson data from 30 K and up.

Figure 3.33 shows the fit with the two data sources.

The thermal conductivity of EPO–TEK H20E is taken from a paper by Amils *et al.* [175]. Their data set is sparse, with only three data points covering the range between 3.2 and 300 K. The epoxy is not expected to show the typical low–temperature conductivity peak seen in pure metals, however. It is worth noting that Amils *et al.* find a room temperature conductivity that is only about 30% the value quoted by the manufacturer. The non–conductive epoxy control sample they use is much more in line with the manufacturer provided data, and since the control and the EPO–TEK H20E samples behave similarly, but with higher conductivity in the silver loaded H20E, it seems likely Amils *et al.* have accurate data for the low–temperature behaviour.

Eccobond® Neither heat capacity nor thermal conductivity data is available for Eccobond® 286 A/B. Since the compound is proprietary it is also not possible to make an educated guess based on known parameters for chemically similar products.

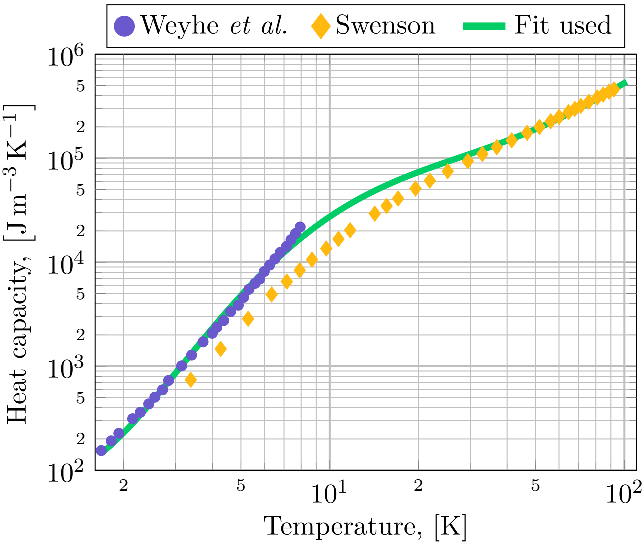

Figure 3.33: Heat capacity data by Weyhe *et al.* and Swenson, together with the fit used herein.

The heat capacity used for Eccobond® is that of Stycast 2850FT (the same as what is used for the high–temperature part of the silver filled epoxy/EPO–TEK H20E heat capacity). Eccobond® 286 A/B is marketed as a thermally conductive compound, just as Stycast 2850FT. Whether this marketing similarity speaks to similarities in chemical composition and material parameters is not known. When using the Stycast 2850FT heat capacity in place of Eccobond®, the full temperature range measured by Swenson is used [172, Figures 4 and 3]. The data from Swenson is used to create a cubic spline fit.

The thermal conductivity used for Eccobond® is that of Eccobond® 285, a single–component epoxy from the same manufacturer, for which a short measurement set exists between 4 and 8 K, by Rondeaux *et al.* [176]. This data indicates a linear temperature dependence of the thermal conductivity. A linear fit to the data suggests $k = aT + b$, where $a = 1.6527 \cdot 10^{-2}$ W m^{-1} K^{-2} and $b = -2.0088 \cdot 10^{-2}$ W m^{-1} K^{-1}. The generally expected result for polymers and other amorphous solids is $k(T) \propto T^2$ [177], although this dependence can be reduced significantly depending on composition and handling. The linear fit is used here, with extrapolation down to 1.7 K, and up to 100 K. It is worth noting that Eccobond® 285 is marketed as a filled epoxy with high thermal conductivity, and its conductivity is similar to that of Stycast 2850FT in Rondeaux *et al.* (Eccobond® 286 A/B is not filled, but otherwise is marketed with similar terms).

GF PEEK The heat capacity of glass–fibre filled PEEK at cryogenic temperatures is not readily available. As a proxy, the heat capacity of Polytetrafluoroethylene (PTFE) (Teflon®) given as a fit by NIST is used [178]. The lowest temperature for which heat capacity of PEEK is available is 175 K [179, Figure 4.2][16], where Theiler gives $C_\mathrm{p}(175\,\mathrm{K}) = 0.58\ \mathrm{J\,g^{-1}\,K^{-1}}$. The NIST fit at this temperature gives a heat capacity of 0.65 $\mathrm{J\,g^{-1}\,K^{-1}}$. PEEK mainly acts as an insulator between the helium bath and the Cernox® sensors, so taking the heat capacity of PTFE as that of PEEK gives a conservative (lower) thermal diffusivity[17].

The heat capacity fit for PTFE by NIST is given by;

$$C = \exp\big(a + b\tau + c\tau^2 + d\tau^3 + e\tau^4 + f\tau^5 + g\tau^6 + h\tau^7 + i\tau^8\big)\ \big[\mathrm{J\,kg^{-1}\,K^{-1}}\big]\,, \tag{3.11}$$

where $\exp(x) = 10^x$, and $\tau = \log_{10}(T)$, where T is the temperature. The fit coefficients are given in Table 3.4.

Table 3.4: Heat capacity fit coefficients for copper, used in Equation (3.11).

a	31.882 65	b	−166.519 49
c	352.018 79	d	−393.442 32
e	259.980 72	f	−104.614 29
g	24.997 26	h	−3.207 92
i	0.165 04		

Note that the applicable range of this fit is given from 4 to 300 K, and below 4 K, the resulting value from Equation (3.11) diverges. In fact, looking at the resulting curve, the slope changes sign between 4 and 5 K indicating that the fit should not be applied below 5 K. To get heat capacity all the way down to the relevant 1.9 K range, the measurements by Boyer *et al.* are used [180]. They measure the heat capacity of PTFE at several pressures between 0.3 and 20 K. The values used are those at $P = 0$ kbar. A cubic spline fit to the data by Boyer *et al.* is nearly parallel with the NIST fit at $T = 17.1982$ K. The NIST fit is lower than the Boyer *et al.* data below this temperature. In line with the conservative choice of taking the heat capacity of PTFE as the proxy for PEEK, the higher Boyer *et al.* data is used below 17.1982 K.

The density of PTFE is 2200 $\mathrm{kg\,m^{-3}}$[181].

Values for the thermal conductivity of PEEK is much more available in literature. A challenge here is that the composite PEEK is anisotropic; thermal conductivity parallel to the direction of extrusion (parallel to the fibres) is higher than thermal conductivity normal to this direction.

The orientation of the PEEK plates in the design described herein is such that the thermal contraction parallel to the heater strip is as low as possible, to prevent delamination of the heater strip from the bottom plates. The thermal path, however, is, generally, perpendicular to this, going from the heater strip region, up/down to the helium bath.

Runyan and Jones provide thermal conductivity measurements of glass–fibre filled PEEK between 0.3 and 4 K, parallel to the direction of the fibres [182]. Rule and

---

[16] Theiler's PEEK is a composite filled with 15% carbon fibre and 15% PTFE, whereas the PEEK used for the support plates in experiments herein is filled with 30% glass fibre.

[17] During transient measurements, the presence of copper leads dominate the heat leakage towards the back of the sample, so using the higher heat capacity is conservative in the sense that when estimating a thermal offset in Section 4.3 on page 117, a higher heat capacity is worse than a lower one.

Sparks provide extensive thermal conductivity measurements on both unfilled and alumina–filled PEEK in both parallel and normal directions [183, figs. 19 and 21].

Runyan and Jones give a fit to their data;

$$k(T) = \alpha T^{\beta+\gamma T^{n}}, \tag{3.12}$$

where $\alpha = 4.14\ \mathrm{mW\,m^{-1}\,K^{-1}}$, $\beta = 3.07$, $\gamma = \text{-}1.84$, and $n = 0.0553$.

Figure 3.34 shows the thermal conductivity of the alumina–filled PEEK by Rule and Sparks, parallel and normal to the direction of extrusion, and the fit by Runyan and Jones (the fit is extrapolated to 10 K). The largest impact on thermal conductivity from orientation is seen at high temperatures. It is also clear that the glass–fibre filled PEEK measured by Runyan and Jones has a higher thermal conductivity than the alumina–filled PEEK measured by Rule and Sparks (the alumina filling fraction is 43% by volume). In order to have a continuous thermal conductivity function from 1.7 K to 100 K, the `Alu, norm` curve is lifted by adding a flat positive number until it is parallel with the Runyan and Jones curve. The addition is $\Delta k = 0.011305\ \mathrm{W\,m^{-1}\,K^{-1}}$, and the two curves become parallel in the region between 6.25 K and 6.54 K. Below $T = 6.4729$ K, the fit by Runyan and Jones is used, while above this temperature, a cubic spline fit to the `Alu, norm` data by Rule and Sparks is used (Δk is added to the Rule and Sparks data before cubic spline fitting).

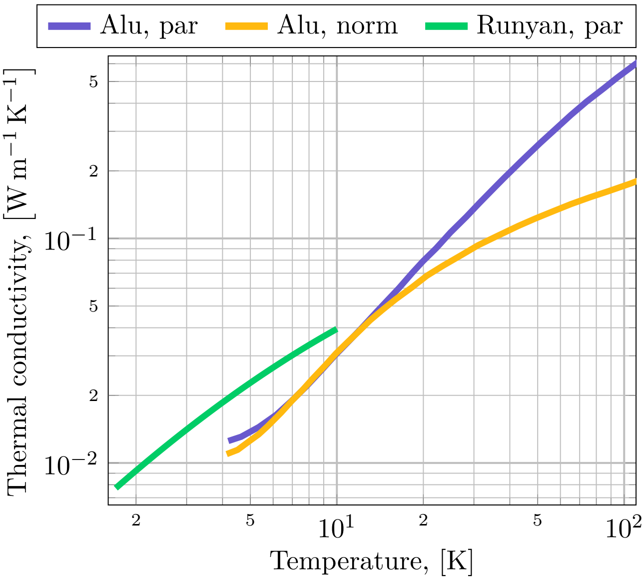

Figure 3.34: Thermal conductivity data by Rule and Sparks, and Runyan and Jones. `par` and `norm` refer to thermal conductivity parallel or normal to the direction of extrusion.

Aluminium The aluminium bolts used to clamp the assembly is the alloy 7075. For this alloy, only thermal conductivity data is found, while heat capacity data is not available.

The heat capacity used in place of the 7075 alloy is that of 6061, referenced by Duthil [184].

The density of 6061 aluminium is 2700 $\mathrm{kg\,m^{-3}}$ [185, p. 103].

Thermal conductivity data is taken from the CryoComp database [186].

Stainless steel The heat capacity of 304 stainless steel used for the heater strips is found in Du Chatenier *et al.* for temperatures below 90 K [187], and in NIST for temperatures above 90 K [188]. The logarithm of the data by Du Chatenier *et al.* is fitted with a fifth degree polynomial, while the NIST data uses the fit provided on their website. The fit is like that for copper, back in Equation (3.7), but with coefficients from Table 3.5.

Table 3.5: Heat capacity fit coefficients for steel, used in Equation (3.7) on page 96.

a	22.0061	b	−127.5528
c	303.647	d	−381.0098
e	274.0328	f	−112.9212
g	24.7593	h	−2.239 153

The density of 304 stainless steel is not well defined, being that the alloy is composed of considerable fractions of elements beyond iron. An industry interest group gives the density as 7955 ±105 $\mathrm{kg\,m^{-3}}$ [189]. Herein, 7955 $\mathrm{kg\,m^{-3}}$ is used.

The thermal conductivity of 304 stainless steel has proven to be more important than other material parameters due to the steady state surface temperature reconstruction method discussed in Section 4.4.1 on page 122. Finding thermal conductivity data in literature is made more difficult by the fact that the material composition of the 304 alloy has certain tolerances, and that it has changed over decades.

Between 1 Kand 1.7 K, Stutius and Dillinger made measurements on 304 stainless steel [190], where they make an estimate to differentiate the thermal conductivity contributions from the lattice and the electrons. Between 6 Kand 110 K, Hust and Sparks give Lorenz ratio measurements for a compositionally similar steel they call HS(347) [191, p. II-34].

Stutius and Dillinger gives an upper bound for the lattice contribution; $k_{\mathrm{lattice}} \simeq 1.231 \cdot 10^{-2}T + 4.379 \cdot 10^{-3}$. Using Hust and Sparks's Lorentz ratio measurements, together with the steel resistivity found from Heater Strip 1, at 43.6 $\mathrm{\mu\Omega\,cm^{-1}}$, the electron contribution is found[18]. The approach is to take the Lorentz ratio numbers by Hust and Sparks, and divide by the measured steel resistivity, and multiply by temperature. This is according to the Wiedemann–Franz law relating the electrical resistivity to thermal conductivity through the Lorentz ratio [33, p. 153].

The resulting thermal conductivity curve is compared to a dedicated measurement made at Commissariat a l'energie atomique (CEA) Saclay in August 2020 [192], the result of which is given in Table 3.6. The fit values based on lattice and electron contributions are about 6.5% higher than the measured values (taking the reference as the linear interpolation halfway between the two measurement points in Table 3.6). This indicates the lattice contribution in the 304 steel composition used by Stutius and Dillinger is a little too high. The thermal conductivity used for steel herein is the fit with a multiplicative factor 0.9383 to compensate for the difference between fit and measurement.

---

[18] Determining the resistivity is done with the 1 A measurement discussed in Section 3.3.1 on page 69; the resistane of Heater Strip 1 is 0.465(2) Ω. The total length of the heater strip is 160 mm, its width is 3 mm, and its thickness is 50 µm. So, $\rho = 4.36 \cdot 10^{-7}\ \Omega\,\mathrm{m}^{-1}$.

Table 3.6: Measured thermal conductivity of steel used for heater strips.

Temperature, [K]	Thermal conductivity, [$\mathrm{W\,m^{-1}\,K^{-1}}$]
4.4	0.423
4.7	0.454

Figures 3.35 and 3.36 show the material parameters of the eight materials discussed here.

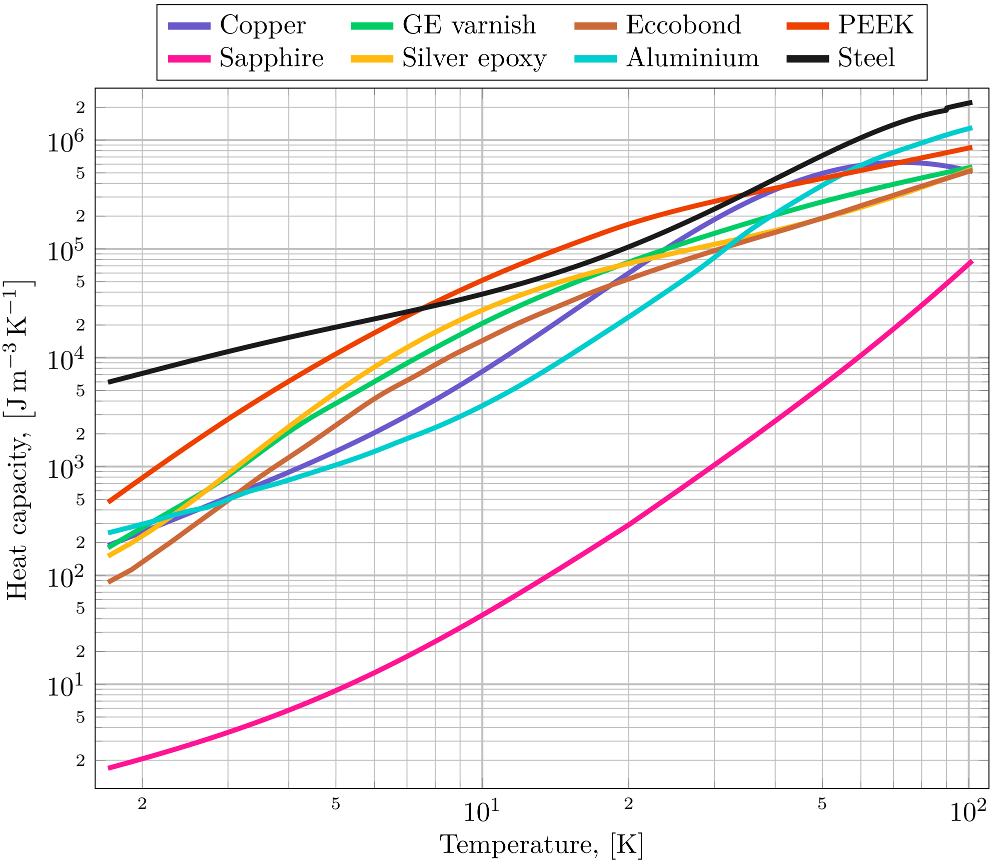

Figure 3.35: Heat capacity of materials relevant to measurements.

3.4.2 Parallel Thermal Paths

When analysing results, simulations of the region around sensors seen in Figure 3.32 on page 95 are necessary. Both steady state and transient simulations must be done. The numerical modelling approach is laid out in Chapter 5, and some simulation results are used in Chapter 4 in the discussion about calibration uncertainty and temperature offset.

The following describes the materials used in the three main kinds of simulations done as part of the analysis herein.

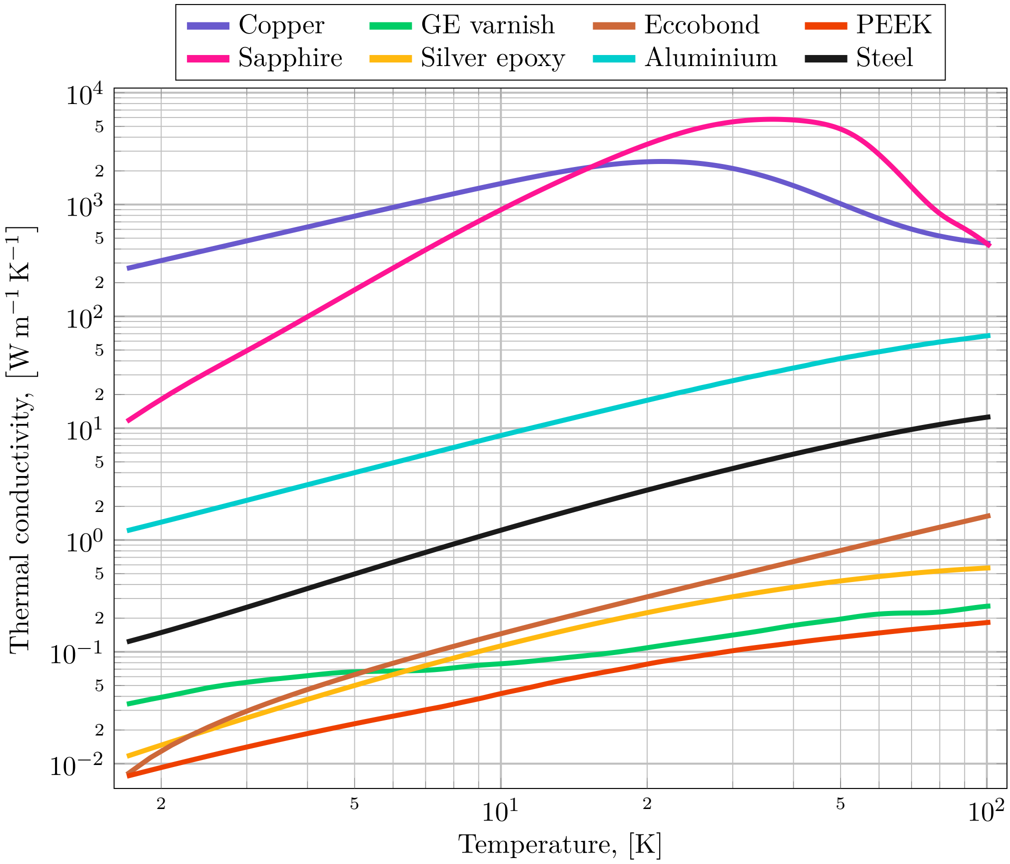

Figure 3.36: Thermal conductivity of materials relevant to measurements.

Steady state, to get heater surface temperature During steady state heating, a fixed current is flowing in the heater strip, and after some time, the temperatures in the system have reached a steady state. At this point, a large fraction of the applied heating power density flows across the interface between the helium cooled surface of the heater strip and the helium. A small fraction also flows backwards, along the sensor leads, to the bath on the insulated side of the experimental samples.

To get the right steady state temperature distribution it is sufficient to model only the thin copper sensor leads; despite the small cross section of copper between the sensor and the backside of the sample, which is effectively always fixed at the bath temperature during measurements, the effective thermal conductivity of the copper leads far surpass that of Eccobond® and/or PEEK. The sensor leads have a diameter of 2.5 mil = 63.5 µm, and there are two of them, giving a total cross sectional area of $6.334 \cdot 10^{-9}$ m^2. The modelling is done in 1D, with the cross sectional area of the Cernox® sensors (762 µm by 965 µm) as reference. For steady state modelling, then, where the heat capacity of materials does not matter, the copper leads are simulated as if they have a thermal conductivity of $6.334 \cdot 10^{-9}$ m^2 / (762 µm × 965 µm) = $8.614 \cdot 10^{-3}$ times the regular thermal conductivity of copper.

The sensor leads are about 25 mm long, attached by Lake Shore Cryotronics, and as seen back in Figure 3.4 on page 62, there is some spare length of lead between the lead hole and the anchoring point at the soldering joint with the lead extensions. The total length of copper between the sensor and the soldering joint is approximately 20 mm. This joint is the region labelled (A) back in Figure 3.32 on page 95.

Fast transient, for comparison with measurements During transient heating, such as the initial time after a step in power is applied, but before the steady state is established, heat capacity of materials plays an important role.

The effective thermal conductivity of the copper sensor leads, after applying the area factor $8.614 \cdot 10^{-3}$ reduction, is about two orders of magnitude above that of Eccobond® through which the sensor leads go. The picture, then, becomes the following: current is applied to the heater strip, and its temperature rises swiftly. This causes the sensor temperature to rise, and in turn, the copper leads heat up. This packet of heat starts moving down the copper leads, but immediately sees cooler Eccobond® surrounding it. The heat must diffuse into the Eccobond® too, not only along the copper leads. As the heat packet propagates along the copper, it keeps meeting cool Eccobond® around it, and heat keeps being siphoned off to warm the surrounding region.

The radius of the sensor lead hole is 1 mm, and aside from the thin copper leads, it is completely filled with Eccobond®. The approximate thermal diffusion time across L metres of a material is given as,

$$\tau = L^2 \frac{\rho C_\mathrm{P}}{k}, \tag{3.13}$$

and is shown in Figure 3.37 for Eccobond® and $L = 1$ mm. Around the initial temperature of the measurements done herein (1.9 to 2.15 K), it takes about 10 ms for heat to diffuse from the centre of the Eccobond® filled sensor lead hole to the edge, 1 mm away. As the temperature of the Eccobond® rises, the diffusion time increases, making the edge of the hole increasingly more insulated from the centre of the hole where the thin copper lead acts as the heat source.

So, for the fast transient measurements, in the numerical implementation, the combined effect of copper and Eccobond® must be used. The copper part uses the same area factor $8.614 \cdot 10^{-3}$, as for the steady state simulations, to adjust both thermal conductivity and heat capacity, while the Eccobond® part uses an area factor $(\pi(1 \cdot 10^{-3})^2 - A_\mathrm{Cu})/(762 \cdot 10^{-6} \times 965 \cdot 10^{-6}) = 4.268$ to adjust thermal conductivity and heat capacity;

$$\begin{aligned} k_\mathrm{combined}(T) &= 8.614 \cdot 10^{-3} \cdot k_\mathrm{Copper}(T) + 4.268 \cdot k_{\mathrm{Eccobond}^{®}}(T), \\ C_\mathrm{combined}(T) &= 8.614 \cdot 10^{-3} \cdot C_\mathrm{Copper}(T) + 4.268 \cdot C_{\mathrm{Eccobond}^{®}}(T), \end{aligned} \tag{3.14}$$

where C refers to the heat capacity at constant pressure of the material. The resulting mix essentially has the heat capacity of the entire hole of Eccobond®, and the thermal conductivity of the thin copper leads. Note that the length of this copper/Eccobond® mix is 20 mm, just like for the steady state simulations.

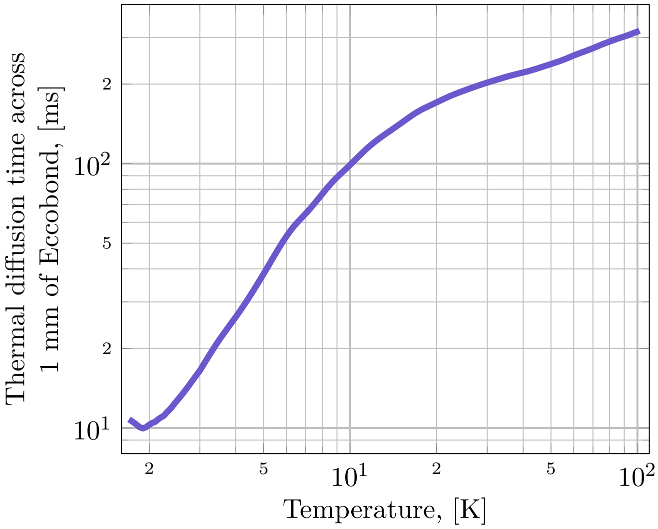

Figure 3.37: Thermal diffusion time across 1 mm of Eccobond®, according to Equation (3.13).

Slow transient, for assessing ΔT between sensors and bath During calibration measurements, discussed in–depth in Section 4.1, when the bath is not stationary, a thermal gradient will exist between the location of the Cernox® sensors and the outside edge of the experimental samples where the surface temperature is equal to the bath temperature. The time–rate of change during these measurements is on the order of millikelvin per minute, and cutting off the effective extent of the material mix at 1 mm in the Eccobond® filled sensor lead hole no longer makes sense; when the thermalisation can happen over several seconds to minutes, and the gradient is on the order of only a few millikelvin across the entire sample, the main sample material dominates the transient behaviour.

So, for simulations aiming to assess the difference between the bath temperature and the temperature at the Cernox® sensor locations, the material behind the sensors is taken as pure PEEK. The effective length of PEEK, when running one–dimensional simulations is the radius of a half–circle with the same area as a rectangle of 10 mm by 30 mm, the thickness and width of the PEEK plates. This gives the PEEK length 13.82 mm.

3.4.3 Implementation of Material Parameters in Simulation Code

For the actual simulations done when analysing results, the spline fits discussed in this section are not used directly. To save considerable run time, lookup tables are used instead. At initialisation of a given simulation, all relevant materials have their material properties calculated by the spline fits along an array of temperature values from 1.7 to 101.7 K split into 1 000 001 identical intervals (meaning one value for each 0.1 mK in the temperature range).

When calling for a particular material parameter value, the temperature at which the parameter is to be evaluated is converted to an equivalent index within the pre-defined temperature range, and the returned value is the material parameter value at that same index in the lookup table.

There is no discernible difference in simulation results when comparing the look–up table approach to calculating each value through the spline fits every time, but the computational time is cut by a factor 10 at the minor expense of using more computer memory at runtime.

CHAPTER 4

TEMPERATURE DATA ANALYSIS

Chapter content:

This chapter explains all the various steps taken when turning the temperature sensor voltage readings obtained from the experimental setup into actual temperatures in kelvin. There are also the two methods used to, 1) get access to the heater surface temperatures in steady state, and 2) get the millisecond transient temperature of the sensors.

The chapter has four main parts; Section 1 lays out the calibration procedure, followed by sections 2 and 3 related to estimates of the measurement uncertainty and the description of a temperature offset associated with an unavoidable consequence of enclosing the helium in a channel. Section 4 then describes how steady state and time–dependent data is extracted from the measurement data. Finally, Section 5 ties it all together, showing some representative measurement results based on the same examples used in Chapter 3. Comprehensive physical interpretation of results is relegated to papers [1] and [2].

4.1 Temperature Sensors and Calibration

As laid out in Section 3.3.2 on page 76, describing the DAQ system of the small bare chip Cernox® sensors embedded in the experimental samples, the measurement only gives the voltage across the sensor. This measurement must be calibrated against the reference probe described in Section 3.3.3 on page 86 in order to get an actual temperature. Recall, the reference probe comes with a calibration provided by Lake

Shore Cryotronics®[1]

To calibrate a sensor the cryostat is, ideally, allowed to reach a steady temperature, then the reference probe temperature and the voltage measured across the sensor are noted. The voltage translates to a measured sensor resistance through the (10 µA) applied excitation current. The measured resistance, for that sensor, will correspond to the reference probe temperature. Each sensor must be sampled at multiple temperatures to build a cubic spline fit for use as the actual calibration function. There will be one such function for each sensor used during a given experiment.

Note that the true excitation current in a sensor is not known, meaning the true resistance of the sensor is not known. Therefore, the calibration is actually of the combined system of sensor and excitation current supply. This makes the measurement setup less complex, since no checks of the current sources are needed, but it does mean that the calibration is slightly less stable, because it will be affected by drift in the current sources as well as the sensors themselves.

Figure 4.1 shows an example of the raw data used for a single calibration point in the open bath configuration. The reference probe temperature is shown in magenta in both subplots, and is read from the magenta y–axis Reference temperature, [K] floating to the left of the right–hand–side subplot. y–axis ΔT per time, [mK/min] reads the jagged black curve; each y–value is the change in reference probe temperature between the current time step and a point one minute further ahead. y–axis ΔR in permille per minute reads the coloured jagged curves, and is similar, but represents the change in sensor resistance in permille over the same one minute forwards in time. These two plots aid in finding regions in the data where the time–rates of change in temperature and sensor readings are as small as possible. The sensor resistances are found by dividing the measured sensor voltage by the 10 µA excitation current, and the reference point for the permille calculation is the resistance at the start of the one minute range of each point. Finally, the sensor voltages are read from y–axis Sensor voltages, [mV] .

The calibration point taken from this particular measurement is 3.3479 K, corresponding to the local minimum in the time–rate of change data around 500 seconds in. The time–rate of change here is about -1.4 $\mathrm{mK\,min^{-1}}$ and +0.6 permille resistance per minute.

The data shown in Figure 4.1 clearly does not represent a steady state. This reflects a general property of the cryostat itself. The main goal of the cryostat design is to provide a volume of superfluid helium that maintains a steady temperature over a long time with relatively low consumption of helium. The double bath design allows the combined use of two separate temperature control methods; pumping on the outer saturated bath ensures a rough temperature control, while the heating element within the inner bath gives fine–tuned control of the bath in which the experimental sample is submerged. This combined method only works when the inner bath is superfluid; below the superfluid transition temperature (around 2.166 K at atmospheric pressure), the thermal gradient within the bath is negligible due to the large effective thermal conductivity of superfluid helium. Above this, however, much poorer heat transfer

---

[1] The reference probe has the serial number `X125772`, and its calibration report can be retrieved from https://cal.lakeshore.com/ (at the expense of providing an email address for verification).

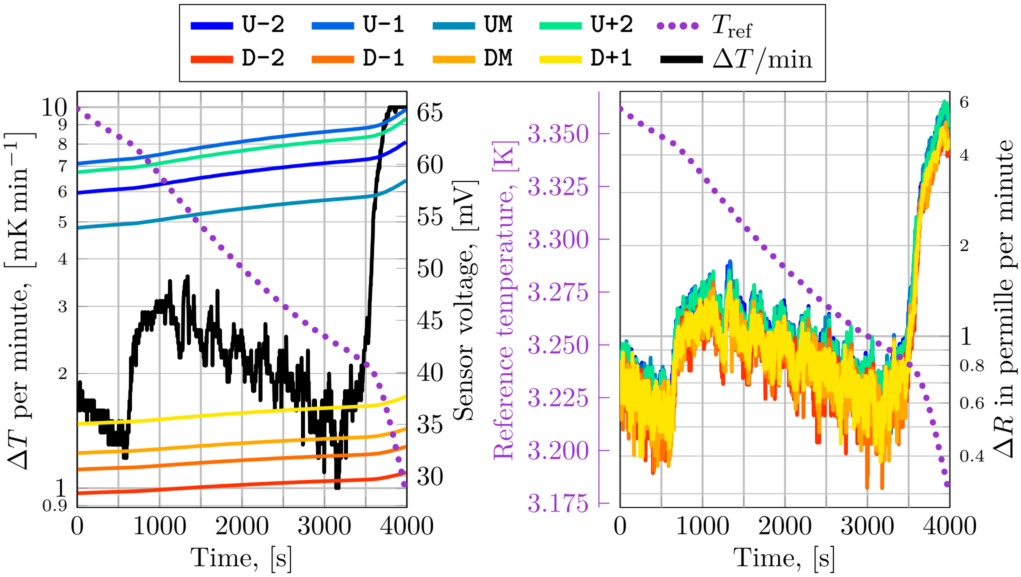

Figure 4.1: Measurement used to make an open bath configuration calibration point at 3.3479 K. The reference temperature data is read from the magenta y–axis Reference temperature, [K]. The temperature time–rate of change is read from y–axis ΔT per time, [mK/min]. The resistance time–rate of change is read from y–axis ΔR in permille per minute. The sensor voltages are read from y–axis Sensor voltages, [mV].

mechanisms in normal–fluid helium reign. For the situation where steady states are sought, and only low heat fluxes exist, natural convection between liquid helium and the experimental sample dominates. This gives a slower thermalisation time, and there can also be thermal gradients within the helium bath.

There are, then, three main temperature regimes at which calibration data is gathered;

1. Below T_λ, it is easy to achieve a steady state to get calibration points, as the temperature is controlled by both pressure and heater methods. In addition, at these low temperatures, the heat capacity of materials is low, so thermalisation is quicker than at higher temperatures.
2. Between T_λ and the boiling point of helium (at atmospheric pressure around 4.216 K), only the pressure method of temperature control is available since heat added by the small heating element in the inner bath no longer distributes itself evenly within the bath fast enough to be useful.

   The pressure control method could, in principle, control steady states all the way up to the critical point of helium ($T_c \simeq 5.195$ K, $P_c \simeq 2.27$ atm), as the cryostat is built for an over–pressure of 2 bar. In practice, since the pumping system works by vacuum pumping only, it is not possible to control for any pressure above ambient. Note also that the pressure controller's pressure reading has an upper range of 100 Torr $\simeq$ 0.13 atm, further frustrating reliable control of temperature above T_λ(even if the controller's range was extended, the pressure sensor itself is meant for the rough vacuum region, and would not give reliable measurements).

This means calibration points above T_λ all display this characteristic; they are not taken from true steady states. Calibration error is discussed in Section 4.2.

3. Above the boiling point of helium, the same concerns as for Point 2 are valid, but exacerbated by natural convection heat transfer being worse in gaseous helium than in liquid helium. Furthermore, the only times the cryostat sees temperatures above the boiling point is during cooldown from room temperature before experiments and warmup from cryogenic temperature after experiments. Warmup is a slower process than cooldown, because during cooldown, liquid helium from an external dewar is transferred into the cryostat (through the transfer pipe labelled (B) back in Figure 3.7 on page 65). During warmup heat seeps into the cryostat only through the insulation layers surrounding the helium vessels and some small amount of conduction along the walls of the cryostat and mechanical supports.

From several individual data files (of which the data shown in Figure 4.1 is an example), a collection of calibration points are taken, and a continuous cubic spline routine fits the data to create a convenient function representation of the calibration. Figure 4.2 shows the resulting splines, with the data points used to build the calibration. The figure also shows, in black with crosses, calibration data provided by Lake Shore Cryotronics® for the reference probe. This reference probe is calibrated against the International Temperature Scale of 1990 at the facilities of Lake Shore Cryotronics®.

Note that the sensors measuring the downwards facing heater in the open bath configuration (sensors labelled `D`) and the sensors measuring the heater in the closed channel configuration (sensors labelled `H`) are the same physical sensors, and share legend entries.

Cernox® sensors do not follow a standard behaviour, but they do tend towards a certain shape; the calibrated sensors show qualitatively the same behaviour as the reference probe, except for a large difference in actual resistance. The bare chips used in the experiment span resistance values from about 7.2 kΩ to 18.1 kΩ around 1.72 K. The Lake Shore Cryotronics® reference probe shows a resistance of about 25.1 kΩ at the same temperature.

During the open bath measurement campaign, one of the battery powered sensor excitation current sources needed to have its battery replaced. Since the calibration includes the current source, it had to be redone during the campaign, and all batteries were changed before resuming experiments. Only points below 4.2 K were redone (due to the cryostat limitation discussed above). The calibration shift was on the order of 5 mK, which is too small to be seen in the plot. In data analysis, however, the two calibrations are considered distinct. All batteries were changed prior to starting the closed channel measurement campaign.

4.2 Temperature Measurement Uncertainty

The total measurement uncertainty is broken into two main sources;

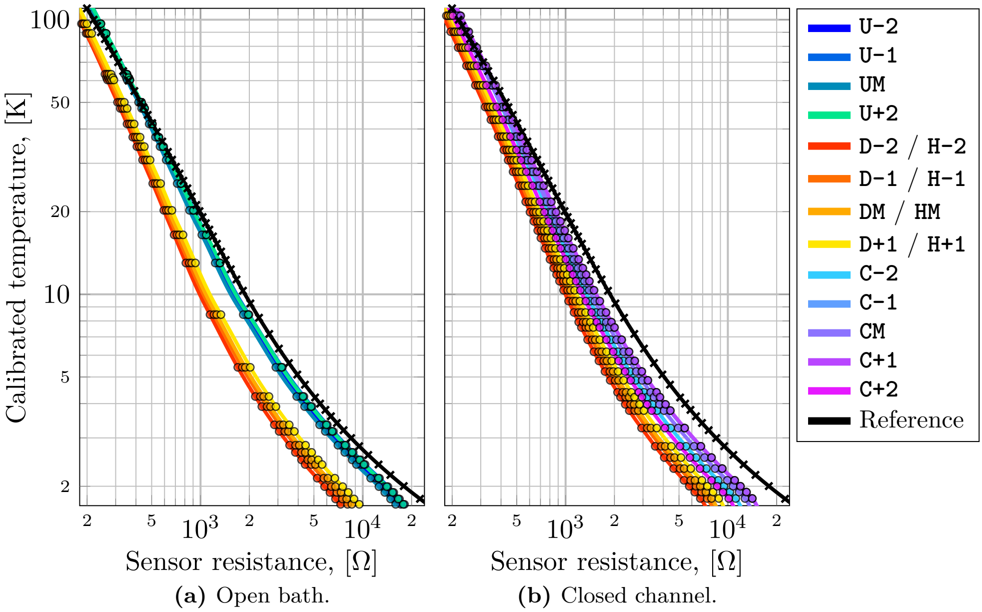

(a) Open bath. **(b)** Closed channel.

Figure 4.2: Calibrations for the open bath (a) and closed channel (b) configurations. Labels with `U` refer to sensors measuring: the upwards facing heater in the open bath configuration, `D`: the downwards facing heater in the open bath configuration, `H`: the heater in the closed channel configuration, and `C`: the helium channel in the closed channel configuration. The heater in the closed channel configuration is the same as the downwards facing heater in the open bath configuration. The circles indicate the actual data points while the curves are continuous cubic splines fitted to the data points. The black curve is the Lake Shore Cryotronics® reference probe data.

1. The non–uniformity of the helium bath means the Cernox® sensors may not be at the same temperature as the measured bath temperature at any given time.
2. The reference probe itself has some calibration uncertainty described by Lake Shore Cryotronics® in their calibration report.

4.2.1 Assessing the Impact of Transient Calibration Measurements

A Cernox® sensor will, over time, thermalise to some temperature T_S. In a true steady state, that temperature will be equal to the bath temperature measured with the reference probe. In a bath whose temperature changes in time, there will also be some degree of non–uniformity in the temperature distribution within the bath. The most obvious is the top–to–bottom gradient, but there will also be convective flows and, in the case of the cooldown and warmup situations before and after measurement campaigns, mass transfer in and out of the inner bath helium pot. Essentially, then, this error quantifies the uncertainty around what temperature the individual Cernox® sensors have approached during the averaging windows used to associate a voltage measurement to a temperature value.

Figure 4.3 shows the data from the example calibration file (Figure 4.1) after applying the calibration to get the sensor temperature readings during the measurement. The left side shows this calibrated data, while the right side shows the reference probe data subtracted from the sensor readings. Recall that the calibration data point taken from this file is at 3.3479 K, which is around 500 seconds into the measurement. In the ΔT plot, the deviation is nearest zero around this point (as is expected when the calibration is expressed with a cubic spline, since the calibration value is guaranteed to pass through the actual measurement point).

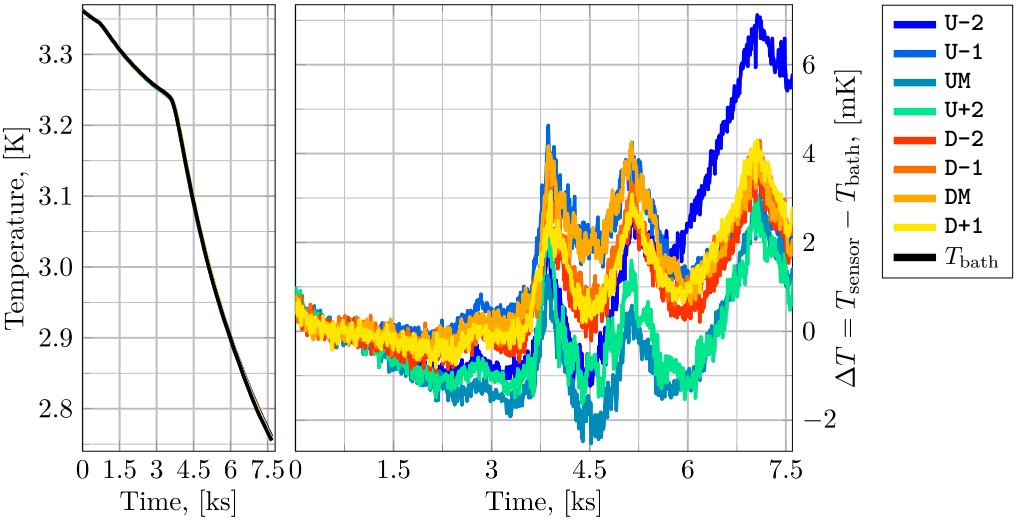

Figure 4.3: Calibrated sensor readings based on the data used to make an open bath configuration calibration point at 3.3479 K. The left side shows the reference probe and calibrated sensor data together, while the right side shows the difference between the calibrated sensor data and the reference probe.

To use this data as a means of estimating the contribution to calibration uncertainty from the transient nature of the calibration measurements, the temperature span from 1.8 K up to 100 K is divided into ranges, shown in Table 4.1.

Table 4.1: Temperature ranges for estimating contribution to calibration uncertainty from transient nature of calibration measurements. Note: Between 2.0 and 2.2 K there is one bin from 2.0 to 2.16 K and one from 2.16 to 2.2 K to isolate the lambda transition. There is also a bin from 4.6 to 5 K, and from 15 to 20 K.

T_{LOW}, [K]	Bin size, [K]	T_{HIGH}, [K]
1.8	0.1	2.0
2.2	0.2	4.6
5	0.5	15
20	5	100

For each range, all measurement files that have data within the range are considered. For ranges above about 4 K it is always only a single file (cooldown file for open bath and warmup file for closed channel), while below 4 K, some ranges have up to five separate contributing measurements. For each relevant slice of the measurement, $\Delta T(t) = T_{\text{sensor}}(t) - T_{\text{bath}}(t)$ is appended to a growing list of deviation data. Once all contributions are found, the RMS value of the entire contributing dataset is found. Using the RMS value gives more weight to larger deviations than what a flat average would do. There will be one such RMS value for each sensor. The final RMS value for the whole range is the RMS value across the sensors (eight in open bath and nine in closed channel). This is the estimated contribution to the total calibration uncertainty from the transient nature of the calibration measurements.

This approach is conservative, as the estimate includes measurement regions where the time–rate of change in the bath temperature was deemed too large to provide a good calibration point.

Figure 4.4 shows the error estimate across the ranges up to 25 K (the plot cuts off at 25 for clarity). The left side shows the error in millikelvin, while the right side expresses the error as a percentage of the temperature across the range. The plot clearly shows a larger error for open bath calibration(s) above 4 K than in the closed channel case. The error is as high as ±100 mK or ±2% around 6 K, while for the closed channel configuration the error in the same region is about one tenth of this. The reason for this is that in the open bath configuration, the cooldown data was used for calibration, while for the closed channel, the slower temperature time–rate of change warmup data was used[2].

Around the lambda temperature (2.168 K), there is always a large increase in uncertainty, and this is the reason for having the odd temperature binning in this region. For some unknown reason, the sensors simply prove less reliable right around the transition temperature. In the closed channel configuration, where the sensitive zirconium oxynitride part of the channel sensors are in direct contact with the helium, the error is worse than in the sensors embedded below the heater strip. This drives up the uncertainty in the closed channel curve. However, also the heater strip sensors display complicated behaviour right around the transition. The reference probe does not display this behaviour, so it is not because the zirconium oxynitride itself has some temperature dependent property around the lambda transition. The reference probe, as described in Section 3.3.3 on page 86, has the zirconium oxynitride in a vacuum, which could be the important difference[3]. Note that the error around the lambda transition is around ±5 mK in the open bath configuration.

---

[2] The original plan was to use the slower warmup data for calibration above 4.2 K also for the open bath configuration, but a computer error early in the measurement went unnoticed over the weekend, and data above 4.7 K was lost. Therefore, the cooldown data is used instead. This data has a steeper time–rate of temperature change because of the helium transfer from the external dewar. Furthermore, the bath sees a larger rate of internal mass flows of helium, since cool helium enters the inner bath from above, through the lambda valve (Label (7) in Figure 3.7 on page 65). For closed channel experiments, extra care was taken to ensure the higher–quality warmup data was gathered successfully.

[3] Lake Shore Cryotronics® explicitly states that when using bare chip sensors, the customer must assume the risk of sensor malfunction. On bare chips, the zirconium oxynitride is exposed completely, and Lake Shore Cryotronics® has not rigorously tested all possible permutations of mounting techniques and environments [193].

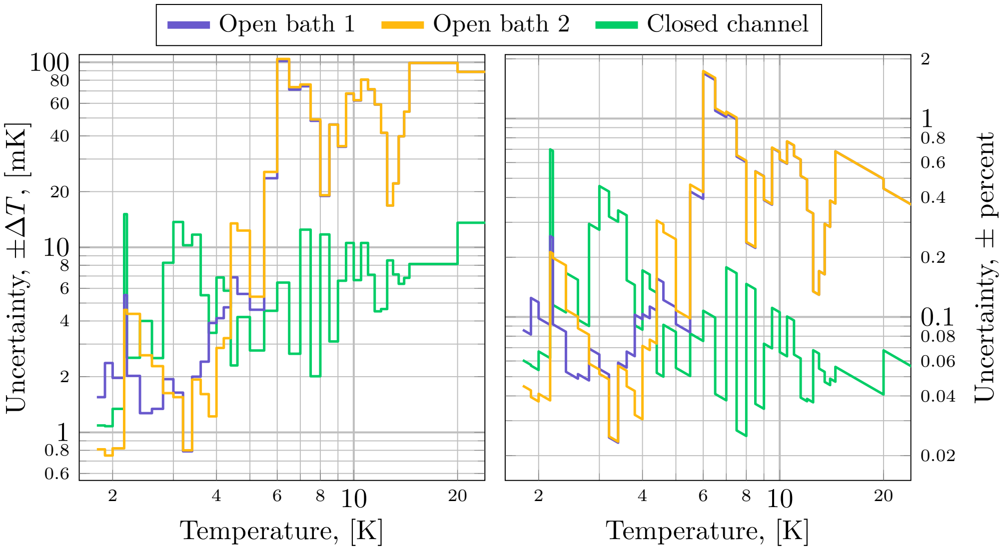

Figure 4.4: Estimated contribution to calibration uncertainty from the transient nature of the calibration measurements. The uncertainty is expressed within temperature ranges, based on the extended calibration measurements.

4.2.2 Calibration Uncertainty of the Reference Probe

Table 4.2 lists the calibration uncertainty of the reference probe, taken from the calibration report, made by Lake Shore Cryotronics®. This uncertainty is added on top of the two other sources of uncertainty already discussed.

Table 4.2: Calibration uncertainty given by Lake Shore Cryotronics® for the reference probe.

Temperature range, [K]	±mK	Temperature range, [K]	±mK
1.4 — 10	4	30 — 50	12
10 — 20	8	50 — 100	17
20 — 30	9	100 — 300	46

Due to the large heat capacity of helium associated with the normal–fluid/superfluid transition temperature, the time at which the transition happens can be recognised by a pronounced change in the time–rate of change of the bath temperature, so long as the change before and after the transition point are both relatively low. In a dedicated measurement, where only the vacuum regulation on the saturated bath was used (meaning no cryostat insert heating), the transition happened when the reference temperature probe read 2.166 K. Other measurements not meant to probe the transition directly, by having too large a time–rate of temperature change around the transition, see the transition around 2.163 K, 2.168 K, 2.165 K, 2.166 K, 2.163 K. With $T_\lambda = 2.165$ K, the Lake Shore Cryotronics® quoted uncertainty of ±4 mK is confirmed.

4.2.3 Total Measurement Uncertainty

The total calibration uncertainty is shown in Figure 4.5. The values for each calibration takes the plot from Figure 4.4 as a base, and then the Lake Shore Cryotronics® calibration uncertainty is added on top of that.

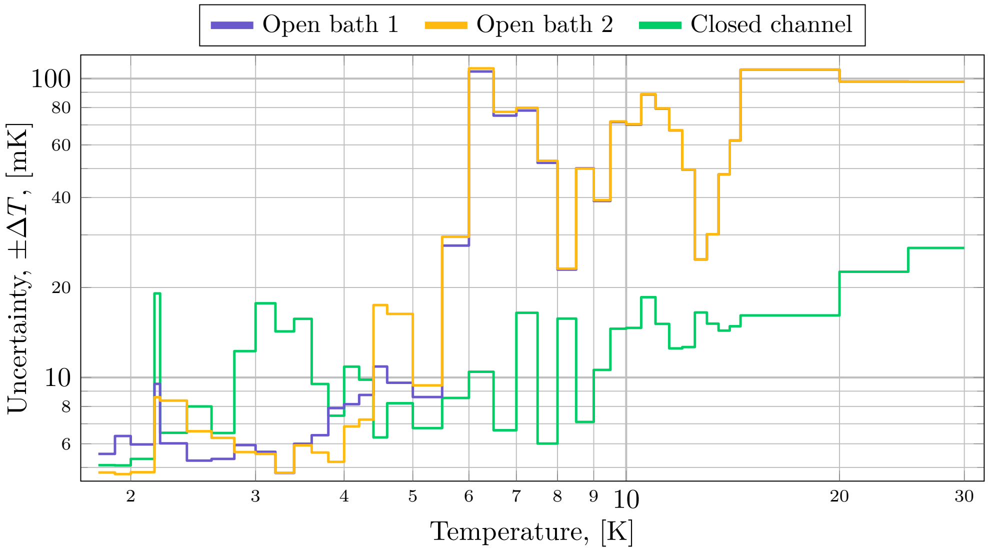

Figure 4.5: Total calibration uncertainty. The contributions from the Lake Shore Cryotronics® reference probe, and the transient nature of the calibration measurements, are taken into account.

4.3 Temperature Offset

In addition to measurement uncertainty discussed in Section 4.2 on page 112, there is also the potential influence of the materials that separate the helium bath and the Cernox® sensors embedded within the experimental samples. This effect is also tied to the bath temperature varying in time, but is treated separately because the calibration measurements themselves cannot be used to illuminate the issue.

As the temperature of the bath goes up or down, albeit slowly, there will, necessarily, be a thermal gradient between the location of the Cernox® sensors and the helium that cools/heats the sample from the surface. Had all calibration data been taken during a true steady state, this gradient would have vanished as heat would have had time to diffuse completely.

4.3.1 Materials Between Sensors and Helium: Open Bath Configuration

In the open bath configuration, 50 µm of steel, 35 µm of GE 7031 varnish, and 200 µm of sapphire separate the sensitive part of the Cernox® sensors from the helium immediately adjacent to the heater, and this simply is not enough material to matter when the time scale is on the order of seconds. This assumes the heater strip surface is at the same temperature as the bath.

This assumption might be wrong; in reality, there is an interface between the steel at the top of the material stack and the helium adjacent to it. Assuming the heater surface is clamped to the bath temperature could overestimate the heat transfer across this interface. To double check this, a natural convection heat transfer boundary condition is used instead, where the heat flux crossing the heater–helium interface is;

$$Q_{\mathrm{NatConv}} = a_{\mathrm{NatConv}} \left(T_{\mathrm{surface}} - T_{\mathrm{bath}}\right), \tag{4.1}$$

where a_{NatConv} is the natural convection heat transfer coefficient. Natural convection as a heat transfer mechanism is well understood in principle but in practice it is hard to describe accurately for modelling purposes. As estimate, the heat transfer coefficient will be taken as [30, eqs. 5.1 and 5.6];

$$a_{\mathrm{NatConv}} = \frac{k_{\mathrm{He}}}{L} C \mathrm{Ra}^n, \tag{4.2}$$

where k_{He} is the temperature dependent thermal conductivity of helium, L is a characteristic length of the heater, C and n are empirical parameters, and Ra is the Rayleigh number. Ra delineates between laminar and turbulent natural convection flows; for Ra above about 10^9, the flow is considered turbulent, and laminar below, although this critical value depends on the heater orientation and geometry. The flow regime determines what values for C and n to use. The value of Ra is [30, Eq. 5.5];

$$\mathrm{Ra} = \frac{g\beta(T_{\mathrm{surface}} - T_{\mathrm{bath}})L^3}{D_{\mathrm{th}}\nu}, \tag{4.3}$$

where g is the gravitational acceleration, β is the bulk expansivity of helium, D_{th} is the thermal diffusivity of helium $= k/\rho C_{\mathrm{p}}$, and ν is the kinematic viscosity of helium $= \mu/\rho$. β is taken from Arp *et al.* [74], k is taken from Van Sciver [30, Appendix A2], and μ is taken from Van Sciver [30, Appendix A2 and A4].

For a horizontal heater strip, the characteristic heater dimension L is A_{s}/p, where A_{s} is the heater surface area and p is its perimeter [194, Tab. 9–1], giving $L = 1.5$ mm. The same source gives values for C and n as well; for the upwards facing heater, $C = 0.54$ and $n = 1/4$ if $\mathrm{Ra} \in [10^4 - 10^7]$, while $C = 0.15$ and $n = 1/4$ if $\mathrm{Ra} \in [10^7 - 10^{11}]$. For the downwards facing heater, $C = 0.27$ and $n = 1/4$ if $\mathrm{Ra} \in [10^5 - 10^{11}]$.

As an example of relevant numbers, take the early parts of the calibration data in Figure 4.3 on page 114; the temperature is around 3.3 K, with $\beta \simeq 0.87\ \mathrm{K}^{-1}$, $\mu \simeq 3.7 \cdot 10^{-6}\ \mathrm{Pa\,s}$, $C_{\mathrm{p}} \simeq 3000\ \mathrm{J\,kg^{-1}\,K^{-1}}$, $\rho \simeq 140\ \mathrm{kg\,K^{-1}}$, and $k \simeq 0.018\ \mathrm{W\,m^{-1}\,K^{-1}}$. Finally, assume for now that there exists a temperature difference of $(T_{\mathrm{surface}} - T_{\mathrm{bath}}) \simeq 1$ mK between the heater and helium bath. This gives $\mathrm{Ra} \simeq 24000$. This gives a final heat transfer coefficient of about $40\ \mathrm{W\,m^{-2}\,K^{-1}}$ for the downwards facing heater and $80\ \mathrm{W\,m^{-2}\,K^{-1}}$ for the upwards facing one. Note that since all the material properties are temperature dependent, a simulation must recalculate a_{NatConv} every time–step.

Figure 4.6 shows the result of running a simulation to ascertain if using natural convection heat transfer as the boundary condition at the heater surface could give rise to a meaningful temperature difference between the bath and the Cernox® sensors. The time–dependent bath temperature is taken from the region in Figure 4.3 between t_{start} = 3085 s and t_{end} = 3266 s. The initial conditions of the simulation are hypothetical, intended to answer the question: if the heater surface starts at a temperature much higher than the bath temperature, does this large temperature discrepancy disappear within a short time? Choosing this hypothetical initial temperature is done by taking the measured bath temperature as it was one minute prior to the start time of the simulation, giving a temperature discontinuity at the heater–helium interface at the start of the simulation of about 1.6 mK.

The material stack consists of the regular lengths of stainless steel, GE 7031 varnish, and sapphire, and then 13.82 mm of PEEK. At the bottom of the PEEK, the temperature is clamped to the bath temperature, while the heater surface is subject to the natural convection heat flux condition. The numerical implementation is identical to that described in Chapter 5, save for using PEEK as the backing material, rather than the copper sensor leads.

The initial condition is implemented as a temperature profile where all nodes of steel, varnish, and sapphire are at the temperature corresponding to the bath temperature one minute before t_{start}, and the PEEK follows a linear drop from this same temperature down to the actual bath temperature at the start of the simulation.

Within two seconds, the difference between the simulated sensor temperature and the bath temperature falls to less than 0.2 mK, and it stays at or below this level for the rest of the simulation. Clearly, the hypothetical temperature discrepancy does not persist for any appreciable time compared to the time scale of the calibration measurements. The conclusion, then, is that in the open bath configuration, even accounting for the small natural convection heat flux boundary condition, there is no appreciable temperature offset between the bath and sensor temperatures.

So, during calibration measurements with very slow time–rate of temperature change, all sensors are, at all times, essentially at the same temperature as the helium adjacent to the part of the heater just above the sensor in question.

4.3.2 Materials Between Sensors and Helium: Closed Channel Configuration

In the closed channel configuration, it is assumed that the cooling power of helium in the channel is negligible; especially for gaseous helium, the small cross sectional area of the pin–holes mean very little heat actually flows in/out of the channel[4]. Without

---

[4] As a very simple estimate, say the temperature of the heater strip should go from 5 K to 5.001 K. Around this temperature, the heat capacity of steel is 20000 $\mathrm{J\,m^{-3}\,K^{-1}}$. So, with $V_{\text{heater}} = 2.25 \cdot 10^{-8}$ m^3, 0.45 mJ must be supplied. This means an average heating power of $P = 4.5 \cdot 10^{-4}/\Delta t$ is necessary. The thermal conductivity of helium (assuming no convection) at 5 K is around 0.01 $\mathrm{W\,m^{-1}\,K^{-1}}$. With a combined pin–hole cross sectional area of about $6.8 \cdot 10^{-8}$ m^2, their heating power becomes $P = 0.01 \cdot 6.8 \cdot 10^{-8} \cdot (\Delta T/\Delta x)$, where Δx is the length of a pin–hole = 4 mm. Equating the average heating power of the steel and the heat flowing through the pin–holes gives that the product $\Delta T \Delta t \simeq 2640$ K s. Say, now, that the heater strip should warm up that one millikelvin within one minute. The temperature difference between the channel helium and the bath helium would have to be about +40 K, which is clearly unrealistic. If instead the temperature difference across the pin–holes is taken as +10 mK, the time to supply 0.45 mJ would be about 70 hours, also clearly not the case.

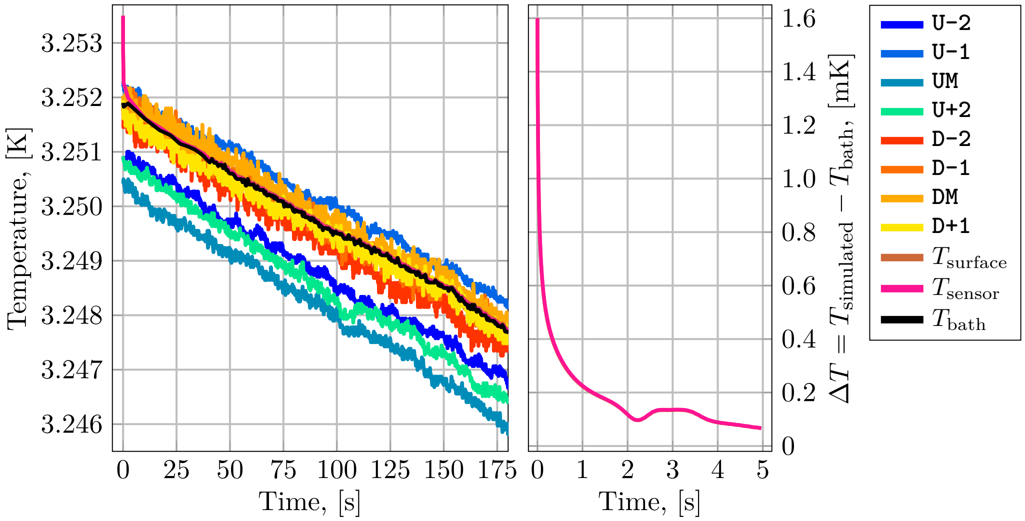

Figure 4.6: Calibration measurement taken from Figure 4.1 on page 111, between $t_{\text{start}} = 3085$ s and $t_{\text{end}} = 3266$ s. The material stack consists of 50 μm of stainless steel, 35 μm of GE 7031 varnish, 200 μm of sapphire, and 10 mm of PEEK. Steel, varnish, and sapphire start at $T_0 = T_{\text{bath}}(t_{\text{start}} - 1\,\text{min})$, while the PEEK has a linear drop in temperature from $T_{\text{bath}}(t_{\text{start}} - 1\,\text{min})$ to $T_{\text{bath}}(t_{\text{start}})$.
The left side plot shows the calibrated sensor temperatures, the simulated temperatures at the heater surface and the sensor location, and the bath temperature. The right side plot shows the difference between the simulated temperatures (heater surface or sensor) and the bath temperature during the first five seconds.

cooling of the Cernox® sensors through the heater surface to helium, a much larger discrepancy between bath and sensor temperatures arises as compared to the open bath configuration.

To assess this discrepancy, a simulation similar to that of the one shown in Figure 4.6 is run, but using the slow warmup data gathered after the closed channel measurement campaign was completed. This data is the basis for all closed channel calibration points above 4.2 K, and spans about 25 hours. Since the natural convection heat transfer coefficient does not depend on the solid in contact with helium, and the natural convection heat transfer boundary condition revealed no significant difference between a clamped temperature and a heat flux condition for the open bath configuration, the bottom of the PEEK is kept clamped to the measured bath temperature, while the top of the heater is insulated, with no heat flowing across the heater/helium interface at all. The simulation uses a spatial grid size of 10 μm to speed up the simulation time. Given the small temperature gradient across the simulation domain, this grid size is sufficiently accurate.

Figure 4.7 shows the result of this simulation. Since the bath temperature rises monotonically in time, a convenient way to express the result is to plot the temperature difference between the bath temperature and the simulated sensor temperature at each bath temperature point passed during the simulation. This is shown on the right. The left side shows the bath temperature in time. None of the measurements made (aside from the dedicated calibration measurement) go above 20 K, so the ΔT plot is capped at 30 K for clarity. The red stepped curve in the ΔT plot is made by taking the RMS value of the green error curve within the same temperature bins as those used in Figure 4.4 on page 116 when assessing the uncertainty contribution by the transient nature of calibration measurements.

The same kind of simulation run with a bath temperature that changes from 2.3 to 4.2 K over about 60000 seconds shows a discrepancy no larger than 1 mK at any temperature. Below 4.2 K, therefore, the offset is considered zero below 4 K.

This temperature offset has its own uncertainty associated with it. For one, the relevant length of PEEK to use is not exactly known. The standard simulation length of 13.82 mm is simply an estimate from the equivalent radius of the cross section of the PEEK plate. Furthermore, the heat capacity and thermal conductivity of PEEK are associated with unknown measurement uncertainty (on top of the fact that for heat capacity, a different material is used altogether). Sources for cryogenic material properties often quote uncertainties below, even well below, 10%. However, for materials with considerable impurity content or complex internal structure, such as metal alloys and polymers, the sample–to–sample variation can be very large. For instance, comparing the 304 stainless steel thermal conductivity used herein (which has been corrected with dedicated measurements) to the standard fit by NIST [188] shows that the steel used herein is about 38% more thermally conductive at 4.2 K than that referred to by NIST. It's hard to say if this level of variation is likely to be seen between samples of other materials as well, but it is an indication that material parameter uncertainty can be quite high even if a particular measurement is accurate. That said, even if the resulting offset has an uncertainty as large as ±20%, the impact is not important. Closed channel experiments where temperatures go above 5 K are steps or slow pulses where the high–temperature region of the measurement happens long after the time–window of interest. The strongest fast–pulse tests approach 5 K, but an offset on the order of -10 ± 2 mK simply does not matter for interpretation of results.

4.4 Post Processing of Raw Data

After calibrating the Cernox® sensor voltage measurements, two important post–processing methods are needed. The first, applied to steady state data only, is a means of getting the surface temperature of the stainless steel heater strip when subject to a known applied heating power density. With this surface temperature it is possible to fit the parameters of the Kapitza model (Equation (2.28) on page 21) to data in order to; 1) have a sanity check of the experimental setup, since the Kapitza expression is expected to describe the open bath steady state situation, and 2) have parameters for the Kapitza surface heat transfer model to use when analysing transient measurements with the simulation framework already used briefly in the previous section, and described in detail in Chapter 5. The second post–processing method pertains to transient data only, and compensates for a filtering capacitor in the Cernox® sensor excitation current sources.

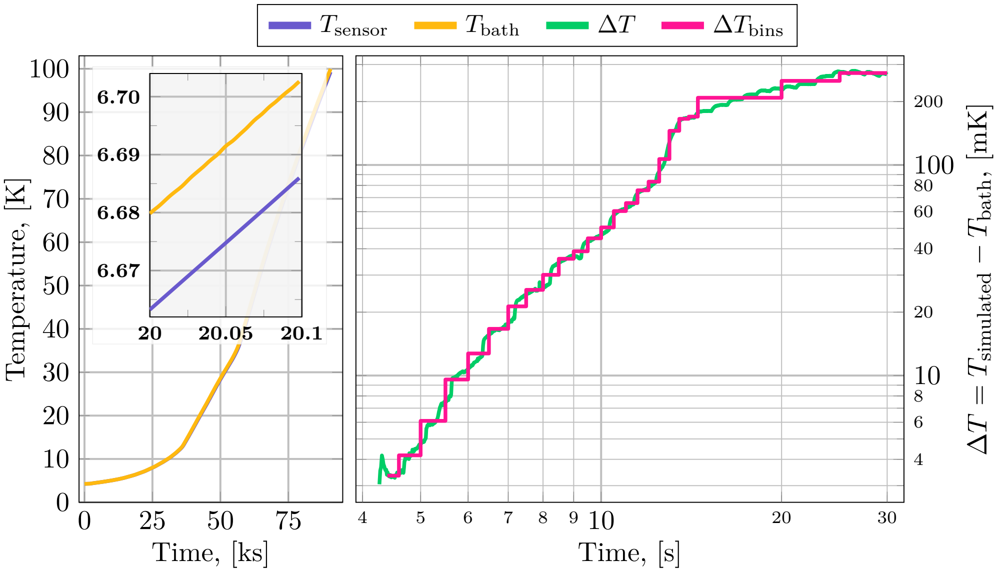

Figure 4.7: Simulation of a material stack consisting of 50 µm of stainless steel, 35 µm of GE 7031 varnish, 200 µm of sapphire, and 13.82 mm of PEEK. Steel, varnish, and sapphire start at $T_0 = T_{\text{bath}}(t_{\text{start}} - 1\,\text{min})$, while the PEEK has a linear rise in temperature from $T_{\text{bath}}(t_{\text{start}} - 1\,\text{min})$ to $T_{\text{bath}}(t_{\text{start}})$. In practice, every node is at the same starting temperature. The bottom of the PEEK is clamped to the measured bath temperature.
The left side plot shows the bath and simulated sensor temperatures in time. The right side plot shows the difference in temperature between the bath and the simulated sensor, plotted against the bath temperature each point in time.

4.4.1 Steady State Surface Temperature Reconstruction Method

The thermal conductivity of stainless steel is low enough that significant thermal gradients will arise across the 50 µm heater strip during heating events. In order to get the heater temperature at the helium/heater interface, these gradients must be modelled and accounted for. The temperature of the heater at the interface is necessary because the Kapitza heat flux depends on it. An important step in building confidence in the experimental setup is to compare measurement results to those in literature which consistently show good agreement with the Kapitza model. The model is intended for steady state heat fluxes, so a large set of steady state measurements were made with this experimental validation in mind.

As for the modelling presented in the previous section, the steady state surface temperature reconstruction method models a version of the material makeup shown in Figure 3.32 on page 95. The simulated domain consists of 50 µm of steel, 20 µm of GE 7031 varnish, 200 µm of sapphire, 20 µm of silver filled epoxy, and 20 mm of copper, where, as discussed in Section 3.4.2 on page 103, the copper thermal conductivity is reduced by a factor $8.614 \cdot 10^{-3}$ to account for its small cross section compared to that of the Cernox® sensors.

The method is summarised by pseudo code in Code 4.1.

`T_sensor_measured` is the steady state temperature seen after a step in applied

Code 4.1: Pseudo code outlining the steady state surface temperature reconstruction method.

```
for each T_sensor_measured:
    make initial T_surface_guess
    while T_sensor_measured is not T_simulated[i_sensor_location]:
        with P_applied, T_surface_guess, T_bath as BC:
            T_simulated = solve(steadyStateHeatEquation, BC)
        make new T_surface_guess
```

heating power density. The initial **`T_surface_guess`** is a starting point chosen based on the accepted surface temperature for the previous, lower, applied heating power density. **`i_sensor_location`** is the index corresponding to the location of the zirconium oxynitride of the Cernox® sensor in the discretised material stack. **`BC`** denote the boundary conditions, and are applied as follows; **`P_applied`** is the volumetric applied heating power density, and it is applied to all nodes corresponding to stainless steel in the simulation domain. The surface of the stainless steel heater strip is clamped to **`T_surface_guess`**. The bottom of the copper leads are clamped to **`T_bath`**.

Figure 4.8 shows an example of the intermediate results of the algorithm. The initial surface temperature guess is set to 4 K in order for the intermediate curves to be distinct. With the better initial guess outlined above, the number of necessary guesses is lower.

Since the thermal conductivity of the various materials in the simulated domain change with temperature, the steady state temperature profile is found by iteration; starting with all nodes at the bath temperature, the heat equation is solved, giving a new temperature distribution along the material stack. This new distribution is used to get a new set of thermal conductivities, which then gives a new solution to the heat equation. Once the maximum of all differences at all nodes between solutions from subsequent iterations is below 1 mK, the steady state is said to be found. From this steady state, the new value for **`T_simulated[i_sensor_location]`** is found. If this new temperature does not equal the measured sensor temperature, a new pass with a new **`T_surface_guess`** is made. The left side of Figure 4.8 shows the typical convergence behaviour; from the flat T_{bath} temperature distribution, the first solution gives $T(x)$ far too high, since the thermal conductivity used along the material stack was consistently too low, and it grows monotonically with temperature. The second solution is better, but a bit too low. After six solutions of the heat equation, convergence is achieved.

The surface temperature guessing is done by taking the new guess to be equal to the old guess minus the temperature difference between the simulated sensor temperature and the measured sensor temperature. This works because, again, thermal conductivities grow monotonically with temperature, so if the steady state solution overshoots the measured temperature target, one will *always* need to lower the surface temperature guess, and if the steady state solution is below the target, the only way to get closer is by *increasing* the surface temperature guess. The final guess is that which gives a difference between the simulated and measured sensor temperatures below $5 \cdot 10^{-5}$ K.

With the steady state temperature profile, estimates for the real heater–surface–to–helium heat flux and heat loss to the back of the sample are made (using the local thermal conductivity and thermal gradient). The final temperature distribution in Figure 4.8 gives a forward heat flux of 16.113 kW m^{-2}, and a backwards heat leak of 0.383 kW m^{-2} which sum to 16.496 kW m^{-2}. The applied volumetric heating power density, from the measured steady state voltage and applied current, is $3.306 \cdot 10^8$ W m^{-3}, which expressed in the usual applied heating power density from Equation (3.2) on page 63 is 16.53 kW m^{-2}. The discrepancy is 0.2%.

Note that Δx is 0.1 µm in all steady state surface temperature reconstruction simulations, while in most time–dependent simulations it is 2 µm to keep simulation times reasonable. Using the small Δx for the steady state simulations ensures a very small discrepancy between heat applied to the system and heat accounted for within the system. This is discussed a little more in Section 5.1.

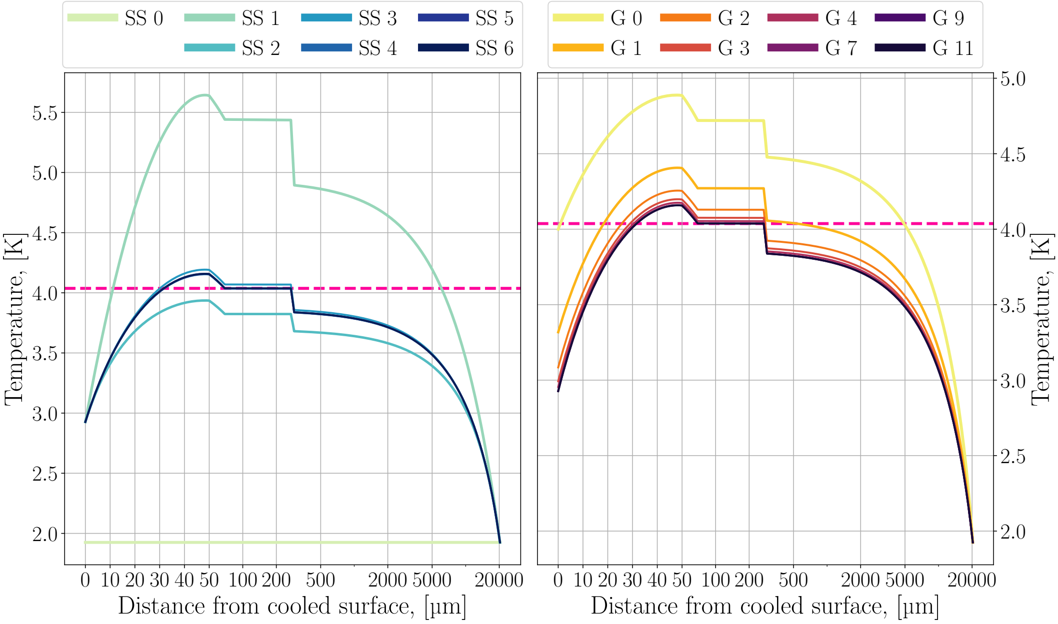

Figure 4.8: Example of intermediate results for steady state surface temperature reconstruction of a measurement where `UM` shows a steady state temperature of 4.037 K, under an applied heating power density of 16.5 kW m^{-2}. The left side shows subsequent solutions of the steady state heat equation, starting from a flat temperature distribution at $T_{\text{bath}} = 1.925$ K, for the last surface temperature guess. The right side shows subsequent guesses of the heater surface temperature, starting at 4 K. The x–axis is linear up to 50 µm, and logarithmic beyond.

An important note about this method, common to all methods where the temperature of interest must be reconstructed from a measurement, across one or more materials, is that it introduces new sources of uncertainty. Here, in particular, the simulated surface temperature result is sensitive to the value of the thermal conductivity of stainless steel. The simulated surface temperature is also sensitive to the lengths of material in the stack.

4.4.2 Capacitive Compensation Method

The Cernox® sensors themselves are expected to be more than responsive enough in time to measure temperature changes over times on the order of 0.1 ms [195][5]. However, the raw transient voltage signals, seen back in figures 3.23 and 3.24 on page 85, show temperature response times on the order of 10 to 20 ms. A simple energy balance estimate shows time constants on this order are not a reflection of the true temperature transient.

Say a step in applied heating power density of 20 $\mathrm{kW\,m^{-2}}$ starts at time $t = 0$, applied to the heater in the open bath configuration. This corresponds to a volumetric heating of about $4 \cdot 10^8$ $\mathrm{W\,m^{-3}}$, or a power of 9 $\mathrm{mJ\,ms^{-1}}$. At this applied heating power density, steady state measurements show the temperature should reach around 4 K (not considering the gradient between the sensor and the heater surface). The heat capacity of steel at 4 K is about 15000 $\mathrm{J\,m^{-3}\,K^{-1}}$. Starting at 1.9 K, this means the total amount of heat put into the steel (taking the heat capacity as constant) is about 15000 $\mathrm{J\,m^{-3}\,K^{-1}} \cdot$ 2.1 K$\cdot$ $2.25 \cdot 10^{-8}$ $\mathrm{m^3}$ = 0.71 mJ. After the steady state is established, all this energy is removed from the surface of the heater strip (with minor leakage backwards along the sensor leads), but during the transient, the input energy is split between a fraction of energy removed from the heater surface to helium by cooling, and a fraction that goes into establishing the steady state temperature distribution. If it really took 10 ms for the surface of the heater strip to reach a temperature where an appreciable amount of heat is removed, there would be a gap between the energy input, at 9 $\mathrm{mJ\,ms^{-1}}$, and the energy accounted for in the steel, at 0.71 mJ (at 4 K), of about 89.3 mJ. Could this energy be found in the materials around the heater strip? Not after just 10 ms; if the PEEK of the entire bottom plate in which the heater strip is mounted was to soak up the 89 mJ of excess energy, using the heat capacity of 2500 $\mathrm{J\,m^{-3}\,K^{-1}}$ at 3 K as a simple average, the PEEK temperature would increase by $\Delta T = 89\ \mathrm{mJ}/\ (2500\ \mathrm{J\,m^{-3}\,K^{-1}} \cdot 4.5 \cdot 10^{-5}\ \mathrm{m^3}) = 0.8$ K. The low thermal diffusivity of PEEK prohibits its temperature from growing by nearly an entire kelvin within 10 ms.

The reason for these excessive time constants turns out to be electric; there is a large filtering capacitor on the output terminals of the sensor current excitation sources. Figure 4.9 shows a simplified schematic of the electronics during a measurement where the Cernox® sensors experience a rapid temperature increase. As laid out in Section 3.3.2 on page 76, the sensors are connected so that two sensors share a single current source. The source itself acts like an ideal source, supplying 10 µA at all times[6], while the filtering capacitor is there to smooth the current output ripple. The real resistance behaviour of the sensors is not captured by an instantaneous drop

---

[5] The measurements by Fuzier and Van Sciver uses Cernox® 1030 sensors, while 1050's are used herein. This difference pertains only to the useful temperature range however, and will not impact the sensor's response time. Note also that modern Cernox® sensors use a thinner layer of sapphire (approximately 300 µm in Fuzier and Van Sciver's measurements, and 200 µm herein), lowering the thermal mass of the sensor, lowering its response time further.

[6] Discussion with Dag Roar Hjelme, professor at the Department of Electronic Systems at NTNU [196], and simulations using MATLAB SimuLink®, confirm that the internal electronics of the excitation current sources are practically independent of the external electronics (filtering capacitor and sensors).

in resistance at time t_0; the circuit is just a simple picture of what the relatively large filtering capacitor sees during temperature transients.

The typical situation right before energy is supplied to the heater strip is that the two sensors in an excitation circuit are stable at 1.9 K, meaning their combined resistance is on the order of 30 kΩ. The rate of resistance change per change in temperature for the Cernox® sensors is on the order of -5 $\mathrm{k\Omega\,K^{-1}}$ at 1.9 K, so once power is applied, and the sensors heat up to, for example, 4 K, their combined resistance will be on the order of 10 kΩ. Right before power is applied, when only the steady 10 µA excitation current flows, the voltage across the two sensors, and hence the filtering capacitor, is $V_\mathrm{C}(t_0^-) = 300$ mV. After the temperatures have settled at 4 K, and the sensor circuit current again is at 10 µA, the voltage across the sensors and filtering capacitors is 100 mV. During the transition from the high to the low voltage state, the filtering capacitor will supply additional current in order to maintain the electric potential from before the sensor resistances started to decrease. The filtering capacitor used in the sources is 1 µF, which, with a circuit resistance on the order of 10 to 30 kΩ, gives an RC time constant $\tau = 10$ to 30 ms. When the applied power is cut off, and the sensors cool back down, the opposite happens: the filtering capacitor siphons off current from the sensors, charging up, to maintain the lower voltage level from before the cooling started.

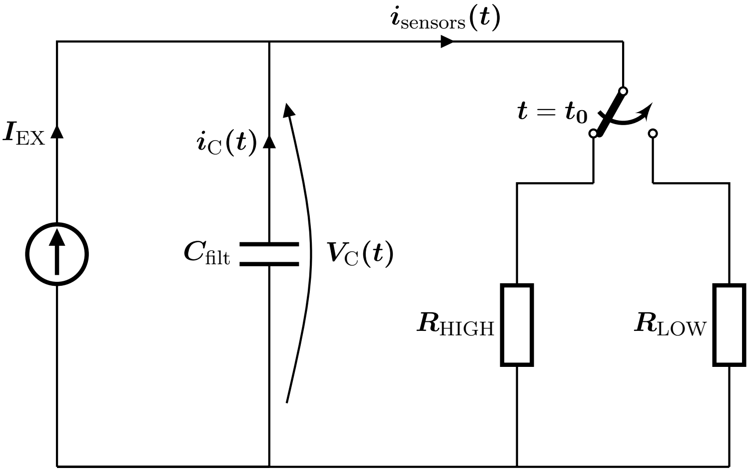

Figure 4.9: Simple circuit diagram representing the moment when the temperature of the Cernox® sensors suddenly rises due to application of power. I_EX is the 10 µA excitation current from the source, which remains constant in time. C_filt is the filtering capacitor on the terminals of the source, while $i_\mathrm{C}(t)$ and $V_\mathrm{C}(t)$ denote the time–dependent current and voltage through/across the capacitor. $i_\mathrm{sensors}(t)$ denotes the time–dependent current flowing though the sensors. t_0 represents the time at which the sensor resistance suddenly drops as the sensor temperature suddenly rises.

Because the excitation current sources are independent of the capacitor and sensor circuit, whatever the circuit resistance, the source always supplies 10 µA, and this makes it possible to estimate the additional current supplied or consumed by the filtering capacitor during transient measurements. This is done by making use of the basic capacitor current/voltage relationship;

$$i_{\mathrm{C}}(t) = C\frac{\mathrm{d}V_{\mathrm{C}}(t)}{\mathrm{d}t}, \tag{4.4}$$

where $V_{\mathrm{C}}(t)$ is the total voltage measured across the two Cernox® sensors in the circuit.

The main challenge with the approach is that the signal to noise ratio is very low when considering a numerically determined derivative of $V_{\mathrm{C}}(t)$, especially for lower power measurements where the temperatures do not change very much or very fast.

Figure 4.10 shows the final smoothed result of $\mathrm{d}V_{\mathrm{C}}/\mathrm{d}t$ for open bath step heating, closed channel step heating, and closed channel slow pulse heating. The data comes from the representative sensor voltage measurements in figures 3.23a, 3.23b, and 3.24b. With $V_{\mathrm{C}}(t)$ as the sum of the two sensor voltages in the excitation circuit, the six curves in the plots are as follows; 1) Raw derivative is the simple $\Delta V_{\mathrm{C}}/\Delta t$, and gives a very noisy signal; 2) SavGol filtered is $V_{\mathrm{C}}(t)$ after applying a 1st order derivative Savitzky–Golay filter of appropriate window size (51 samples for open bath steps, and 101 samples for closed channel steps and slow pulses); 3) Butter low cutoff is Savitzky–Golay filtered curve after applying a Butterworth low–pass filter with a low cutoff frequency; 4) Butter high cutoff is Savitzky–Golay filtered curve after applying a Butterworth low–pass filter with a high cutoff frequency; 5) Polynomial fit fits a 5th degree polynomial to the first few milliseconds of the Raw derivative for open bath steps and closed channel slow pulses, and to the Savitzky–Golay filtered curve for closed channel steps; and 6) Smoothed result is the combination of results 2), 3), 4), and 5).

Savitzky–Golay filtering The Savitzky–Golay filter acts similarly to a moving average/median filter in that it looks at input data across a certain window around any given point, and then determines the filtered signal value at the middle of this window. Unlike a moving average, which returns the average value across the window, the Savitzky–Golay filter instead fits (in a least squares error sense) a polynomial (of any order) to the data within the window [197, 198]. The Savitzky–Golay filtering approach amounts to a discrete convolution of a polynomial of fixed coefficients with the signal one wants to filter. This fixed coefficient polynomial need only be calculated once for a given window size and polynomial order. Furthermore, such convolution polynomials are defined for arbitrary differentiation order. Herein, the 1st order derivative is needed to obtain the numerical approximation to $\mathrm{d}V_{\mathrm{C}}(t)/\mathrm{d}t$. The Python function `scipy.signal.savgol_filter()` conveniently implements the convolution, including the request for the 1st order derivative. The result of this filtering of the measured voltage signal, using a first order polynomial applied over all windows, is the yellow curve in the plots. Note, the SavGol filtered curves in the plots are *not* made from applying the Savitzky–Golay filter to the Raw derivative, but rather by directly applying the relevant 1st derivative convolution coefficients on the measured $V_{\mathrm{C}}(t)$.

Butterworth low–pass filter The Butterworth low–pass filter was designed to provide a completely flat frequency response below the cutoff frequency, and a monotonic roll–off above the cutoff frequency [199]. Its application is widespread due to

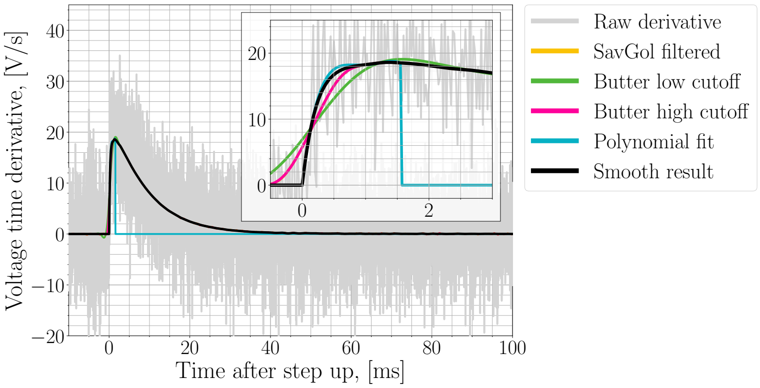

(a) dV_C/dt during open bath step.

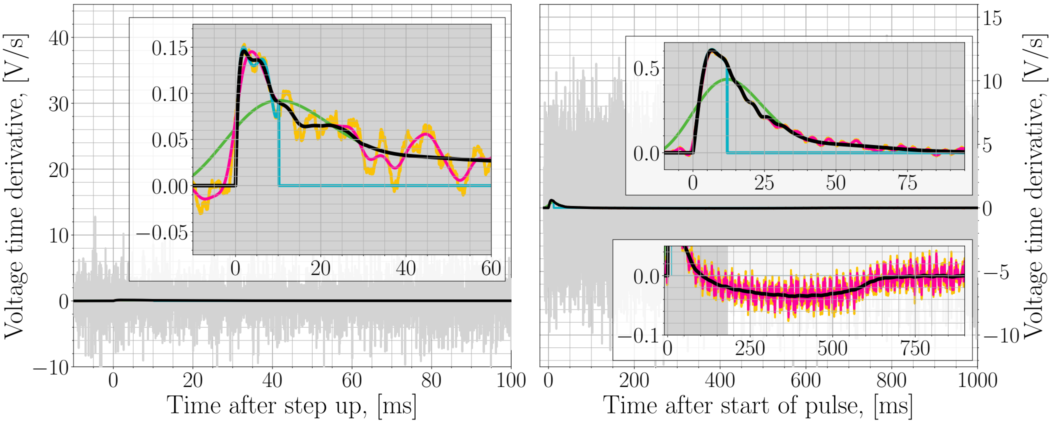

(b) dV_C/dt during closed channel step.

(c) dV_C/dt during closed channel slow pulse.

Figure 4.10: Smoothed dV_C/dt from the representative measurements whose sensor voltage measurements were shown in figures 3.23a, 3.23b, and 3.24b on the previous page (open bath step heating, closed channel step heating, and closed channel slow pulse heating). For the step heating plots, the data shows the time after power turns on. All plots share the legend from 4.10a. These are the smoothing results for the second sensor circuit (`UM` and `U+2` in open bath, and `HM` and `H+1` in closed channel.

its ease of implementation. The Python function **`scipy.signal.butter()`** is used to design a digital filter which then is applied both forwards and backwards on the noisy data by the Python function **`scipy.signal.sosfiltfilt()`**. By applying the filter both forwards and backwards, the phase shift between raw signal and filtered signal is zero, which keeps features like edges and peaks where they are in time. The double application also means that the total order of the filter is twice that of the Butterworth design (herein, 3rd order Butterworth filtering is used, for a total order of 6).

In order to apply the Butterworth filter, a cutoff frequency must be determined. The signals to be filtered typically have two distinct regions in time; 1) immediately after the switching on of power (either step or pulse), a rapid signal rise from zero to some level is seen; then, 2) a slow decay to zero, the duration of which is at least an order of magnitude longer than the initial rise. For pulsed heating, the decay to zero includes a slow dip below zero as the Cernox® sensors cool back down. There is no fixed cutoff frequency to apply, since the desired temperature signal measured has unknown behaviour. For the filtering, though, an exact cutoff frequency is not needed. A successful method is simply to look at the power spectrum of the Raw derivative curve (square of the absolute value of the fast Fourier transform of the signal), reject all frequency components above 1 kHz, then take as the cutoff frequency the frequency corresponding to the power closest to the geometric average of highest and lowest powers in the signal[7]. In cases where this approach finds a frequency below 25 Hz, the cutoff frequency is taken as 25 Hz.

The Butter low cutoff uses this cutoff frequency directly, while the Butter high cutoff uses five times this frequency. This way there is a filtered signal to use right after the Polynomial fit (high cutoff), and one for the long signal tail (low cutoff).

Note that for most measurements, Butter high cutoff very accurately follows SavGol filtered, and hence the yellow curve tends to be hidden.

Polynomial fit In the time span between the time of turning on power and the time at which the Butter low cutoff reaches its peak, a 5th degree polynomial is fitted to the Raw derivative curve. For closed channel steps of low power, the Raw derivative signal is too noisy to give a good fit, so the polynomial is fitted to the Savitzky–Golay filtered curve instead. This affects roughly 40% of the closed channel steps. When fitting the polynomial to the raw derivative for low powered steps, the polynomial oscillates, because the raw derivative is so noisy that the least squares condition for determining the polynomial coefficients does not reliably discriminate between a real signal rise and signal oscillations due to noise. A lower degree polynomial fails to capture the rapid initial rise, so fitting to the Savitzky–Golay filtered data is the better compromise.

The first point of the polynomial is fixed to 0 by applying a large weight to this point (the time derivative must be zero when the system is in steady state). The last point of the polynomial is made to be equal to the corresponding point along the Butter high cutoff curve by applying a large weight to this point (though smaller than the weight of the zero at the start of the polynomial).

Smooth result There are now a total of four different representations of the data that are smooth in various regions during the transient. Four points in time are defined: t_{SWITCH} = the time at which power is switch on; $t_{\text{POLYNOMIAL}}$ = the time where polynomial fitting ends; $t_{\text{HIGH CUTOFF}}$ = the time where Butter high cutoff starts to capture too much noise; and $t_{\text{LOW CUTOFF}}$ = the time after which the smooth result is kept equal to Butter low cutoff. The Smooth result curve is generated by the following method:

---

[7] For steps up in power, the frequency corresponding to the geometric mean of powers typically give frequencies around 300 Hz, while steps down in power give around 100 Hz. For slow pulses, the cutoff frequency is typically around 30 Hz, while for fast pulses, a different approach is used, without Butterworth filtering altogether.

- Between t_{SWITCH} and $t_{\text{POLYNOMIAL}}$, Smooth result is the weighted sum of the polynomial and Butter high cutoff. The weighting is a linear rise or drop between 0 and 1 such that the start of Smooth result is dominated by the polynomial fit, while the end of the region is dominated by Butter high cutoff.
- Between $t_{\text{POLYNOMIAL}}$ and $t_{\text{HIGH CUTOFF}}$, Smooth result is equal to Butter high cutoff.
- Between $t_{\text{HIGH CUTOFF}}$ and $t_{\text{LOW CUTOFF}}$, Smooth result is the weighted sum of Butter high cutoff and Butter low cutoff, in a similar way as for the polynomial and Butter high cutoff between t_{SWITCH} and $t_{\text{POLYNOMIAL}}$.
- After $t_{\text{LOW CUTOFF}}$, Smooth result is equal to Butter low cutoff.

Step down in power When a step in applied heating power density is turned off, a completely analogous situation arises, in terms of the filtering effort, though the signal is weaker, because cooling down proves to be a slower process than warming up, especially when the helium temperature has reached above T_λ. The exception is for points in time where the helium temperature during cooldown drops below T_λ again, which is associated with a rapid temperature drop, and hence a spike in $\mathrm{d}V_{\mathrm{C}}(t)/\mathrm{d}t$. Around these peaks, Smooth result is taken as Butter high cutoff again, with a transition from Butter low cutoff to Butter high cutoff before the peak and then back to Butter low cutoff after the peak.

Fast Pulses in Closed Channel

To obtain $\mathrm{d}V_{\mathrm{C}}(t)/\mathrm{d}t$ for fast pulses in the closed channel configuration, the previous approach of Butterworth filtering with different cutoff frequencies did not prove successful. Fast pulses are characterised by the entire transient heating event being over within just 2 ms, and the high frequency noise is hard to differentiate from the high frequency signal. Instead, Savitzky–Golay filtering with successively wider windows are used.

Figure 4.11 shows the voltage derivative during the measurement shown back in Figure 3.24a (for the second sensor circuit with `HM` and `H+1`). The curves labelled SavGol, n = x in the legend refer to the number of samples used in the Savitzky–Golay filtering windows to obtain the 1st derivative of $V_{\mathrm{C}}(t)$.

These curves intersect at various points, and these points can be used to limit regions across which polynomials are fitted to the curves. Only the first intersection point *after* the peak of the first SavGol curve is considered for each successive curve. For instance, n = 5 and n = 19 first intersect around 0.5 ms, while n = 19 and n = 41 intersect around 0.8 ms.

At these intersection points, Smooth result transitions from one smooth 5th degree polynomial fit to another, all the way up to the global minimum of n = 91 (around 11 ms). From here, Smooth result transitions into n = 375, and follows this value till the end of the measurement.

The transition from the polynomial fit of n = 91 to n = 375 tends to be a bit jagged, and so a correction is used by making the region around the minimum of Smooth result equal to the n = 201 data.

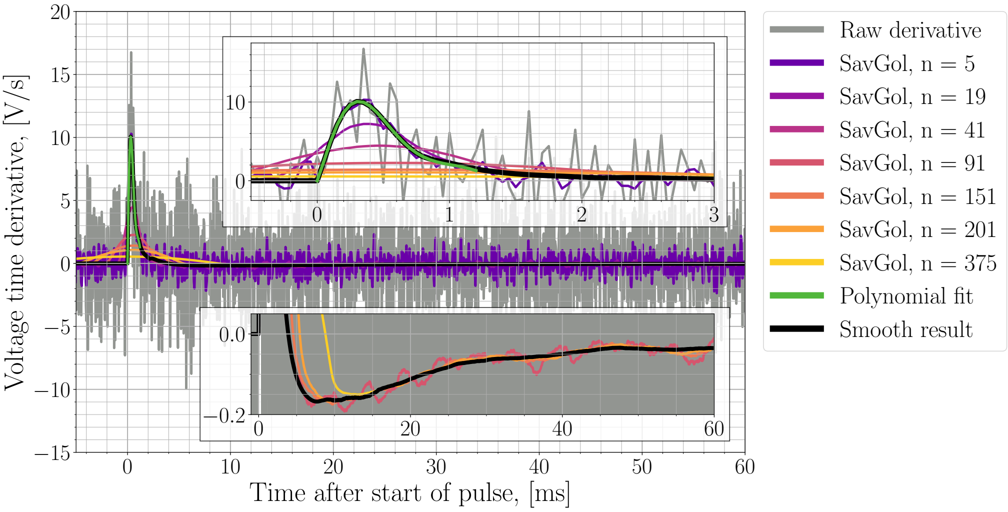

Figure 4.11: Smoothed $\mathrm{d}V_\mathrm{C}/\mathrm{d}t$ from the representative fast pulse measurement, whose sensor voltage was shown in Figure 3.24a. This is only the smoothing result for the second sensor circuit, with sensors `HM` and `H+1`.

Recalibration of Temperature Measurements

Once $\mathrm{d}V_\mathrm{C}(t)/\mathrm{d}t$ is known, the real sensor excitation current is found by Equation (4.4) on page 127;

$$i_\text{sensors}(t) = I_\text{EX} + C\frac{\mathrm{d}V_\mathrm{C}(t)}{\mathrm{d}t}, \tag{4.5}$$

where $i_\text{sensors}(t)$ is the current in the two sensors that share a current source, I_EX is the 10 µA steady state excitation current, and C is the filtering capacitor.

With this, the new measured sensor resistance is found;

$$R_\text{sensor}(t) = \frac{V_\text{sensor}(t)}{i_\text{sensors}(t)}, \tag{4.6}$$

where $R_\text{sensor}(t)$ and $V_\text{sensor}(t)$ refer to the individual sensor within the excitation current circuit. When the sensor temperature rises, the sensor resistance drops, and current flows *out* of the capacitor and *into* the sensors, meaning that $C\mathrm{d}V_\mathrm{C}(t)/\mathrm{d}t$ is added current.

With this, the new measured temperature is found by applying the relevant spline fit to the calibration curves shown in Figure 4.2.

The process of finding $\mathrm{d}V_\mathrm{C}(t)/\mathrm{d}t$ does not depend on the exact value of C. This means that the general shape of the compensated temperature curves remain the same in time, regardless of C. However, the amplitude of the added or subtracted current does depend on C. Dedicated measurements of the capacitors as they are mounted within the circuit give values of 0.929 ±0.03 µF. This uncertainty has a sufficiently small impact on results it will be neglected.

Voltage Spikes in Open Bath Steps and Closed Channel Fast Pulses

In the plots showing the raw voltage measurements of open bath steps and closed channel fast pulses (figures 3.23a and 3.24a respectively), voltage spikes right as power is turned on were seen.

So far, the capacitive compensation method has tacitly assumed the source of any such spikes to be solely the time–rate of change in sensor resistances; the first step in the capacitive compensation is to add together the two contributing sensor voltages within the same excitation circuit. The result shows no spike at all, but rather a continuously falling voltage, starting from the expected sum of the two measurements, because the spikes are perfectly symmetrical. However, since the spikes themselves are not visible in all sensor voltages, but the $\mathrm{d}V_\mathrm{C}(t)/\mathrm{d}t$ curves are very similar for all sensor circuits of the same measurement, a voltage spike is not a *necessary* feature of the transient response of the sensor circuits. Other reasons for the spikes are conceivable.

As the X–ray image in Figure 3.20 on page 80 shows, the sensor lead wires (red parts of the sensor wiring circuit diagram in Figure 3.22 on page 82) are twisted with a separation on the order of 200 to 400 µm (using the sensor substrate thickness of 200 µm for scale). The relative permeability μ_r of the GE 7031 varnish that insulates the sensor leads, and sits between the twisted wires, is not explicitly known, but for most non–metals it is practically unity. By assuming the separation of ~300 µm to be much larger than the lead diameter, which is 63.5 µm, a rough estimate of the inductance of this twisted wire pair is [200, Slide 16],

$$L \simeq \frac{\mu_0}{\pi} \log \left[\frac{2 \cdot 300\ \mu\mathrm{m}}{63.5\ \mu\mathrm{m}} \right] = 900\ \mathrm{nH\,m^{-1}}, \tag{4.7}$$

where $\mu_0 = 1.2566 \cdot 10^{-6}\ \mathrm{H\,m^{-1}}$ is the permeability of vacuum.

With a total length on the order of 15 mm, the total inductance is roughly 13.5 nH. Voltage across an inductance is proportional to the time–rate of change in current passing through it. As seen in this section, there *is* a large change in sensor current. When zooming in on the voltage spike in sensor `U-2` in Figure 3.23a, the peak voltage value is about 63 mV above the starting voltage value. The peak happens 0.5 ms after power is turned on, but the most rapidly changing part of the curve is over after 0.2 ms, coincident with the part of the $\mathrm{d}V_\mathrm{C}(t)/\mathrm{d}t$ curve that changes the most rapidly in time. Equation (4.5) gives the time dependent current through the sensor circuit, so another time–differentiation expresses the voltage across the sensor lead inductance by multiplying with L. The largest $\mathrm{d}i/\mathrm{d}t$ is 0.013 $\mathrm{A\,s^{-1}}$, which leads to a voltage of 180 pV. Clearly much smaller than the observed 63 mV spike. For the sensor lead inductance to give a spike of 63 mV, it would need to be almost 5 H, which is impossible with the dimensions of the sample.

Another explanation could be that there is magnetic coupling between the current flowing in the heater strip and the sensor lead wire loops. This is also ruled out, however, because no voltage spikes are seen in the helium channel sensors in the fast pulse plot; in the X–ray image in Figure 3.20 on page 80, it is clear that the distance between sensor wire loops is roughly the same on either side of the heater strip. So, if the current in the heater strip magnetically coupled to the heater strip sensors, it should couple about equally strongly to the channel sensors.

In conclusion, the spikes have no obvious origin, but, since they are symmetric, they do not impact results, and are assumed to be an odd feature of the complete electrical circuitry of the measurement system, and are not considered further.

4.5 Representative Measurements

This section will show the measurements from back in figures 3.23 on page 84 and 3.24 on page 85, after calibration and capacitive compensation, as typical examples of results. Discussion of the results is relegated to the relevant papers appended to this thesis, and typically only very basic and cursory observations are mentioned here. Before those four plots, the temperature behaviour around the lambda transition will be shown, though, serving as valuable checks of some of the geometrical features of the design.

4.5.1 Temperature Around Lambda Transition

Lambda transition in open bath Figure 4.12 shows the ten seconds around the lambda transition of the helium bath during cooldown before the open bath measurement campaign. A few things are immediately visible; 1) After the transition is complete, the difference between the reference probe and the calibrated Cernox® sensors is much smaller than before the transition. 2) There is a distinct difference between when the upwards facing and downwards facing heater sensors register the transition.

The lower scatter of temperature around the reference probe is due to the superfluid bath suddenly no longer having thermal gradients to speak of. As opposed to the normal–fluid bath before the transition, all sensors now approach the same bath temperature. This stark difference is clear evidence that the non–uniformity of the bath is a large contributor to measurement uncertainty at temperatures above T_λ.

The clear separation in time of when the sensors appear to register the transition has to do with the superfluid/normal–fluid interface slowly moving upwards from the bottom of the bath as it cools down. After the cryostat has stabilised at free surface liquid helium temperature (around 4.22 K), and a buffer level of liquid helium has built up above the lambda plate (Label (6) in Figure 3.7 on page 65), the lambda valve (Label (7) in Figure 3.7) is closed. At this point, cooling mostly happens downwards across the copper wall of the inner bath pot to the saturated bath below it. As more and more helium cools below T_λ, the lambda front moves upwards. The heater strip facing downwards has its contact surface a little below the reference probe height in the bath, and is touched by superfluid helium before the reference probe. Then it takes another 3 to 3.5 seconds before the upwards facing heater is covered with superfluid helium.

Seeing that the transition happens at different times, but still essentially at the same rate between the downwards and upwards facing heater sensors is clear evidence that the predominant cooling path of the Cernox® sensors is that through the helium cooled heater surface. If it was through the bottom of the PEEK, the upwards facing sensors would have started their transition together with the downwards facing ones, since the superfluid reaches the bottoms of both PEEK plates at the same time, and it would be more smeared out as slower heat transfer through the PEEK acted on the sensor location.

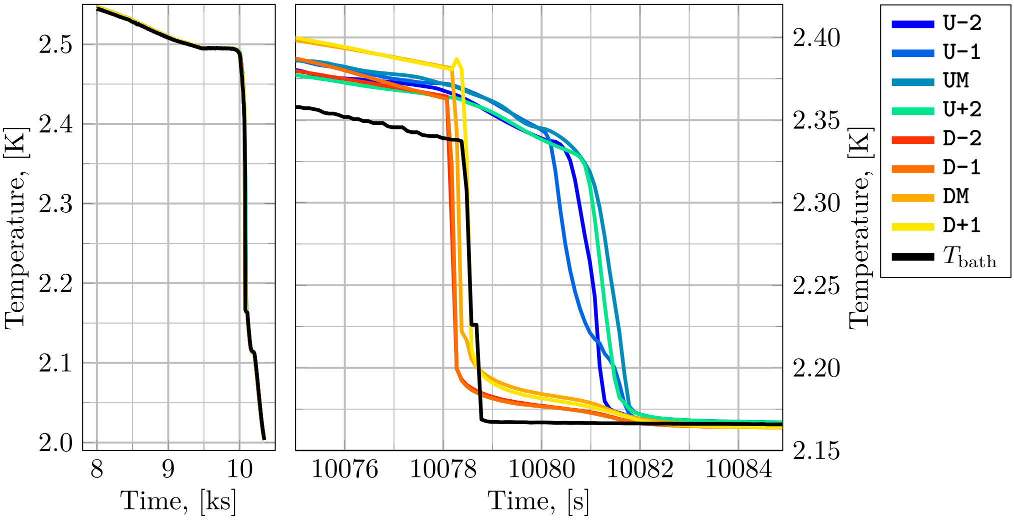

Figure 4.12: Highlight of temperature behaviour during the ten seconds around the lambda transition (from above) in the open bath configuration.

Lambda transition in closed channel Figure 4.13 shows the 25 seconds around the lambda transition of the helium bath during cooldown before the closed channel measurement campaign. In the open bath, it takes between 3 and 4 seconds for all sensors to transition, while in the closed channel it takes about 11. The closed channel environment is much more complicated than the open bath one, mostly because there are two relevant cooling paths of the sensors, with a transition from one to the other during the time–window plotted. Once the helium is superfluid He II, the channel provides ample cooling power, and the cooling path becomes the same as in the open bath; the short bit of steel, varnish, and sapphire. For as long as the helium remains normal–fluid He I, however, cooling happens mostly through the PEEK. Furthermore, in the closed channel, the cooled bottom of the channel sensors lie 20 mm higher in the bath than the cooled bottom of the heater sensors. In the open bath, the height difference associated with heater orientation is the determining factor for when a sensor sees the lambda transition. In the closed channel, however, it is the distance from the edges of the channel that most reliably predicts when a sensor sees the transition.

The first sensors to see the sharp drop characteristic of the superfluid transition are `H-2` and `C-2`. They face each other, on the left side of the channel. The next sensor is `C+2`. That there is a small difference in time between when channel sensors on opposite sides of the channel see the transition could be an indication that the pin–holes are not exactly identical. Next comes `C-1` and `H-1`. The expected next set of sensors would be the `+1`'s, but instead `HM` and `CM` transition, while `H+1` and `C+1` transition just a little later. So, from the edges of the channel, the superfluid/normal–

fluid interface propagates inwards, and it takes about ten seconds to cross the 75 mm to reach the middle of the channel. However, for some reason, the propagation is slower from the right side of the channel, needing about ten seconds to cross only a quarter the length of the channel. If this process is dominated by heat transfer to the outside bath, an explanation could be that the right–side pin–hole is somewhat smaller than the left–side one. Since the temperature obviously drops markedly at the transition, energy transfer is an important part of it.

Note also that the linear region of temperature decay just prior to the transition lasts longer the further into the channel the sensors are, and it starts around the same time. The linear drop in temperature could stem from cooling across the PEEK; if the lambda surface in the bath rises faster than the lambda front propagates down the channel, there could be sufficient time to see the drop in bath temperature propagate along the PEEK. The three smooth curves $x \cdot k_{\mathrm{PEEK}}$ denote simulations of the material stack like the one used to determine the temperature calibration offset at higher temperatures due to the 13.82 mm of PEEK between the bath and the sensors. The factor in front is applied to the standard thermal conductivity value of PEEK. The simulations use the black reference probe data as its boundary condition at the bottom of the PEEK, and do not include any transition from bottom–of–PEEK cooling to channel cooling at the lambda transition. For illustration purposes the simulated curves have been shifted in time and temperature to match the start of the downwards slope in the data of `H+1`.

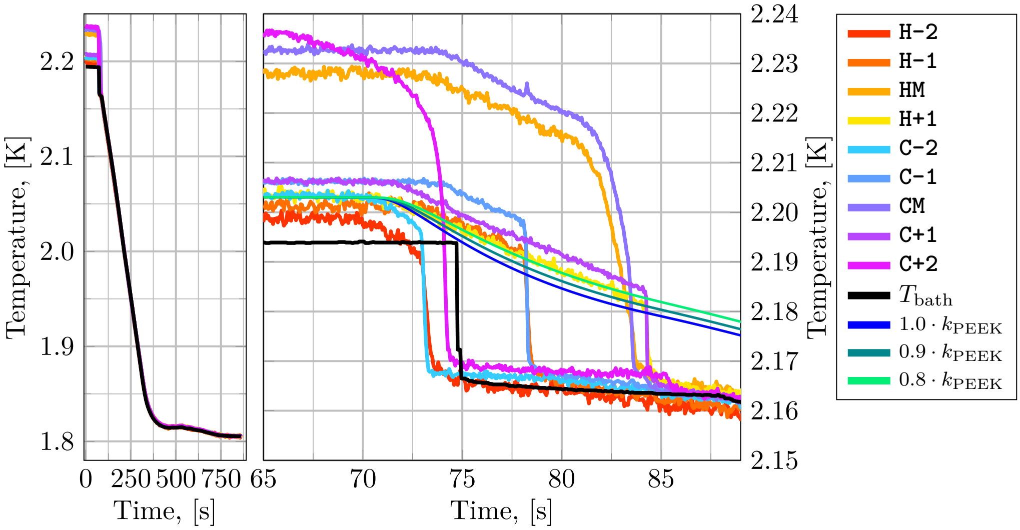

Figure 4.13: Highlight of temperature behaviour during the 25 seconds around the lambda transition (from above) in the closed channel configuration. The plot includes simulations of the material stack of 50 µm of steel, 35 µm of GE 7031 varnish, 200 µm of sapphire, and 13.82 mm of PEEK. The bottom of the PEEK is clamped to the bath temperature, while the heater surface is insulated. Note that the simulation results have been adjusted in time and temperature to match the start of the linear region in the `H+1` curve for easier comparison.

In both the open bath and the closed channel plots, there is a sharp temperature drop to T_λ, which first appears strange, since there is no latent heat associated with the lambda transition. However, as noted in Section 2.4.3 on page 30, helium around and below T_λ is a strongly interacting system, where the phase transition is not actually sharp like it is in the case of superconductors, for instance. Looking at Figure 4.13 it is apparent that the peak in heat capacity happens long after the sharp drop in temperature; the peak is seen where the reference probe has the smallest temperature gradient, around $t = 87$ s. So, what is happening is that the super–heat–conductivity of He II manifests itself a little before the phase transition itself. The He I just above the upwards–moving lambda surface gains the large thermal conductivity of He II, and thus temperature nearly instantly equilibrates across the helium volume. The same thing happens in the open bath, of course, but the time–resolution of the plot isn't quite as good, and the cooling rate was higher than for the closed channel case, making it hard to notice the heat capacity peak clue.

4.5.2 Open Bath Step Heating

Figure 4.14 shows the complete measurement during a step in applied heating power density in the open bath configuration. The sensor temperature data is taken from the same test shown in Figure 3.23a after calibration and capacitive compensation, while the bath temperature data is that shown in Figure 3.26a. The applied heating power density is the heater voltage shown in Figure 3.14a, after median and Butterworth (low–pass) filtering, then converted from measured voltage to applied heating power density through Equation (3.2) on page 63. Recall that Equation (3.2) does not account for the small heat loss to the back of the sample, which tends to be on the order of 2 to 3%.

Note that the temperature curves show *sensor* temperatures, not heater surface temperatures. The transient heater surface temperatures must be modelled (as described in Chapter 5). Results of such modelling are shown in Paper [1] for open bath step heating.

One clear feature of the plot is that `U-2` behaves erratically, compared to the other seven sensors. For measurements where all sensor temperatures stay below about 3.5 to 4 K, `U-2` behaves in line with the other seven on the longer time–scales, rather than displaying the bulge seen around 2000 ms into the measurement. On the fast time–scale, though, the sensor still behaves as seen in the figure insert. These observations lead to using Bottom Plate 2 (the downwards facing plate) for closed channel measurements, as mentioned briefly in Section 3.3.2 on page 83. The reason for this bulging behaviour is unclear. However, from a previous design attempt of the experiment, similar erratic behaviour was seen, and after extensive 3D x–ray tomography it was concluded that the old design suffered from connected voids and channels that allowed helium from the bath to be in some level of contact with the sensors. For analysis of results presented herein, `U-2` is considered broken, and its measurements will be disregarded (also in the region where the long time–scale data does not display the bulge).

The oscillatory behaviour of P_heater was discussed in relation to Figure 3.14a, and stems from the power supply not being able to deliver a clean step in current.

Due to the considerable amount of heat transferred into the He II bath, its temperature rises slightly over the course of the measurement, from 1.899 K at t_0 to 1.916 K at t_end.

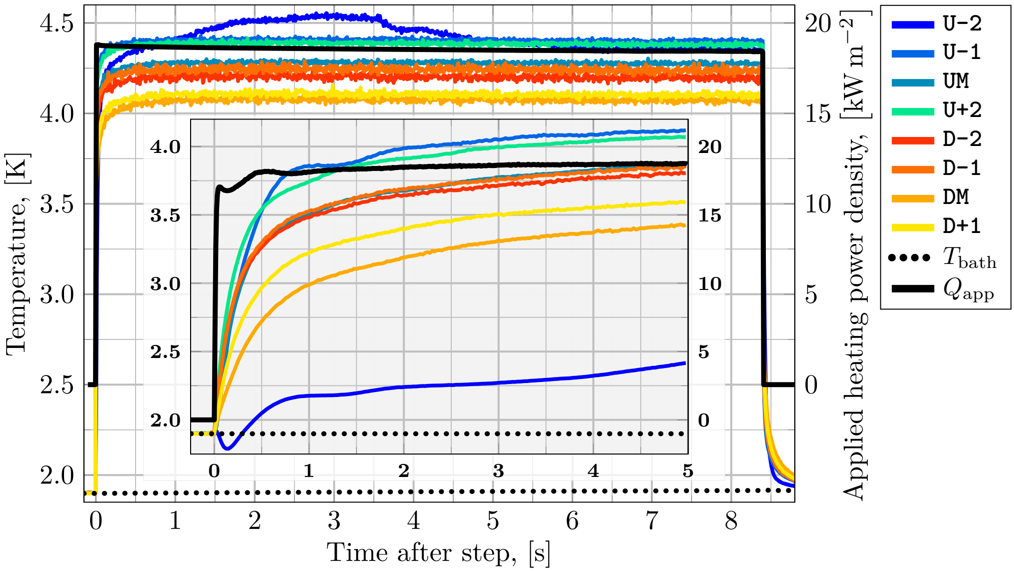

Figure 4.14: Temperature measurement after calibration of voltage signals from Figure 3.23a, with capacitive compensation. Also included is the bath temperature from Figure 3.26a, and the heater voltage from Figure 3.14a, after smoothing, converted to applied heating power density according to Equation (3.2). For clarity, only Heater Strip 1 is shown, since the two curves have the same shape, with only a small difference in amplitude. The insert highlights the first 5 ms of the transient. Note that the insert shows time in units of milliseconds.

4.5.3 Closed Channel Step Heating

Figure 4.15 shows the complete measurement during a step in applied heating power density in the closed channel configuration. The sensor temperature data is that shown in Figure 3.23b, after calibration and capacitive compensation, while the bath temperature data is that shown in Figure 3.26b. The applied heating power density is the heater voltage shown in Figure 3.14b, after median and low–pass filtering, then converted from voltage to applied heating power density through Equation (3.2).

A clear difference between this closed channel step response and the open bath step response, looking at the long time–scale behaviour, is that in the closed channel, the steady state takes much longer to establish itself. Looking at the insert, however, it is clear that the initial rise has similar characteristics to the open bath step. This is due to the long time–scale step response in the closed channel is ultimately dominated by heat transfer out of the confined helium across one or more layers of solids, such as PEEK or Eccobond®. There is also the weak cooling through the pin–holes.

4.5.4 Fast–Pulse Heating

Figure 4.16 shows the complete measurement during a fast pulse in applied heating power density in the closed channel configuration. The sensor temperature data is that shown in Figure 3.24a, after calibration and capacitive compensation; the bath temperature data was not previously shown as it remains constant during the entire

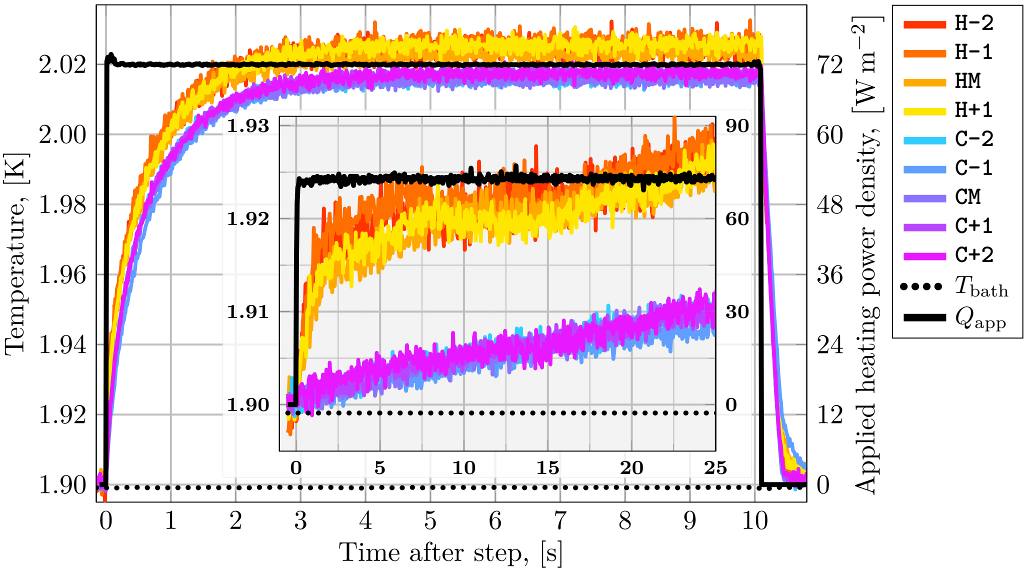

Figure 4.15: Temperature measurement after calibration of voltage signals from Figure 3.23b, with capacitive compensation. Also included is the bath temperature from Figure 3.26b, and the heater voltage from Figure 3.14b, after smoothing, converted to applied heating power density according to Equation (3.2). The insert highlights the first 25 ms of the transient. Note that the insert shows time in units of milliseconds.

measurement, but the data is collected in the same file as the sensor voltages. The applied heating power density is the heater voltage shown in Figure 3.15a, after filtering, then converted from voltage to applied heating power density through Equation (3.2). The filtering for fast–pulse heater voltages is a little different than the one for steps; the base is a median filter with a narrow window, but around the voltage peak, a high–cutoff Butterworth filter is used to smooth the signal.

The applied heating is over within 1 ms, while within 5 ms the heater and helium temperatures have equalised, and then follows 100 ms of slow heat transfer through the various cooling paths, eventually bringing the channel back to its initial temperature.

The peak applied heating power density for fast pulses are comparable to the open bath steps, though, of course, the fast pulses deliver much less energy in total to the system. The highest peak fast pulse heating power tested is about 120 $\mathrm{kW\,m^{-2}}$.

4.5.5 Slow–Pulse Heating

Figure 4.17 shows the complete measurement during a fast pulse in applied heating power density in the closed channel configuration. The sensor temperature data is that shown in Figure 3.24b, after calibration and capacitive compensation; the bath temperature data was not previously shown as it remains constant during the entire measurement. The applied heating power density is the heater voltage shown in Figure 3.15b, after smoothing, then converted from voltage to applied heating power density through Equation (3.2). Smoothing of slow–pulse heater voltages does not rely on filtering, but on fitting. As was seen in Figure 3.15b, a least–squares fit of the RLC

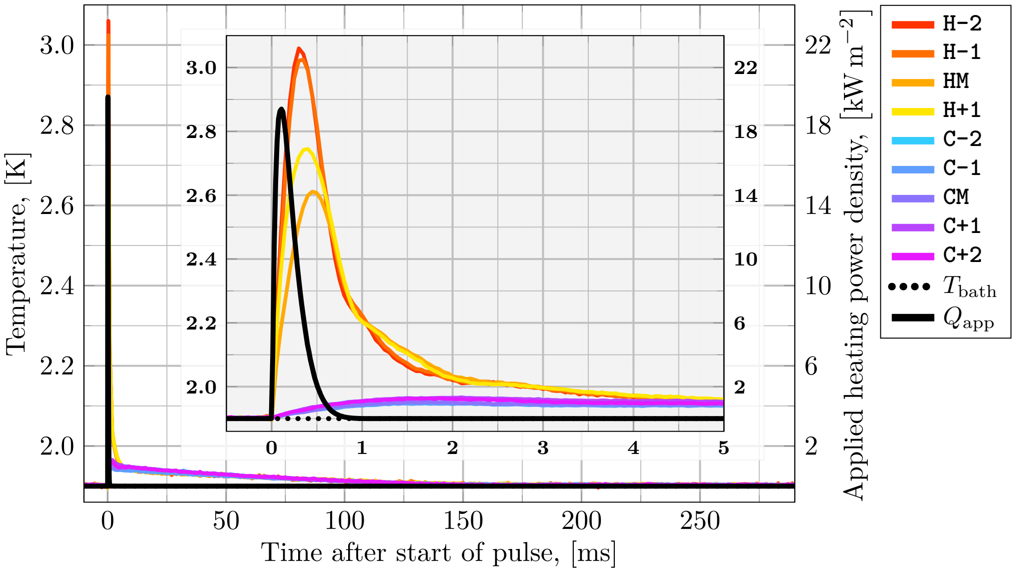

Figure 4.16: Temperature measurement after calibration of voltage signals from Figure 3.24a, with capacitive compensation. Also included heater voltage from Figure 3.15a, after smoothing, converted to applied heating power density according to Equation (3.2). The insert highlights the first 5 ms of the transient.

model in Appendix A works well to capture the temperature evolution of the voltage signal.

The first, obvious feature is that `C-1` appears to lag the other sensors. The behaviour looks as if the sensor somehow has a much higher heat capacity than the others. In fact, from an earlier design of this same experiment it was found by x–ray tomography that the region right around the sensors in the old setup had voids that were in contact with the helium bath. This made the local effective heat capacity of the sensors much higher, because they were exposed to small helium reservoirs that slowed their temperature rise. The transient results from the old setup look qualitatively similar to the curves seen for `C-1`, and it is concluded that the sensor is exposed to a parasitic reservoir of helium despite the improved design and mounting technique as compared with the old setup. For this reason, the sensor will be disregarded from the analysis presented in Paper [2].

Looking at the peak temperatures, they are quite similar to the closed channel step in Figure 4.15, and the transient up to the peak share qualitative features with the step heating as well, though the initial rise during a step in applied power is an order of magnitude faster. The heater temperatures during the slow pulse rise to a point after about 10 ms where the slope slackens markedly, while the helium heats up more evenly. For the step, there was an equilibrium warming state for the applied 130 $\mathrm{W\,m^{-2}}$ heating power density where helium and heater remains at a relatively fixed temperature difference. For the slow pulse, where the heating power density is never steady, there is no such fixed temperature difference state.

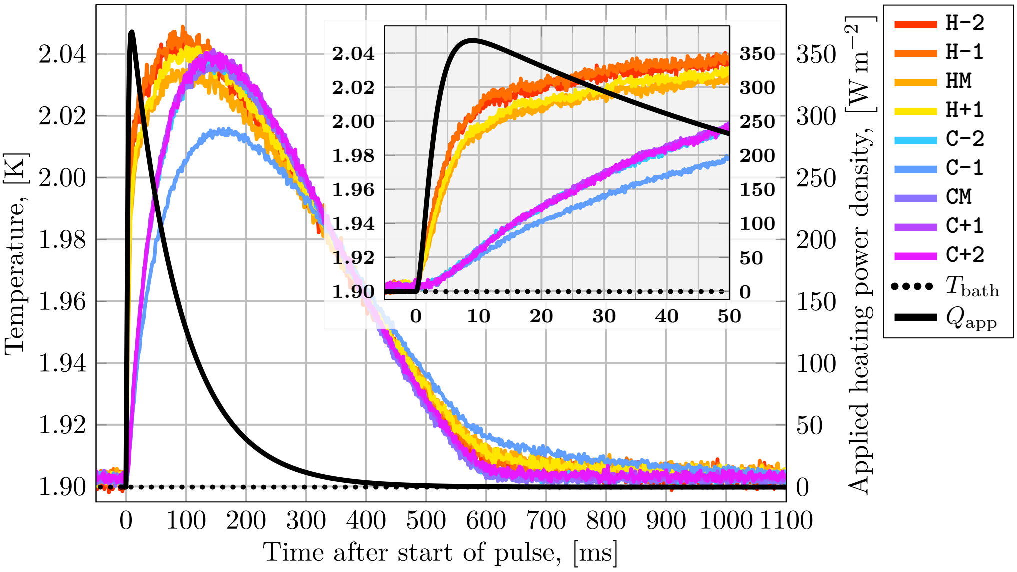

Figure 4.17: Temperature measurement after calibration of voltage signals from Figure 3.24b, with capacitive compensation. Also included heater voltage from Figure 3.15b, after smoothing, converted to applied heating power density according to Equation (3.2). The insert highlights the first 50 ms of the transient.

Chapter 5

Numerical Modelling

Chapter content:

Numerical modelling is an integral part of the interpretation of measurements, and this chapter lays out the approach to steady state and time–dependent simulations of heat transfer to and in helium. The chapter is detailed, explaining all steps taken to obtain simulation results, including the numerical implementation itself. This way, the barrier someone continuing this work needs to overcome is as low as possible.

The chapter is divided into two main parts; Section 1 detailing heat transfer in the heater side of the setup, and Section 2 pertaining to heat transfer within the helium channel.

5.1 Material Stack with Heater Strip

The one–dimensional heat equation, taking account of temperature dependent material properties, is,

$$C_{\mathrm{p}}(x,T)\frac{\partial T}{\partial t} = \frac{\partial}{\partial x}\left\{k(x,T)\frac{\partial T}{\partial x}\right\} + P(x,t), \tag{5.1}$$

where,

$T(x,t)$:	Temperature at location x and time t	[K]
$C_{\mathrm{p}}(x,T)$:	Volumetric heat capacity	[$\mathrm{J\,m^{-3}\,K^{-1}}$]
$k(x,T)$:	Thermal conductivity	[$\mathrm{W\,m^{-1}\,K^{-1}}$]
$P(x,t)$:	Heat generation at location x and time t	[$\mathrm{W\,m^{-3}}$]

The temperature dependent material parameters are discussed in Section 3.4 on page 95.

Figure 5.1 schematically represents the chain of materials making up the thermal path between the helium cooled surface of the stainless steel heater, down through the steel itself, the varnish holding the Cernox® sensor in place, the sapphire substrate making up the brunt of the sensor, the silver filled epoxy used to attach the copper sensor leads, and, finally, the sensor leads themselves, with the Eccobond® sheath. The standard thicknesses used in simulations are indicated in the figure.

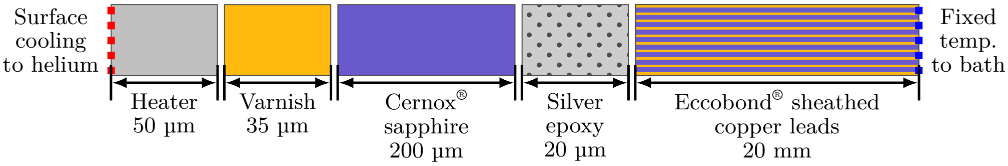

Figure 5.1: Schematic representation of the chain of materials (and their default thickness in simulation) going from the helium cooled surface of the heater strip on the left, through 50 µm of stainless steel, 35 µm of GE Varnish, 200 µm of sapphire, 20 µm of silver filled epoxy, and 20 mm of Eccobond® sheathed copper.

The simulated domain, represented by a chain of nodes, is shown in Figure 5.2. The first N_H nodes are those representing the stainless steel heater strip. The following N_V nodes are those of the GE Varnish. The nodes after these (indicated by dots in the figure) are N_S nodes for the Sapphire sensor substrate, N_E nodes for the silver filled Epoxy, and finally, N_L nodes for the sensor leads.

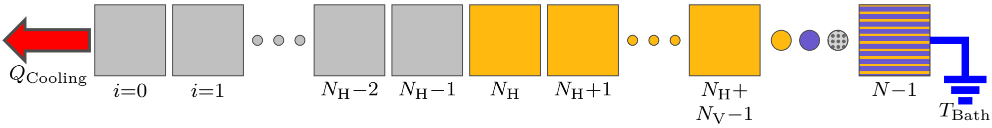

Figure 5.2: Schematic representation of the chain of nodes making up the simulated domain from the helium cooled top surface of the heater strip on the left side, to the backside of the sample on the right side. The red arrow on the left side indicates the action of a Neumann boundary condition describing the helium surface cooling heat flux. The blue grounding symbol on the right side indicates the action of a Dirichlet boundary condition representing the assumption that the last node of the simulated domain is kept at the temperature of the external helium bath. N_H is the number of nodes in the Heater part of the domain, N_V is the number of nodes in the Varnish part of the domain, and N is the total number of nodes in the domain.

Boundary Conditions: The two boundary conditions for the heat equation (Equation (5.1)) are;

1. The Dirichlet boundary at the right end of the simulated domain, being the far end of the sensor leads, with temperature fixed to the bath temperature, indicated with dark blue in figures 5.1 and 5.2;
2. The Neumann boundary at the left end of the simulated domain, being the helium cooled surface of the stainless steel heater strip, with the cooling flux from stainless steel to helium, indicated with red in figures 5.1 and 5.2.

The two conditions are formulated mathematically as,

$$T(x=L,t) = T_\mathrm{Bath}(t), \tag{5.2}$$

$$\left.\frac{\partial T}{\partial x}\right|_{x=0} = \frac{Q_\mathrm{Cooling}(t)}{k_\mathrm{steel}(0,T(0,t))}, \tag{5.3}$$

where L is the total length of the material stack, $T_{\mathrm{Bath}}(t)$ is the time–dependent temperature of the He II bath, $Q_{\mathrm{Cooling}}(t)$ is a function giving the heat flux from the stainless steel heater surface to the helium touching it, and $k_{\mathrm{steel}}(0, T(0,t))$ is the thermal conductivity of steel at the temperature of the heater surface.

The Q_{Cooling} function is usually taken as the Kapitza model from Equation (2.28) on page 21, which depends on the temperature at the surface of the steel and the temperature of the helium far from the heater. In cases where heat transfer regime changes occur, such as the onset of film boiling, Q_{Cooling} changes accordingly, but the boundary condition implementation is otherwise the same.

Discretisation: Discretised versions of equations (5.1), (5.2), and (5.3) are necessary. The domain is one–dimensional in both time and space, with grid points;

$$x_i = i \cdot \Delta x, \text{for } i \in [0, 1, 2, \ \dots \ , N-1] \tag{5.4}$$

$$t_n = n \cdot \Delta t, \text{for } n \in [0, 1, 2, \ \dots] \tag{5.5}$$

On this grid we have,

$$T(x_i, t_n) = T_i^n. \tag{5.6}$$

To account for there being several material interfaces in the simulation, and the material parameters being temperature dependent, a method of looking at the Fourier heat transfer law as if it is applied to the midpoint between two spatial nodes is used. The approach is to take the thermal conductivity at node i as the average of the thermal conductivities of node i and that of the forward or backward node:

$$\begin{aligned} \kappa_{i+1/2} &= \frac{1}{2}(k_{i+1} + k_i) \\ \kappa_{i-1/2} &= \frac{1}{2}(k_{i-1} + k_i) \end{aligned} \tag{5.7}$$

Note that the material properties do not depend on time, only on the time–dependent temperature as it varies in space along the material stack.

Central differences are used to discretise the partial derivatives on the right hand side of the heat equation, leading to a Crank–Nicolson scheme;

$$\begin{aligned} \frac{\partial}{\partial x}\left\{k\frac{\partial T}{\partial x}\right\}\bigg|_{x_i,t_n} &= \frac{\partial}{\partial x}\left\{k(x_i, T_i^n)\frac{\partial T(x_i,t_n)}{\partial x}\right\} \\ &\simeq \frac{1}{2\Delta x^2}\left[\kappa_{i+1/2}\left(T_{i+1}^{n+1} - T_i^{n+1}\right) - \kappa_{i-1/2}\left(T_i^{n+1} - T_{i-1}^{n+1}\right)\right] \\ &+ \frac{1}{2\Delta x^2}\left[\kappa_{i+1/2}\left(T_{i+1}^{n} - T_i^{n}\right) - \kappa_{i-1/2}\left(T_i^{n} - T_{i-1}^{n}\right)\right] \end{aligned} \tag{5.8}$$

Note that material parameters are taken only at time step n, not $n+1$.

For the left hand side of the heat equation, a forward difference in time is used;

$$\begin{aligned} C_{\mathrm{p}}\frac{\partial T}{\partial t}\bigg|_{x_i,t_n} &= C_{\mathrm{p}}(x_i, T(x_i,t_n))\frac{\partial T(x_i,t_n)}{\partial t} \\ &\simeq C_i\frac{T_i^{n+1} - T_i^n}{\Delta t} \end{aligned} \tag{5.9}$$

The source term on the right hand side will be the average power dissipation of the current and next time steps, based on the voltage across the entire heater strip;

$$P(x_i, t_n) = \frac{(V_i^n)^2 + (V_i^{n+1})^2}{2R_\mathrm{H} v_\mathrm{H}}, \tag{5.10}$$

where R_H is the electrical resistance of the heater strip, and v_H is the volume of the heater strip.

The power input is assumed homogeneous inside the entire stainless steel domain, meaning that all V_i within the steel are identical for a given time step, while all those outside the steel are zero.

Equation (5.9) equals the sum of equations (5.8) and (5.10), and after collecting the forwards–in–time and current–in–time terms on either side of the resulting discretised equation gives the numerical scheme;

$$\begin{aligned} &- \delta\frac{\kappa_{i-1/2}}{C_i}T_{i-1}^{n+1} + \left[1 + \delta\frac{1}{C_i}\left(\kappa_{i-1/2} + \kappa_{i+1/2}\right)\right]T_i^{n+1} - \delta\frac{\kappa_{i+1/2}}{C_i}T_{i+1}^{n+1} - \frac{\Delta t}{C_i}\frac{(V_i^{n+1})^2}{2R_\mathrm{s}v_\mathrm{s}} \\ = \quad & \delta\frac{\kappa_{i-1/2}}{C_i}T_{i-1}^{n} + \left[1 - \delta\frac{1}{C_i}\left(\kappa_{i-1/2} + \kappa_{i+1/2}\right)\right]T_i^{n} + \delta\frac{\kappa_{i+1/2}}{C_i}T_{i+1}^{n} + \frac{\Delta t}{C_i}\frac{(V_i^{n})^2}{2R_\mathrm{s}v_\mathrm{s}}, \end{aligned} \tag{5.11}$$

where $\delta = \Delta t / 2\Delta x^2$ and $C_i = C_\mathrm{p}(x_i, T_i^n)$

By defining a temperature vector of the entire material stack at time–step n,

$$\mathbf{T}^n = \left[T_0^n,\, T_1^n,\, \ldots\; T_{N-1}^n\right]^\intercal \tag{5.12}$$

Equation (5.11) is written as a matrix equation;

$$\begin{aligned} \boldsymbol{\mathcal{L}}\mathbf{T}^{n+1} &= \boldsymbol{\mathcal{R}}\mathbf{T}^n + \mathbf{P}^n \\ \Rightarrow \quad \mathbf{T}^{n+1} &= \boldsymbol{\mathcal{L}}^{-1}\left[\boldsymbol{\mathcal{R}}\mathbf{T}^n + \mathbf{P}^n\right] \end{aligned} \tag{5.13}$$

where,

$$\boldsymbol{\mathcal{L}} = \begin{bmatrix} \mathcal{L}_{0,0} & \mathcal{L}_{0,1} & 0 & & & \cdots & & 0 \\ -X_1^- & 1{+}D_1 & -X_1^+ & & & & & \\ 0 & -X_2^- & 1{+}D_2 & -X_2^+ & & & & \\ & & \ddots & \ddots & \ddots & & & \vdots \\ \vdots & & & -X_i^- & 1{+}D_i & -X_i^+ & & \\ & & & & \ddots & \ddots & \ddots & 0 \\ & & & & & -X_{N-2}^- & 1{+}D_{N-2} & -X_{N-2}^+ \\ 0 & & \cdots & & & 0 & \mathcal{L}_{N-1,N-2} & \mathcal{L}_{N-1,N-1} \end{bmatrix}, \tag{5.14}$$

$$\boldsymbol{\mathcal{R}} = \begin{bmatrix} \mathcal{R}_{0,0} & \mathcal{R}_{0,1} & 0 & & \cdots & 0 \\ X_1^- & 1\text{–}D_1 & X_1^+ & & & \\ 0 & X_2^- & 1\text{–}D_2 & X_2^+ & & \\ & \ddots & \ddots & \ddots & & \vdots \\ \vdots & & X_i^- & 1\text{–}D_i & X_i^+ & \\ & & \ddots & \ddots & \ddots & 0 \\ & & & X_{N-2}^- & 1\text{–}D_{N-2} & X_{N-2}^+ \\ 0 & & \cdots & 0 & \mathcal{R}_{N-1,N-2} & \mathcal{R}_{N-1,N-1} \end{bmatrix}, \tag{5.15}$$

and

$$\mathbf{P}^n = \left[\frac{1}{2}\left(Q_0^n + Q_0^{n+1}\right), \frac{1}{2}\left(Q_1^n + Q_1^{n+1}\right), \ldots, \frac{1}{2}\left(Q_{N-1}^n + Q_{N-1}^{n+1}\right)\right]^{\mathsf{T}} \tag{5.16}$$

where,

$$X_i^+ = \delta\frac{\kappa_{i+1/2}}{C_i} \tag{5.17}$$

$$X_i^- = \delta\frac{\kappa_{i-1/2}}{C_i} \tag{5.18}$$

$$D_i = \delta\frac{1}{C_i}(\kappa_{i-1/2} + \kappa_{i+1/2}) \tag{5.19}$$

$$Q_i^n = \frac{\Delta t(V_i^n)^2}{C_i R_{\mathrm{H}} v_{\mathrm{H}}} \tag{5.20}$$

The last step is to determine how the boundary conditions influence $\boldsymbol{\mathcal{L}}$ and $\boldsymbol{\mathcal{R}}$.

The clamped temperature at the right end of the stack, ensuring $T_{N-1}^{n+1} = T_{N-1}^n = T_{\mathrm{Bath}}(t_n)$, is straightforward;

$$\begin{aligned} \mathcal{L}_{N-1,N-2} &= \mathcal{R}_{N-1,N-2} = 0, \\ \mathcal{L}_{N-1,N-1} &= \mathcal{R}_{N-1,N-1} = 1. \end{aligned} \tag{5.21}$$

The heat flux condition on the left end of the material stack, used to account for cooling of the stainless steel heater strip, needs the "ghost point" T_{-1}^n, outside the simulated domain. It is introduced to facilitate the use of a central difference of second order accuracy to maintain the second order accuracy of the rest of the Crank–Nicolson scheme;

$$\left.\frac{\partial T(x,t)}{\partial x}\right|_{x=0} \simeq \frac{T_1^n - T_{-1}^n}{2\Delta x} = \frac{Q_{\mathrm{Cooling}}}{k_0} \tag{5.22}$$

where k_0 is the thermal conductivity of stainless steel at the temperature of the boundary grid point. For convenience, in the following, Q_{Cooling} is taken to be the Kapitza model; $Q_{\mathrm{Kap}} = a_{\mathrm{Kap}}\left[(T_0^n)^{n_{\mathrm{Kap}}} - (T_{\mathrm{Bath}}^n)^{n_{\mathrm{Kap}}}\right]$.

So, at the boundary point, where $i = 0$, using this ghost point;

$$T_{-1}^n = T_1^n - \frac{2\Delta x Q_{\mathrm{Kap}}}{k_0}, \tag{5.23}$$

and the numerical scheme (Equation (5.11)) becomes;

$$\begin{aligned}
&-\delta\frac{\kappa_{0-1/2}}{C_0}T_{-1}^{n+1}+\left[1+\delta\frac{1}{C_0}\left(\kappa_{0-1/2}+\kappa_{0+1/2}\right)\right]T_0^{n+1}-\delta\frac{\kappa_{0+1/2}}{C_0}T_1^{n+1}\\
=\quad&\delta\frac{\kappa_{0-1/2}}{C_0}T_{-1}^{n}+\left[1-\delta\frac{1}{C_0}\left(\kappa_{0-1/2}+\kappa_{0+1/2}\right)\right]T_0^{n}+\delta\frac{\kappa_{0+1/2}}{C_i}T_1^{n}+\frac{1}{2}\left(Q_0^n+Q_0^{n+1}\right).
\end{aligned}\tag{5.24}$$

Using the temperature in the ghost point (Equation (5.23)) gives,

$$\begin{aligned}
&-\delta\frac{\kappa_{0-1/2}}{C_0}\left[T_1^{n+1}-\frac{2\Delta x Q_{\text{Kap}}}{k_0}\right]+\left[1+\delta\frac{1}{C_0}\left(\kappa_{0-1/2}+\kappa_{0+1/2}\right)\right]T_0^{n+1}-\delta\frac{\kappa_{0+1/2}}{C_0}T_1^{n+1}\\
=\quad&\delta\frac{\kappa_{0-1/2}}{C_0}\left[T_1^{n}-\frac{2\Delta x Q_{\text{Kap}}}{k_0}\right]+\left[1-\delta\frac{1}{C_0}\left(\kappa_{0-1/2}+\kappa_{0+1/2}\right)\right]T_0^{n}+\delta\frac{\kappa_{0+1/2}}{C_i}T_1^{n}\\
&+\frac{1}{2}\left(Q_0^n+Q_0^{n+1}\right)
\end{aligned}\tag{5.25}$$

leading to,

$$\begin{aligned}
&\left[1+\delta\frac{1}{C_0}\left(\kappa_{0-1/2}+\kappa_{0+1/2}\right)\right]T_0^{n+1}-\delta\frac{1}{C_0}\left(\kappa_{0-1/2}+\kappa_{0+1/2}\right)T_1^{n+1}\\
=&\left[1-\delta\frac{1}{C_0}\left(\kappa_{0-1/2}+\kappa_{0+1/2}\right)\right]T_0^{n}+\delta\frac{1}{C_0}\left(\kappa_{0-1/2}+\kappa_{0+1/2}\right)T_1^{n}\\
&+\frac{1}{2}\left(Q_0^n+Q_0^{n+1}\right)-2\frac{\delta}{C_0}\kappa_{0-1/2}\frac{2\Delta x}{k_0}Q_{\text{Kap}}.
\end{aligned}\tag{5.26}$$

The thermal conductivity $\kappa_{0-1/2}=\frac{1}{2}(k_0+k_{-1})$ is found by taking $k_{-1}=k_1$, as suggested by the Neumann boundary condition; $\kappa_{0-1/2}=\frac{1}{2}(k_0+k_1)$.

This gives;

$$\mathcal{L}_{0,0}=1+\delta\frac{1}{C_0}\left(\kappa_{0-1/2}+\kappa_{0+1/2}\right)\tag{5.27}$$

$$\mathcal{L}_{0,1}=-\delta\frac{1}{C_0}\left(\kappa_{0-1/2}+\kappa_{0+1/2}\right)\tag{5.28}$$

$$\mathcal{R}_{0,0}=1-\delta\frac{1}{C_0}\left(\kappa_{0-1/2}+\kappa_{0+1/2}\right)\tag{5.29}$$

$$\mathcal{R}_{0,1}=\delta\frac{1}{C_0}\left(\kappa_{0-1/2}+\kappa_{0+1/2}\right)\tag{5.30}$$

$$P_0^n=\frac{1}{2}\left(Q_0^n+Q_0^{n+1}\right)-2\frac{\delta}{C_0}\kappa_{0-1/2}\frac{2\Delta x}{k_0}Q_{\text{Kap}}.\tag{5.31}$$

Testing the Formulation

In order to keep simulation times reasonable, adaptive time stepping is implemented. The method is straightforward; simulations are started with some small Δt, usually 0.1 µs. Then, if the change in heater surface temperature from the previous time step is smaller than 50 µK, Δt is *increased* by a factor 1.025. If the change in heater surface temperature from the previous time step is larger than 250 µK, Δt is *reduced* by a factor 0.95. Any time–steps that saw a reduction in Δt are discarded. The spatial discretisation length Δx is usually taken as 1 µm. During a transient simulation Δt stabilises around between 0.5 and 1 µs during parts of the simulation where strong heating is applied, then grows to between 2 and 5 µs for weaker heating. Note that the adaptive time–stepping is only active starting at 50 µs into the simulation, since the applied heating power density during certain tests takes some time to build up (in particular the slow pulses). Until then, the initial Δt is used.

Figure 5.3 shows the energy balance during a simulation where the source heating is a the same step in applied heating power density as that seen in Figure 4.14 on page 137. The applied heating power density is defined in Equation (3.2) on page 63. The various curves are the cumulative sums across time of the energy flow associated with each individual time step, for a particular region in or aspect of the simulation;

Source heat	The volumetric heating power in the heater strip multiplied by Δt and the total heater strip volume.
Surface cooling	The heat flux calculated by the Kapitza expression, multiplied by Δt and the surface area of the heater strip.
Stack to bath	The heat flux going from the second–to–last to the last node on the right side of the simulated domain, multiplied by Δt and the cross sectional area of the sensor leads. This represents the energy that leaks into the bath.
In stack	Energy contained within all the materials in the stack, according to the heat capacity and volume of each part.
Stack, sum	The sum of Surface cooling, Stack to bath, and In stack.

Stack, sum should, of course, equal the input energy, dotted grey curve should be on top of the blue. The trade–off between simulation time and accuracy means some numerical error is expected. After 10 ms, the energy accounted for within the simulation domain is about 2.4% less than the energy input.

A similar simulation, but with Δt fixed at 0.02 µs for the entire simulation, and $\Delta x = 0.2$ µm gives an energy discrepancy of just 0.45%. Note, this is not a statement about whether or not the simulations accurately reproduce measured results; it just means the numerical formulation, as it is implemented, has an acceptable numerical consistency when looking at the estimated energy balance. The error is tied to the spatial discretisation, not the time–stepping; running with $\Delta x = 0.2$ µm but allowing adaptive time–stepping, with Δt stabilising around 0.2 µs, gives an energy discrepancy around 0.46%.

Finally, a simulation just like that in Figure 5.3, meaning Δt starting at 0.1 µs, $\Delta x = 1$ µm, and adaptive time–stepping, but with no Kapitza cooling applied at the heater surface, sees an energy discrepancy of 0.8% after 10 ms, which means that the main contribution to numerical error comes from the cooling boundary condition, and not from the approach of using thermal conductivity between grid–points (see Equation (5.7)).

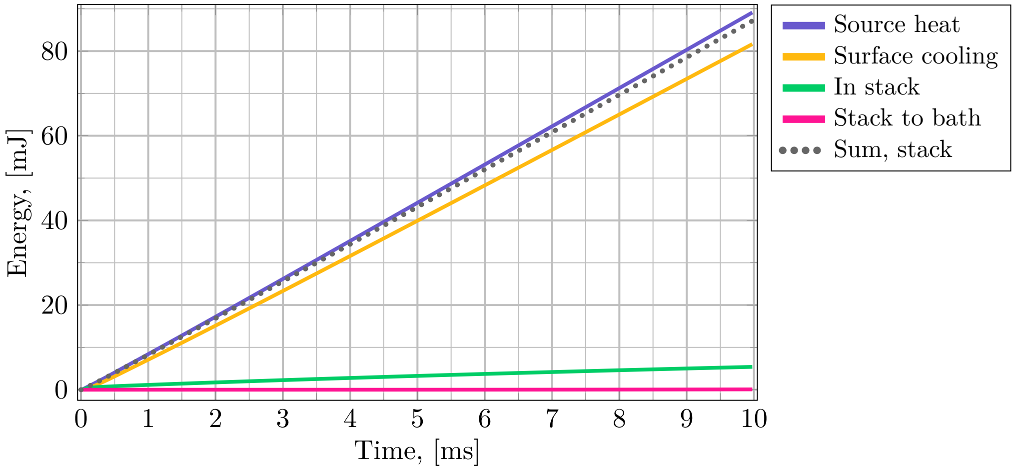

Figure 5.3: Energy balance during a simulation of the material stack submerged in an open helium bath at 1.9 K, experiencing a step in applied heating power density up to around 20 kW m^{-2} (using the same curve as seen in Figure 4.14 on page 137). The simulation was run with $\Delta x = 1$ µm, and adaptive time steps starting at 0.1 µs. All material lengths are standard: $L_{\text{heater}} = 50$ µm, $L_{\text{varnish}} = 35$ µm, $L_{\text{sapphire}} = 200$ µm, $L_{\text{EPO–TEK}} = 20$ µm, and $L_{\text{leads}} = 20$ mm.

5.1.1 Steady State

For steps in applied heating power density, after some time, a steady state is reached, where the heat transfer from the heater surface to the helium bath and the temperature profile within the material stack no longer change.

Starting with Equation (5.1), and using that at steady state $\partial T/\partial t = 0$;

$$\frac{\partial}{\partial x}\left\{k(x,T)\frac{\partial T}{\partial x}\right\} = -P(x,t). \tag{5.32}$$

The numerical scheme, simplified now that there is no time dependence, becomes;

$$\frac{1}{\Delta x^2}\left[\kappa_{i+1/2}\left(T_{i+1}-T_i\right)-\kappa_{i-1/2}\left(T_i-T_{i-1}\right)\right] = -P_i. \tag{5.33}$$

At first glance, it may seem that the boundary conditions should be the same as those used for the transient solution; at node $i = 0$ there is a prescribed heat flux from the Kapitza expression, while at node $i = N-1$ the temperature is kept at the bulk bath temperature. This, however, does not work in steady state. There will, necessarily, be some small heat flux flowing through the back of the sample to the bulk bath. The steady state solution represents the transient heat equation after infinite time, so any imbalance between the sum of Kapitza heat flux at the heater surface and energy drained to the bath from the back and the energy supplied by the power source will mean an infinite amount of energy is either drained or stored in the system.

This leads to the steady state surface temperature reconstruction method discussed in Section 4.4.1 on page 122; fix the temperature at both ends of the simulation domain and, using the Levenberg–Marquardt algorithm implemented in the Python package `lmfit`, make successive guesses at the heater surface temperature, with the criterion being that the simulated temperature at the location of the sensor must be equal to the steady state measured temperature of the sensor.

The matrix equation to solve is straightforward;

$$\begin{aligned} \boldsymbol{\mathcal{L}}\mathbf{T} &= -\Delta x^2 \mathbf{P} \\ \Rightarrow \quad \mathbf{T} &= -\Delta x^2 \boldsymbol{\mathcal{L}}^{-1}\mathbf{P}, \end{aligned} \tag{5.34}$$

where $\mathbf{T} = [T_0, T_1, \ \dots \ T_{N-1}]^\intercal$ as for the time–dependent formulation,

$$\boldsymbol{\mathcal{L}} = \begin{bmatrix} 1 & 0 & 0 & & & \cdots & & 0 \\ X_1^- & D_1 & X_1^+ & & & & & \\ 0 & X_2^- & D_2 & X_2^+ & & & & \\ & & \ddots & \ddots & \ddots & & & \vdots \\ \vdots & & & X_i^- & D_i & X_i^+ & & \\ & & & & \ddots & \ddots & \ddots & 0 \\ & & & & & X_{N-2}^- & D_{N-2} & X_{N-2}^+ \\ 0 & & \cdots & & & 0 & 0 & 1 \end{bmatrix}, \tag{5.35}$$

and,

$$\mathbf{P} = [Q_0, Q_1, \ \dots, \ Q_{N-1}]^\intercal, \tag{5.36}$$

with,

$$X_i^- = \kappa_{i-1/2} \tag{5.37}$$

$$X_i^+ = \kappa_{i+1/2} \tag{5.38}$$

$$D_i = -(\kappa_{i-1/2} + \kappa_{i+1/2}) \tag{5.39}$$

$$Q_i = \frac{(V_i)^2}{R_\mathrm{H} v_\mathrm{H}}. \tag{5.40}$$

The transient simulations are run with Kapitza parameters that come from an average of the fits to steady state open bath data (See Paper [1]). This means that a particular transient simulation will not exactly converge to a particular steady state temperature distribution, since it isn't possible to get Kapitza fit parameters for only a single measurement point. However, some comparisons can still be made.

Figure 5.4 shows in grey the steady state profiles found using the heater surface temperature reconstruction method described in Section 4.4.1 on page 122, which uses the steady state solution described above. The coloured curves are the temperature distributions at a few time steps during a transient simulation of the same measurement (seen in Figure 4.14 on page 137). It shows that after just 100 ms (green curve), in the region $0 < x < 295$ µm, which covers the material stack up to the sensitive part of the Cernox® sensor, the transient simulation has reached a temperature distribution that is within 15 mK of the solution after 2 s (purple curve). The copper leads, with the Eccobond® sheath, need more time to reach a steady state, being about 35 mK away after 100 ms. It is still clear, though, that the transient simulation approaches a steady state that matches the solutions that come from solving the steady state heat equation directly.

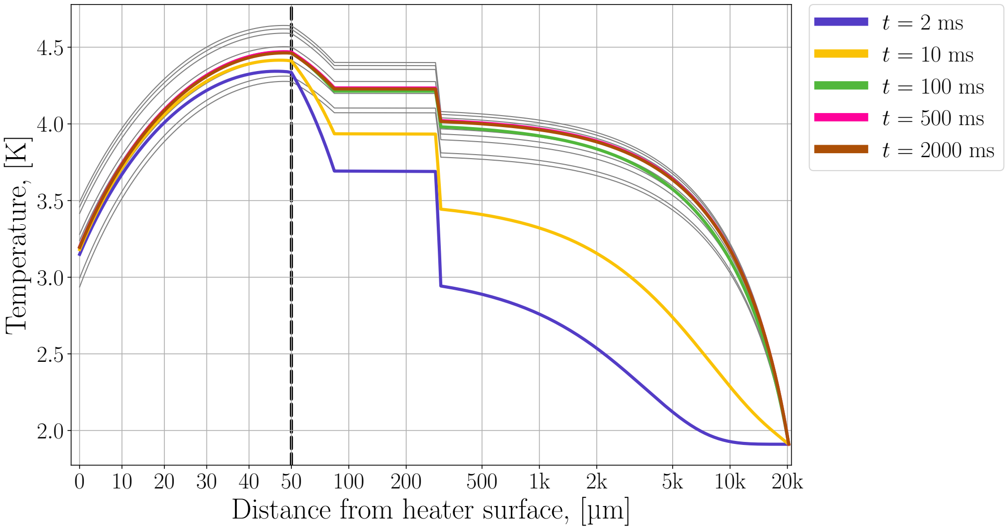

Figure 5.4: Comparison between the simulated steady state temperature distribution from the same measurement shown in Figure 4.14 on page 137 and the temperature distribution at several time steps during a transient simulation of the measurement. The x–axis is linear up to 50 µm, and logarithmic beyond. The steady state temperature distributions are shown in grey, with one curve for each sensor.

5.2 Helium in the Closed Channel Configuration

Modelling heat transfer in the helium is based on the modified heat equation shown in Equation (2.60) on page 44, applied along a one–dimensional domain;

$$C(T)\frac{\partial T}{\partial t} = \frac{\partial}{\partial x}\left\{\left[-f^{-1}(T)\frac{1}{\left|\frac{\partial}{\partial x}T\right|^{m-1}}\right]^{1/m}\frac{\partial}{\partial x}T\right\}, \tag{5.41}$$

where C is the volumetric heat capacity of helium at constant volume (since the channel has a fixed geometry during tests), f^{-1} is the turbulent helium thermal conductivity function (see Section 2.4.5 on page 35), and $m = 3.4$.

With the exception of the effective thermal conductivity term in front of the inner temperature gradient being more complicated than that in the regular heat equation (Equation (5.1) on page 141), solving Equation (5.41) numerically is approached in essentially the same way.

There are two subdomains considered for the helium after the channel is closed; the main channel, plus the helium in the pin–holes at either end. The two are schematically represented in Figure 5.5.

Figure 5.6 shows the string of nodes that represent the channel helium and pin–hole helium domains, with the simulated dimension parallel to the channel length. The interface heat fluxes, $Q_{\text{toPinHole}}$ and $Q_{\text{alongPinHole}}$, between the two subdomains will be described in the following. P_{Kapitza} represents the source/sink term that normally

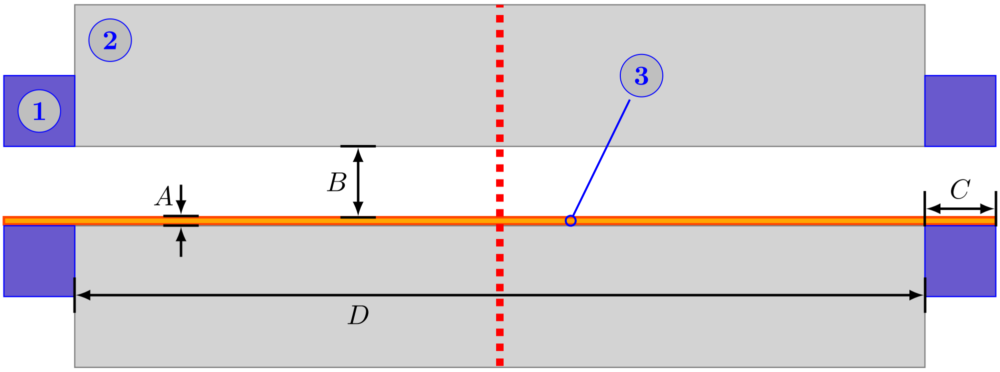

Figure 5.5: Side view of the length of the channel. Region (1): Eccobond through which the pin holes to the bath are made; (2): PEEK plates; (3): Heater strip.
Length A: Thickness of heater strip = 50 µm; B: Channel depth = 120 µm; C: Pin hole length = 4 mm; and D: Channel length = 150 mm. The red dotted line is the centre line of the channel around which the left and right sides are symmetrical.

stems from the Kapitza heat flux across the heater–helium interface. For heat transfer where a regime change takes place, the function changes accordingly.

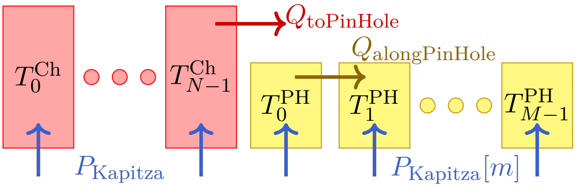

Figure 5.6: Diagram of channel and pin–hole nodes, and how they interface. There are N channel nodes, denoted by the "Ch" superscript, and M pin–hole nodes, denoted by the "PH" superscript. From the temperature distribution in the pin–hole we find $Q_{\mathrm{alongPinHole}}$, and use this with the cross section of the pin–hole to determine $Q_{\mathrm{toPinHole}}$. P_{Kapitza} denotes the volumetric heat flow into (or out of) the node from the heater strip. The index $[m]$ indicates that we use the pin–hole temperature at each node in the Kapitza expression.

5.2.1 Along the Closed Channel

The discretised version of Equation (5.41), including a volumetric heat source is;

$$
\begin{aligned}
C_i \frac{T_i^{n+1} - T_i^n}{\Delta t} = & \frac{1}{2\Delta x}\left[\mathcal{A}_i \frac{T_{i+1}^{n+1} - T_i^{n+1}}{\Delta x} - \mathcal{B}_i \frac{T_i^{n+1} - T_{i-1}^{n+1}}{\Delta x}\right] \\
& + \frac{1}{2\Delta x}\left[\mathcal{A}_i \frac{T_{i+1}^{n} - T_i^{n}}{\Delta x} - \mathcal{B}_i \frac{T_i^{n} - T_{i-1}^{n}}{\Delta x}\right] + P_i^n,
\end{aligned}
\tag{5.42}
$$

where C_i is the volumetric heat capacity at node i, T_i^n is the helium temperature at node i and time step n, Δx is the spatial step size along the length of the channel, P_i^n

is a volumetric heat source/sink in that same node (called P_{Kapitza} in Figure 5.6),

$$\mathcal{A}_i = \left(\frac{1}{f\left(\frac{1}{2}\left[T_i^n + T_{i+1}^n\right]\right)} \right)^{1/m} \left(\frac{\Delta x}{\left|T_{i+1}^n - T_i^n\right| + \epsilon} \right)^{(m-1)/m}, \tag{5.43}$$

and,

$$\mathcal{B}_i = \left(\frac{1}{f\left(\frac{1}{2}\left[T_i^n + T_{i-1}^n\right]\right)} \right)^{1/m} \left(\frac{\Delta x}{\left|T_i^n - T_{i-1}^n\right| + \epsilon} \right)^{(m-1)/m}, \tag{5.44}$$

where, as before, f^{-1} is the thermal conductivity function of He II, and ϵ is a small number, taken as $1 \cdot 10^{-8}$, used to stabilise the simulation in regions/at times where the thermal gradient is very small. Note that with respect to Figure 5.5, the simulated dimension of the helium channel is perpendicular to the simulated dimension of the material stack below it.

This leads to the following relationship between the previous and the next time step;

$$\begin{aligned} &-\alpha_i \mathcal{B}_i T_{i-1}^{n+1} + \left[1 + \alpha_i \left(\mathcal{A}_i + \mathcal{B}_i\right)\right] T_i^{n+1} - \alpha_i \mathcal{A}_i T_{i+1}^{n+1} \\ &= \alpha_i \mathcal{B}_i T_{i-1}^n + \left[1 - \alpha_i \left(\mathcal{A}_i + \mathcal{B}_i\right)\right] T_i^n + \alpha_i \mathcal{A}_i T_{i+1}^n + \gamma_i P_i^n \end{aligned} \tag{5.45}$$

where,

$$\begin{aligned} \alpha_i &= \frac{\Delta t}{2 \Delta x^2 C_i} \\ \gamma_i &= \frac{\Delta t}{C_i}. \end{aligned} \tag{5.46}$$

This can be formulated as a matrix equation, using $\mathbf{T} = [T_0,\ T_1,\ \dots\ T_{N-1}]^\intercal$, where the left hand side matrix corresponds to the $(n+1)$–terms in Equation (5.45), and the right hand side matrix corresponds to the n–terms;

$$\boldsymbol{\mathcal{L}} \mathbf{T}^{n+1} = \boldsymbol{\mathcal{R}} \mathbf{T}^n + \mathbf{P}^n \tag{5.47}$$

$$\Rightarrow \quad \mathbf{T}^{n+1} = \boldsymbol{\mathcal{L}}^{-1} \left[\boldsymbol{\mathcal{R}} \mathbf{T}^n + \mathbf{P}^n\right]. \tag{5.48}$$

The left and right hand side matrices are both tridiagonal matrices, structurally identical to those for the one–dimensional material stack (equations (5.14) and (5.15)).

The left–most node in the simulated channel helium domain corresponds to the middle of the channel (red dotted line in Figure 5.5), and the boundary condition here is zero flux, based on the assumption that the sample is symmetrical, and that therefore the middle of the channel must be the hottest point (if there is a gradient at all). This boundary is handled identically to how the Kapitza heat flux node was dealt with in the material stack simulation, just with zero heat flux at the boundary.

The right–most node in the simulated channel helium domain corresponds to the end of the channel (the right side end of Dimension D in Figure 5.5). This is considered the end of the channel since the pin hole means there is a discontinuous change in cross section here. From this node, there is a cooling flux (to be discussed in detail in Section 5.2.2) from the hot channel helium into the cooler pin–hole helium, and the numerical implementation is like that for the Kapitza cooled node in the material stack simulation using a ghost node outside the domain. With a ghost node $i_{\text{ghost}} = N$, such that the boundary condition can be expressed numerically as $T_N = T_{N-2} - 2\Delta x Q_{\text{toPinHole}}/k_{\text{eff}}$ where $k_{\text{eff}} = f^{-1}(T_{N-1})/Q^2_{\text{toPinHole}}$ [201, Eq. 5.19], the relationship between the previous and the next time step becomes;

$$\begin{aligned}&\left[1+\alpha_{N-1}\left(\mathcal{A}_{N-1}+\mathcal{B}_{N-1}\right)\right]T^{n+1}_{N-1} - \alpha_{N-1}\left[\mathcal{A}_{N-1}+\mathcal{B}_{N-1}\right]T^{n+1}_{N-2}\\ &= \left[1-\alpha_{N-1}\left(\mathcal{A}_{N-1}+\mathcal{B}_{N-1}\right)\right]T^{n}_{N-1} + \alpha_{N-1}\left[\mathcal{A}_{N-1}+\mathcal{B}_{N-1}\right]T^{n}_{N-2}\\ &+ 2\cdot 2\Delta x \alpha_{N-1} Q_{\text{toPinHole}}\frac{\mathcal{A}_{N-1}}{k_{\text{eff}}}.\end{aligned} \tag{5.49}$$

Finally, there is the volumetric heat input accounting for heat transfer into the helium from the heater strip. Since the simulated dimension runs along the length of the channel, there is no simulated dimension across which an interface between metal and helium can exist, so the heat flux from the heater strip must be converted to an equivalent volumetric heat source at each node in the simulation. This is simply,

$$P_{\text{in},i} = \gamma_i \frac{Q_{\text{Kapitza}}}{L_z}, \tag{5.50}$$

where L_z is the depth of the channel (120 µm).

5.2.2 Pin–Hole Helium

The pin–hole helium is simulated in the same way as the channel helium. The difference is that the cross section is smaller (only relevant for the boundary condition at the channel–to–pin hole node in the channel), and that the end points of the domain have fixed temperatures, not defined heat fluxes. On the left side of the pin–hole, which is touching the channel helium, the temperature is clamped to the temperature of the right–most node of the channel domain. On the right side of the pin hole, which is touching the external bath, the temperature is clamped to the bath temperature.

Figure 5.7 shows the channel and pin–hole nodes near the interface between the subdomains. It illustrates how the boundary heat flux $Q_{\text{toPinHole}}$ in Equation (5.49) is found. The thermal gradient from Node 0 to Node 1 in the pin–hole (blue nodes) gives the heat flux flowing between the two nodes according to;

$$Q_{\text{alongPinHole}} = \left[f^{-1}\left(\frac{1}{2}\left[T_{\text{pH, 0}} + T_{\text{pH, 1}}\right]\right)\frac{T_{\text{pH, 0}} - T_{\text{pH, 1}}}{\Delta x_{\text{pH}}}\right]^{1/m}, \tag{5.51}$$

where $m = 3.4$.

The heat flux $Q_{\text{toPinHole}}$ is this heat flux, adjusted for the ratio $r_{\text{pH to Ch}}$ of cross sectional area between the pin–hole and the channel;

$$Q_{\text{toPinHole}} = r_{\text{pH to Ch}}\, Q_{\text{alongPinHole}}. \tag{5.52}$$

From Section 3.2 and Figure 3.12 on page 69, this ratio is about 0.092, meaning that the pin hole leaves about 9% of the channel cross section open to the bath.

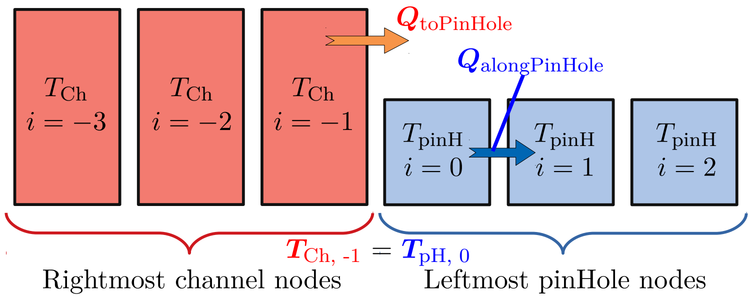

Figure 5.7: Rightmost nodes in the channel helium and leftmost nodes in the pin hole helium, showing the interface between the two simulation domains.

As indicated in Figure 5.6, the pin–hole nodes also experience heating from the heater strip. The heat input is found by using the heater surface temperature from the material stack sub–simulation, and calculating a Kapitza heat flux using as reference temperature the pin–hole temperature of each individual node. In the channel helium this is not necessary, because, as it turns out, the pin–holes do not represent a large enough cooling power to actually cause a gradient in the channel. Within the pin–hole, however, there is, obviously, such a gradient, from the channel–temperature end to the bath–temperature end.

Testing the Formulation

The three sub–domains of the combined material stack and helium domains have their forward time steps calculated one after the other, with Code 5.1 outlining the steps. The material stack temperature distribution is found first, and it is here the Kapitza heat flux is calculated. To find the Kapitza heat flux, the temperature in the middle of the helium channel is used as the reference temperature. In practice, which node is used does not matter, because the thermal gradient along the channel towards the pin–hole is small. The material stack step also depends on the external bath temperature, since the sensor leads are fixed to the bath temperature. The new channel temperature distribution is found next, using the Kapitza heat flux and pin–hole heat flux from the previous time–step. Last is the pin–hole temperature distribution, using the Kapitza heat flux, channel temperature at the interface node, and the bath temperature. In the simulation, $\Delta x_{\mathrm{materialStack}} = 1\ \mu\mathrm{m}$, $\Delta x_{\mathrm{channel}} = 250\ \mu\mathrm{m}$, $\Delta x_{\mathrm{pinHole}} = 100\ \mu\mathrm{m}$, and Δt starts at 0.1 µs.

Figure 5.8 shows the energy balance during a simulation that uses the applied heating power density of the fast pulse back in Figure 4.16 on page 139.

The material stack sub–simulation shows the same qualitative energy–balance behaviour as in Figure 5.3; the sum of all energies associated with the stack is a little below the energy developed in the heater strip (about 2%). Note that Sum, stack remains essentially constant after the end of the fast pulse at around 1 ms, as is expected when no more energy is supplied.

The curve Surface cooling represents the energy associated with heat transfer away from the heater surface, and at the same time into the channel helium, so the

Code 5.1: Pseudo code outlining the computational steps performed at each forward step in time. `BC` denotes "boundary conditions".

```
while t < t_end:
    T_materialStack_NEW = timeStep_materialStack(
        T_materialStack_OLD, BC=[ T_channel_OLD, T_bath(t) ]
    )
    T_channel_NEW = timeStep_channel(
        T_channel_OLD, BC=[ P_Kapitza, Q_toPinHole ]
    )
    T_pinHole_NEW = timeStep_pinHole(
    T_pinHole_OLD,
        BC=[ P_Kapitza, T_channel_OLD[-1], T_bath(t) ]
    )

    t += Δt

    temperatureChanges = NEW - OLD

    if temperatureChanges > limits_for_reduction
        Δt *= 0.95
    if temperatureChanges > limits_for_increase:
        Δt *= 1.025
```

sum of energies associated with the two helium sub–simulation, Sum, helium, should be equal to this. There is, of course, a discrepancy, on the order of 4%.

As can be seen, Surface cooling starts to fall slightly after about 7 ms. This is because in the simulation, the heat flow backwards along the sensor leads effectively outgrows the cooling of the pin–holes, and now the channel helium actually supplies heat to the heater surface through the Kapitza expression. While it is expected that the pin–holes themselves will not provide much cooling power, it is not actually true that the cooling predominantly happens along the sensor leads. The slope of temperature decay in the measured data is much steeper than that from these simulations. As such, 7 ms becomes an estimated upper limit for when the model can reasonably be considered to be valid. As is discussed in Paper [2], the time during which this very simple model appears reliable is on the order of 5 ms.

Sum, helium, rather than decay like Surface cooling does, keeps slowly growing after 7 ms. This is driven by PH to bath, which appears to be slightly overestimated compared with the energy that actually leaves the channel helium. The source of this numerical discrepancy is not clear. The choice of the small parameter ϵ influence results a little; the default is $\epsilon = 10^{-8}$, and when increasing ϵ to 10^{-6}, the discrepancy grows slightly. Lowering it to 10^{-10} does not cause an appreciable change from the default parameters. It also does not improve significantly after reducing the spatial discretisation in both the channel and the pin–hole sub–domains by a factor 10. As such, it could simply be that the formulation of the modified heat equation as it is used here is not quite energy conservative. The impact of this error is small, and only appears to matter on longer time–scales, at which point the simulation results start deviating from measured data on other grounds that the small numerical error from over–estimation of pin–hole cooling in the model.

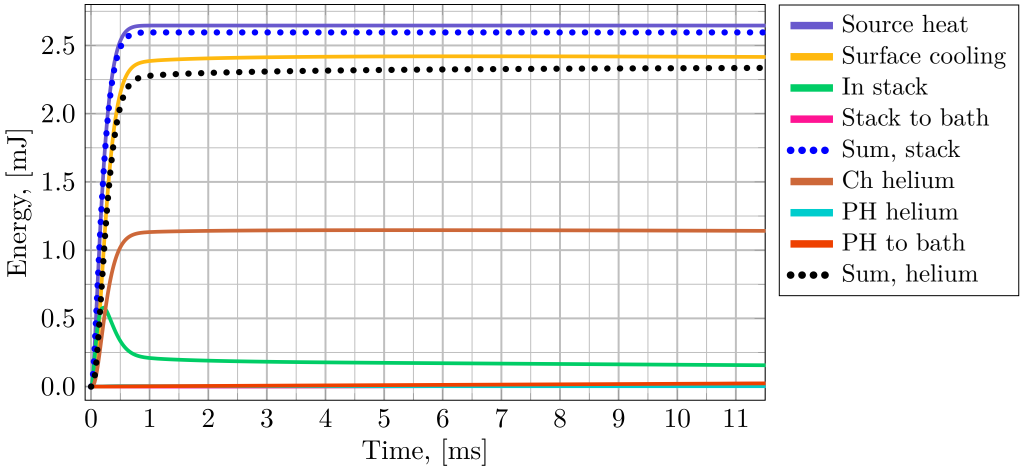

Figure 5.8: Energy balance during a simulation of the material stack, helium channel, and pin hole sub–simulations, all submerged within a bulk helium bath at 1.9 K, subject to the applied heating power density seen in Figure 4.16.
Source heat, Surface cooling, In stack, Stack to bath, and Sum, stack represent the same energies as in Figure 5.3. Ch helium: energy contained in the channel helium (due to heat capacity); PH helium: energy contained in the pin hole helium (due to heat capacity); PH to bath: energy that flows from the end of the pin hole helium domain into the bulk bath; Sum, helium: sum of helium related curves.

5.2.3 Heat Flow Across Channel Depth

In light of the pin–holes representing such a small cooling power, an obvious question is how the simulation results might change when looking at heat flow across the 120 µm channel depth, rather than along the length like has been discussed so far.

To implement this new simulation dimension only minor changes are needed; the string of helium nodes now runs upwards from the heater surface, and at the surface node a Neumann boundary condition accounts for the Kapitza heat flux into the channel. At the top of the channel it is assumed no heat flows, considering the PEEK as a perfect thermal insulator.

In node $i = 0$, the bottom of the channel, where helium is in contact with the heater surface, a Neumann condition will give rise to a heat transfer balance that looks exactly like Equation (5.49), just with Q_{Kapitza} instead of $Q_{\text{toPinHole}}$, since heat comes from the heater surface. The sign is also flipped, defining heat flow as positive into the helium domain. On the top of the channel, the zero–flux Neumann condition gives a similar expression, but with $Q_{\text{toPinHole}}$ replaced by 0, since no heat is assumed to flow out of the channel that way.

The resulting simulation does not significantly differ, in terms of temperature result, from the standard approach above, and show a similar energy balance discrepancy. Since there is no pin–hole, the numerical error from the overestimation of pin–hole heat flux does not impact the simulation of heat across the channel. This alternative simulation serves to investigate a potential temperature gradient across the channel. No such gradient is found for any applied heating power density, as discussed in Paper [2].

Chapter 6

Conclusion and Outlook

The core question that first motivated the work described in this thesis is “How come the LHC magnets survive UFO attacks much larger than expected?”

The electro–thermal models of LHC magnets used to predict how much energy a UFO needed to deposit within its approximately 1 ms duration rely on the steady state Kapitza heat transfer expression to describe the cooling heat flux that flows from the cable strands to the He II that permeates all the tiny gaps and channels in the cable. These models can correctly predict the thermal behaviour during heating events that are over within a few microseconds or within several tens of milliseconds. But somewhere in the range of one millisecond there are significant discrepancies between the energy input from a beam loss event and the simulated temperature response of the magnet. A test that intentionally provoked beam losses on the relevant time–scale revealed that a consistent underestimation of the cooling capabilities of He II could be to blame.

Only one thing about heat transfer to He II was held as absolutely certain at the start of this work; in steady state, when exposed to an open bath of He II, heat transfer from a heater to helium is described by the steady state Kapitza model.

A UFO event in an LHC magnet presents conditions far from the steady state open bath situation; the UFO event lasts only a millisecond in total, and the He II is confined to volumes of dimensions on the sub–millimetre scale.

The experimental work designed to investigate this begins with a validation of the steady state open bath behaviour of the setup. With the steady–state results in Paper [1] we confirm this. Next we look at the transient temperature response to steps in applied heating power density, still in an open bath of He II. The transient results in Paper [1] reveal that past the first millisecond after a step, the steady state Kapitza model accurately captures the temperature response of the heater. During that first millisecond, however, the measurements show a slower temperature rise than what a simulation using the Kapitza model predicts.

To more accurately approximate the conditions relevant to LHC magnets, in Paper [2] we confine the He II near the heater to a shallow channel. For slow heat pulses that deliver peak power after 9 ms, the steady state Kapitza model accurately predicts the heater response when using the measured channel helium temperature as the reference in the Kapitza model. When we also simulate the channel helium, assuming the Gorter–Mellink heat transfer regime is valid at all times, we still obtain agreement between simulation and measurement during the first 5 ms after the start of a slow pulse. However, for fast UFO–like heat pulses that deliver peak power after 100 µs with total duration under 1 ms, the temperature rise is consistently slower than what modelling predicts. This is qualitatively in line with the LHC observation of UFOs not quenching magnets unless they deliver much more energy than what similar modelling predicts is necessary. Importantly, we find that both the heater and helium temperature responses are slower than expected, which points towards the steady state Kapitza model not adequately accounting for the transient heat transfer from heater to helium during millisecond time–scale heat pulses.

Outlook

What would I do differently, if given the chance to redesign the experiment? Or what would I give as advice to someone trying to build on the findings presented here?

Any temperature measurement that deals with surface heat transfer to a coolant will face the challenge of obtaining the heater surface temperature based on the sensor data available. We have found good ways to account for the various materials that separate the heater surface from the temperature sensors, but a design that requires fewer steps and assumptions to get access to the sought–after heater surface temperature is obviously preferable. Choosing a completely different heater material with higher thermal conductivity could be helpful, but this would also raise different considerations regarding the analysis. For instance, using a material for the heater strip that allows temperature measurement based on the temperature dependent electrical resistivity could be a good approach. A drawback with such a heater is that it would give access only to the average temperature of the whole heater volume, which would obscure possible temperature variations along its length. A thinner heater of the same material might work, though this makes handling the heater strip more difficult, and would likely introduce the need for some kind of heater strip substrate to improve mechanical support.

The thickness of the varnish layer between the heater strip and the Cernox® sensors proved to be an important factor in determining the Kapitza fit parameter uncertainty, and it also plays an important part in the transient measurement response. While a new design would still use the same varnish, which has material properties readily available in literature, the ideal would be to do a complete three–dimensional x–ray characterisation of the gap between heater and sensor.

In that vein, a general, not very quantitative remark about the assembly procedure is that the Cernox® sensors are more robust than they appear. It certainly does not take much to detach a sensor lead or scratch the region near the temperature sensitive zirconium oxynitride film, but they can withstand evenly distributed pressure quite well. When attaching them to the heater strip, it would have been fine to press them more firmly against the heater strip than what I did. The advice would be to use something like a toothpick and press down evenly on both lead attachment beads.

The goal would, of course, be to make the varnish layer as thin as possible after the varnish cures.

Although the capacitive compensation method is very successful in obtaining the instantaneous sensor temperature, it would clearly be better to not need the compensation step at all. It is not clear what change would solve this however. Reducing the filtering capacitor would significantly increase the noise level of the output current, which could just end up trading one problem for another; random signal noise could obscure the true signal to a greater extent than the capacitive response that at least can be compensated. At the very least it is clear a rigorous characterisation of the transient response of the current sources would be necessary before a new experiment.

One of our key conclusions is that the steady state Kapitza model works well for heating pulses with peak power delivery after around 10 ms, but stops being valid during heating that peaks after 100 µs. A new experiment should obviously try heating pulses that peak somewhere within this range, around 1 ms.

As seen in the closed channel measurements, after around 5 ms, it appears that parasitic cooling effects acting on the helium in the enclosed channel start to play a significant part in determining the temperature evolution in the channel. The first suggested explanation for this is that since two separate plates are pressed together to form the channel, some He II can surely enter part of the crack that necessarily remains. It should be possible to apply an amount of vacuum grease on the bottom plate that, after closing and tightening, gets squeezed very close to the channel edge without actually pouring into it. This grease would fill in at least some of the crack, reducing the stray volumes of He II.

It is a great regret of mine that the pressure sensors in the channel did not turn out to work as well as expected. This is no fault of the sensors themselves; a channel as small as the one used here would always make self–heating of these probes a challenge, but for a new experiment it could be worth looking more into how these pressure sensors would need to be operated so as to give useful data even at limited excitation current.

During the two main measurement campaigns I became too focused on making step measurements, losing track of the real motivation behind the project; having pulsed heating data from the open bath would have been good, but more importantly, having pulsed heating data at several bath temperatures in the closed channel configuration would have given a more complete picture of the behaviour for heating strong enough to approach T_λ in the channel.

Finally, for a new experiment it would be useful to run tests also for bath temperatures above T_λ in the liquid He I region in order to help narrow down potential explanations for the observed behaviour. The double bath cryostat used for tests is not really regulated above T_λ but with patience, it would be possible to have a somewhat well–defined initial state, at least for the fast pulses which deposit very little total energy in the bath.

APPENDIX A

RLC CIRCUITS

Figure A.1 shows a simple RLC series circuit. Such a circuit will display of of three characteristic responses; over–damped, critically damped, or under–damped response [202, Sec. 8.3].

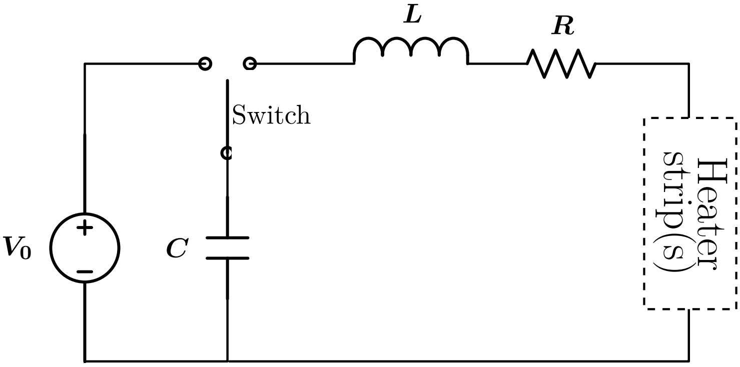

Figure A.1: Simplified series RLC circuit used to generate pulses for the experiment. The “Heater strip(s)” block represents either one or two heater strips, depending on whether the open bath or closed channel experimental configuration is used.

When the switch is flipped from the position where the capacitor, C, is charged by the voltage source, to a voltage V_0, to the position where the discharge through the rest of the circuit is possible, an expression for the current that flows, in series, through all the circuit elements is given as:

$$I(t) = A\mathrm{e}^{s_1 t} + B\mathrm{e}^{s_2 t}, \tag{A.1}$$

where A, B, s_1, and s_2 are (generally) complex numbers. Furthermore, by defining three parameters, α, the attenuation, ω_0, the undamped natural frequency, and ζ, the damping factor, as such,

$$\begin{aligned} \alpha &= \frac{R_{\text{total}}}{2L}, \\ \omega_0 &= \frac{1}{\sqrt{LC}}, \\ \zeta &= \frac{\alpha}{\omega_0} = \frac{R_{\text{total}}}{2}\sqrt{\frac{C}{L}}, \end{aligned} \tag{A.2}$$

we have s_1 and s_2;

$$\begin{aligned} s_1 &= -\alpha + \sqrt{\alpha^2 - \omega_0^2} = \omega_0\left[-\zeta + \sqrt{\zeta^2 - 1}\right], \\ s_2 &= -\alpha - \sqrt{\alpha^2 - \omega_0^2} = \omega_0\left[-\zeta - \sqrt{\zeta^2 - 1}\right]. \end{aligned} \tag{A.3}$$

Boundary conditions The two boundary conditions applied to the circuit are **(1)**, no current flows in the RLC branch at the start ($t = 0$) of the discharge, and **(2)**, at the start of the discharge, all voltage falls across the inductor;

$$I(t = 0^-) = 0 \tag{A.4}$$

$$V_{\text{L}}(t = 0^+) = V_0 \tag{A.5}$$

Over–damped circuit response The damping factor of such a circuit is larger than one, meaning that in Equation (A.3), the two factors that go into the exponentials in Equation (A.1) on the previous page are purely real.

Boundary condition (A.4) means that $B = -A$, so that,

$$I(t) = A\left(\mathrm{e}^{s_1 t} - \mathrm{e}^{s_2 t}\right). \tag{A.6}$$

Boundary condition (A.5) means that $L\,\mathrm{d}I/\mathrm{d}t = V_0$, so that,

$$\begin{aligned} LA\left(s_1\mathrm{e}^{s_1 t} - s_2\mathrm{e}^{s_2 t}\right)\Big|_{t=0} &= V_0 \\ A = \frac{V_0}{L(s_1 - s_2)} = \frac{V_0}{2L\omega_0\sqrt{\zeta^2 - 1}} &= \frac{V_0}{R_{\text{total}}}\frac{\zeta}{\sqrt{\zeta^2 - 1}}. \end{aligned} \tag{A.7}$$

With this inserted into Equation (A.6), the current flowing in the circuit during the discharge is given as,

$$I(t) = \frac{V_0}{R_{\text{total}}}\frac{\zeta}{\sqrt{\zeta^2 - 1}}\left(\mathrm{e}^{\omega_0\left[-\zeta + \sqrt{\zeta^2 - 1}\right]t} - \mathrm{e}^{\omega_0\left[-\zeta - \sqrt{\zeta^2 - 1}\right]t}\right). \tag{A.8}$$

Under–damped circuit response Now the damping factor is smaller than one, physically interpreted as such: the attenuation in the circuit is not strong enough to dampen the natural oscillation of energy between the capacitor and the inductor before *at least one* oscillation is completed.

With the damping factor smaller than one, the coefficients in Equation (A.3) are complex, but otherwise, the derivation from the previous paragraph follow the same steps, based on the boundary conditions.

Boundary condition (A.4) means that $B = -A$, so that,

$$I(t) = A\left(\mathrm{e}^{s_1 t} - \mathrm{e}^{s_2 t}\right). \tag{A.9}$$

Boundary condition (A.5) means that $L\ \mathrm{d}I/\mathrm{d}t = V_0$, so that,

$$\begin{aligned} LA\left(s_1\mathrm{e}^{s_1 t} - s_2\mathrm{e}^{s_2 t}\right)\Big|_{t=0} &= V_0 \\ A = \frac{V_0}{L(s_1 - s_2)} = \frac{V_0}{2L\omega_0\sqrt{\zeta^2-1}} &= \frac{V_0}{R_{\text{total}}}\frac{\zeta}{\sqrt{1-\zeta^2}}\frac{1}{j}. \end{aligned} \tag{A.10}$$

With this inserted into Equation (A.9), the current flowing in the circuit during the discharge is given as,

$$\begin{aligned} I(t) &= \frac{V_0}{R_{\text{total}}}\frac{\zeta}{\sqrt{1-\zeta^2}}\frac{1}{j}\left(\mathrm{e}^{\omega_0\left[-\zeta+j\sqrt{1-\zeta^2}\right]t} - \mathrm{e}^{\omega_0\left[-\zeta-j\sqrt{1-\zeta^2}\right]t}\right) \\ I(t) &= \frac{V_0}{R_{\text{total}}}\frac{\zeta}{\sqrt{1-\zeta^2}}\mathrm{e}^{\omega_0\zeta t}\cdot 2\sin\left(\omega_0\sqrt{1-\zeta^2}t\right) \end{aligned} \tag{A.11}$$

Critically damped circuit response When solving the under and over–damped circuit, it was assumed that the system behaved as a second order one. If, however, the attenuation is exactly equal to the natural frequency of the circuit ($\alpha = \omega_0$), Equation (A.3) says that s_1 and s_2 are equal, in turn meaning that, given the boundary condition of zero initial current, Equation (A.1) will be constantly equal to zero. The crux here is that the circuit now must be solved as a first order system. Without further derivation, the current flowing in the circuit will be,

$$I(t) = \frac{V_0}{L}t\mathrm{e}^{\alpha t}. \tag{A.12}$$

This particular solution is not in itself very useful, because the circuit is easily chosen to avoid this, and, given that these analytic expressions will be used in computer simulations to aid in the experimental design, it is very unlikely for the condition of the damping factor being equal to one to be fulfilled.

Resulting Pulse Shapes Figure A.2 shows the effect of the dampening factor ζ on the shape of the RLC discharge pulse. With appropriately chosen circuit elements, an acceptable approximation to the asymmetric Gaussian profile is possible.

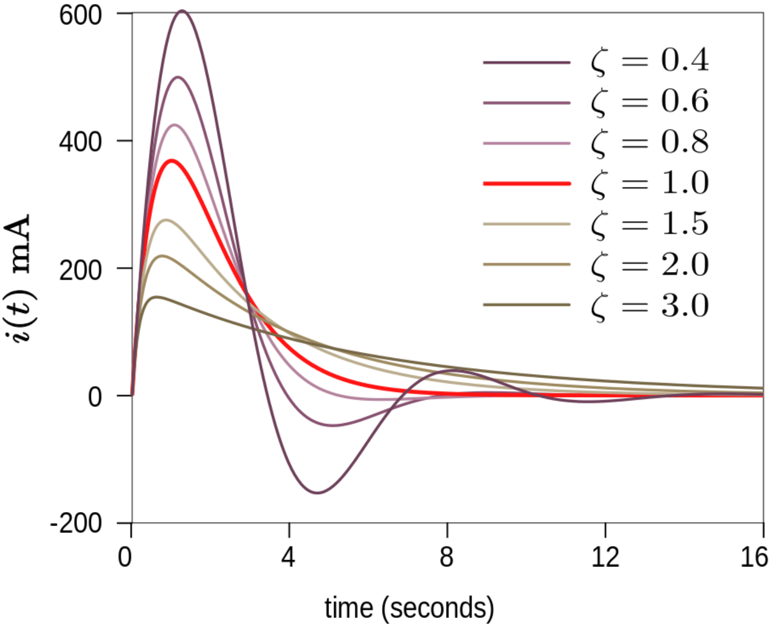

Figure A.2: Current vs time during the discharging of a capacitor through an inductor and a resistance (in series), where ζ is the damping factor from Equation (A.2) [203].

A.1 RLC Circuit for Pulse Generation

Figure A.1 assumes all elements in the circuit behave as ideal lumped elements, where R accounts for all resistances that are not the “Heater strip(s)” resistance. In Section 3.1.2 on page 62, Figure 3.5 on page 64 shows the full circuit.

For a measurement where the applied heating power density is a pulse, be it fast or slow, the capacitor C is charged to some voltage V_0, with the switch turned to the source. To apply the heating, the switch is flipped. The current in the C–R–L–“Heater strip(s)” circuit now follows the relationship given in Equation (A.1).

Figure A.3 shows the effect of varying the capacitance value C and the discharge resistance value R. Note that the total discharge resistance in the real circuit is the sum of R_{pulse} and R_{strip} (the resistance of the heater strip(s)). In the simple simulations shown here, the total circuit resistance is taken as indicated in the figure legend/caption. The curves are generated by using the analytical model above.

For measurements driven by fast RLC pulses, the chosen capacitance, C is 160 µF, and the pulse resistance R_{pulse} is 0.5 Ω. For slow pulses, C is 36.4 mF, and R_{pulse} is 0.9 Ω.

The exact value of the inductance turns out to be less important than the other two circuit parameters in terms of how large of an impact a change of several tens of percent in inductance value has on the real pulse shape. In addition to this, purchasing inductors with well–defined values proved difficult because larger inductance values came with lower rated current. Solving this issue meant trial and error of hand–made inductors with materials available in the laboratory, and lead to using one of two inductor setups during tests;

- For fast pulses, two identical steel bolts were wrapped with three layers of wire. The resulting inductance is not well defined, but estimates based on the long–solenoid approximation [147, Eq. 6–135] $L = \mu_0 \mu_\mathrm{r} N^2 A/l$, where μ_0 is the permeability of vacuum ($4\pi \cdot 10^{-7}\ \mathrm{H\,m^{-1}}$), μ_r is the relative permeability of the bolt material (not known, but the bolts do not stick to magnets, indicating they are some kind of austenitic stainless steel, with μ_r between 1 and 7[204, Austenitic stainless steel in the table]), N is the number of wire loops around the bolt (100), A is the cross sectional area of the solenoid (approximately $\pi(7.5 \cdot 10^{-3})^2 = 1.77 \cdot 10^{-4}\ \mathrm{m}^2$), and l is the length of the solenoid (5 cm). This gives $L =$ 44 µH (this uses $\mu_\mathrm{r} = 1$).
- For slow pulses, a large cable reel of 2 mm wide wire is used. The loops have a radius of approximately 17 cm. The reel is 5 cm tall, and there are 3 layers of wire, meaning 75 loops in total. Using the same approximation as for the bolt inductors (with an air–core, meaning $\mu_\mathrm{r} = 1$) gives $L = 12.8$ mH.

These inductance values only serve as order–of–magnitude estimates. Their exact values do not influence the analysis of data, and is not needed.

Note that in the real circuit, the resistance in addition to the heater strip is higher than the 0.5 or 0.9 Ω suggested. The real circuit has several metres worth of power leads leading from the external circuit down to the cryostat insert where the experimental sample is placed, as well as contact resistances, and internal resistances in lumped circuit elements (capacitor, inductor, and transistor). With the 0.5 Ω R_pulse resistor and the two fast–pulse inductors in parallel, a multimeter resistance measurement across all circuit elements to the right of the capacitor in Figure 3.5 on page 64 (with the transistor *on*) yields 2.315 Ω, of which 0.5 Ω is R_pulse, and 0.923 Ω is from the two heater strips used in open bath experiments. So various circuit elements account for at least 0.892 Ω. The resistance value of the heater strips in series was determined by running a 1 A current through them, and measuring the voltage across the two strips. The way this measurement is done is discussed in Section 3.3.1 on page 69.

Figure 3.15 on page 74, back in Section 3.3.1, showed representative heater strip voltage measurements, together with simulated voltage curves using the RLC model in this appendix, determining the circuit parameters by a least–squares fit to data. All circuit elements are treated as free, but they are constrained.

For the fast pulse, a 160 µF capacitor is used. Its capacitance has been measured with a Fluke 87 V multimeter. The measurement yields 160 µF, with an expected measurement accuracy within ±3.6 µF. Note that five capacitors rated at 160 µF were bought for the experiment. Their real values ranges from 150 µF to 160 µF as per the capacitance measurement. Looking at the fitting result quoted in the caption of Figure 3.15a, 179.0 µF also gives a good fit to the data, even if it is almost 12% higher than the rated value of the real capacitor. An important note about the fitting procedure is that it is not a measure of the real component values. Several configurations of circuit parameters gives sufficiently similar curves that the Levenberg–Marquardt algorithm cannot differentiate them. As stated in Section 3.1.2 on page 62, the circuit parameters are not in themselves important to the project. Only the resulting time–dependent heating pulse is.

For the slow pulse, four capacitors rated at 10 mF are used in parallel. The sum of their individual values is measured to 36.4 mF. For each sub–capacitor, the accuracy is expected to be within ±102 µF, so in total, it will be within ±408 µF. Note that the measurement device is older than the one year the manufacturer states as the validity of the factory calibration. The fitting suggests the slow–pulse C is 39.5 mF, which is 9% higher than the measured value. Just as for the fast pulse, the suggested best–fit value for C is not the real value of C. It is only a value that, together with the other circuit parameters, that are also freely adjusted by the fitting algorithm, gives a good least–squares fit to the noisy data.

As for the inductances, the fit to the representative fast pulse shown in Figure 3.15a, suggests that the real inductance of the circuit is much larger than the one estimated earlier in this section. It comes down to the assumption that $\mu_\mathrm{r} = 1$. With $\mu_\mathrm{r} = 5$, the parallel connection of the two steel bolt core inductors would give a value similar to the 100 µH typically found by the fitting algorithm. For the slow pulse, the fitting suggests values quite in line with the estimated value.

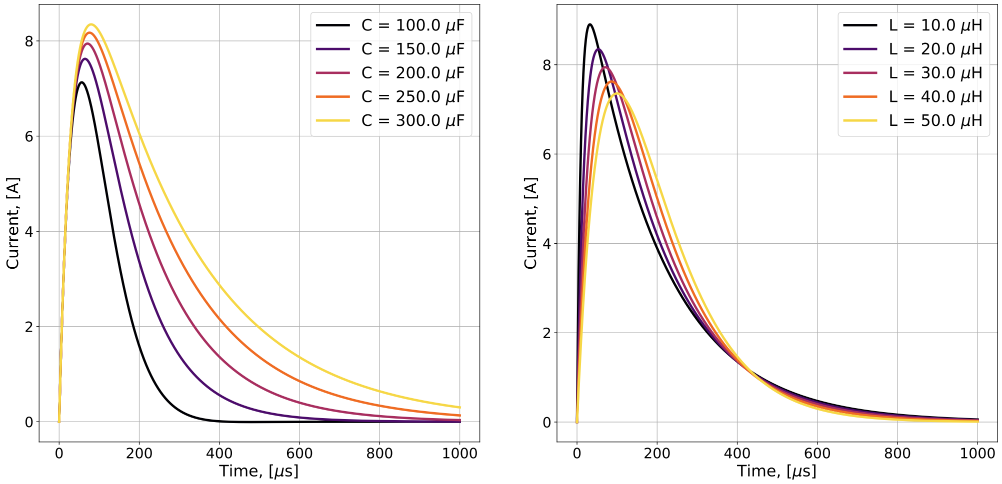

(a) Current as function of time during discharge of a capacitor C, charged to 10 V, for varying capacitance values. The total circuit resistance R, is 1 Ω, and the inductance L, is 30 µH.

(b) Current as function of time during discharge of a capacitor C, charged to 10 V, for varying inductance values. The total circuit resistance R, is 1 Ω, and the capacitance is 200 µF.

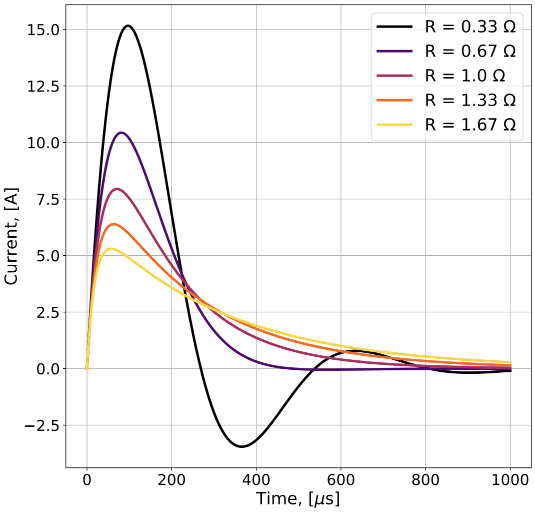

(c) Current as function of time during discharge of a capacitor C, charged to 10 V, for varying circuit resistance. The capacitance is 200 µF, and the inductance L, is 30 µH.

Figure A.3: Figures showing the effect of changing the capacitance (Figure A.3a), circuit inductance (Figure A.3b), and discharge resistance (Figure A.3c) of the pulse generation circuit.

Appendix B

Inter–Plate Helium Modelling

The simulation configuration with material stack, channel helium, and pin–hole helium sub–simulations is the tool used to interpret results. However, an attempt was made to try and expand the helium domain to include the helium trapped between the two PEEK plates after assembly and Eccobond® sealing. This effort was driven by the desire to obtain modelling results more in–line with the long–time–scale measured test data, as well as look into the parasitic cooling effects mentioned in Paper [2]. Both of these goals are outside the scope of the thesis itself, and are included here as an example of a path followed that did not lead to reliable results.

Figure B.1 shows a schematic representation of the cross section of the channel along the length of the sample. The goal is to formulate a one–dimensional domain that accounts for the helium (white region in the figure) as well as the aluminium bolts. Those two sub–domains form the dotted blue path that illustrate the hypothetical path that heat could flow along, from the main channel to the external bath.

The first assumption made when defining a one–dimensional domain for all these parts is that the inter–plate helium can be represented by a continuous and uniform gap of some height between the top and bottom PEEK plates. This is obviously a significant simplification over the real sample, since the two PEEK plates must at the very least rest against each other in a few points along their mating surfaces after bolting them together.

The second assumption is that the holes in the PEEK plates, through which the aluminium bolts go, can be considered an effectively homogenous additional helium volume in contact with the inter–plate helium. This is also a significant simplification, since the bolt–holes are located at 16 discrete points along the sides of each PEEK plate.

A further assumption is that the aluminium bolts can be represented as a homogenous block of material that is in contact with the bolt–hole helium, which essentially follows directly from the bolt–hole helium assumption.

The three contributions to the total helium volume confined in the sample are then;

1. The helium in the channel itself, which amounts to $V_{\mathrm{Ch}} = 150 \cdot 10^{-3} \times 3.1 \cdot$

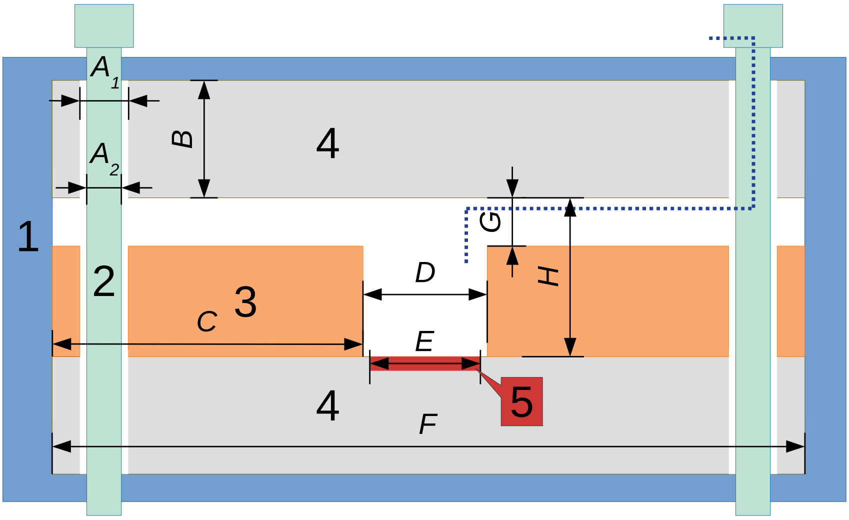

Figure B.1: Cross sectional view down the length of the channel.
Region 1: Eccobond encasing filling gaps to contain the helium. 2: Aluminium bolts holding the Top and Bottom plates together. 3: Kapton tape attached to Bottom plate. 4: PEEK Top/Bottom plate. 5: Stainless steel heater strip. The white region is filled with helium.
Length A_1: Diameter holes for bolts in PEEK plates = 4.35 mm (between 4.2 and 4.5 mm). A_2: Diameter of aluminium bolts = 3.78 mm (average of 4 mm and 3.55 mm, accounting for threads). B: Thickness of PEEK plates = 10 mm. C: Width of Kapton tape = 13.5 mm (the smooth machined edge of the tape lies along the channel, while the hand–cut jagged edge lies long the outside, towards the Eccobond encasing). D: Channel width = 3.1 mm. E: Heater strip width = 3 mm. F: Width of PEEK plates = 30 mm. G: Gap between Kapton tape and Top plate (this is an unknown length, present due to manufacturing tolerances etc.) = 5 µm. H: Channel depth = 120 µm.
The dark blue dotted lines indicate the thermal path between the channel helium and the bulk helium outside the Eccobond® sealing.

$10^{-3} \times 120 \cdot 10^{-6} = 5.58 \cdot 10^{-8}$ m^3.

2. The inter–plate helium between the Kapton tape and the PEEK Top Plate, which amounts to $V_{\mathrm{IP}} = 2 \times 150 \cdot 10^{-3} \times 13.5 \cdot 10^{-3} \times 5 \cdot 10^{-6} = 2.03 \cdot 10^{-8}$ m^3 (the factor 2 stems from there being one inter–plate volume on either side of the heater). Note that the 5 µm depth of the inter–plate helium volume is assumed, not measured, and it is in practice a free parameter in the model.
3. The helium within the 32 10 mm long bolt holes in the PEEK plates, which amounts to $V_{\mathrm{BH,\,total}} = 32V_{\mathrm{BH}} = 32 \times \pi \left([2.175 \cdot 10^{-3}]^2 - [1.89 \cdot 10^{-3}]^2\right) \times 10 \cdot 10^{-3} = 1.16 \cdot 10^{-6}$ m^3 (the bolt holes have a radius of 2.175 mm, while the aluminium bolts, accounting for the threads, have an average radius of 1.89 mm).

The aluminium bolts have a total length of approximately two times 13 mm (the same bolt goes through, from top to bottom, 3 mm of Eccobond, 10 mm of plate hole with helium around it, then another 10 mm of plate hole, then 3 mm of Eccobond) = 26 mm. The volume of aluminium is then $V_{\mathrm{Alu}} = 16 \times \pi[1.89 \cdot 10^{-3}]^2 \times 26 \cdot 10^{-3} = 4.67 \cdot 10^{-6}$ m^3.

Modelling the inter–plate and bolt–hole helium is approached in a similar way as when modelling the pin–hole helium; the main channel helium has one sub–simulation, and the inter–plate/bolt–hole helium has its own sub–simulation, using the same heat equation, but with boundary conditions that depend on the channel temperature.

Modelling the complicated 3D volume of helium and aluminium in 1D requires morphing both domains into simple 1D domains that still account for the correct heat capacity and heat transfer as that seen in the real sample.

Figure B.2 shows a 3D representation of the helium volume and aluminium bolts. Clearly, there would be heat flow in several directions; 1) within the main helium channel (blue cuboid), there is heat flowing along the length of the channel from the middle towards the pin holes, and also heat flowing sideways into/from the inter–plate helium (green slab); 2) within the inter–plate helium heat flows only sideways, so this will be the simulation axis, however, where the bolt–hole helium (red hollow cylinders) intersects the inter–plate helium, heat flows upwards/downwards instead; 3) within the bolt–hole helium there is heat flowing upwards/downwards, and also radial heat flow into the aluminium bolts (yellow cylinders); 4) within the aluminium bolts, heat flows upwards/downwards, and heat enters/leaves radially from the bolt–hole helium that surrounds the bolts.

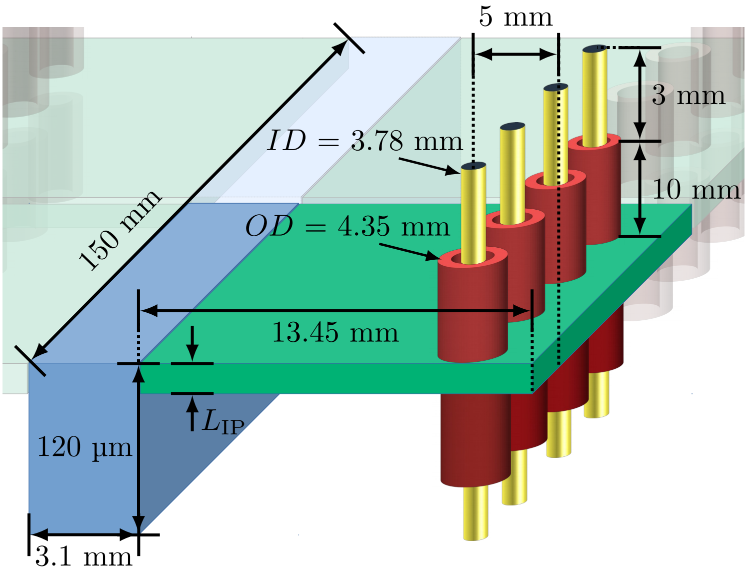

Figure B.2: Simplified 3D view of the main helium channel (light blue cuboid), inter–plate helium (green plate), bolt–hole helium (red hollow cylinders), and aluminium bolts (yellow bars). Transparent regions are not simulated, but accounted for by symmetry). Note, for clarity, most aluminium bolts are not shown, but there is one bolt going through each hole indicated by a hollow cylinder.

The inter–plate helium is straight forward; it is just a thin slab of helium that is completely uniform along the 150 mm length of the channel. The simulated width of it, however, will be 6.5 mm, which is where the bolt–holes intersect the green slab as measured from the edge of the main channel.

The bolt–hole helium is accounted for by the following method: the inter–plate helium is considered a uniform slab of 5 µm depth, and width 75 mm (as Figure B.2 indicates, only half the 150 mm length of the channel is simulated on symmetry grounds). Its length, along the simulated axis, is 6.5 mm, which is the distance from the edge of the channel helium to where the bolt–hole helium intersects the inter–plate helium. In the model geometry, the domain continues from this intersection point with the same depth and width, for another 10 mm along the simulated dimension (this length corresponds to the thickness of a PEEK plate which is also the length along which the bolt–hole helium touches aluminium). For these 10 mm, the helium heat capacity is increased by a factor according to the ratio between inter–plate helium and bolt–hole helium volumes. This ratio is calculated as follows:

$$r = \frac{V_{\text{IP, after BH}} + 8V_{\text{BH}}}{V_{\text{IP, after BH}}},$$

where $V_{\text{IP, after BH}}$ is the volume of the inter–plate helium that remains after the intersection point between inter–plate helium and bolt–hole helium. $V_{\text{IP, after BH}}$ is the depth of the inter–plate helium (5 µm) times the width of it (75 mm) times the length *after* the intersection (7 mm); $V_{\text{IP, after BH}} = 75 \cdot 10^{-3} \times 5 \cdot 10^{-6} \times 7 \cdot 10^{-3} = 2.63 \cdot 10^{-9}$ m^3. So the ratio between the volumes becomes[1] 111.93.

By making the heat capacity of helium larger in the part of the helium that accounts for the bolt–hole helium, we have the benefit of a single simulated domain, with fewer boundary conditions between sub–simulations and no need to account for the eight bolt holes individually, we get an effective heat capacity that accounts for the total volume, and hence, the correct thermal diffusion time through the bolt–hole helium, and we have the correct thermal length of the bolt–hole helium. We also avoid the issue of changing the simulated axis at the inter–plate/bolt–hole helium intersection, since they are taken as one continuous volume. Finally, to account for the fact that the bolt–hole helium conducts heat away from the inter–plate helium intersection in both the upwards and downwards directions, a factor 2 is used to adjust the effective thermal conductivity of the bolt–hole helium part.

The aluminium bolts have their own sub–simulation where they are treated as a bar of 13 mm length, along which the first 10 mm are wetted by the 10 mm bolt–hole helium section of the inter–plate helium sub–simulation. Heat transfer relations between a metal surface and superfluid helium tends to be expressed with the assumption that the metal is hot and the helium is cold. Here, the typical case will be that the helium is hot, and the aluminium bolts will be cold, since heat will flow from the main helium channel out to the bolts through the inter–plate helium. The heat transfer relation at this interface will be the Kapitza model (Equation (2.28) on page 21), using parameters for aluminium; $a_{\text{K}} = 490\ \text{W}\,\text{m}^{-2}\,\text{K}^{-n_{\text{K}}}$, and $n_{\text{K}} = 3.4$[30, Table 7.4].

Figure B.3 shows a schematic representation of the four parts of the 1D modelling domain with colours matching those in Figure B.2. Note, the sub–simulation of the material stack with the stainless steel heater strip is still used, but not indicated in

---

[1] Recall, V_{BH} is $\pi \left(\left[2.175 \cdot 10^{-3}\right]^2 - \left[1.89 \cdot 10^{-3}\right]^2 \right) \cdot 10 \cdot 10^{-3} = 3.64 \cdot 10^{-8}$ m^3. So,

$$r = \frac{2.63 \cdot 10^{-9} + 8 \times 3.64 \cdot 10^{-8}}{2.63 \cdot 10^{-9}} = 111.93$$

the figure (that simulation provides heat input through the bottom edge of the blue rectangle representing the main helium channel).

The blue rectangle represents the main helium channel, as if seen down along the length of it. The inter–plate region is the green rectangle with B–labels. Its width B_x is 6.5 mm, and depth B_y is 5 µm. It continuously transitions into the bolt–hole helium region, the red rectangle, of width C_x 10 mm, and depth equal to that of the inter–plate helium region, B_y, 5 µm. In the figure, the red rectangle is made much taller than the green one to indicate that this is where the heat capacity is adjusted by the volume ratio between inter–plate and bolt–hole helium. The yellow rectangle is the aluminium bolt domain, of width D_x 13 mm, and height D_y 1.2 mm. The height is determined by taking the volume of the eight aluminium bolts in the simulation ($8 \times 13 \cdot 10^{-3} \times \pi \left[1.89 \cdot 10^{-3}\right]^2 = 1.17 \cdot 10^{-6}$ m^3) divided by the half–length of the channel (75 mm) and the length of the aluminium bolts (13 mm). The heat transfer area between the bolt–hole helium and the aluminium bolts as defined in the simulation is 10 mm times 75 mm which means $7.5 \cdot 10^{-4}$ m^2. In the real sample, the heat transfer area, due to bolt–hole helium surrounding the bolts, is $8 \times 2\pi \times 1.89 \cdot 10^{-3} \times 10 \cdot 10^{-3} = 9.5 \cdot 10^{-4}$ m^2. The discrepancy is small enough that a multiplicative factor of (9.5 / 7.5) can be used to adjust the heat transfer between the two domains for ease of implementation, without significant error being introduced. Heat flow in the aluminium bolts goes along the 13 mm length, and the cross section of the aluminium domain in the simulation is $75 \cdot 10^{-3} \times 1.2 \cdot 10^{-3} = 9 \cdot 10^{-5}$ m^2. This matches the real sample; $8 \times \pi \left[1.89 \cdot 10^{-3}\right]^2 = 8.98 \cdot 10^{-5}$ m^2.

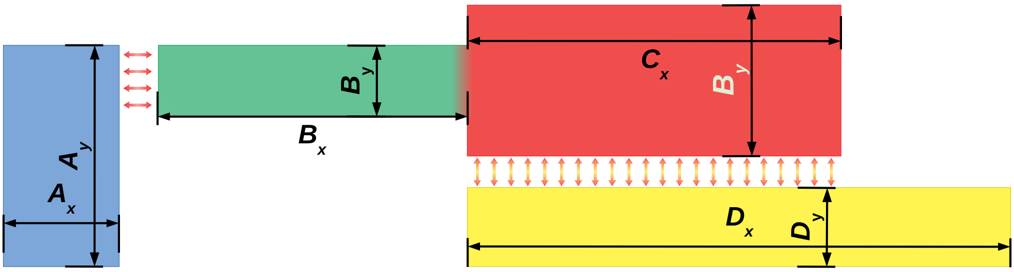

Figure B.3: Schematic representation of the equivalent 1D version of the 3D thermal path in Figure B.1.
Length A_x: width of main helium channel = 3.1 mm. A_y: depth of main helium channel = 120 µm. B_x: width inter–plate helium = 6.5 mm. B_y: depth of inter–plate helium = 5 µm. C_x: length of bolt–hole helium = 10 mm. D_x: length of aluminium bolts = 13 mm. D_y: equivalent thickness of aluminium bolts = 1.2 mm. The light green B_y denotes the depth of the bolt–hole helium region, which is the same 5 µm as the inter–plate helium. The rectangle representing the bolt–hole helium is taller than the one for inter–plate helium to indicate that this region is where the heat capacity is made larger to account for the real volume of helium.

Figure B.4 shows how the parts of the inter–plate / bolt–hole helium and aluminium bolt simulation domains interact from node to node. The colours of nodes match those used in figures B.2 and B.3.

To facilitate the calculation of heat transfer across the interface between the bolt–hole helium and aluminium, the aluminium domain has the same spatial grid size as the inter–plate/bolt–hole helium. Heat flux across the helium/aluminium boundary is calculated at each node, and handled like a volumetric source/sink. The left–most node of the aluminium sub–domain (yellow nodes) represents the middle of the real aluminium bolt that goes through the two bolt holes in the Top and Bottom PEEK plates (as seen in Figure B.2). As such, there is no heat flux to the left across this edge, so a zero–flux Neumann condition in the left–most node is used. The aluminium node touching the bulk bath outside the sample is kept at the bath temperature by a Dirichlet boundary condition.

The interface between the inter–plate helium and the channel helium is handled in a similar way to the interface between the main channel and the pin hole helium; the inter–plate helium has its left–most node kept at the channel temperature, and then the energy flowing from the hot channel into the cooler inter–plate region is determined by the temperature difference between the two left–most nodes in the inter–plate helium. Note that the sub–simulation of the channel helium runs along an axis that is essentially into/out of the plane of the paper in Figure B.4. Along this axis there is a small temperature gradient in the channel, which means the boundary temperature of the inter–plate helium, strictly speaking, changes along the length of the channel. However, the gradient is small, and a simplification has proven successful. By taking the boundary temperature on the edge of the inter–plate helium (left–most node of the green nodes in Figure B.4) as the hottest temperature in the channel helium, namely the temperature in the middle of the channel, and then scaling the heat flowing from channel to inter–plate helium by the ratio between the peak temperature and the local channel helium temperature, only a single inter–plate sub–simulation needs to be run, instead of one for each channel helium node. This method works because by the time energy is about to flow backwards, from inter–plate helium into the channel, the large equivalent heat capacity of the bolt–hole helium has kept the inter–plate helium temperature and channel helium temperatures relatively similar, so the actual reverse heat flow is small. This means the error made has a negligible impact on the simulation result in absolute terms.

Aside from the issues that arise from simplifying the 3D heat transfer path to 1D where all regions have been turned into blocks of material with roughly the right total volume and heat capacity, there are two important additional shortcomings with the approach that ultimately lead to this modelling effort not being considered reliable;

Inter–plate helium depth The inter–plate helium depth, taken to be a uniform 5 µm along the length of the channel, works as a free parameter in the model. When fitting the model result to measurement data, this depth is not the same from one measurement to another. For tests that deposit more energy into the channel helium, the inter–plate depth must be adjusted upwards. The largest steps require 7 µm to match the measured helium temperature rise, while small steps need it down at 2 µm. Some inter–plate helium exists; the two PEEK plates do not touch at all points, so there must be small tunnels/cracks along the length of the channel where tendrils of helium extend outwards. As such, if the random distribution of such tendrils is dense enough, their effect could probably be captured by a simple effective heat transfer area. But this area should not change from one test to another, since the sample itself remains the same.

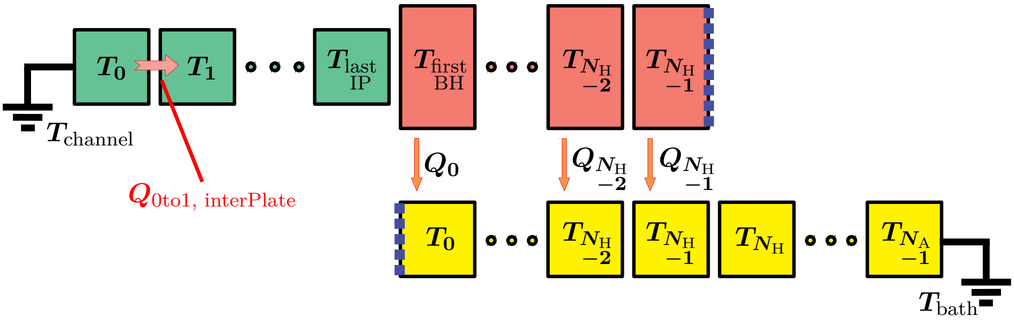

Figure B.4: Schematic representation of the chains of nodes making up the 1D inter–plate / bolt–hole helium and aluminium bolt simulation domains. T_0 in the inter–plate region (green) is fixed to T_{channel}, the peak temperature in the channel. $Q_{\text{0to1, interPlate}}$ denotes the heat flux flowing from the boundary node of the inter–plate helium to its neighbouring node, using Equation ((5.51)). This heat flux is used to determine the heat transfer from the main channel into the inter–plate helium. $T_{\text{last IP}}$ refers to the last node in the constricted part of the inter–plate helium, while $T_{\text{first BH}}$ refers to the first node in the bolt–hole part of the helium region. N_{H} is the total number of nodes in the helium region. The nodes starting from i = first BH (red) are made larger to indicate the adjusted heat capacity in these nodes. Q_i denotes the heat flux passing from a given bolt–hole helium node to the corresponding aluminium bolt node. The blue dashed line at the end of the bolt–hole helium region indicates the insulation boundary condition applied here. N_{A} is the number of nodes in the aluminium region. The aluminium bolt nodes protruding past the bolt–hole helium have no external heat sources, and they end in a node with its temperature fixed to that of the bulk bath outside the sample.

Continuity of thermal path The most important shortcoming of this modelling approach is that without the presence of the bolt–hole helium, which represents a much larger volume than the channel itself, there is no way to fit measured data. So the inter–plate helium would need to represent a uniform and continuous thermal connection to the bolt–hole helium. However, the bolt–hole helium is almost certainly effectively cut off from whatever inter–plate helium exists in the sample. The aluminium bolts are very tight, and obviously, nearest the holes themselves, the clamping force is the largest. Furthermore, the Kapton tape between the PEEK plates provide an additional seal, making it even less likely that a thermal connection really exists between the channel helium and the reservoirs of the bolt–holes.

BIBLIOGRAPHY

[1] J. B. Ghini, B. Auchmann, and B. Baudouy. “Millisecond Time–Scale Measurements of Heat Transfer to an Open Bath of He II”. In: *ArXiv: applied physics* (2022). DOI: `10.48550/arXiv.2203.04626`.

[2] J. B. Ghini, B. Auchmann, and B. Baudouy. “Millisecond Time–Scale Measurements of Heat Transfer to Confined He II”. In: *ArXiv: applied physics* (2022). DOI: `10.48550/arXiv.2203.04701`.

[3] ATLAS collaboration. “Observation of a new particle in the search for the Standard Model Higgs boson with the ATLAS detector at the LHC”. In: *Physics Letters B* 716.1 (2012), pp. 1–29. ISSN: 0370–2693. DOI: `10.1016/j.physletb.2012.08.020`.

[4] CMS collaboration. “Observation of a new boson at a mass of 125 GeV with the CMS experiment at the LHC”. In: *Physics Letters B* 716.1 (2012), pp. 30–61. ISSN: 0370–2693. DOI: `10.1016/j.physletb.2012.08.021`.

[5] T. S. Virdee. “Beyond the standard model of particle physics”. In: *Philosophical Transactions of the Royal Society A: Mathematical, Physical and Engineering Sciences* 374.2075 (2016), p. 20150259. DOI: `10.1098/rsta.2015.0259`.

[6] Burkhard Schmidt. “The High-Luminosity upgrade of the LHC: Physics and Technology Challenges for the Accelerator and the Experiments”. In: *Journal of Physics: Conference Series* 706 (Apr. 2016), p. 022002. DOI: `10.1088/1742-6596/706/2/022002`.

[7] Frank Zimmermann et al. *HE-LHC: The High-Energy Large Hadron Collider: Future Circular Collider Conceptual Design Report Volume 4. Future Circular Collider*. Tech. rep. Geneva: CERN, 2018. DOI: `10.1140/epjst/e2019-900088-6`. URL: `https://cds.cern.ch/record/2651305`.

[8] A.W. Chao. *Handbook of Accelerator Physics and Engineering*. World Scientific, 2013. ISBN: 9789814415842.

[9] Y. Iwasa. *Case Studies in Superconducting Magnets: Design and Operational Issues*. Springer US, 2010. ISBN: 9781441935397.

[10] L Bottura. "Cable Stability". In: (2014). Comments: 51 pages, contribution to the CAS-CERN Accelerator School: Superconductivity for Accelerators, Erice, Italy, 24 April - 4 May 2013, edited by R. Bailey, 50 p. DOI: `10.5170/CERN-2014-005.401`. URL: `https://cds.cern.ch/record/1974064`.

[11] Helmut Wiedemann. "Beam Life Time". In: *Particle Accelerator Physics: Basic Principles and Linear Beam Dynamics*. Berlin, Heidelberg: Springer Berlin Heidelberg, 1993, pp. 370–383. ISBN: 978–3–6620–2903–9. DOI: `10.1007/978-3-662-02903-9_11`.

[12] M. Sapinski et al. "Beam Induced Quenches of LHC Magnets". In: *Proceedings of IPAC 2013, Shanghai, China*. THPEA045. 2013, pp. 3243–3245.

[13] K. Wittenburg. "Beam Losses and Machine Protection". In: *AIP Conference Proceedings*. Vol. 773. 2004.

[14] A. Valishev. "Tevatron Accelerator Physics and Operational Highlights". In: *AIP Conference Proceedings*. Vol. 773. 2004.

[15] M. Bai. "Beam–Losses and Beam–Induced Quenches at BNL". In: *Proceedings of the 2014 Workshop on Beam-Induced Quenches, Geneva, Switzerland*. 2014.

[16] T Baer et al. "UFOs in the LHC after LS1". In: (2012), 5 p. DOI: `10.5170/CERN-2012-006.294`. URL: `http://cds.cern.ch/record/1493018`.

[17] B Auchmann, J Ghini, L Grob, G Iadarola, A Lechner, and G Papotti. "How to survive a UFO attack". In: (2016). 6th Evian Workshop on LHC beam operation, pp. 81–86. URL: `http://cds.cern.ch/record/2294520`.

[18] Tobias Baer. "Very Fast Losses of the Circulating LHC Beam, their Mitigation and Machine Protection". 2013. URL: `https://cds.cern.ch/record/1637966`.

[19] Scott M. Rowan. "LHC main dipole magnet circuits: sustaining near–nominal beam energies". PhD thesis. 2016. URL: `http://cds.cern.ch/record/2229989`.

[20] Bernhard Auchmann. Personal communication. 2016.

[21] B Dehning, A Priebe, and M Sapinski. *Simulation of Beam Loss in LHC MB Magnet and Quench threshold test*. Tech. rep. Geneva: CERN, 2009. URL: `https://cds.cern.ch/record/1174032`.

[22] B. Auchmann et al. "Testing beam–induced quench levels of LHC superconducting magnets". In: *Phys. Rev. ST Accel. Beams* 18 (6 June 2015), p. 061002. DOI: `10.1103/PhysRevSTAB.18.061002`.

[23] A. Verweij. *QP3: User's Manual*. CERN. 2008. URL: `https://edms.cern.ch/document/1150045/1`.

[24] A. Priebe, J. Steckert, A. Verweij, et al. “Beam-induced Quench Test of a LHC Main Quadrupole”. In: *Conf. Proc. C* 110904 (2011). Ed. by Christine Petit-Jean-Genaz, pp. 2388–2390. URL: `http://accelconf.web.cern.ch/AccelConf/IPAC2011/papers/WEPC172.pdf`.

[25] Oliver Sim Brüning, Paul Collier, P Lebrun, Stephen Myers, Ranko Ostojic, John Poole, and Paul Proudlock. *LHC Design Report*. CERN Yellow Reports: Monographs. Geneva: CERN, 2004. DOI: `10.5170/CERN-2004-003-V-1`. URL: `https://cds.cern.ch/record/782076`.

[26] L. Bottura. “Magnet Quench 101”. In: (2014). Comments: 9 pages, Contribution to WAMSDO 2013: Workshop on Accelerator Magnet, Superconductor, Design and Optimization; 15 - 16 Jan 2013, CERN, Geneva, Switzerland. DOI: `10.5170/CERN-2013-006.1`. arXiv: `1401.3927`. URL: `https://cds.cern.ch/record/1643429`.

[27] A. Apollonio, B. Auchmann, L. Ponce, C. Roderick, R. Schmidt, M. Solfaroli, B. Todd, D. Wollmann, and M. Zerlauth. “2015 availability summary”. In: *6th Evian Workshop on LHC beam operation*. CERN, 2016, pp. 19–28.

[28] Robert D. Mc Carty. “Thermodynamic Properties of Helium 4 from 2 to 1500 K at Pressures to 10^8 Pa”. In: *Journal of Physical and Chemical Reference Data* 2.4 (1973), pp. 923–1042. DOI: `10.1063/1.3253133`.

[29] A. Driessen, E. van der Poll, and Isaac F. Silvera. “Equation of state of solid ^{4}He”. In: *Phys. Rev. B* 33 (5 1986), pp. 3269–3288. DOI: `10.1103/PhysRevB.33.3269`.

[30] S.W. Van Sciver. *Helium Cryogenics*. 2nd ed. International Cryogenics Monograph Series. Springer New York, 2012. ISBN: 978–1–4419–9978–8. DOI: `10.1007/978-1-4419-9979-5`.

[31] H. Kinder, J. Weber, and W. Dietsche. “Kapitza Resistance Studies Using Phonon Pulse Reflection”. In: *Phonon Scattering in Condensed Matter*. Ed. by Humphrey J. Maris. Boston, MA: Springer US, 1980, pp. 173–180. ISBN: 978-1-4613-3063-9. DOI: `10.1007/978-1-4613-3063-9_41`.

[32] P. L. Kapitza. “The Study of Heat Transfer in Helium II”. In: *Journal of Physics USSR* 4 (1941). Source used: Chapter 38 in *Collected Papers of P.L. Kapitza, Volume 2*, by D. Ter Haar, Pergamon, 1965.

[33] C Kittel. *Introduction to Solid State Physics*. 6th edition. Wiley, 1986. ISBN: 978–0–4718–7474–4.

[34] J. D. N. Cheeke. “The Kapitza Resistance and Heat Transfer at Low Temperatures”. In: *Journal de Physique Colloques* 31.C3 (1970), pp. C3-129–C3-136. DOI: `10.1051/jphyscol:1970312`. URL: `https://hal.archives-ouvertes.fr/jpa-00213855`.

[35] A. F. G. Wyatt. “KAPITZA CONDUCTANCE OF SOLID-LIQUID He INTERFACES”. In: *Nonequilibrium Superconductivity, Phonons, and Kapitza Boundaries*. Ed. by K. E. Gray. Nato Science Series B: 1981, pp. 31–72. ISBN: 9781468439359.

[36] RS Hydro. *Sound Speeds in Water, Liquid and Materials*. [Online; accessed 28-Oct-2021]. 2021. URL: `https://www.rshydro.co.uk/sound-speeds/`.

[37] Vedran Rajevac. “Lattice dynamics in Hydrogenated Austenitic Stainless Steels and in the Superionic Conductor Cu 2-δ Se.” PhD thesis. Darmstadt, Technische Universität, 2005.

[38] Euro Inox. *Roughness measurements of stainless steel surfaces*. [Online; accessed 28-Oct-2021]. 2014. URL: `https://www.worldstainless.org/Files/issf/non-image-files/PDF/Euro_Inox/RoughnessMeasurement_EN.pdf`.

[39] R. J. Donnelly and C. F. Barenghi. “The Observed Properties of Liquid Helium at the Saturated Vapor Pressure”. In: *Journal of Physical and Chemical Reference Data* 27.6 (1998), pp. 1217–1274. DOI: `10.1063/1.556028`.

[40] L J Challis. “Kapitza resistance and acoustic transmission across boundaries at high frequencies”. In: 7.3 (1974), pp. 481–495. DOI: `10.1088/0022-3719/7/3/005`.

[41] I. M. Khalatnikov. *An Introduction to the Theory of Superfluidity*. Ed. by David Pines. Trans. Russian by Pierre C. Hohenberg. Advanced Book Classics. Russian printing in 1965. Westview Press, 2000.

[42] N.S. Snyder. *Thermal Conductance at the Interface of a Solid and Helium II (Kapitza Conductance)*. NBS technical note. U.S. National Bureau of Standards, 1969. URL: `https://nvlpubs.nist.gov/nistpubs/Legacy/TN/nbstechnicalnote385.pdf`.

[43] J. M. Winey, Y. M. Gupta, and D. E. Hare. “r-Axis Sound Speed and Elastic Properties of Sapphire Single Crystals”. In: *Journal of Applied Physics* 90.6 (2001), pp. 3109–3111. DOI: `10.1063/1.1391420`.

[44] M. K. Wallace, J. M. Winey, and Y. M. Gupta. “Sound speed measurements in lithium fluoride single crystals shock compressed to 168 GPa along [100]”. In: *Journal of Applied Physics* 130.3 (2021), p. 035901. DOI: `10.1063/5.0056659`.

[45] L. J. Challis, K. Dransfeld, and J. Wilks. “Heat transfer between solids and liquid helium II”. In: *Proceedings of the Royal Society of London. Series A. Mathematical and Physical Sciences* 260.1300 (1961). Communicated by Bleaney, Brebis, pp. 31–46. DOI: `10.1098/rspa.1961.0011`.

[46] M Vuorio. “The effect of low energy vibrational modes on the Kapitza resistance”. In: 5.11 (1972), pp. 1216–1221. DOI: `10.1088/0022-3719/5/11/016`.

[47] Paul H. E. Meijer and Joseph S. J. Peri. “New Kapitza heat-transfer model for liquid ^{4}He”. In: *Phys. Rev. B* 22 (1 1980), pp. 195–205. DOI: 10.1103/PhysRevB.22.195.

[48] R. C. Johnson and W. A. Little. “Experiments on the Kapitza Resistance”. In: *Phys. Rev.* 130 (2 1963), pp. 596–604. DOI: 10.1103/PhysRev.130.596.

[49] R.E. Peterson and A.C. Anderson. “Acoustic-mismatch model of the Kaptiza resistance”. In: *Physics Letters A* 40.4 (1972), pp. 317–319. ISSN: 0375-9601. DOI: 10.1016/0375-9601(72)90589-0.

[50] H. Haug and K. Weiss. “A modified theory of the Kapitza resistance”. In: *Physics Letters A* 40.1 (1972), pp. 19–21. ISSN: 0375-9601. DOI: 10.1016/0375-9601(72)90179-X.

[51] W. A. Little. “The Transport of Heat Between Dissimilar Solids at Low Temperatures”. In: *Canadian Journal of Physics* 37.3 (1959), pp. 334–349. DOI: 10.1139/p59-037. URL: 10.1139/p59-037.

[52] W. A. Little. “Unimportance of Surface Roughness Upon the Kapitza Resistance”. In: *Phys. Rev.* 123 (6 1961), pp. 1909–1911. DOI: 10.1103/PhysRev.123.1909.

[53] N. S. Shiren. “Surface Roughness Contribution to Kapitza Conductance”. In: *Phys. Rev. Lett.* 47 (20 1981), pp. 1466–1469. DOI: 10.1103/PhysRevLett.47.1466.

[54] A. Khater and J. Szeftel. “Theory of the Kapitza resistance”. In: *Phys. Rev. B* 35 (13 1987), pp. 6749–6755. DOI: 10.1103/PhysRevB.35.6749.

[55] Aymeric Ramiere, Sebastian Volz, and Jay Amrit. “Thermal resistance at a solid/superfluid helium interface”. In: *Nature materials* 15.5 (2016), pp. 512–516. DOI: 10.1038/nmat4574.

[56] I. N. Adamenko and I. M. Fuks. “Roughness and thermal resistance of the boundary between a solid and liquid helium”. In: *Soviet Journal of Experimental and Theoretical Physics* 32.6 (1971), pp. 1123–1129.

[57] J. G. Dash. “7 - Solid Phases and Melting Phenomena”. In: *Films on Solid Surfaces*. Ed. by J. G. Dash. Academic Press, 1975, pp. 145–186. ISBN: 978-0-12-203350-6. DOI: 10.1016/B978-0-12-203350-6.50011-6.

[58] B. W. Clement and T. H. K. Frederking. “Thermal Boundary Resistance and Related Peak Flux During Supercritical Heat Transport from a Horizontal Surface Through a Short Tube to a Saturated Bath of Liquid He II”. In: *Liquid Helium Technology*. Vol. 6. Pure and Applied Cryogenics. Elsevier, 1966, pp. 49–59. DOI: 10.1016/B978-0-08-012409-4.50008-5.

[59] S.W. Van Sciver. “Kapitza conductance of aluminium and heat transport through subcooled He II”. In: *Cryogenics* 18.9 (1978), pp. 521–527. ISSN: 0011-2275. DOI: 10.1016/0011-2275(78)90152-2.

[60] K. Mittag. “Kapitza conductance and thermal conductivity of copper niobium and aluminium in the range from 1.3 to 2.1 K”. In: *Cryogenics* 13.2 (1973), pp. 94–99. ISSN: 0011-2275. DOI: 10.1016/0011-2275(73)90132-X.

[61] G. Claudet and P. Seyfert. “Bath cooling with subcooled superfluid helium”. In: *Advances in Cyrogenic Engineering, Vol. 27*. Ed. by R. W. Fast. Plenum Press, 1982, pp. 441–450.

[62] A. Kashani and S. W. Van Sciver. “High heat flux Kapitza conductance of technical copper with several different surface preparations”. In: *Cryogenics* 25.5 (1985), pp. 238–242. ISSN: 0011–2275. DOI: 10.1016/0011-2275(85)90202-4.

[63] J. S. Goodling and R. K. Irey. “Non-Boiling and Film Boiling Heat Transfer to a Saturated Bath of Liquid Helium”. In: *Advances in Cryogenic Engineering*. Ed. by K. D. Timmerhaus. Vol. 14. Springer US, 1969, pp. 159–169. ISBN: 978-1-4757-0549-2. DOI: 10.1007/978-1-4757-0549-2_19.

[64] E.A. Jones and J. C. A. van der Sluijs. “Some experiments on the influence of surface treatment on the Kapitza conductance between copper and He4 at temperatures from 1.2 to 2.0 k”. In: *Cryogenics* 13.9 (1973), pp. 535–542. ISSN: 0011-2275. DOI: 10.1016/0011-2275(73)90242-7.

[65] M. Shiotsu, K. Hata, and A. Sakurai. “Comparison of transient heat transfer characteristics for large stepwise heat input in He I and He II”. In: *Cryogenics* 32.5 (1992). Basic Mechanisms of Helium Heat Transfer and Related Influence on Stability of Superconducting Magnets, pp. 455–460. ISSN: 0011–2275. DOI: 10.1016/0011-2275(92)90075-L.

[66] A. Sakurai, M. Shiotsu, and K. Hata. “Effect of System Pressure and Liquid Subcooling on Quasi-Steady Nucleate Boiling and its Life for Liquid Helium I”. In: *Advances in Cryogenic Engineering: Part A & B*. Ed. by R. W. Fast. Springer US, 1990, pp. 377–385. ISBN: 978-1-4613-0639-9. DOI: 10.1007/978-1-4613-0639-9_45.

[67] M. Taneda, T. Miki, and T. Ohtani. “The Kapitza conductance of PVF-coated copper and some materials used for superconducting magnets”. In: *Cryogenics* 32.5 (1992). Basic Mechanisms of Helium Heat Transfer and Related Influence on Stability of Superconducting Magnets, pp. 479–484. ISSN: 0011–2275. DOI: 10.1016/0011-2275(92)90079-P.

[68] Wikipedia. *Levenberg-–Marquardt algorithm*. [Online; accessed 08-Nov-2021]. 2021. URL: https://en.wikipedia.org/wiki/Levenberg%E2%80%93Marquardt_algorithm.

[69] W.H. Keesom and A.P. Keesom. “New measurements on the specific heat of liquid helium”. In: *Physica* 2.1 (1935), pp. 557–572. ISSN: 0031-8914. DOI: `10.1016/S0031-8914(35)90128-8`.

[70] Tony Guenault. *Basic superfluids.* 1st ed. Master’s Series in Physics and Astronomy. CRC Press, 2002. ISBN: 978–0–4292–1799–9. DOI: `10.1201/9780203212332`.

[71] W.H. Keesom and A.P. Keesom. “On the heat conductivity of liquid helium”. In: *Physica* 3.5 (1936), pp. 359–360. ISSN: 0031-8914. DOI: `10.1016/S0031-8914(36)80312-7`.

[72] Kapitza P. L. “Viscosity of Liquid Helium below the λ-Point”. In: *Nature* 141 (1938), p. 74. DOI: `10.1038/141074a0`.

[73] Allen J. F. and Misener A. D. “Flow of Liquid Helium II”. In: *Nature* 141 (1938), p. 75. DOI: `10.1038/141075a0`.

[74] V. D. Arp, R. D. McCarty, and Friend D. G. *Thermophysical properties of Helium-4 from 0. 8 to 1500 K with pressures to 2000 MPa.* Tech. rep. NIST Technical Note 1334 (revised). National Institute of Standards and Technology, 1989. URL: `https://nvlpubs.nist.gov/nistpubs/Legacy/TN/nbstechnicalnote1334.pdf`.

[75] F. London. “The λ–Phenomenon of Liquid Helium and the Bose-Einstein Degeneracy”. In: *Nature* 141 (Apr. 1938), pp. 643–644. DOI: `10.1038/141643a0`.

[76] L. Tisza. “Transport Phenomena in Helium II”. In: *Nature* 141 (May 1938), p. 913. DOI: `10.1038/141913a0`.

[77] L. Landau. “Theory of the Superfluidity of Helium II”. In: *Phys. Rev.* 60 (4 1941), pp. 356–358. DOI: `10.1103/PhysRev.60.356`.

[78] James F Annett et al. *Superconductivity, superfluids and condensates.* Oxford Master Series in Condensed Matter Physics. Oxford University Press, 2004.

[79] R. P. Feynman. *Statistical Mechanics. A set of lectures.* Ed. by David Pines and Jacob Shaham. Advanced Book Classics. The Benjamin/Cummings Publishing Company, 1972. ISBN: 0–8053–2509–3.

[80] L. Landau. “On the Theory of Superfluidity of Helium II”. In: *Journal of Physics* 11 (1947). Reprinted in Khalatnikov’s book[41, Part V.], pp. 91–92.

[81] D. R. Tilley and J. Tilley. *Superfluidity and Superconductivity.* Modern University Physics Series. Van Nostrand Reinhold Company, 1974. ISBN: 978–0–4423–0015–9.

[82] H. Godfrin, K. Beauvois, A. Sultan, E. Krotscheck, J. Dawidowski, B. Fåk, and J. Ollivier. “Dispersion relation of Landau elementary excitations and ther-

modynamic properties of superfluid ^{4}He”. In: *Phys. Rev. B* 103 (10 2021), p. 104516. DOI: 10.1103/PhysRevB.103.104516.

[83] L. Tisza. “Sur la théorie des liquides quantiques. Application a l’hélium liquide”. In: *J. Phys. Radium* 1.5 (1940), pp. 164–172. DOI: 10.1051/jphysrad:0194000105016400.

[84] L. Tisza. “Sur la théorie des liquides quantiques. Application à l’hélium liquide. II”. In: *J. Phys. Radium* 1.8 (1940), pp. 350–358. DOI: 10.1051/jphysrad:0194000108035000.

[85] Laszlo Tisza. “The Theory of Liquid Helium”. In: *Physical Review* 72 (9 1947), pp. 838–854. DOI: 10.1103/PhysRev.72.838.

[86] Russell J. Donnelly. “The two-fluid theory and second sound in liquid helium”. In: *Physics Today* 62.10 (2009), pp. 34–39. DOI: 10.1063/1.3248499.

[87] E. Andronikashvili. “A Direct Observation of Two Kinds of Motion in Helium II”. In: *Helium 4*. Ed. by Zygmunt M. Galasiewicz. Original English translation published in: J. Phys. (U.S.S.R.) 10, 201 (1946). Pergamon, 1971, pp. 154–165. ISBN: 978-0-08-015816-7. DOI: /10.1016/B978-0-08-015816-7.50015-8.

[88] R. G. Hussey, B. J. Good, and J. M. Reynolds. “Oscillation of Two Cylinders in Liquid Helium”. In: *The Physics of Fluids* 10.1 (1967), pp. 89–95. DOI: 10.1063/1.1762000.

[89] S. Caspi. “Gravitational Convection of Sub–cooled He I and the Transition into Superfluid He II at Atmospheric Pressure”. In: *Presented at the 8th International Cryogenic Engineering Conference, Genoa, Italy*. 1980. URL: https://escholarship.org/content/qt6x0277ts/qt6x0277ts.pdf.

[90] L. J. Campbell. “Relation between the condensate fraction and the surface tension of superfluid ^{4}He”. In: *Physical Review B* 27 (3 1983), pp. 1913–1915. DOI: 10.1103/PhysRevB.27.1913.

[91] A. J. Leggett. *Quantum Liquids: Bose Condensation and Cooper Pairing in Condensed-matter Systems*. Oxford Graduate Texts. Oxford University Press, 2006. ISBN: 978–0–1985–2643–8. DOI: 10.1093/acprof:oso/9780198526438.001.0001.

[92] C.J. Gorter and J.H. Mellink. “On the irreversible processes in liquid helium II”. In: *Physica* 15.3 (1949), pp. 285–304. ISSN: 0031-8914. DOI: 10.1016/0031-8914(49)90105-6.

[93] F.M. White. *Fluid Mechanics*. McGraw–Hill series in mechanical engineering. International edition. McGraw–Hill, 2009. ISBN: 978–0–0712–7038–0.

[94] F. London and P. R. Zilsel. “Heat Transfer in Liquid Helium II by Internal Convection”. In: *Physical Review* 74 (9 1948), pp. 1148–1156. DOI: 10.1103/PhysRev.74.1148.

[95] P. P. Granieri, B. Baudouy, A. Four, F. Lentijo, A. Mapelli, P. Petagna, and D. Tommasini. “Steady-State heat transfer through micro-channels in pressurized He II”. In: *AIP Conference Proceedings* 1434.1 (2012), pp. 231–238. DOI: `10.1063/1.4706925`.

[96] Pier Paolo Granieri. “Heat transfer between the superconducting cables of the LHC accelerator magnets and the superfluid helium bath”. Presented 29 Aug 2012. Apr. 2012. URL: `https://cds.cern.ch/record/1479179`.

[97] P. C. Hemmer, H. Holden, and S. K. Ratkje. *The Collected Works of Lars Onsager*. WORLD SCIENTIFIC, 1996. DOI: `10.1142/3027`.

[98] R. P. Feynman. “Chapter II Application of Quantum Mechanics to Liquid Helium”. In: ed. by C.J. Gorter. Vol. 1. Progress in Low Temperature Physics. Elsevier, 1955, pp. 17–53. DOI: `10.1016/S0079-6417(08)60077-3`.

[99] W. F. Vinen. “Mutual friction in a heat current in liquid helium II III. Theory of the mutual friction”. In: *Proceedings of the Royal Society of London. Series A. Mathematical and Physical Sciences* 242.1231 (1957). Communicated by David Shoenberg, pp. 493–515. DOI: `10.1098/rspa.1957.0191`.

[100] W. F. Vinen. “Mutual friction in a heat current in liquid helium II. II. Experiments on transient effects”. In: *Proceedings of the Royal Society of London. Series A. Mathematical and Physical Sciences* 240.1220 (1957). Communicated by David Shoenberg, pp. 128–143. DOI: `10.1098/rspa.1957.0072`.

[101] C. E. Chase. “Thermal Conduction in Liquid Helium II. II. Effects of Channel Geometry”. In: *Phys. Rev.* 131 (5 Sept. 1963), pp. 1898–1903. DOI: `10.1103/PhysRev.131.1898`.

[102] C. E. Chase. “Thermal Conduction in Liquid Helium II. I. Temperature Dependence”. In: *Physical Review* 127 (2 July 1962), pp. 361–370. DOI: `10.1103/PhysRev.127.361`.

[103] R. Wang. “Criterion for quantum turbulence onset after rectangular heat pulse in superfluid helium”. In: *Cryogenics* 35.12 (1995), pp. 883–886. ISSN: 0011–2275. DOI: `10.1016/0011-2275(95)96886-Q`.

[104] R. J. Donnelly and C. E. Swanson. “Quantum turbulence”. In: *Journal of Fluid Mechanics* 173 (1986), pp. 387–429. DOI: `10.1017/S0022112086001210`.

[105] A. Sato, M. Maeda, and Y. Kamioka. “Chapter 201 - Normalized representation for steady state heat transport in a channel containing He II covering pressure range up to 1.5 MPa”. In: *Proceedings of the Twentieth International Cryogenic Engineering Conference (ICEC 20)*. Ed. by Liang Zhang, Liangzhen Lin, and Guobang Chen. Oxford: Elsevier Science, 2005, pp. 849–852. ISBN: 978-0-08-044559-5. DOI: `10.1016/B978-008044559-5/50204-0`.

[106] A. Sato, M. Maeda, T. Dantsuka, M. Yuyama, and Y. Kamioka. “Temperature Dependence of the Gorter–Mellink Exponent m Measured in a Channel Con-

taining He II". In: *AIP Conference Proceedings* 823.1 (2006), pp. 387–392. DOI: 10.1063/1.2202439.

[107] A. Vitrano, R. Bruce, and B. Baudouy. "Transient Conjugate Heat Transfer Numerical Simulation in Superfluid Helium". In: *IOP Conference Series: Materials Science and Engineering* 755 (2020), p. 012068. DOI: 10.1088/1757-899x/755/1/012068.

[108] Andrea Vitrano and Bertrand Baudouy. "Double phase transition numerical modeling of superfluid helium for fixed non-uniform grids". In: *Computer Physics Communications* 273 (2022), p. 108275. ISSN: 0010–4655. DOI: 10.1016/j.cpc.2021.108275.

[109] S. W. Van Sciver. "Developments in He II Heat Transfer and Applications to Superconducting Magnets". In: *Advances in Cyrogenic Engineering, Vol. 27*. Ed. by R. W. Fast. Plenum Press, 1982, pp. 375–398.

[110] A. Sakurai, M. Shiotsu, and K. Hata. "Transient Heat Transfer for Large Stepwise Heat Inputs to a Horizontal Wire in Saturated He II". In: *Advances in Cryogenic Engineering, 37A*. Ed. by R. W. Fast. Plenum Press, 1992, pp. 25–35.

[111] G. P. Lemieux and A. C. Leonard. "Maximum and Minimum Heat Flux in Helium II for a 76.2 µm Diameter Horizontal Wire at Depths of Immersion up to 70 Centimetres". In: *Advances in Cyrogenic Engineering, 13*. Ed. by K. D. Timmerhaus. Springer Science+Business Media, 1967, pp. 624–631.

[112] M. Shiotsu, K. Hata, and A. Sakurai. "Transient Heat Transfer for Large Stepwise Heat Inputs to a Horizontal Wire in Subcooled He II". In: *Advances in Cryogenic Engineering, 37A*. Ed. by R. W. Fast. Plenum Press, 1992, pp. 37–46.

[113] M. Shiotsu, K. Hata, and A. Sakurai. "Effect of Test Heater Diameter on Critical Heat Flux in He II". In: *Advances in Cryogenic Engineering, 39*. Ed. by P. Kittel. (Note: data for two more wire diameters at lower temperatures are available in the Annual Report of National Institute for Fusion Science: `https://nifs-repository.repo.nii.ac.jp/?action=repository_uri&item_id=7875&file_id=25&file_no=1)`. Plenum Press, 1994, pp. 1797–1804.

[114] H. Tatsumoto, K. Hata, K. Hama, Y. Shirai, and M. Shiotsu. "Critical heat flux on a flat plate in pressurized He II". In: *Cryogenics* 41.1 (2001), pp. 35–38. ISSN: 0011–2275. DOI: 10.1016/S0011-2275(01)00048-0.

[115] H. Tatsumoto, K. Hata, K. Hama, Y. Shirai, and M. Shiotsu. "Heat Transfer in Superfluid Helium (1) Steady–state Heat Tansfer and Its Critical Heat Flux". In: *TEION KOGAKU (Journal of Cryogenics and Superconductivity Society of Japan)* 36.12 (2001), pp. 656–663. DOI: 10.2221/jcsj.36.656.

[116] J. A. Katerberg and A. C. Anderson. "Comparison of steady-state and second-sound measurements of the Kapitza resistance". In: *Journal of Low Temperature Physics* 42.1 (1981), pp. 165–176. DOI: 10.1007/BF00116702.

[117] H. Kobayashi, K. Yasukochi, and K. Tokuyama. "Heat Transfer to Liquid Helium in a Narrow Channel Below 4.2 K". In: *Proceedings of the Sixth International Cryogenic Engineering Conference (ICEC 6)*. Ed. by K. Mendelssohn. IPC Science and Technology Press, 1976, pp. 307–309.

[118] Th. Gradt, U. Ruppert, K. Lüders, and Wang Ruzhu. "Transient Heat Transfer to Superfluid Liquid Helium". In: *Advances in Cryogenic Engineering 35A*. Ed. by R. W. Fast. Boston, MA: Springer US, 1990, pp. 117–123. ISBN: 978-1-4613-0639-9. DOI: 10.1007/978-1-4613-0639-9_14.

[119] S. W. Van Sciver and R. L. Lee. "Heat Transfer to Helium-II in Cylindrical Geometries". In: *Advances in Cryogenic Engineering 35A*. Ed. by K. D. Timmerhaus and H. A. Snyder. Springer US, 1980, pp. 363–371. ISBN: 978-1-4613-9856-1. DOI: 10.1007/978-1-4613-9856-1_43.

[120] S. Caspi and T.H.K. Frederking. "Triple–phase phenomena during quenches of superconductors cooled by pressurized superfluid helium II". In: *Cryogenics* 19.9 (1979), pp. 513–516. ISSN: 0011–2275. DOI: 10.1016/0011-2275(79)90003-1.

[121] S.W. Van Sciver. "Transient heat transport in He II". In: *Cryogenics* 19.7 (1979), pp. 385–392. ISSN: 0011–2275. DOI: 10.1016/0011-2275(79)90120-6.

[122] Baudouy Bertrand. "Heat-balance integral method for heat transfer in superfluid helium". In: *Thermal Science* 13.2 (2009), pp. 121–132. DOI: 10.2298/TSCI0902121B.

[123] P. Seyfert, J. Lafferranderie, and G. Claudet. "Time dependent heat transport in subcooled superfluid helium". In: *Cryogenics* 22.8 (1982), pp. 401–408. ISSN: 0011–2275. DOI: 10.1016/0011-2275(82)90084-4.

[124] R. Wang, T. Gradt, U. Ruppert, L. Xu, H. D. Denner, and G. Klipping. "Film Boiling Onset Time in Subcooled Superfluid Helium: The Influence of Bath Temperature and Pressure". In: *Proceedings of the Thirteenth International Cryogenic Engineering Conference (ICEC 13)*. Ed. by C. S. Hong. Cryogenics 1990 Vol 30 September supplement. 1990, pp. 360–364.

[125] Shiotsu M., Hata K., Hama K., and Shirai Y. "Transient Heat Transfer Produced by a Stepwise Heat Input to a Flat Plate on One End of a Rectangular Duct Containing Pressurized He II". In: *Advances in Cyrogenic Engineering 45B*. Ed. by Q. Shu. Plenum Press, 2000, pp. 1065–1072. ISBN: 978-1-4615-4215-5. DOI: 10.1007/978-1-4615-4215-5_14.

[126] Shiotsu M., Hata K., and A. Sakurai. "Transient Heat Transfer From a Horizontal Wire in Subcooled He II at Atmospheric Pressure for a Wide Range of

Wire Diameter”. In: *Advances in Cyrogenic Engineering 41*. Ed. by P. Kittel. Plenum Press, 1996, pp. 1065–1072. ISBN: 978-1-4613-0373-2. DOI: 10.1007/978-1-4613-0373-2_31.

[127] S.K. Nemirovskii and A.N. Tsoi. “Transient thermal and hydrodynamic processes in superfluid helium”. In: *Cryogenics* 29.10 (1989), pp. 985–994. ISSN: 0011–2275. DOI: 10.1016/0011-2275(89)90246-4.

[128] W. Fiszdon, M. von Schwerdtner, G. Stamm, and W. Poppe. “Temperature overshoot due to quantum turbulence during the evolution of moderate heat pulses in He II”. In: *Journal of Fluid Mechanics* 212 (1990), pp. 663–684. DOI: 10.1017/S0022112090002130.

[129] T. Shimazaki, M. Murakami, and T. Iida. “Second sound wave heat transfer, thermal boundary layer formation and boiling: highly transient heat transport phenomena in He II”. In: *Cryogenics* 35.10 (1995), pp. 645–651. ISSN: 0011–2275. DOI: 10.1016/S0011-2275(99)80005-8.

[130] T. Okamura, Y. Yoshizawa, A. Sato, K. Ishito, S. Kabashima, and S. Shioda. “Time dependent heat transfer in pressurized superfluid helium”. In: *Cryogenics* 29.11 (1989), pp. 1070–1074. ISSN: 0011–2275. DOI: 10.1016/0011-2275(89)90263-4.

[131] S. Fuzier and S.W. Van Sciver. “Experimental measurements and modeling of transient heat transfer in forced flow of He II at high velocities”. In: *Cryogenics* 48.3 (2008), pp. 130–137. ISSN: 0011–2275. DOI: 10.1016/j.cryogenics.2008.02.004.

[132] *Measurements of heat transfer to helium II at atmospheric pressure in a confined geometry*. 1981. URL: https://escholarship.org/content/qt2gg9z5zh/qt2gg9z5zh.pdf.

[133] H. Kobayashi, Y. Fujimura, T. Murata, and M. Sakata. “Heat transfer through subcooled He I layer from distributed heat source in a pressurized He II channel”. In: *Cryogenics* 37.12 (1997), pp. 851–855. ISSN: 0011–2275. DOI: 10.1016/S0011-2275(97)00145-8.

[134] S.R. Breon and S.W. Van Sciver. “Boiling phenomena in pressurized He II confined to a channel”. In: *Cryogenics* 26.12 (1986), pp. 682–691. ISSN: 0011–2275. DOI: 10.1016/0011-2275(86)90169-4.

[135] Z. Chen and S.W. Van Sciver. “Channel heat transfer in He II — steady state orientation dependence”. In: *Cryogenics* 27.11 (1987), pp. 635–640. ISSN: 0011–2275. DOI: 10.1016/0011-2275(87)90086-5.

[136] J. C. Lottin and S. W. Van Sciver. “Heat Transport Mechanisms in a 2.3 m Long Cooling Loop Containing He II”. In: *Proceedings of the Ninth International Cryogenic Engineering Conference, Kobe, Japan, 11–14 May 1982*. Ed.

by Yasukochi and Nagano. Butterworth–Heinemann, 1982, pp. 269–272. ISBN: 978–0–408–01252–2. DOI: 10.1016/B978-0-408-01252-2.50070-4.

[137] T. Okamura, T. Suzuki, N. Seki, and S. Kabashima. “Heat transport in He II channel with phase transition”. In: *Cryogenics* 34.3 (1994), pp. 187–193. ISSN: 0011–2275. DOI: 10.1016/0011-2275(94)90168-6.

[138] D. D. Awschalom and K. W. Schwarz. “Observation of a Remanent Vortex-Line Density in Superfluid Helium”. In: *Physical Review Letters* 52 (1 1984), pp. 49–52. DOI: 10.1103/PhysRevLett.52.49.

[139] A. Verweij. *CUDI: User’s Manual.* CERN. 2007.

[140] L. Bottura, M. Breschi, E. Felcini, and A. Lechner. “Stability modeling of the LHC Nb-Ti Rutherford cables subjected to beam losses”. In: *Phys. Rev. Accel. Beams* 22 (4 2019), p. 041002. DOI: 10.1103/PhysRevAccelBeams.22.041002.

[141] A Perin, R Macias-Jareño, and L Métral. “Study of Materials and Adhesives for Superconducting Cable Feedthroughs”. In: *AIP Conf. Proc.* 613 (2001), 551–558. 9 p. DOI: 10.1063/1.1472065. URL: https://cds.cern.ch/record/524909.

[142] B. Baudouy, J. Polinski, and L. Vieillard. *Comissioning of the NED cryostat.* Tech. rep. EDMS 794381. EU contract number RII3-CT-2003-506395. 2006. URL: http://irfu.cea.fr/Phocea/file.php?class=std&&file=Doc/Care/care-report-06-031.pdf.

[143] Tektronix. *Series 2400 SourceMeter® SMU Instruments Datasheet.* [Online; accessed 13-Aug-2021]. URL: https://download.tek.com/datasheet/1KW-2798-3_2400_SourceMeter_SMU_Datasheet_041121.pdf.

[144] Keysight Technologies. *Data Sheet N8700 Series System DC Power Supplies.* Tech. rep. 2021. URL: https://www.keysight.com/zz/en/assets/7018-02120/data-sheets/5990-3881.pdf.

[145] Natinal Instruments. *DEVICE SPECIFICATIONS NI 6251.* Tech. rep. 2016. URL: https://www.ni.com/pdf/manuals/375213c.pdf.

[146] Aim & Thurlby Thandar Instruments. *EL–R & EX–R Series.* [Online; accessed 06-Oct-2021]. URL: https://www.farnell.com/datasheets/1733184.pdf.

[147] D.K. Cheng. *Field and Wave Electromagnetics.* Addison-Wesley series in electrical engineering. Addison-Wesley Publishing Company, 1989. ISBN: 9780201128192.

[148] N. Wilson and P. Bunch. “Magnetic permeability of stainless steel for use in accelerator beam transport systems”. In: *Conference Record of the 1991 IEEE Particle Accelerator Conference.* 1991, 2322–2324 vol.4. DOI: 10.1109/PAC.1991.164953.

[149] S. Scott Courts and Philip R. Swinehart. "Review of Cernox™ (Zirconium Oxy–Nitride) Thin–Film Resistance Temperature Sensors". In: *AIP Conference Proceedings* 684.1 (2003), pp. 393–398. DOI: 10.1063/1.1627157. URL: https://aip.scitation.org/doi/abs/10.1063/1.1627157.

[150] Lake Shore Cryotronix Inc. Manufacturer website. Last accessed: 22-jul-2021. 2019. URL: https://www.lakeshore.com/products/categories/specification/temperature-products/cryogenic-temperature-sensors/cernox.

[151] Inc. Kulite Semiconductor Products. *CRYOGENIC ULTRAMINIATURE PRESSURE TRANSDUCER CCQ-062 SERIES*. Tech. rep. 2014. URL: https://kulite.com//assets/media/2021/07/CCQ-062.pdf.

[152] Lake Shore Cryotronix Inc. *Model 121 Programmable DC Current Source*. Tech. rep. 2015. URL: https://www.lakeshore.com/docs/default-source/product-downloads/literature/121.pdf?sfvrsn=fa07b2b_1.

[153] V. Arp, R. McCarty, and D. Friend. *Thermophysical Properties of Helium–4 from 0.8 to 1500 K with Pressures to 2000 MPa*. 1998.

[154] Emmanuele Ravaioli, Maxim Martchevskii, GianLuca Sabbi, Tengming Shen, and Kai Zhang. "Quench Detection Utilizing Stray Capacitances". In: *IEEE Transactions on Applied Superconductivity* 28.4 (2018), pp. 1–5. DOI: 10.1109/TASC.2018.2812909.

[155] E Ravaioli, D Davis, M Marchevsky, GL Sabbi, T Shen, A Verweij, and K Zhang. "A new quench detection method for HTS magnets: stray-capacitance change monitoring". In: *Physica Scripta* 95.1 (2019), p. 015002. DOI: 10.1088/1402-4896/ab4570. URL: https://doi.org/10.1088/1402-4896/ab4570.

[156] Wikipedia. *Runge's phenomenon*. [Online; accessed 19-Oct-2021]. 2021. URL: https://en.wikipedia.org/wiki/Runge%27s_phenomenon.

[157] National Institute of Standards and Technology. *Material Properties: OFHC Copper (UNS C10100/C10200)*. [Online; accessed 31-Mar-2020]. 2010. URL: https://trc.nist.gov/cryogenics/materials/OFHC%20Copper/OFHC_Copper_rev1.htm.

[158] R. B. Stewart and V. J. Johnson. "A COMPENDIUM OF THE PROPERTIES OF MATERIALS AT LOW TEMPERATURE (PHASE II)". In: 1960. URL: https://apps.dtic.mil/dtic/tr/fulltext/u2/249786.pdf.

[159] Engineering Toolbox. *Metals and Alloys - Densities*. [Online; accessed 14-Sept-2019]. 2004. URL: https://www.engineeringtoolbox.com/metal-alloys-densities-d_50.html.

[160] N.J. Simon, E.S. Drexler, and R.P. Reed. *Properties of Copper and Copper Alloys at Cryogenic Temperature*. Tech. rep. NIST Monograph 177. National Institute of Standards and Technology, 1992. URL: https://www.researchgate.net/profile/Elizabeth-Drexler/publication/255527811_Properties

_of_Copper_and_Copper_Alloys_at_Cryogenic_Temperatures/links/5695594c08ae425c6898332b/Properties-of-Copper-and-Copper-Alloys-at-Cryogenic-Temperatures.pdf.

[161] R. Viswanathan. “Heat capacity of sapphire between 2 and 10 K by AC technique”. In: *Journal of Applied Physics* 46.9 (1975), pp. 4086–4087. DOI: 10.1063/1.322119.

[162] R. Q. Fugate and C. A. Swenson. “Specific Heat of α Al2O3 from 2 to 25 K”. In: *Journal of Applied Physics* 40.7 (1969), pp. 3034–3036. DOI: 10.1063/1.1658118.

[163] D. A. Ditmars, S. Ishihara, S. S. Chang, and G. Bernstein. “Enthalpy and Heat-Capacity Standard Reference Material: Synthetic Sapphire (α-Al_20_3) from 10 to 2250 K”. In: *Journal of Research of the National Beureau of Standards* 87.2 (1982), pp. 159–163.

[164] Roditi International Corporation Ltd. *Sapphire Properties.* [Online; accessed 9-Aug-2021]. URL: http://www.roditi.com/SingleCrystal/Sapphire/Properties.html.

[165] Lake Shore Cryotronics. *Appendix I: Cryogenic Reference Tables.* [Manufacturer’s note]. 2000. URL: https://www.lakeshore.com/docs/default-source/product-downloads/literature/lstc_appendixi_l.pdf?sfvrsn=5f2ab85b_4.

[166] R. Berman, E. L. Foster, and J. M. Ziman. “Thermal conduction in artificial sapphire crystals at low temperatures I. Nearly perfect crystals”. In: *Proceedings of the Royal Society of London. Series A. Mathematical and Physical Sciences* 231.1184 (1955), pp. 130–144. DOI: 10.1098/rspa.1955.0161.

[167] Ankit Rohatgi. *Webplotdigitizer: Version 4.4.* 2020. URL: https://automeris.io/WebPlotDigitizer.

[168] J.T. Heessels. “Specific heat of general electric 7031 varnish from 2 to 80 K”. In: *Cryogenics* 11.6 (1971), pp. 483–484. ISSN: 0011-2275. DOI: 10.1016/0011-2275(71)90275-X.

[169] CMR Direct. *Product Specification: GE / IMI 7031.* [Online; accessed 9-Aug-2021]. URL: http://www.cmr-direct.com/en/product/download/get?download_id=4.

[170] J. H. McTaggart and G. A. Slack. “Thermal conductivity of general electric No. 7031 varnish”. In: *Cryogenics* 9.5 (1969), pp. 384–385. ISSN: 0011-2275. DOI: 10.1016/0011-2275(69)90019-8.

[171] S. Weyhe, B. Junge, F. Petzoldt, S. Bruns, and W. Gey. “Specific heat of delta bond 152, EPO-TEK H2OE, and wood’s metal at low temperatures”. In: *Cryogenics* 23.3 (1983), pp. 166–167. ISSN: 0011-2275. DOI: 10.1016/0011-2275(83)90180-7.

[172] C. A. Swenson. “Linear thermal expansivity (1.5–300 K) and heat capacity (1.2–90 K) of Stycast 2850FT”. In: *Review of Scientific Instruments* 68.2 (1997), pp. 1312–1315. DOI: 10.1063/1.1148064.

[173] Epoxy Technology. *Technical data sheet: EPO-TEK H20E.* [Online; accessed 09-Aug-2021]. 2014. URL: `https://www.tedpella.com/technote_html/16014_H20E_TN.pdf`.

[174] Loctite. *Technical data sheet: LOCTITE STYCAST 2850FT.* [Online; accessed 09-Aug-2021]. 2015. URL: `https://tdsna.henkel.com/americas/na/adhesives/hnauttds.nsf/web/35541AEFDE6FDF8485257576004480E6/%5C$File/STYCAST%202850FT-EN.pdf`.

[175] Ricardo I. Amils, Juan Daniel Gallego, José Luis Sebastián, Sagrario Muñoz, Agustín Martín, and Arnulf Leuther. “Thermal conductivity of silver loaded conductive epoxy from cryogenic to ambient temperature and its application for precision cryogenic noise measurements”. In: *Cryogenics* 76 (2016), pp. 23–28. ISSN: 0011-2275. DOI: 10.1016/j.cryogenics.2016.03.001.

[176] F. Rondeaux, Ph. Bredy, and J. M. Rey. “Thermal conductivity measurements of epoxy systems at low temperature”. In: *AIP Conference Proceedings* 614.1 (2002), pp. 197–203. DOI: 10.1063/1.1472543.

[177] D. Greig. “Low temperature thermal conductivity of polymers”. In: *Cryogenics* 28.4 (1988), pp. 243–247. ISSN: 0011-2275. DOI: 10.1016/0011-2275(88)90008-2.

[178] National Institute of Standards and Technology. *Material Properties: Teflon.* [Online; accessed 27-Sep-2021]. 2000. URL: `https://trc.nist.gov/cryogenics/materials/Teflon/Teflon_rev.htm`.

[179] Géraldine Theiler. “PTFE– and PEEK–Matrix Composites for Tribological Applications at Cryogenic Temperatures and in Hydrogen”. PhD thesis. Technical University of Berlin, 2005.

[180] J. D. Boyer, J. C. Lasjaunias, R. A. Fisher, and N. E. Phillips. “The low-temperature specific heat of PTFE (Teflon) at pressures to 5.2 kbar”. In: *Journal of Non-Crystalline Solids* 55.3 (1983), pp. 413–432. ISSN: 0022-3093. DOI: 10.1016/0022-3093(83)90046-7.

[181] National Institute of Standards and Technology. *Composition of POLYTETRAFLUOROETHYLENE (TEFLON).* [Online; accessed 27-Sep-2021]. URL: `https://physics.nist.gov/cgi-bin/Star/compos.pl?matno=227`.

[182] M. C. Runyan and W. C. Jones. “Thermal conductivity of thermally-isolating polymeric and composite structural support materials between 0.3 and 4K”. In: *Cryogenics* 48.9 (2008), pp. 448–454. ISSN: 0011-2275. DOI: 10.1016/j.cryogenics.2008.06.002.

[183] D. L. Rule and L. L. Sparks. *Low-temperature thermal conductivity of composites: alumina fiber/epoxy and alumina fiber/PEEK*. Tech. rep. National Inst. of Standards and Technology (NEL), Boulder, CO USA, 1989.

[184] P Duthil. “Material Properties at Low Temperature”. In: (2015). Comments: 18 pages, contribution to the CAS-CERN Accelerator School: Superconductivity for Accelerators, Erice, Italy, 24 April - 4 May 2013, edited by R. Bailey, 77–95. 18 p. DOI: `10.5170/CERN-2014-005.77`. arXiv: `1501.07100`. URL: `https://cds.cern.ch/record/1973682`.

[185] ASM International. *ASM Handbook Volume 2: Properties and Selection: Nonferrous Alloys and Special-Purpose Materials*. Metals Handbook Series. ASM International, 1990. ISBN: 9780871703781. URL: `https://materialsdata.nist.gov/bitstream/handle/11115/179/Properties%20of%20Wrought%20Aluminum.pdf?sequence=3&isAllowed=y`.

[186] Eckels Engineering Inc. *CryoComp Rapid Design*. [Computer software; version 5.3]. 2017.

[187] F. J. Du Chatenier, B. M. Boerstoel, and J. De Nobel. “Specific heat capacity of a stainless steel”. In: *Physica* 31.7 (1965), pp. 1061–1062. ISSN: 0031-8914. DOI: `10.1016/0031-8914(65)90148-5`.

[188] National Institute of Standards and Technology. *Material Properties: 304 Stainless (UNS S30400)*. [Online; accessed 31-Mar-2020]. 1999. URL: `https://trc.nist.gov/cryogenics/materials/304Stainless/304Stainless_rev.htm`.

[189] AZO Materials. *Stainless Steel - Grade 304 (UNS S30400)*. [Online; accessed 11-Aug-2021]. 2001. URL: `https://www.azom.com/properties.aspx?ArticleID=965`.

[190] W. Stutius and J. R. Dillinger. “Magnetic and thermal properties of some austenitic stainless steels at low temperatures”. In: *Journal of Applied Physics* 44.6 (1973), pp. 2887–2888. DOI: `10.1063/1.1662665`.

[191] J. G. Hust and L. L. Sparks. *Lorenz Ratios of Technically Important Metals and Alloys*. Tech. rep. 634. National Bureau of Standards, 1973.

[192] Bertrand Baudouy. Private communication. 2020.

[193] Lake Shore Cryotronix Inc. *Instructions, Mounting a Bare Chip*. Manufacturer technical note. Last accessed: 30-sep-2021. 2014. URL: `https://www.lakeshore.com/docs/default-source/product-downloads/installation-instructions/f002-00-00.pdf?sfvrsn=ae9682e2_4`.

[194] Yunus A. Çengel. *Heat and Mass Transfer. A Practical Approach*. 3rd ed. McGraw–Hill Education, 2006. ISBN: 978–007–125739–8.

[195] S. Fuzier and S.W. Van Sciver. “Use of the bare chip Cernox™ thermometer for the detection of second sound in superfluid helium”. In: *Cryogenics* 44.3 (2004), pp. 211–213. ISSN: 0011–2275. DOI: 10.1016/j.cryogenics.2003.11.005.

[196] Dag Roar Hjelme. Private communication. 2020.

[197] Wikipedia. *Savitzky–Golay filter*. [Online; accessed 19-Oct-2021]. 2021. URL: https://en.wikipedia.org/wiki/Savitzky%E2%80%93Golay_filter.

[198] Ronald W Schafer. “What is a Savitzky-Golay filter?[lecture notes]”. In: *IEEE Signal processing magazine* 28.4 (2011), pp. 111–117.

[199] Wikipedia. *Savitzky–Golay filter*. [Online; accessed 19-Oct-2021]. 2021. URL: https://en.wikipedia.org/wiki/Butterworth_filter.

[200] Nils Holte. *Lecture notes on Transmission Properties of Pair Cables*. 2002. URL: https://www.ceid.upatras.gr/webpages/faculty/alexiou/ahts/other_pdf/4_Twisted_p.pdf.

[201] Sylvie Fuzier. “Heat Transfer and Pressure Drop in Forced Flow Helium II at High Reynolds Numbers”. PhD thesis. Florida State University, 2004.

[202] Charles K. Alexander and Matthew N. O. Sadiku. *Fundamentals of Electric Circuits*. 5th Edition. McGraw–Hill, 2013.

[203] Wikipedia. *RLC circuit*. [Online; accessed 08-Jun-2017]. 2017. URL: https://en.wikipedia.org/wiki/RLC_circuit.

[204] Engineering Tool Box. *Permeability*. [Online; accessed 14-Jul-2021]. 2021. URL: https://www.engineeringtoolbox.com/permeability-d_1923.html.

Paper I

Jonas Blomberg Ghini, Bernhard Auchmann, and Bertrand Baudouy

Millisecond Time–Scale Measurements of Heat Transfer to an Open Bath of He II

ArXiv:2203.04626 [1]

Millisecond Time–Scale Measurements of Heat Transfer to an Open Bath of He II

Jonas Blomberg Ghini[1,2,*] Bernhard Auchmann[2] Bertrand Baudouy[3]

[1]Department of Physics, Norwegian University of Science and Technology, NTNU, Norway
[2]European Organization for Nuclear Research, CERN, Switzerland
[3]Irfu, CEA, Université Paris–Saclay, F-91191 Gif–sur–Yvette, France
[*]Corresponding author: *jonas.blomberg.ghini@ntnu.no*

Abstract

We explore steady state and transient heat transfer from a narrow, rectangular stainless steel heater strip cooled from one side by an open bath of He II. Setup validation is done by fitting the Kapitza heat transfer expression $Q = a_{\mathrm{K}}\ (T_{\mathrm{s}}^{n_{\mathrm{K}}} - T_{\mathrm{b}}^{n_{\mathrm{K}}})$ to steady state measurements, finding fit parameters within the expected range; $a_{\mathrm{K}} = 1316.8\pm10\%\ \mathrm{W\,m^{-2}\,K^{-n_K}}$, $n_{\mathrm{K}} = 2.528\pm10\%$.

We find critical heat flux in line with estimates from literature, and the time between a step in heating and the onset of film boiling follows the expected $\propto Q^{-4}$ dependence.

During the first millisecond after a step in applied heating power density our measurements show a slower thermal rise time than that found by a time–dependent one–dimensional model of our setup using the steady state Kapitza heat transfer expression as the cooling boundary condition. However, the results compare favourably with transient measurements in literature. After the first millisecond, agreement between measurement and model is excellent.

We do not find conclusive evidence of an orientation dependence of the Kapitza heat transfer mechanism, nor heat transfer differences that can be attributed to local surface variations along the same heater.

1 Introduction

During operation of a particle accelerator, such as the Large Hadron Collider (LHC), it is inevitable that some particles from the circulating beam are lost, depositing their kinetic energy in equipment surrounding the beam pipe[1]. There are three main sources of beam loss[2, p. 370]; 1) malfunctioning equipment, such as a magnet losing power, thus no longer bending the beam; 2) beam instabilities that over time cause parts of, or the whole, beam to veer off course; 3) scattering events in which some particles from the beam collide with stray matter in the beam pipe outside the dedicated interaction regions of the machine. Losses of the first and second kind usually arise at the collimators which intercept the stray beam[3], leading to particle showers absorbed in the machine components downstream[4].

In the work presented here, the loss event of most relevance is characterised by the beam interacting with a dust particle in the beam pipe, which gives rise to a particle shower that deposits energy, over the course of about 1 ms, into the bulk of the superconducting magnets that surround the beam pipe along the length of the bending sections of the LHC[5]. This kind of loss event is called a UFO event, as the dust particle is an Unidentified Falling Object. UFOs occur about 10 to 30 times per hour of operation of the LHC[5, Fig. 2]. If the energy deposition is sufficiently large, a UFO can quench a magnet, meaning the superconducting magnet, locally, becomes normal conducting[6, p. 656]. In large accelerator magnets this transition is usually irreversible, and to protect the magnet from damage the beam is dumped, and the magnet quench protection system kicks in to dissipate the energy stored in the magnetic field. This aborts the operation of the LHC, and it then takes several hours to return the machine to normal operating conditions[5].

Analysing this kind of transient beam loss event, with the aim of determining whether or not the magnet would quench, requires modelling the physical behaviour of the system. This includes the energy input from the particle shower, magnet with its superconducting to normal–conducting transition, and the helium that permeates the LHC magnets in the interstitial voids between both cable strands and insulation layers. Models pertaining to the LHC mainly account for the presence of helium in the magnets in one of two ways; 1) they assume no heat transfer directly from magnet to helium, but rather considers helium as an added heat capacity[7, 8], or 2) includes surface heat transfer from the superconducting strands into the helium, but assumes no heat transfer within the helium itself[9, 10]. The first approach is valid for very fast losses ($\lesssim$10 µs range) when it is safe to assume no significant cooling takes place either to the helium nor by way of heat transfer along the cable strands. The second approach is valid for steady state situations where the helium volume is large. At the millisecond time scale of UFOs, when the helium is confined within the LHC magnet cables, however, the validity of the models have not been experimentally investigated to give the assumptions physical basis. The lacking validity of modelling only a single strand with local helium cooling was confirmed by a discovery made after analysing the orbit–bump quench test in the LHC done in 2011[11].

The orbit–bump test revealed that for a purposefully induced loss in the 10 ms time range the model accounting for helium cooling of the magnet cable strands severely underestimates the amount of energy needed to quench. The model predicts that an energy deposition of about 50 to 80 $\mathrm{mJ\,cm^{-3}}$ should be sufficient to cause a quench, while the lower limit found during the test is 198 $\mathrm{mJ\,cm^{-3}}$, for which no quench occurred, and an upper limit of 405 $\mathrm{mJ\,cm^{-3}}$ for which a quench was observed[12, Tab. V].

In order to better understand how helium cooling works on the millisecond time scale in confined volumes, new experimental work is needed. Section 2 expands on both theory and background from previous experimental work, but in summary, the shortcomings of current understanding are the following; 1) the standard surface heat transfer model was developed for steady state heating into large volumes of helium and we need to give physical basis for using the same heat transfer expression for time–dependent modelling; 2) while prediction of the critical heat flux beyond which helium boiling begins is possible, the film boiling onset, with associated loss of cooling capability, is heavily dependent on local geometrical conditions.

Beyond this we will expand the millisecond–timescale data available in literature, and investigate two minor effects that may change heat transfer in the Kapitza regime; 1) a heat transfer dependence on orientation, and 2) a heat transfer dependence on position along a heater. Furthermore, no reliable Kapitza fit parameters were previously available for stainless steel.

The measurement campaign presented in this paper was conducted in two main steps; 1) gather steady state data from heat transfer to an open bath of He II in order to validate the setup against expected behaviour; and 2) explore the transient behaviour of surface heat transfer to an open bath of He II, including the transition to film boiling.

Validation of the setup in steady state is done by fitting Kapitza parameters to our results between applied heating power densities between 0 and 85 $\mathrm{kW\,m^{-2}}$, and comparing these with those found in literature. The transient measurements rely on steps in applied heating power density, up to 85 $\mathrm{kW\,m^{-2}}$, to investigate transient heat transfer. We compare our results with the millisecond–timescale data available in literature.

2 Theory and Background

In this paper, we consider heat transfer from a narrow, rectangular heater strip cooled from one side by a large volume of He II. For analysis of results, two main heat transfer characteristics are necessary;

- Heat transfer from the hot surface to the cold He II for heat fluxes, or heating durations, that do not trigger the onset of film boiling. We call this the Kapitza regime under both steady state and transient conditions;
- Heat transfer from the surface to He II for heat fluxes, or heating durations, that do cause the onset of film boiling. We call this the film boiling onset regime.

Van Sciver provides reviews of these topics, and only the most relevant aspects are discussed herein (see Section 7.5 for the Kapitza regime, and 7.6 for film boiling, in Ref. [13]).

2.1 Kapitza Heat Transfer

Claudet and Seyfert initially proposed the phenomenological expression that describes heat transfer in the Kapitza regime, which will be used herein[14, Eq. 1];

$$Q_\mathrm{K} = a_\mathrm{K}\ \left(T_\mathrm{s}^{n_\mathrm{K}} - T_\mathrm{b}^{n_\mathrm{K}}\right), \tag{1}$$

where Q_K is the Kapitza heat flux, T_s is the temperature of the heater at heater–He II interface, referred to as the surface temperature, T_b is the bath temperature of He II far from the heater, and a_K and n_K are two fit parameters. This expression fits data for large heat fluxes, on the order of 1 $\mathrm{kW\,m^{-2}}$ and up.

The two fit parameters depend on the heater material as well as the local surface conditions of the heater, and for any given heater, if high accuracy is desired, dedicated measurements must be done to obtain them. Claudet and Seyfert's original measurements showed that copper heaters whose surfaces were prepared identically showed the same variation in measurement results as heaters where the surface preparation was purposefully different (such as after baking or annealing). From across literature there are, however, ranges; a_K tends to be in the range 200 to 1300 $\mathrm{W\,m^{-2}\,K^{-n_K}}$, and n_K in the range 2 to 4[14–19]. From the phonon radiation limit, describing the largest possible heat transfer rate across the interface, n_K is considered to have an upper limit of 4, stemming from the T^3–dependence of the density of phonon states in the Debye approximation[20, p. 108]. A physically consistent theory explaining the Kapitza resistance is the acoustic mismatch theory originally developed by Khalatnikov[21, Chap. 23]. Here, the actual acoustic impedance mismatch between the solid heater material and the He II is considered, as well as the non–zero reflection probability of a phonon incident upon the interface. This AM theory consistently underestimates measured results, and several attempts have been made to bring it in line with observations.

Two important avenues attempting to explain the discrepancy are; 1) the presence of an adsorbed/solidified layer of helium atoms on the heater surface that improves acoustic matching[22, 23], and 2) random surface roughness of the interface that increase the effective heat transfer area[24–26]. Khater and Szeftel merged the two approaches[27] and found convincing agreement with Anderson *et al.*'s old measurements below 1 K[28]. Ramiere *et al.* recently found that Adamenko and Fuks's surface roughness model[25] gives excellent agreement with their measurements on a silicon single–crystal over a wide range of temperatures[29]. The surface roughness considered for these kinds of models is on the order of the phonon wavelength so as to scatter phonons significantly better than the unmodified AM theory. This means roughness amplitudes on the order of a few nanometres at temperatures around 2 K. This is about two orders of magnitude smaller than the surface roughness expected on steel after high–grade mechanical polishing[30].

2.1.1 Day–to–day Variations

An important note about measurements pertaining to heat transfer in He II is that results have a layer of uncertainty tied to the variation of the Kapitza resistance over long time scales. Rawlings and van der Sluijs find in their study on steady and transient heat transfer in He II, during the early days of large–heat–flux experiments, that they needed to repeat their measurements multiple times over several days until they could obtain results within 5% of each other for the same applied heating power densities[31].

2.1.2 Orientation Dependence

In the AM theory of Kapitza heat transfer there is no dependence on gravity, which makes intuitive sense since the mechanism is governed by the transmission of thermal phonons across the interface between a heater and He II. Phonons are governed by the strong inter–atomic potentials in matter, and are not appreciably affected by a weak gravitational potential[20, p. 83–84].

2.2 Film Boiling in He II

The Kapitza regime persists until the heat flux across the interface exceeds some critical value, Q_crit, defined as the steady state heat flux above which a film of gaseous helium covers the heater surface. The following relationship governs the heat transfer;

$$Q_\mathrm{FB} = a_\mathrm{FB}\left(T_\mathrm{s} - T_\mathrm{b}\right), \tag{2}$$

where Q_FB is the film boiling heat flux, and a_FB is a coefficient that depends on heater material and configuration (typically 200 to 1000 $\mathrm{W\,m^{-2}\,K^{-1}}$[13, Table 7.5, “flat plate” entries]). Heat transfer in the film boiling regime tends to be chaotic; even if the heater surface is coated with a continuous layer of vapour, bubbles may form and depart, causing unpredictable local behaviour.

That said, after Kobayashi *et al.* found that the Kapitza regime persists for some time even after the steady state critical heat flux is exceeded[32], a large amount of experimental work was done to study the onset of film boiling in He II for various geometries[18, 33–40]. Several expressions to determine the critical heat flux were found, and the one Tatsumoto *et al.*[38] propose for a flat rectangular plate in an open bath is relevant here;

$$Q_\mathrm{crit} = K\left[\frac{2}{\frac{Lw}{2(L+w)}}\int_{T_\mathrm{b}}^{T_\lambda}\frac{1}{f(T)}\mathrm{d}T\right]^{1/3}, \tag{3}$$

where K is a fit factor equal to 0.58, L is the length of the heater, w its width, and $f^{-1}(T)$ is the thermal conductivity function of turbulent He II;

$$\begin{aligned} f^{-1}(T) &= g(T_\lambda)\left[\left(\frac{T}{T_\lambda}\right)^{6.8}\left(1-\left(\frac{T}{T_\lambda}\right)^{6.8}\right)\right]^{3}, \\ g(T_\lambda) &= \frac{\rho^2 {s_\lambda}^4 {T_\lambda}^3}{A_\mathrm{GM}(T_\lambda)}, \end{aligned} \tag{4}$$

with $s_\lambda \simeq 1559\ \mathrm{J\,kg^{-1}\,K^{-1}}$, and $A_\mathrm{GM}(T_\lambda) \simeq 1150\ \mathrm{m\,s\,kg^{-1}}$. Note, this expression for the thermal conductivity function was modified from the traditional one where the exponent is 5.7, not 6.8, and $A_\mathrm{GM}(T_\lambda)$ was taken as 1450, not 1150 $\mathrm{m\,s\,kg^{-1}}$[13, Eq. 7.2]. Sakurai *et al.* originally proposed this modified version[41].

The typical observation from these measurements is that after applying a heating power density Q_app, there is a rapid temperature rise of the heater, in accordance with the Kapitza regime (Equation (1)), which flattens out and remains constant for some time τ_Kapitza. After this quasi–steady state, the heater temperature shoots up, as film boiling starts. τ_Kapitza is called the quasi–steady state Kapitza regime life–time, and it relates to Q_app in one of two main ways;

$$\begin{aligned} &\tau_\mathrm{Kapitza} \propto Q_\mathrm{app}^{-4} \quad \text{weak heating,} \\ &\tau_\mathrm{Kapitza} \propto Q_\mathrm{app}^{-2} \quad \text{strong heating,} \end{aligned} \tag{5}$$

where the delineation between weak and strong heating (though, always above Q_crit), is geometry dependent. The strong–heating behaviour appears to be exclusive to He II channels[42] or heating sufficiently strong that boiling onset starts after less than about 1 ms[39]. Note also that the time to boiling onset may not follow Equation (5) until the applied heating power density is as much as a factor 2 above Q_crit.

2.3 Transient Measurements

Transient measurements on the millisecond time–scale not intended to investigate second–sound heat transfer have previously only been done as part of the aforementioned studies on transition to film boiling. Generally, the time–dependent data is only presented summarily, such as by Gradt *et al.* (see Ref. [34]) and Shiotsu *et al.*(see Ref. [37]) with no emphasis on the initial temperature rise, nor on any time–dependent modelling efforts to explain the behaviour. Gradt *et al.* show a time–dependent measurement that appears to take about 0.5 to 0.6 ms to reach the quasi–steady state before then seeing the onset of film boiling after another 1 ms. Shiotsu *et al.*'s measurements take about 0.4 ms to reach the quasi–steady state. Once film boiling is established, the further temperature rise in both measurement sets appears roughly linear with time, though none of their plots go beyond 10 ms at most.

3 Setup

Figure 1 schematically represents the setup placed into the cryostat. The key features in each sample are the stainless steel heater strips, heated by passing current through them, and the Cernox® sensors used to the measure temperatures. Steel was chosen for three main reasons; 1) its high electrical resistance, meaning a relatively low current leads to strong heating; 2) for being easy to work with by hand, relevant for assembly of the setup; and 3) having low thermal conductivity which limits longitudinal heat flow in order to observe potential temperature variation along the heater strips.

Bare chip Cernox® sensors by Lake Shore Cryotronics were chosen for their excellent thermal response time and temperature sensitivity[43, 44]. Sensor labelling refers to Upwards or Downwards heater orientation and the indexed position relative to the middle sensor in each plate. The plates themselves are made of glass–fibre filled PEEK, in order to better match the thermal contraction of the heater strips, and thus prevent delamination during cooldown. `T_bath` represents the pre–calibrated probe used both for in–situ calibration of the other sensors, and as the temperature reference for control of the helium bath temperature.

Figure 2 shows schematically the immediate surroundings of an individual Cernox® sensor (material parameters are provided in Appendix A, and thickness approximations are discussed in Section 3.3);

(1) PEEK (poly–ether ether ketone), filled with 30% (by volume) glass fibre, oriented so the fibres are parallel to the axis of thermal contraction. The thermal path between the sensors and the back of the sample is dominated by the thin copper leads, so PEEK material parameters are not relevant for the steady state or transient thermal modelling presented in sections 4 and 5;

(2) Eccobond® epoxy used to fill in holes, chosen for its He II leak–proofness[45];

(3) Copper sensor leads (two per sensor), attached by manufacturer. Diameter 63.5 µm, and length between sensor and thermal anchor (A) 20 mm;

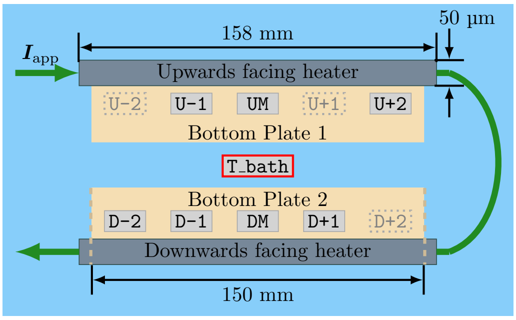

Figure 1: Diagram of the measurement setup. The light blue outer rectangle represents the helium bath. Light grey rectangles represent the Cernox® sensors. `D`: downwards facing heater sensors. `U`: upwards facing heater sensors. The number refers to the sensor's relative left (negative) or right (positive) of the middle sensor (`UM` or `DM`). The red–edged rectangle represents the reference probe. Edge sensors are 12.5 mm from the edge of their PEEK plates, and 31.25 mm apart. The heater strips are 3 mm wide (in the plane of the paper). Dashed and greyed out sensors broke during assembly or cooldown.

(4) GE 7031 varnish used to attach Cernox® sensors to the underside of the heater strip. Approximate layer thickness 25 µm. A discussion of this dimension is given in Section 3.3;

(5) Sapphire substrate making up the bulk of the Cernox® sensor body. Thickness 203 ±25 µm;

(6) EPO–TEK H20E silver filled epoxy used by Lake Shore Cryotronics to attach leads to sensor body. Approximate thickness (separating sensor from sensor lead) 20 µm;

(7) Kapton tape lining the underside of the heater strip, in which a hole is cut so sensors can attach directly to the stainless steel heater. This means kapton, like PEEK (1), is not in the thermal path considered in the modelling. Thickness 100 µm;

(8) Stainless steel heater strip. Thickness 50 ±2 µm;

(A) Soldering points (one per sensor lead) joining the sensor leads to larger external lead attachments, acting as thermal anchoring for the Cernox® sensors.

The thermal path considered for simulations in sections 4 and 5 runs from the top/surface of the heater strip (8), down through the varnish (4), then the sapphire of the Cernox® sensor (5), then the EPO–TEK (6), and finally the sensor lead wires (3). The wires end in the thermal anchor (A). Note that all interfaces between materials along this thermal path are between a solid and a liquid (that then solidifies upon curing after assembly); the varnish (4) between the steel heater strip (8) and the Cernox® sensor (5) is liquid during assembly, as is the EPO–TEK (6) and the solder (A). For this reason, we will not consider thermal contact resistances as relevant for the heat transfer modelling as there are no interfaces whose contact depend on solids pressed together.

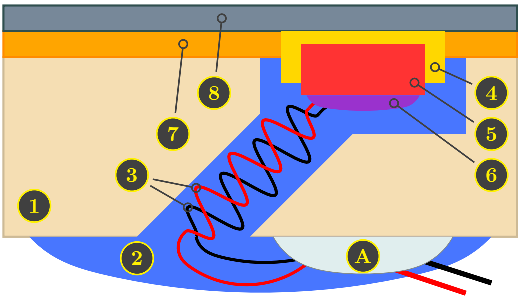

Figure 2: Schematic representation of the region around the Cernox® temperature sensors. Label (1): Glass–fibre filled PEEK. (2) Eccobond®. (3): copper sensor lead wires. (4): GE 7031 varnish. (5): sapphire sensor substrate. (6): EPO–TEK H20E epoxy. (7): kapton insulation tape. (8): stainless steel heater strip. (A): Soldering point where thin sensor leads join larger sensor lead attachments (one anchor point for each lead wire).

3.1 Calibration

The Cernox® sensors are calibrated in–situ against the reference probe. The double–bath cryostat used for experiments does not permit temperature control above 4.2 K, so in this region, only quasi–steady temperature readings from the slow cooldown process are available for calibration purposes. A possible impact of this is a temperature offset caused by the thermal diffusion time between the helium–cooled surface of the heater and the sensitive part of the Cernox® sensors. However, in the temperature range 4 to 50 K, adding the thermal diffusion times through the various layers of materials gives an overall diffusion time (through 50 µm of stainless steel, 25 µm of varnish, and 200 µm of sapphire) $\tau_{\text{diff}} \simeq 0.1$ ms at around 4 K, growing to 1 ms at around 50 K. This is much shorter than the time–rate of temperature change of the helium bath during cooldown, which is on the order of 1 to 10 $\text{mK}\,\text{min}^{-1}$.

The calibration is done by associating the measured resistance of each individual Cernox® sensor at several temperatures (known from the reference probe), and using a cubic spline function to represent this calibration for analysis. This means our calibrated Cernox® sensors have a contribution to their total measurement uncertainty equal to the calibration uncertainty of the reference probe (provided by Lake Shore Cryotronics).

While there is no temperature offset, there is a source of uncertainty due to the transient nature of the calibration data. Only below T_λ does the cryostat temperature control permit long–term temperature stability. So each calibration data point collected above T_λ is based on data that is changing, albeit slowly, in time. To estimate this additional contribution, we take the calibration spline and apply it to the raw data of each individual point. This gives time–dependent temperature curves for each Cernox® sensor that deviate slightly from the time–dependent reference probe reading. As an example; we have a measurement that gives the calibration point we use at around 3.35 K. During the measurement the reference probe reading drops from around 3.37 down to 3.23 K over the course of an hour. Outside the narrow time–window we use for the calibration point itself, we find the root–mean–square deviation between the reference and all Cernox® sensors, and then take the uncertainty contribution within this temperature range as the average RMS deviation across all the sensors. The total estimated measurement uncertainty is listed for temperature ranges in Table 1. Below 4 K, the main contribution is from the reference probe uncertainty, while above 4 K, the main contribution is from the transience of the calibration measurements.

Table 1: Estimated measurement uncertainty ΔT.

Range, [K]			$\pm\Delta T$, [mK]
1.8	—	T_λ	5
T_λ	—	4	7
4	—	6	15
6	—	50	50

3.2 Instrumentation

The data acquisition is split across two systems; one system for triggering current pulses in the heater strips and measuring the resulting voltage across them, and another system to measure the voltage across the temperature sensors, which then are converted to temperature by the calibration spline function. Both systems are run through LabView®.

For the heater strips, voltage is measured across only the upwards facing heater, and the voltage for the downwards facing heater is obtained by scaling with the resistance ratio between the two strips. To find the resistance ratio, we fed a steady 1 A current and measured the voltage across both strips, and then across just the upwards facing heater. This yielded $R_{\text{up}} = 0.465 \pm 0.001$ Ω and $R_{\text{down}} = 0.458 \pm 0.001$ Ω. During transient measurements, the strip current is found using these resistances and Ohm's law. Since stainless steel has only a negligible resistivity change with temperature below liquid nitrogen temperatures, this method introduces no uncertainty beyond that of R_{up} and R_{down}. The data acquisition frequency is typically 500 kHz.

For the Cernox® sensors, a four–lead circuit is used, where two sensors share a single 10 µA excitation current source but have individual voltage measurement leads. Sensors `U-2` and `U-1` are excited by the same source. The same goes for the pairs `UM` and `U+2`, `D-2` and `D-1`, and `DM` and `D+1`. Typical data acquisition frequency is 40 kHz per sensor. In order to provide a smooth output current, the excitation current sources each have a low–pass filtering capacitor measured to 0.929 ±0.03 µF in parallel with the output terminals. The effect of this capacitor will be discussed in Section 3.5.

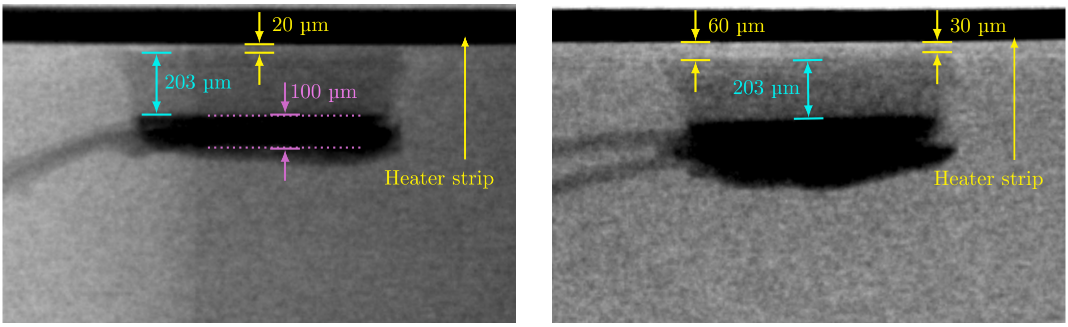

(a) X–ray image of `U-1`. Distance between heater and sensor base is about 20 µm. Purple dimensions indicate the thickness of the EPO–TEK beads.

(b) X–ray image of `UM`. Distance between heater and sensor base is goes from about 60 to 30 µm, for an average of 45 µm.

Figure 3: X–ray images of `U-1` and `UM`, showing approximate distances. The imaging resolution was 6 µm. Cyan dimensions are used as the scale in the images.

3.3 Region Around Sensors

To better characterise the geometry around the sensors in the real samples after assembly and curing, we have some x–ray images taken at 6 µm resolution. Figure 3 shows the images for `U-1` and `UM` with approximate dimensions indicated. Regions of denser material show up with darker pixels in the images, but note that since the EPO–TEK is loaded with silver particles, the x–rays see an effectively denser material than that expected from the average epoxy density.

The known height of the Cernox® sensors, 203 µm, is used as the scale in both images, and this way we can estimate the distance between the heater strip and the sensors. `U-1` is about 20 µm from the heater, while `UM` is a little tilted, going from 60 to 30 µm away. We have similar images for `U-2` and `U+1`. `U-2` is flush with the heater, to within the image resolution; there cannot be zero varnish, so we take 6 µm as the varnish length here. `U+1` is, like `UM`, tilted, going from 50 to 0 µm; again we take 6 µm in place of zero.

The final varnish length we use for analysis is the root–mean–square value of estimated dimensions, without first taking the average of the estimates for titled sensors. This leads to $l_{\text{varnish}} = 35{\pm}6$ µm. The uncertainty is taken as the image resolution.

Also in Figure 3a is the approximate thickness of the EPO–TEK lead attachment bead, shown as $\simeq$100 µm, which means, assuming the copper leads are in the middle of the bead, there is 20 µm of EPO–TEK between the sensor sapphire bulk and the sensor leads. The variation in EPO–TEK thickness will be considered between 10 and 30 µm when estimating uncertainty and parameter sensitivity in thermal modelling.

The copper lead wires come attached from Lake Shore Cryotronics with length around 25 mm, and after assembly, where part of the wire end is used for soldering to the anchor, 20 mm of wire runs between the thermal anchor and the EPO–TEK attachment points on the sensors. There is, however, a variation in the length of each lead. The x–ray images were taken with much larger field of view than shown in Figure 3, and from these we estimate the leads vary between 18 and 22 mm long.

In summary, the one–dimensional thermal path considered as the reference domain for modelling purposes consists of 50 µm of stainless steel, 35 µm of varnish, 200 µm of sapphire, 20 µm of EPO–TEK, and 20 mm of copper. Appendix B describes the implementation of the one–dimensional heat equation we use.

There are two copper leads per sensor, of diameter 63.5 µm, giving a cross sectional ratio to the sensor cross section of $2 \cdot A_{\text{lead}}/A_{\text{sensor}}$, with $A_{\text{lead}} = \pi(63.5\,\text{µm}/2)^2$ and $A_{\text{sensor}} = 762 \times 965$ µm^2. This ratio is used to lower the effective thermal conductivity of the copper leads. We also account for the sensor leads passing through Eccobond®, which poses an additional heat capacity.

3.4 Measurement Procedure

All measurements follow the same general approach; trigger a step in current, from zero to some value, through the heater strips, and measure the voltages across the heater strip and the Cernox® sensors. All our measurements are thus transient, and steady state results are extracted from measurements after all voltages/temperatures have stabilised. Once current is turned off again, we let all temperatures settle at the bath temperature before applying a new step.

To represent the heating power we use an equivalent applied heating power density, Q_{app};

$$Q_{\text{app}} = \frac{{V_{\text{strip}}}^2}{R_{\text{strip}}}\frac{1}{A_{\text{strip}}}, \tag{6}$$

with $R_{\text{strip}} = 0.465$ Ω for the upwards facing heater, and 0.458 Ω for the downwards facing heater, $A_{\text{strip}} = 158 \times 3$ mm^2 the heat transfer area of a strip. V_{strip} is simply the measured voltage V_{meas} across the upwards facing heater, while for the downwards facing heater the measurement must be scaled by the resistance ratio between the two strips; $V_{\text{strip, down}} = V_{\text{meas}} \cdot (R_{\text{down}}/R_{\text{up}})$.

This calculated applied heating power density is not the heat flux crossing the heater–to–helium interface. Q_{app} represents the applied volumetric heating power expressed as watts per square metre. The instantaneous or steady state heat flux across the interface depends on the heat loss to the back of the sample as well as the heat capacities of materials. The steady state analysis in Section 4 finds the heat loss through the steady state heat equation and the measured sensor temperatures, while the transient analysis in Section 5 finds the interface heat flux using the applied heating power density and the time–dependent heat equation.

Measurements were done at two bath temperatures; at 1.9 K we go up to $Q_{\text{app}} = 85\ \text{kW}\,\text{m}^{-2}$, while at 2.05 K we go up to $Q_{\text{app}} = 68\ \text{kW}\,\text{m}^{-2}$.

3.5 Capacitance Compensation

The presence of the filtering capacitors in parallel with the current output from the Cernox® sensor excitation current sources mean we must account for this effect during the initial stages of the temperature transient. The Cernox® sensors in each excitation circuit constitute total electrical resistance on the order of 20 to 30 kΩ for an initial temperature of 1.9 K. The filtering capacitors are 0.929 µF. During the rapid heating of the sensors, their resistance falls to much lower values, meaning the electrical circuit approaches that of a charged capacitor releasing energy into a resistor. The expected electrical time–constant is on the order of 20 to 30 ms, while the thermal time–constant we intend to measure is on the order of 1 ms.

During the transient time between turning on the applied heating power and reaching a steady state, the excitation current in the Cernox® sensors is composed of two independent parts;

$$i_{\text{sensors}}(t) = I_{\text{EX}} + C\frac{\mathrm{d}V_{\text{C}}(t)}{\mathrm{d}t}, \tag{7}$$

where I_{EX} is the steady 10 µA current, fed by the ideal part of the excitation circuit, and $V_{\text{C}}(t)$ is the time–dependent voltage across the filtering capacitor C. This voltage is the sum of voltages across the two sensors in the same excitation circuit.

The left axis of Figure 4 shows the sum, $V_{\text{C}}(t)$, of the raw voltage signals of sensors `UM` and `U+2` from a measurement during a step in applied heating power density. The right axis shows the numerical time derivative $\Delta V_{\text{C}}/\Delta t$ of this voltage sum. The shape of the voltage time derivative is representative of all measurements made; only the signal amplitude varies with applied heating power density. As is expected, the numerical differentiation introduces significant noise, so some form of filtering is necessary. Our approach is roughly split in three, relying on the use of the Savitzky–Golay filter from the Python function `scipy.signal.savgol_filter`, and the low–pass Butterworth filter from `scipy.signal.butter`;

1. Using the `savgol_filter`, we directly obtain the numerical derivative from the voltage signal, instead of using the very noisy $\Delta V/\Delta t$ approach;

2. The low–pass `butter` filter is used to obtain two filtered versions of the `savgol_filter` result; one with a high cut–off frequency, that captures the early region around the peak of the response, and one with a low cut–off frequency that captures the long tail of the signal;

3. The `savgol_filter`, due to it representing a numerical derivative, tends to give non–zero voltage derivative values at the time of the step. *Before* the step in heating power, the sensors are at their initial temperature, and no voltage change should be present. Therefore, a polynomial is fitted to the first millisecond of the `savgol_filter` result such that all values before the step are zero.

These three parts combine, with smooth transitions from one region to the next, to give the much improved voltage time derivative curve $\mathrm{d}V_{\text{C}}/\mathrm{d}t$. Each of the four sensor excitation circuits will have their own voltage time derivative curve. The same behaviour is seen also when power is turned off at the end of a step, although the signal is much weaker.

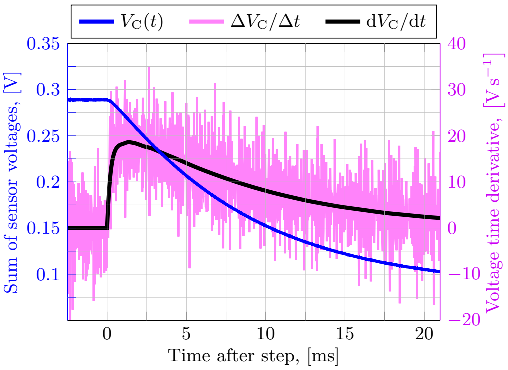

Figure 4: Sensor voltages and voltage time derivative to be used in Equation (7). Left axis: sum of voltages across `UM` and `U+2`. Right axis, raw and smooth voltage time derivative.

The smooth $\mathrm{d}V_{\text{C}}/\mathrm{d}t$ is used to find the time–dependent sensor excitation current from Equation (7), and this is used to calculate the instantaneous sensor resistance of each individual sensor (since we measure the individual sensor voltages). This compensated resistance is converted to temperature using the calibration spline fits for each sensor.

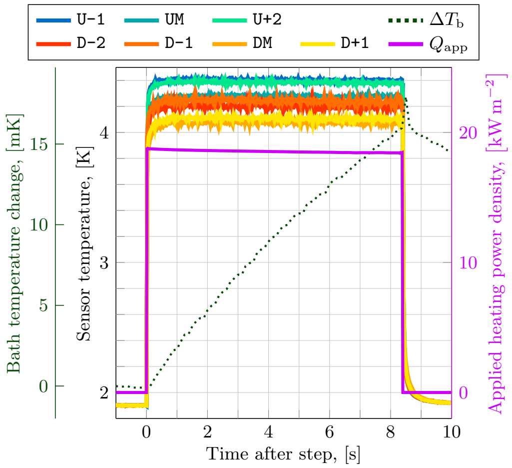

Figure 5: Representative measurement for a single step in applied heating power density, whence steady state data is extracted. Initial bath temperature is 1.9 K. For clarity, only one in every thousand data points is shown.

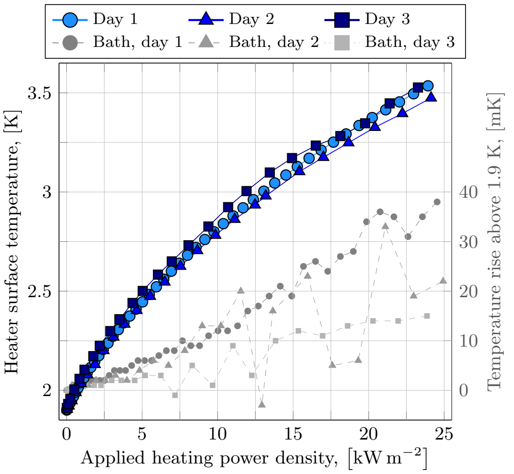

Figure 6: Heater surface temperatures of sensor `UM`, for applied heating power densities up to 25 kW m^{-2}, for three separate measurement days. Initial bath temperature is 1.9 K.

4 Steady State Results

Figure 5 shows a representative measurement result where a step up to 4.4 A is applied at time $t = 0$, and turned off after about 8 seconds. For plot clarity, only the upwards facing heater has its Q_app shown.

There is a slight bath temperature increase, peaking around 16 mK, because the two heater strips supply a large amount of heat over the course of the test. For the highest applied heating power densities used, around 85 kW m^{-2}, the peak bath temperature rise is about 50 mK.

Steady state data is taken as an average over the last 2 to 3 seconds. The bath temperature considered for steady state analysis is the average in the same time–window.

4.1 Steady State Heater Surface Temperature

The temperatures in Figure 5 are those from the Cernox® sensors themselves, which, recall, are separated from the surface by about 200 µm of sapphire, 35 µm of varnish, and 50 µm of stainless steel. So, as with any measurement where the heater surface is not directly instrumented (or itself used as a sensing element), the heater surface temperature must be obtained from the measurements by way of a thermal model. We use the steady state heat equation with temperature dependent thermal conductivities and the Python library `lmfit` to determine the surface temperature at each sensor location. We know the thermal anchor at the back of the sample is at the bath temperature, and we know the applied heating power density. The `lmfit` routine then guesses the value of the surface temperature under the condition of minimising the difference between the measured sensor temperature and the temperature at the location of the sensor in the simulated domain.

4.1.1 Our Day–to–Day Variation

Figure 6 shows the modelled surface temperature for `UM` as it varies with applied heating power density up to around 25 kW m^{-2}, for three separate measurement days. The main measurement campaign, with the highest heating powers, was Day 3 (dataset is truncated here). Between measurement days, several days passed, and going from Day 1 to Day 2, the setup spent a weekend at 4.2 K. It is not clear what causes the small variation across long time scales, but, as mentioned in Section 2.1.1, this is not unexpected. The estimated measurement uncertainty from Table 1 is smaller than the observed variation by about a factor 4 across all measurements. Between Day 1 and Day 2, the calibration was redone after finding an apparent calibration shift of around 10 mK, but as seen, the day–to–day variation is larger than this.

4.2 Kapitza Model Fit

Figure 7 shows calculated surface temperatures from the full data set from Day 3, for all sensors, up to an applied heating power density of about 85 kW m^{-2}. Upwards–pointing triangles belong to sensors on the upwards facing heater. The temperature variation between sensors at the highest applied heating is 1.46 K, from 4.67 K on `DM` to 6.13 K on `U+2`, which is roughly in line with the variation of 1.4 K (from 4.78 to 6.16 K) Claudet and Seyfert found for their various copper samples at $Q_\mathrm{app} = 80$ kW m^{-2} (Ref. [14]). Kashani and Van Sciver also found variations between identical samples (around

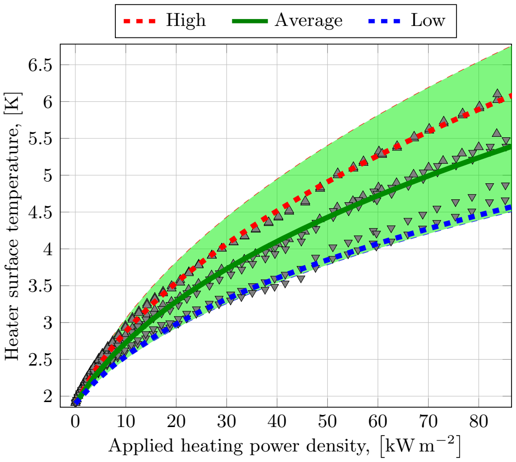

Figure 7: Range of heater surface temperatures within the estimated parameter space, represented by fits to Equation (1). Fit parameters are shown in Table 2.

0.17 K at 50 $\mathrm{kW\,m^{-2}}$), though not nearly as large as Claudet and Seyfert (Ref. [16]). There does appear to be an orientation dependence present, since the downwards facing heater shows consistently lower temperatures. No such effect is expected from the theory of Kapitza conductance, however. The variation between sensors could also stem from there being significant differences in the Kapitza conductance from one heater surface location to another. An important caveat to this is that there is a certain parameter sensitivity to the method used to obtain the heater surface temperatures. This sensitivity is explored in the following section.

The three curves in Figure 7 represent fits to the Kapitza heat transfer expression in Equation (1). The fits are made using, again, the Python package `lmfit`, with a_K and n_K as free parameters. The input to the fitting procedure is the set of simulated heater surface temperatures belonging to one sensor at a time, together with the corresponding surface–to–helium heat fluxes adjusted for the heat leak backwards to the bath. The heat leaks are estimated from the heater surface temperature calculation, and represents between 2 and 3% of the total applied heating power density. The `lmfit` routine then varies a_K and n_K looking for the combination of parameters that minimise, in a least–squares sense, the difference between the simulated surface temperature and that calculated from Equation (1).

Table 2 gives the Kapitza parameters for the three curves. High is the fit to `U+2`, which shows the highest temperatures, while Low is the fit to `DM`, which shows the lowest temperatures. Average is the the fit to the average of all seven sensors at each heating power density. The green shading represents the area between the limits in Equation (8).

$$a_\mathrm{K} \;=\; 1316.8 \pm 10\%, \quad n_\mathrm{K} \;=\; 2.528 \pm 10\% \tag{8}$$

Equation (8) represent the first reliable Kapitza parameters published for stainless steel. Note that the upper limit in the plot goes with the lower values in the range in Equation (8).

Table 2: Least–squares fit parameters for `U+2` and `DM`, and the average temperature at each heating power density, to Equation (1).

Curve	$a_\mathrm{K}\left[\mathrm{W\,m^{-2}\,K^{-n_K}}\right]$	n_K
High	1335.5	2.35
Average	**1316.8**	**2.53**
Low	1213.6	2.86

4.2.1 Parameter Sensitivity

Along and between the heater strips, looking now only at the highest applied heating power density in Figure 7 for the sake of clarity, there appears to be considerable temperature variation, on the order of 0.5 to 0.6 K on the same heater, and 1 K between the upwards and downwards facing heaters.

The method used to obtain the heater surface temperatures has a certain sensitivity to variations in the input parameters. The most important parameters that may impact the calculated heater surface temperature are; 1) the length of the copper leads (Label 3 in Figure 2) between sensor and anchor (Label A); 2) the thickness of the EPO–TEK layer (Label 6) between the sensor and the sensor leads; 3) the thickness of the varnish layer between the heater strip and the sensor (Label 4); and 4) the thermal conductivity of stainless steel (Label 8).

Comparisons will be made between the reference temperatures at the highest applied heating power density in Figure 7 and the temperature found for the same heating power after changing one of the parameters.

Copper lead wires Using a lead length of 22 mm lowers the surface temperature about 95 mK, or 1.9%, below the reference, while using a length of 18 mm increases the surface temperatures by about 110 mK, or 2.2% above the reference.

EPO–TEK silver filled epoxy Using an EPO–TEK length of 10 µm gives surface temperatures 70 mK, or 1.4%, above reference, while using a length of 30 µm gives temperatures 65 mK, or 1.2%, lower.

GE 7031 varnish Using a varnish layer thickness of 29 µm gives surface temperatures about 240 mK, or 4.2%, lower than reference, while using 41 µm gives temperatures 230 mK, or 4.2%, higher than reference.

Stainless steel Typical thermal conductivity measurement uncertainty is on the order of ±5% [46, p. 13]; by lowering the stainless steel conductivity by 5% we find heater surface temperatures 460 mK, or 8.0%, lower than the reference, while increasing the conductivity by 5% increases the surface temperatures by 350 mK, or 6.1%. We assume the thermal conductivity is uniform along and between heater strips, so the effect of this uncertainty cannot help explain the sensor variations in Figure 7. This uncertainty simply moves all curves up or down.

4.2.2 Surface Temperature Variation

The total variation in local dimensions around the sensors lead to about ±400 mK uncertainty in the calculated heater surface temperatures. This is a smaller variation in temperature than that seen in Figure 7, meaning that the spread in surface temperatures cannot fully be explained by the uncertainty range we have characterised.

Looking only at the temperature variation between sensors on the same heater strip, ±400 mK is large enough to give the same calculated heater surface temperatures, so we cannot conclude there is significant temperature variation along the same sample.

Claudet and Seyfert's results on identical copper heaters show variation between samples similar to what we see between upwards and downwards facing heaters. We cannot, therefore, conclude there is an orientation dependence of the Kapitza conductance.

5 Transient Results

Figure 8 shows the same test as that in Figure 5, focusing on the first 10 ms, after applying the capacitive compensation method described in Section 3.5. Note that these are sensor temperatures.

The first important observation is that all curves look very similar, the main difference being the steady state temperature they approach. This similarity represents an important validation that there are no small leaks or reservoirs of He II influencing the measurements; if there were, we would see the characteristic impact of the large helium heat capacity at the lambda transition. Furthermore, the impact would be different between sensors, since such reservoirs or leaks would not be of equal size and location for each sensor.

For all heating power densities tested, the temperature rise follows this general behaviour; rapid initial rise lasting about 1 ms, then a long, slow rise towards the steady state value. It takes on the order of a full second to reach the final steady state.

The tests in a bath of 2.05 K where the applied heating power density is sufficiently high to see film boiling onset has a different behaviour once boiling starts to develop, but show the same characteristic early temperature rise (discussed more in Section 5.3).

A general remark about all measurements shown in this section; unless otherwise noted, during the time windows shown in figures and considered for analysis, the bath temperature remained constant at its initial value.

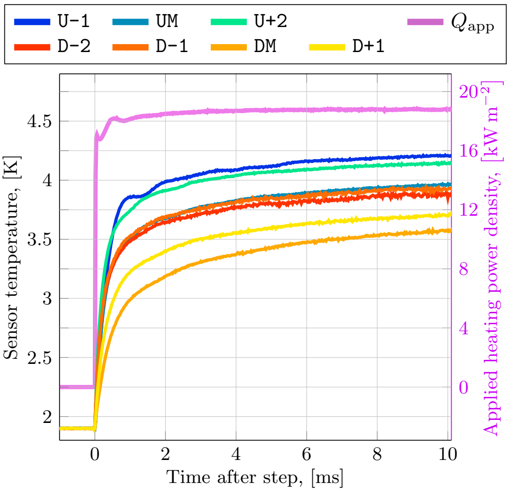

Figure 8: Representative transient measurement. Same test as in Figure 5, after compensating for the filtering capacitor in the current excitation sources, showing only the first 10 ms.

5.1 Thermal Time–Constants

To quantify the initial temperature rise we define a thermal time constant for the curves, τ, as the time it takes each sensor, for each heating power, to reach the temperature $(1 - 1/e)\,[T(t = 10\,\mathrm{ms}) - T_\mathrm{b}] + T_\mathrm{b}$. Looking at `DM` in Figure 8, this is the time at which the temperature has reached about 2.97 K, which is around 0.9 ms. Figure 9 shows this time constant for all sensors and all applied heating power densities from tests in a bath of 1.9 K. Sensors `DM` and `D+1` are significantly slower than the others, and also slow further for growing Q_{app}. Otherwise, the sensors all show time constants between 0.3 and 0.5 ms. For tests in a bath of 2.05 K, there is no significant difference in the thermal time constant as compared with Figure 9. The largest heat capacity in the system is that of stainless steel, which only grows by about 10% from 1.9 to 2.05 K. This percentage increase in the thermal time constant would only be on the order of 30 to 50 µs, which is roughly the same as the sampling period of 25 µs, and thus too small a difference to reliably measure. The increase we see for higher heating power densities stems from the temperature going up, meaning the heat capacity goes up, slowing the temperature rise.

Note that thermal time constants on the order of 0.3 to 0.5 µs is quite in line with those found by Gradt *et al.* (see Ref. [34]) and Shiotsu *et al.*(see Ref. [37]).

So, an obvious question is why `DM` and `D+1` deviate so much from the other sensors; thermal time constants are dominated by the total heat capacity of materials in the thermal path. For `DM` and `D+1` the various dimensions discussed in Section 4.2.1 must be towards their upper limits, slowing down heat transfer from increased length and thermal mass.

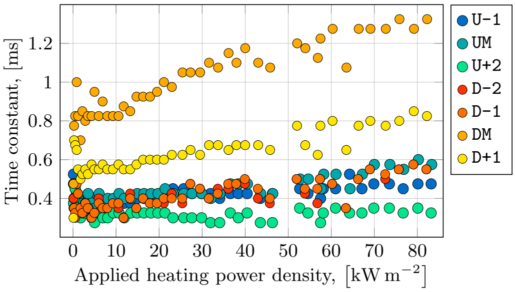

Figure 9: Estimated thermal time constants for all steps in applied heating power density in a bath of 1.9 K.

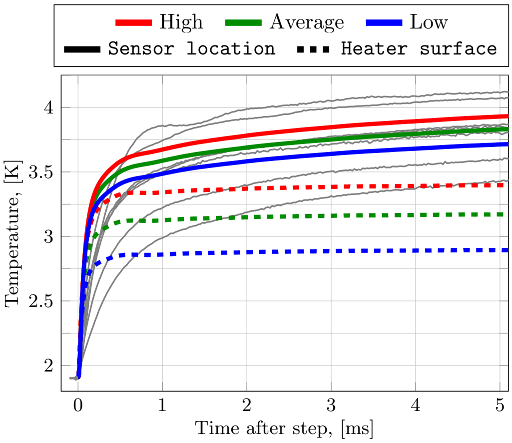

Figure 10: Representative transient measurement with simulated temperatures. Same test as that shown in Figure 8. Grey curves are measured sensor temperatures. The solid coloured curves are the temperatures at the sensor location in the transient simulation, while the dashed coloured curves are the heater surface temperatures in the simulation. `High`, `Average`, and `Low` refer to the Kapitza parameters in Table 2.

5.2 Simulating a Step

Using the time–dependent heat equation (see Appendix B), with Equation (1) defining the instantaneous heat flux across the interface between the heater surface and the bath of He II, we can simulate how the thermal response of the setup using the measured heater strip voltage as a volumetric heat source in the stainless steel heater. This simulation does not consider any dynamics in the helium, beyond using the measured bath temperature as input to the Kapitza heat transfer expression. Figure 10 shows the result of this simulation for the three Kapitza parameter sets in Table 2, compared with the measurement shown in Figure 8. We use standard material lengths; 50 µm of steel, 35 µm of varnish, 200 µm of sapphire, 20 µm of EPO–TEK, and 20 mm of copper leads. The applied heating power density, not shown in the plot for clarity, is that from the upwards facing heater; the downwards facing heater has lower resistance, and therefore, about 1.5% lower heating power density than that used in the simulation. The grey curves in the figure are the measured sensor temperatures shown in Figure 8.

The rapid early temperature rise, which is faster in simulations than measurements, stems from the Kapitza heat transfer mechanism needing a substantial temperature difference across the heater–to–helium interface to move appreciable amounts of heat. Before this temperature difference is established, the heater strip warms up nearly adiabatically. After the initial rise, after between 1 and 1.5 ms, simulations are in excellent agreement with the measured temperatures. The slow rise after 1.5 ms is dominated by the thermal mass behind the sensor needing time to heat up. Note that the simulated heater surface temperature remains nearly steady even if the sensor temperature keeps growing.

Figure 11 shows simulation results using parameters that give the largest sensor temperature variation within the estimated parameter ranges. `Upper limit` uses `High` Kapitza parameters from Table 2 with 29 µm varnish, 30 µm EPO–TEK, and 22 mm copper lead length. `Lower limit` is on the other end of the spectrum; `Low` Kapitza parameters, 41 µm varnish, 10 µm EPO–TEK, and 18 mm copper lead length.

The simulated heater surface temperatures are only marginally different from those shown in Figure 10 because the Kapitza parameters used are the same; the small heat leak backwards does not represent a sufficiently large fraction of the total heat flow to lower the surface temperature appreciably. The simulated sensor temperatures match the range of measured sensor temperatures very well, but, again, only after about 1 to 1.5 ms.

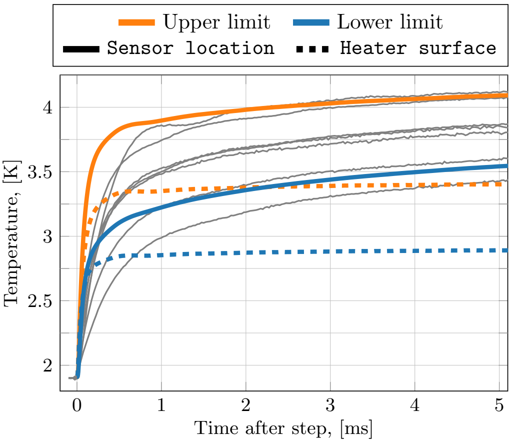

Figure 11: Like Figure 10, with simulations using the extrema in the parameter space. `Upper limit` is the simulation that gives the highest simulated sensor temperature within the parameter space, and `Lower limit` the lowest.

5.2.1 Slowing Down the Simulated Temperature Rise

We seek an explanation for why superconducting magnets subject to losses in the millisecond time–scale need much larger energy depositions to quench than what is actually observed. We see from figures 10 and 11 that simulations, using Equation (1) to represent the transient Kapitza cooling mechanism, consistently show faster temperature rises than the measured values. The discrepancy we see between simulation and measurement clearly means the system heats up slower than expected. The question is if the discrepancy is due to a feature of the setup not correctly accounted for in the model, or because the Kapitza expression represents a less effective cooling than what is really going on during the first millisecond of the transient.

A simple test of this is to replace the Kapitza boundary condition with a fixed temperature, representing a form of perfect cooling. With the reference simulation parameters, but the heater surface temperature clamped to the bath temperature, we get an initial sensor temperature rise essentially identical to the other simulated sensor temperature curves in figures 10 and 11. The difference being that with the heater surface temperature fixed at 1.9 K, the sensor temperature approaches a lower steady state value than that seen in measurements. That the "perfect cooling" gives a similar initial temperature rise is as expected; the early temperature rise is effectively adiabatic as the thermal gradient within the steel develops in order to move the required heat flux to balance the applied heating power density.

This result, where excessive cooling still does not slow down the temperature rise, points towards there being effects unaccounted for when translating the real three–dimensional setup to the simplified one–dimensional model. The discrepancy exists at all tested applied heating power densities. For the highest heating power densities (70 $\mathrm{kW\,m^{-2}}$ and up), the discrepancy appears to last a little longer; as long as 2 ms for 85 $\mathrm{kW\,m^{-2}}$. This points towards the model not adequately accounting for the effective heat capacity of the region around the sensor; heat capacity depends strongly on temperature, growing by a factor 5 to 10 just going from 2 to 4 K. Stronger heating leads to higher temperatures reached more quickly, and therefore higher heat capacities for the materials involved.

5.3 Film Boiling Onset

In a bath of 2.05 K we see the onset of film boiling for applied heating power densities above 58 $\mathrm{kW\,m^{-2}}$. Figure 12 shows the sensor temperature rise above the initial bath temperature of Sensor `UM` for the same three heating power densities in 1.9 and 2.05 K baths. The small discrepancy in Q_{app} stems from slight variations in the output current from the power source between tests.

Two immediate observations are clear; 1) at low applied heating power density, the transient behaviour is essentially indistinguishable between the two bath temperatures, which is as expected; in the Kapitza expression, the bath temperature changes the resulting heat flux only very little for high heater surface temperatures. And 2) near the critical heat flux, the film boiling onset is a very gradual process; during the test that gave 2.05 K, 58 $\mathrm{kW\,m^{-2}}$, the sensor temperature reaches about 24 K, undoubtedly a fully developed film boiling situation, and yet the transition seen in the figure is very smooth, as opposed to that for the higher applied heating power density.

Applying Equation (3) to our setup, with $L = 158$ mm and $w = 3$ mm, gives an estimated critical heat flux, at which boiling should start, of 47 $\mathrm{kW\,m^{-2}}$. The lowest applied heating power density for which we see boiling is $Q_{\mathrm{app}} = 55$ $\mathrm{kW\,m^{-2}}$, which starts after around 300 ms. During these 300 ms, the bath temperature rose by 2.5 mK. The difference between the critical heat flux from Equation (3) and the one we observe can easily be explained by a slight change in Tatsumoto *et al.*'s fit parameter K; changing its value to 0.66, instead of 0.58, gives a critical heat flux of 54 $\mathrm{kW\,m^{-2}}$.

Shiotsu *et al.* find that at about 70 $\mathrm{kW\,m^{-2}}$ the time to film boiling onset on a flat–plate–heater in an open bath is on the order of 5 ms in a bath of 2 K and 0.8 ms in a bath of 2.1 K (see Ref. [39]). Our measurements in a bath of 2.05 K find film boiling onset after between 3.1 and 4.5 ms for Q_{app} around 68 $\mathrm{kW\,m^{-2}}$, entirely in line with Shiotsu *et al.*.

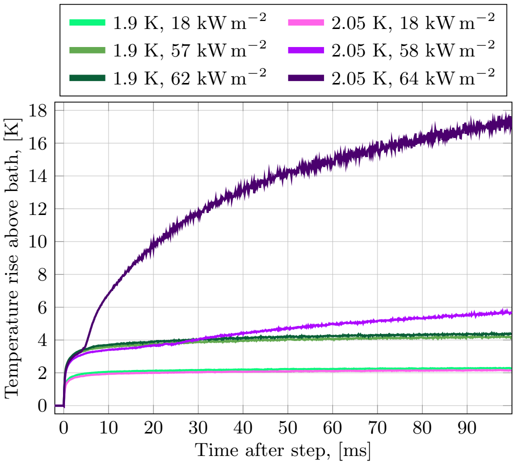

Figure 12: Measured sensor temperatures for the same applied heating power densities in baths of 1.9 and 2.05 K, represented by Sensor `UM`. The variation in Q_{app} stems from the current source not supplying exactly the same current from one test to another.

Figure 13 shows how, in a bath of 2.05 K, the upwards and downwards facing heaters differ. The Kapitza quasi–steady life–time is clearly visible; `UM`, 61 kW m^{-2}, for instance, flattens out between 2.5 and 7.5 ms, before then showing the characteristic rise due to film boiling onset. There also appears to be a slight difference in how long it takes for boiling to start; for an upwards facing plate, a bubble forming at the surface will have the help of gravity to detach and carry off energy, while for a bubble forming on the surface of a downwards facing heater, the bubble must both fight gravity as its centre of mass is moved downwards in the fluid, and also move sideways, rather than straight up, in order to move away from the heater. This helps explain why boiling starts a little sooner on the upwards facing plate seeing as there is the additional energy barrier of buoyancy to overcome on the downwards facing heater. Now, as more and more bubbles form, it will be harder for an individual bubble on the surface of the downwards facing heater to move sideways without coalescing with another bubble. This means there will be a less defined delineation between a situation with individual bubbles and one where the bubbles form a continuous film as compared with the upwards facing heater where the film only fully forms once bubbles arise across the entire surface at once. These two effects are subtle, as the time to boiling onset becomes more similar for higher heat flux, and the upwards/downwards difference becomes less pronounced. Shiotsu *et al.* show transitions to film boiling from a thin wire that are about equally smooth to ours for the downwards facing heater, while the transition for our upwards facing heaters appear sharper than theirs (see Ref. [37]). Our measurements transition into a linear temperature rise with time, as theirs do.

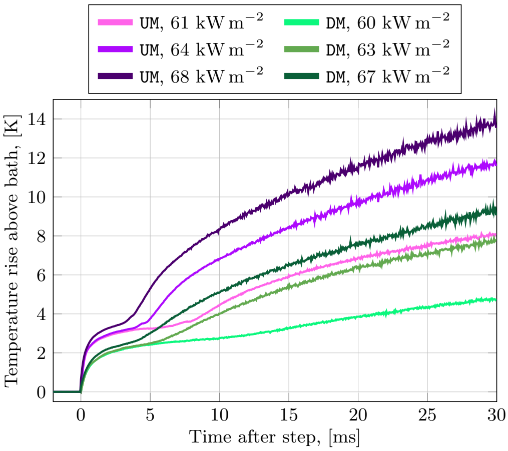

Figure 13: Measured sensor temperatures for the same heating power densities, represented by both middle sensors (`UM` and `DM`). The variation in Q_{app} stems from the small difference in heater strip resistance.

During our tests, we typically only let the film boiling regime develop for about 2 seconds. A steady state is not reached within this time, and sensor temperatures increase linearly for most of the test. As we turn off power, the sensors have reached as much as 40 to 45 K. Temperatures return to the initial bath temperature in a smooth process, lasting as long as 3 to 4 times longer than the duration of the step. The linear temperature rise lasts from about 100 ms after the step until power is turned off. Note that while the sensor temperatures are growing rapidly, the bath temperature hardly changes at all; the peak bath temperature measured during the strongest step is only 20 mK above the initial bath temperature.

The long transition period between onset of film boiling and this linear region (seen in full for 2.05 K, 64 kW m^{-2} in Figure 12) is completely smooth, without any obvious regime changes. So, the identifiable heat transfer regimes appear to be the quasi–steady Kapitza regime, before film boiling onset, and the single film–boiling–like regime without any other clear transitions, where the film boiling onset is not a distinct regime

5.3.1 Time to Film Boiling Onset

Although our setup was not designed to measure the life–time of the Kapitza regime accurately, we can get rough estimates of Kapitza regime life–time, τ_{Kapitza}, from the curves in Figure 13 by taking τ_{Kapitza} as the time of the kink upwards as the criterion for identifying the film boiling onset. Figure 14 shows the film boiling onset time (or Kapitza regime life–time) for all measurements where we saw film boiling onset within a few tens of milliseconds after the step in power. The curve in the figure is an example of a curve $\tau_{\text{Kapitza}} \propto Q^{-4}$, which our measurements tend to follow as Q_{app} goes above 60 kW m^{-2}, like expected from Equation (5).

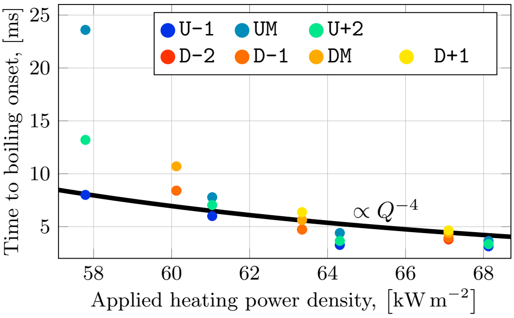

Figure 14: Time to boiling onset as function of Q_{app}, showing also a curve $\propto Q^{-4}$.

5.3.2 Simulate Quasi–Steady Life–Time

Figure 15 shows the step in applied heating power density up to 68 kW m^{-2}, in a bath of 2.05 K together with a simulation using reference parameters. At $t = 3.5$ ms we instantaneously change the heat transfer regime from the Kapitza expression in Equation (1) to the much weaker film boiling expression in Equation (2) with $a_{\mathrm{FB}} = 500\ \mathrm{W\,m^{-2}\,K^{-1}}$. The quasi–steady Kapitza life–time is obvious; the simulated sensor temperature stabilises between $t = 1$ and 3 ms, at which point the film boiling onset is reached. At 3.5 ms we trigger the fully developed film boiling heat transfer regime. An important insight from this very simple modelling approach is that the drop in heat transfer capability when going into film boiling is so large that most of the heat is now transferred backwards through the material stack rather than by the film boiling heat flux itself. It is also clear that the real film boiling onset is a much smoother process than a hard transition from a high to a low heat transfer regime, seeing as even the sharper `U-1` and `U+2` sensors see a mellower transition into the film boiling onset temperature rise.

Note also that, save for the discrepancy during the first millisecond, also a step that leads to film boiling can be accurately simulated using the simple steady state Kapitza expression as the cooling boundary condition before film boiling onset.

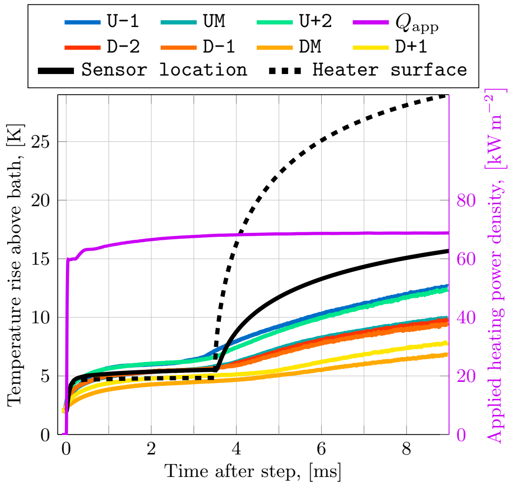

Figure 15: Measured sensor temperatures during step in applied heating power density to 68 $\mathrm{kW\,m^{-2}}$, in bath of 2.05 K, together with simulation using reference parameters.

6 Conclusion

To begin investigating the observation that significantly more heat input is necessary to quench an LHC superconducting magnet than what models have predicted, we built an experimental setup with the aim of making millisecond time–scale measurements of transient cooling of a heater cooled by an open bath of He II. We confirm the setup behaves as expected in steady state, where the Kapitza heat transfer model is known to work, and quantify the measurement uncertainty from a wide range of parameters. The result is a set of Kapitza fit parameters valid for applied heating power densities Q_{app} between 1 and 85 $\mathrm{kW\,m^{-2}}$; $a_{\mathrm{K}} = 1316.8\pm10\%$, and $n_{\mathrm{K}} = 2.528\pm10\%$.

Further validation of the experimental setup is found by the critical heat flux being in line with approximate expressions from literature relevant to our heating geometry, and then by seeing that the time from turning on heating power to onset of film boiling follows the expected $\propto Q^{-4}$ behaviour.

The setup allowed us to investigate heat transfer variations along heaters and between upwards and downwards facing heaters. We do not find evidence of significant differences attributable to local surface conditions along the heaters, nor differences attributable to an orientation dependence. The difference between the upwards and downwards facing heater temperatures is in line with what can be expected simply from the two heaters being unique.

The rise time of the initial measured temperature response after a step in applied heating power density is on the order of 0.3 to 0.5 ms, which is similar to the data found in literature, and we provide considerably more time–resolved data than that which has previously been published.

We have made a time–dependent one–dimensional model representation of the setup. The model's thermal response to a step in Q_{app} is faster than what we measure during the first millisecond after the step, with an initial rise time about half that of measurements, but after this, the agreement between measurement and model is excellent. This means we confirm the assumption that the steady state Kapitza heat transfer expression can be used for fast transient modelling.

A Material Parameters

Figure A.1 shows the thermal conductivity and heat capacity of the seven materials included in the analysis of data. The figures stop at 30 K, since measured temperature never go above this, but all materials have known parameters in the range 1.7 to 100 K.

The data, with densities from Table 3, comes from the following sources;

Copper Heat capacity is a fit by NIST[47]. Note that although the range is from 4 to 300 K, the expression they propose fit their source data by Stewart and Johnson down to 1 K[48, p. 4.112–1]. Thermal conductivity is a fit function proposed by Simon *et al.*[49], where we assume here that the RRR of copper is 100.

Sapphire Heat capacity is Viswanathan's polynomial fit below 20.0661 K[50], and Fugate and Swenson's polynomial fit above[51]. Lake Shore Cryotronics provide thermal conductivity data for sapphire[52, Figure 1.], and the curve seen in Figure A.1 is a cubic spline fit to the Lake Shore Cryotronics curve.

GE 7031 varnish Heat capacity data for the GE 7031 varnish is taken from a measurement by Heessels[53]. No fit function is provided, so a cubic spline fit to the data

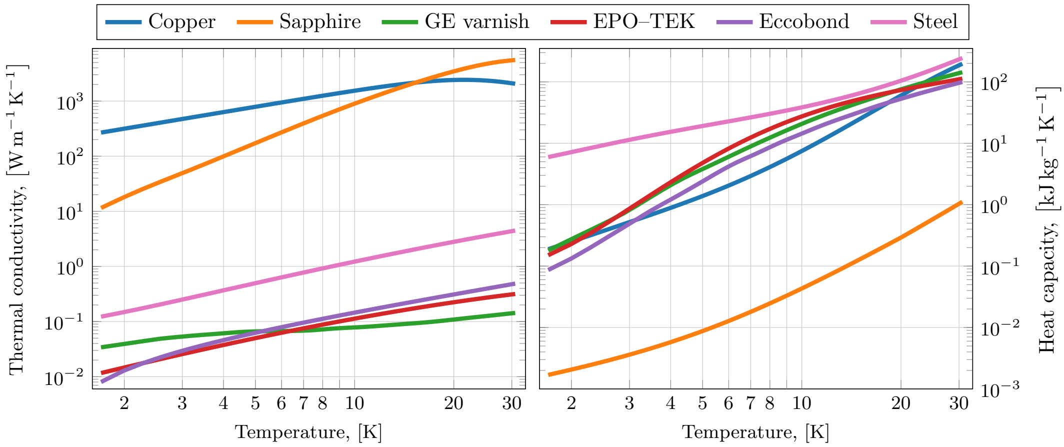

Figure A.1: Thermal conductivity (left) and heat capacity (right) as used in analysis herein. Plots highlight the most relevant region below 30 K, though the parameters are known till 100 K.

is used. For thermal conductivity, the measurements by McTaggart and Slack are used[54]. They do not provide fit functions, so cubic splines are fitted to the data.

EPO–TEK H20E This proprietary compound does not have readily available data across the entire relevant temperature range. Heat capacity data up to 9 K is taken from Weyhe *et al.*[55]. Extending the range is done by using heat capacity data for Stycast 2850FT, measured by Swenson[56, Figure 3]. The final heat capacity curve is made by making a fifth degree polynomial fit to the logarithm of Weyhe *et al.*'s data up to 8 K and the Swenson data from 30 K up. Thermal conductivity is a third degree polynomial fit of the logarithm of Amils *et al.*'s data[57].

Eccobond® Neither heat capacity nor thermal conductivity data is available for Eccobond® 286 A/B. The heat capacity used for Eccobond® is that of Stycast 2850FT based on the full temperature range measured by Swenson[56, figures 4 and 3]. A cubic spline fit to this data is used. The thermal conductivity used for Eccobond® is that of Eccobond® 285, a single–component epoxy from the same manufacturer, for which a short measurement set exists between 4 and 8 K, by Rondeaux *et al.*[58]. This data indicates a linear temperature dependence of the thermal conductivity, and this relationship is extrapolated from 1.7 K up. Since heat capacity is that of Stycast 2850FT, the density of Eccobond® is taken as that of Stycast. This probably leads to a higher thermal diffusion time than what is true, for Eccobond®'s actual density, 1400 kg m^{-3}, is only 60% that of Stycast.

Stainless steel The heat capacity of 304 stainless steel used for the heater strips is found in Du Chatenier *et al.* for temperatures below 90 K[59], and in NIST reference data above 90 K[60]. The logarithm of Du Chatenier *et al.*'s data is fitted by a fifth degree polynomial, while NIST provide their own fit.

Thermal conductivity is more complicated. Between 1 K and 1.7 K, Stutius and Dillinger made measurements on 304 stainless steel[61], and they quantify the lattice contribution to thermal conductivity. Between 6 K and 110 K, Hust and Sparks give Lorenz ratio measurements for a compositionally similar steel they call HS(347)[46, p. II-34]. The Wiedemann–Franz law relate the electrical resistivity to thermal conductivity through the Lorentz ratio[20, p. 153]. The sum of these two constrictions is compared with dedicated measurements on our steel samples around 4.2 K, in order to scale the Wiedemann–Franz result. The measurements, and thus the thermal conductivity used herein, are a factor 0.9383 lower than the WF result.

Table 3: Volumetric density of relevant materials

Material	Density [kg m^{-3}]
Copper[62]	8960
Sapphire[63]	3980
GE Varnish[64]	887
EPO–TEK H20E[65]	2550
Eccobond/Stycast[66]	2292
Steel[67]	7955

B Heat Equation

During a transient where some voltage is measured across the heater strip, the one–dimensional heat equation takes the form,

$$C_{\mathrm{p}}(x,T)\rho(x,T)\frac{\partial T}{\partial t} = \frac{\partial}{\partial x}\left\{k(x,T)\frac{\partial T}{\partial x}\right\} + \frac{V_{\mathrm{meas}}^2}{R_{\mathrm{s}}v_{\mathrm{s}}}, \quad \text{(B.1)}$$

where R_{s} is the electrical resistance of a heater strip, and v_{s} is the volume of it.

The two boundary conditions are, 1) a Dirichlet condition at the extreme end of the material stack where Eccobond® touches helium, with temperature fixed to the bath temperature, and 2) a Neumann condition at the cooled surface of the stainless steel heater strip;

$$T(x = x_{\mathrm{end}}, t) = T_{\mathrm{bath}}(t), \quad \text{(B.2)}$$

$$\left.\frac{\partial T}{\partial x}\right|_{x=0} = \frac{Q_{\mathrm{Cooling}}(t)}{k_{\mathrm{steel}}(T(x=0,t))}, \quad \text{(B.3)}$$

where Q_{Cooling} is cooling–regime dependent. In the Kapitza regime, for instance, Equation 1 is used. The Neumann condition is implemented as a central difference in the numerical scheme to preserve second order accuracy in space.

To solve Eq. B.1, a Crank–Nicolson scheme is used. To account for the temperature dependent thermal conductivities, as well as there being interfaces between several materials, the thermal conductivity is evaluated between adjacent points by an average;

$$\kappa_{i+1/2}^n = \frac{1}{2}(k_{i+1}^n + k_i^n) \quad \text{(B.4)}$$

$$\kappa_{i-1/2}^n = \frac{1}{2}(k_{i-1}^n + k_i^n) \quad \text{(B.5)}$$

where k_i^n is the thermal conductivity of the material at location x_i at time t_n.

The discretised Eq. B.1, with $V_i^n = V_{\mathrm{meas}}(x_i, t_n)$, then becomes;

$$\begin{aligned} &C_i\rho_i\frac{T_i^{n+1} - T_i^n}{\Delta t} = \\ &\frac{1}{2\Delta x^2}\left[\kappa_{i+1/2}\left(T_{i+1}^{n+1} - T_i^{n+1}\right) - \kappa_{i-1/2}\left(T_i^{n+1} - T_{i-1}^{n+1}\right)\right] \\ &+ \frac{1}{2\Delta x^2}\left[\kappa_{i+1/2}\left(T_{i+1}^{n} - T_i^{n}\right) - \kappa_{i-1/2}\left(T_i^{n} - T_{i-1}^{n}\right)\right] \\ &+ \frac{(V_i^n)^2 + (V_i^{n+1})^2}{2R_{\mathrm{s}}v_{\mathrm{s}}} \end{aligned} \quad \text{(B.6)}$$

When obtaining the steady state surface temperature discussed in Section 4, the Neumann condition from Equation B.3 is replaced by a Dirichlet condition where the boundary temperature is obtained by refining guesses that minimise the difference between simulated sensor temperature and measured sensor temperature.

References

[1] R.A. Jameson. "Beam losses and beam halos in accelerators for new energy sources". In: *Fusion Engineering and Design* 32-33 (1996). Proceedings of the Seventh International Symposium on Heavy Ion Inertial Fusion, pp. 149–157. ISSN: 0920–3796. DOI: `10.1016/S0920-3796(96)00463-2`.

[2] Helmut Wiedemann. "Beam Life Time". In: *Particle Accelerator Physics: Basic Principles and Linear Beam Dynamics*. Berlin, Heidelberg: Springer Berlin Heidelberg, 1993, pp. 370–383. ISBN: 978–3–6620–2903–9. DOI: `10.1007/978-3-662-02903-9_11`.

[3] R W Assmann et al. "LHC Collimation: Design and Results from Prototyping and Beam Tests". In: (2005), 4 p. URL: `https://cds.cern.ch/record/882889`.

[4] Eleftherios Skordis et al. "Study of the 2015 Top Energy LHC Collimation Quench Tests Through an Advanced Simulation Chain". In: (2017), MOPAB012. 4 p. DOI: `10.18429/JACoW-IPAC2017-MOPAB012`. URL: `http://cds.cern.ch/record/2287339`.

[5] Giulia Papotti, Markus Albert, Bernhard Auchmann, Eva Barbara Holzer, Matti Kalliokoski, and Anton Lechner. "Macroparticle-Induced Losses During 6.5 TeV LHC Operation". In: CERN–ACC–2016–249 (2016), TUPMW023. 4 p. DOI: `10.18429/JACoW-IPAC2016-TUPMW023`.

[6] Y. Iwasa. *Case Studies in Superconducting Magnets: Design and Operational Issues*. Springer US, 2009. ISBN: 978–0–3870–9800–5.

[7] J.B. Jeanneret, D. Leroy, L. Oberli, and T. Trenkler. *Quench levels and transient beam losses in LHC magnets*. CERN–LHC–PROJECT–REPORT–044. 1996.

[8] Emmanuele Ravaioli. "CLIQ. A new quench protection technology for superconducting magnets". 2015. URL: `https://cds.cern.ch/record/2031159`.

[9] A. Verweij. *CUDI: User's Manual*. CERN. 2007. URL: `http://cern-verweij.web.cern.ch/Manual%20CUDI%20v13.doc`.

[10] Marco Breschi, Enrico Felcini, Francesca Breccia, P. P. Granieri, Eleonora Bergonzoni, Alessandro Bevilacqua, Pietro Galassi, Tiemo Winkler, and Luca Bottura. "Modeling of Beam Loss Induced Quenches in the LHC Main Dipole Magnets". In: *IEEE Transactions on Applied Superconductivity* 29.5 (2019), pp. 1–7. DOI: `10.1109/TASC.2019.2906636`.

[11] A. Priebe, J. Steckert, A. Verweij, et al. "Beam-induced Quench Test of a LHC Main Quadrupole". In: *Conf. Proc. C* 110904 (2011). Ed. by Christine Petit-Jean-Genaz, pp. 2388–2390. URL: `http://accelconf.web.cern.ch/AccelConf/IPAC2011/papers/WEPC172.pdf`.

[12] B. Auchmann et al. "Testing beam–induced quench levels of LHC superconducting magnets". In: *Phys. Rev. ST Accel. Beams* 18 (6 June 2015), p. 061002. DOI: `10.1103/PhysRevSTAB.18.061002`.

[13] S. W. Van Sciver. *Helium Cryogenics*. International Cryogenics Monograph Series. Springer New York, 2012. ISBN: 978–1–4419–9978–8.

[14] G. Claudet and P. Seyfert. “Bath cooling with subcooled superfluid helium”. In: *Advances in Cryogenic Engineering 27* (1981), pp. 441–449.

[15] J. S. Goodling and R. K. Irey. “Non–Boiling and Film Boiling Heat Transfer to a Saturated Bath of Liquid Helium”. In: *Advances in Cryogenic Engineering 14*. Ed. by K. D. Timmerhaus. Springer US, 1969, pp. 159–169. ISBN: 978–1–4757–0549–2. DOI: 10.1007/978-1-4757-0549-2_19.

[16] A. Kashani and S. W. Van Sciver. “High heat flux Kapitza conductance of technical copper with several different surface preparations”. In: *Cryogenics* 25.5 (1985), pp. 238–242. ISSN: 0011–2275. DOI: 10.1016/0011-2275(85)90202-4.

[17] B. W. Clement and T. H. K. Frederking. “Thermal Boundary Resistance and Related Peak Flux During Supercritical Heat Transport from a Horizontal Surface Through a Short Tube to a Saturated Bath of Liquid He II”. In: *Liquid Helium Technology*. Vol. 6. Pure and Applied Cryogenics. Elsevier, 1966, pp. 49–59. DOI: 10.1016/B978-0-08-012409-4.50008-5.

[18] M. Shiotsu, K. Hata, and A. Sakurai. “Comparison of transient heat transfer characteristics for large stepwise heat input in He I and He II”. In: *Cryogenics* 32.5 (1992). Basic Mechanisms of Helium Heat Transfer and Related Influence on Stability of Superconducting Magnets, pp. 455–460. ISSN: 0011-2275. DOI: 10.1016/0011-2275(92)90075-L.

[19] M. Taneda, T. Miki, and T. Ohtani. “The Kapitza conductance of PVF-coated copper and some materials used for superconducting magnets”. In: *Cryogenics* 32.5 (1992). Basic Mechanisms of Helium Heat Transfer and Related Influence on Stability of Superconducting Magnets, pp. 479–484. ISSN: 0011–2275. DOI: 10.1016/0011-2275(92)90079-P.

[20] C Kittel. *Introduction to Solid State Physics*. 6th edition. Wiley, 1986. ISBN: 978–0–4718–7474–4.

[21] I. M. Khalatnikov. *An Introduction to the Theory of Superfluidity*. Ed. by David Pines. Trans. Russian by Pierre C. Hohenberg. Advanced Book Classics. Russian printing in 1965. Westview Press, 2000.

[22] L. J. Challis, K. Dransfeld, and J. Wilks. “Heat transfer between solids and liquid helium II”. In: *Proceedings of the Royal Society of London. Series A. Mathematical and Physical Sciences* 260.1300 (1961). Communicated by Bleaney, Brebis, pp. 31–46. DOI: 10.1098/rspa.1961.0011.

[23] Paul H. E. Meijer and Joseph S. J. Peri. “New Kapitza heat–transfer model for liquid ^{4}He”. In: *Phys. Rev. B* 22 (1 1980), pp. 195–205. DOI: 10.1103/PhysRevB.22.195.

[24] W. A. Little. “The Transport of Heat Between Dissimilar Solids at Low Temperatures”. In: *Canadian Journal of Physics* 37.3 (1959), pp. 334–349. DOI: 10.1139/p59-037.

[25] I. N. Adamenko and I. M. Fuks. “Roughness and thermal resistance of the boundary between a solid and liquid helium”. In: *Soviet Journal of Experimental and Theoretical Physics* 32.6 (1971), pp. 1123–1129.

[26] N. S. Shiren. “Surface Roughness Contribution to Kapitza Conductance”. In: *Phys. Rev. Lett.* 47 (20 1981), pp. 1466–1469. DOI: 10.1103/PhysRevLett.47.1466.

[27] A. Khater and J. Szeftel. “Theory of the Kapitza resistance”. In: *Phys. Rev. B* 35 (13 1987), pp. 6749–6755. DOI: 10.1103/PhysRevB.35.6749.

[28] A. C. Anderson, J. I. Connolly, and J. C. Wheatley. “Thermal Boundary Resistance between Solids and Helium below 1°K”. In: *Phys. Rev.* 135 (4A 1964), A910–A921. DOI: 10.1103/PhysRev.135.A910.

[29] Aymeric Ramiere, Sebastian Volz, and Jay Amrit. “Thermal resistance at a solid/superfluid helium interface”. In: *Nature materials* 15.5 (2016), pp. 512–516. DOI: 10.1038/nmat4574.

[30] Pradeep L. Menezes Kishore and Satish V. Kailas. “Chapter 14 - Studies On Friction And Transfer Layer Using Inclined Scratch”. In: *Scratching of Materials and Applications*. Ed. by Sujeet Sinha. Vol. 51. Tribology and Interface Engineering Series. Elsevier, 2006, pp. 262–279. DOI: 10.1016/S0167-8922(06)80050-7.

[31] K. C. Rawlings and J. C. A. van der Sluijs. “New experimental results on the static and the transient anomalous Kapitza conductance of clean copper to ^{4}He interfaces”. In: *Journal of Low Temperature Physics* 33.3/4 (1978), pp. 313–329. DOI: 10.1007/bf00115002.

[32] H. Kobayashi, K. Yasukochi, and K. Tokuyama. “Heat Transfer to Liquid Helium in a Narrow Channel Below 4.2 K”. In: *Proceedings of the Sixth International Cryogenic Engineering Conference (ICEC 6)*. Ed. by K. Mendelssohn. IPC Science and Technology Press, 1976, pp. 307–309.

[33] S.W. Van Sciver. “Transient heat transport in He II”. In: *Cryogenics* 19.7 (1979), pp. 385–392. ISSN: 0011–2275. DOI: 10.1016/0011-2275(79)90120-6.

[34] Th. Gradt, U. Ruppert, K. Lüders, and Wang Ruzhu. “Transient Heat Transfer to Superfluid Liquid Helium”. In: *Advances in Cryogenic Engineering 35A*. Ed. by R. W. Fast. Boston, MA: Springer US, 1990, pp. 117–123. ISBN: 978-1-4613-0639-9. DOI: 10.1007/978-1-4613-0639-9_14.

[35] R. Wang, T. Gradt, U. Ruppert, L. Xu, H. D. Denner, and G. Klipping. “Film Boiling Onset Time in Subcooled Superfluid Helium: The Influence of Bath Temperature and Pressure”. In: *Proceedings of the Thirteenth International Cryogenic Engineering Conference (ICEC 13)*. Ed. by C. S. Hong. Cryogenics 1990 Vol 30 September supplement. 1990, pp. 360–364.

[36] M. Shiotsu, K. Hata, and A. Sakurai. “Transient Heat Transfer for Large Stepwise Heat Inputs to a Horizontal Wire in Subcooled He II”. In: *Advances in Cryogenic Engineering, 37A*. Ed. by R. W. Fast. Plenum Press, 1992, pp. 37–46.

[37] Shiotsu M., Hata K., and A. Sakurai. “Transient Heat Transfer From a Horizontal Wire in Subcooled He II at Atmospheric Pressure for a Wide Range of Wire Diameter”. In: *Advances in Cyrogenic Engineering 41*. Ed. by P. Kittel. Plenum Press, 1996, pp. 1065–1072. ISBN: 978-1-4613-0373-2. DOI: 10.1007/978-1-4613-0373-2_31.

[38] H. Tatsumoto, K. Hata, Y. Takeuchi, K. Hama, Y. Shirai, and M. Shiotsu. "Critical Heat Flux on Various Sized Flat Plates in Pressurized He II". In: *Proceedings of the Seventeenth International Cryogenic Engineering Conference (ICEC 17).* Ed. by D. Dew–Hughes, R. G. Scurlock, and J. H. P. Watson. Institute of Physics Publishing, 1998, pp. 683–686.

[39] Shiotsu M., Hata K., Hama K., and Shirai Y. "Transient Heat Transfer Produced by a Stepwise Heat Input to a Flat Plate on One End of a Rectangular Duct Containing Pressurized He II". In: *Advances in Cyrogenic Engineering 45B*. Ed. by Q. Shu. Plenum Press, 2000, pp. 1065–1072. ISBN: 978-1-4615-4215-5. DOI: `10.1007/978-1-4615-4215-5_14`.

[40] H. Tatsumoto, K. Hata, K. Hama, Y. Shirai, and M. Shiotsu. "Critical heat flux on a flat plate in pressurized He II". In: *Cryogenics* 41.1 (2001), pp. 35–38. ISSN: 0011–2275. DOI: `10.1016/S0011-2275(01)00048-0`.

[41] A. Sakurai, M. Shiotsu, and K. Hata. "Transient Heat Transfer for Large Stepwise Heat Inputs to a Horizontal Wire in Saturated He II". In: *Advances in Cryogenic Engineering, 37A*. Ed. by R. W. Fast. Plenum Press, 1992, pp. 25–35.

[42] P. Seyfert, J. Lafferranderie, and G. Claudet. "Time dependent heat transport in subcooled superfluid helium". In: *Cryogenics* 22.8 (1982), pp. 401–408. ISSN: 0011–2275. DOI: `10.1016/0011-2275(82)90084-4`.

[43] S. S. Courts and P. R. Swinehart. "Review of Cernox™ (Zirconium Oxy–Nitride) Thin–Film Resistance Temperature Sensors". In: *AIP Conference Proceedings* 684.1 (2003), pp. 393–398. DOI: `10.1063/1.1627157`.

[44] S. Fuzier and S.W. Van Sciver. "Use of the bare chip Cernox™ thermometer for the detection of second sound in superfluid helium". In: *Cryogenics* 44.3 (2004), pp. 211–213. ISSN: 0011–2275. DOI: `10.1016/j.cryogenics.2003.11.005`.

[45] A Perin, R Macias–Jareño, and L Métral. "Study of Materials and Adhesives for Superconducting Cable Feedthroughs". In: *AIP Conf. Proc.* 613 (2001), 551–558. 9 p. DOI: `10.1063/1.1472065`. URL: `https://cds.cern.ch/record/524909`.

[46] J. G. Hust and L. L. Sparks. *Lorenz Ratios of Technically Important Metals and Alloys.* Tech. rep. 634. National Bureau of Standards, 1973. URL: `https://www.govinfo.gov/content/pkg/GOVPUB-C13-aee47505ca1ecea2f91b3342696c2fed/pdf/GOVPUB-C13-aee47505ca1ecea2f91b3342696c2fed.pdf`.

[47] National Institute of Standards and Technology. *Material Properties: OFHC Copper (UNS C10100/C10200).* [Online; accessed 31-Mar-2020]. 2010. URL: `https://trc.nist.gov/cryogenics/materials/OFHC%20Copper/OFHC_Copper_rev1.htm`.

[48] R. B. Stewart and V. J. Johnson. "A COMPENDIUM OF THE PROPERTIES OF MATERIALS AT LOW TEMPERATURE (PHASE II)". In: 1960. URL: `https://apps.dtic.mil/dtic/tr/fulltext/u2/249786.pdf`.

[49] N.J. Simon, E.S. Drexler, and R.P. Reed. *Properties of Copper and Copper Alloys at Cryogenic Temperature.* Tech. rep. NIST Monograph 177. National Institute of Standards and Technology, 1992.

[50] R. Viswanathan. "Heat capacity of sapphire between 2 and 10 K by AC technique". In: *Journal of Applied Physics* 46.9 (1975), pp. 4086–4087. DOI: `10.1063/1.322119`.

[51] R. Q. Fugate and C. A. Swenson. "Specific Heat of α Al2O3 from 2 to 25 K". In: *Journal of Applied Physics* 40.7 (1969), pp. 3034–3036. DOI: `10.1063/1.1658118`.

[52] Lake Shore Cryotronics. *Appendix I: Cryogenic Reference Tables.* [Manufacturer's note]. 2000. URL: `https://www.lakeshore.com/docs/default-source/product-downloads/literature/lstc_appendixi_l.pdf?sfvrsn=5f2ab85b_4`.

[53] J.T. Heessels. "Specific heat of general electric 7031 varnish from 2 to 80 K". In: *Cryogenics* 11.6 (1971), pp. 483–484. ISSN: 0011–2275. DOI: `10.1016/0011-2275(71)90275-X`.

[54] J.H. McTaggart and G.A. Slack. "Thermal conductivity of general electric No. 7031 varnish". In: *Cryogenics* 9.5 (1969), pp. 384–385. ISSN: 0011-2275. DOI: `https://doi.org/10.1016/0011-2275(69)90019-8`. URL: `http://www.sciencedirect.com/science/article/pii/0011227569900198`.

[55] S. Weyhe, B. Junge, F. Petzoldt, S. Bruns, and W. Gey. "Specific heat of delta bond 152, EPO-TEK H2OE, and wood's metal at low temperatures". In: *Cryogenics* 23.3 (1983), pp. 166–167. ISSN: 0011-2275. DOI: `https://doi.org/10.1016/0011-2275(83)90180-7`. URL: `https://www.sciencedirect.com/science/article/pii/0011227583901807`.

[56] C. A. Swenson. "Linear thermal expansivity (1.5–300 K) and heat capacity (1.2–90 K) of Stycast 2850FT". In: *Review of Scientific Instruments* 68.2 (1997), pp. 1312–1315. DOI: `10.1063/1.1148064`. eprint: `https://doi.org/10.1063/1.1148064`. URL: `https://doi.org/10.1063/1.1148064`.

[57] Ricardo I. Amils, Juan Daniel Gallego, José Luis Sebastián, Sagrario Muñoz, Agustín Martín, and Arnulf Leuther. "Thermal conductivity of silver loaded conductive epoxy from cryogenic to ambient temperature and its application for precision cryogenic noise measurements". In: *Cryogenics* 76 (2016), pp. 23–28. ISSN: 0011-2275. DOI: `https://doi.org/10.1016/j.cryogenics.2016.03.001`. URL: `https://www.sciencedirect.com/science/article/pii/S0011227515300400`.

[58] F. Rondeaux, Ph. Bredy, and J. M. Rey. "Thermal conductivity measurements of epoxy systems at low temperature". In: *AIP Conference Proceedings* 614.1 (2002), pp. 197–203. DOI: `10.1063/1.1472543`. eprint: `https://aip.scitation.org/doi/pdf/10.1063/1.1472543`. URL: `https://aip.scitation.org/doi/abs/10.1063/1.1472543`.

[59] F.J. Du Chatenier, B.M. Boerstoel, and J. De Nobel. "Specific heat capacity of a stainless steel". In: *Physica* 31.7 (1965), pp. 1061–1062. ISSN: 0031–8914. DOI: `10.1016/0031-8914(65)90148-5`.

[60] National Institute of Standards and Technology. *Material Properties: 304 Stainless (UNS S30400).* [Online; accessed 31-Mar-2020]. 1999. URL: `https://trc.nist.gov/cryogenics/materials/304Stainless/304Stainless_rev.htm`.

[61] W. Stutius and J. R. Dillinger. “Magnetic and thermal properties of some austenitic stainless steels at low temperatures”. In: *Journal of Applied Physics* 44.6 (1973), pp. 2887–2888. DOI: `10.1063/1.1662665`.

[62] Engineering Toolbox. *Metals and Alloys - Densities.* [Online; accessed 14-Sept-2019]. 2004. URL: `https://www.engineeringtoolbox.com/metal-alloys-densities-d_50.html`.

[63] Roditi International Corporation Ltd. *Sapphire Properties.* [Online; accessed 9-Aug-2021]. URL: `http://www.roditi.com/SingleCrystal/Sapphire/Properties.html`.

[64] CMR Direct. *Product Specification: GE / IMI 7031.* [Online; accessed 9-Aug-2021]. URL: `http://www.cmr-direct.com/en/product/download/get?download_id=4`.

[65] Epoxy Technology. *Technical data sheet: EPO-TEK H20E.* [Online; accessed 09-Aug-2021]. 2014. URL: `https://www.tedpella.com/technote_html/16014_H20E_TN.pdf`.

[66] Loctite. *Technical data sheet: LOCTITE STYCAST 2850FT.* [Online; accessed 09-Aug-2021]. 2015. URL: `https://tdsna.henkel.com/americas/na/adhesives/hnauttds.nsf/web/35541AEFDE6FDF8485257576004480E6/%5C$File/STYCAST%202850FT-EN.pdf`.

[67] AZO Materials. *Stainless Steel - Grade 304 (UNS S30400).* [Online; accessed 11-Aug-2021]. 2001. URL: `https://www.azom.com/properties.aspx?ArticleID=965`.

Paper II

Jonas Blomberg Ghini, Bernhard Auchmann, and Bertrand Baudouy

Millisecond Time–Scale Measurements of Heat Transfer to Confined He II

ArXiv:2203.04701 [2]

Millisecond Time–Scale Measurements of Heat Transfer to Confined He II

Jonas Blomberg Ghini[1,2,*] Bernhard Auchmann[2] Bertrand Baudouy[3]

[1]Department of Physics, Norwegian University of Science and Technology, NTNU, Norway
[2]European Organization for Nuclear Research, CERN, Switzerland
[3]Irfu, CEA, Université Paris–Saclay, F-91191 Gif–sur–Yvette, France
[*]Corresponding author: *jonas.blomberg.ghini@ntnu.no*

Abstract

We explore transient heat transfer, on the millisecond time–scale, from a narrow, rectangular stainless steel heater cooled from one side by He II confined to a channel of 120 µm depth. The helium is isolated from the external bath with the exception of two pin–holes of cross section about 10% that of the channel.

We measure the temperatures of both the heater strip and the channel helium during slow–pulse heating that reaches peak power after 9 ms, fast–pulse heating that reaches peak power after 100 µs, and step heating that reaches steady power after 100 µs.

Using the steady state Kapitza heat transfer expression at the interface between heater and helium, and the Gorter–Mellink heat transfer regime in the helium channel, we obtain excellent agreement between simulation and measurement during the first 5 ms of slow–pulse tests. Using instead the measured helium temperature in the Kapitza expression, we obtain excellent agreement between the simulated and measured heater response during the first 150 ms of slow–pulse tests.

The same model fails to explain the fast–pulse transient response of the heater and helium, while it can explain the helium response to a step in applied power but not the heater response. The steady state Kapitza expression may therefore not be applicable to heating events that are over within a single millisecond.

1 Introduction

The Large Hadron Collider (LHC) is subject to a recurrent beam loss event called an Unidentified Falling Object (UFO) [1], happening on the order of 10 to 30 times per hour of LHC operation [2, Fig. 2]. A UFO event is an interaction between the particle beam and dust or debris that is assumed to fall from the top of the LHC beam pipe into the path of the beam, causing inelastic collisions between the beam particles and the dust [3, Sec. 3.3.1]. The interaction leads to energy deposition in the superconducting magnet that surrounds the beam pipe. This transient energy deposition has an asymmetric Gaussian shape, and the entire UFO event is typically over after just 1 ms [3, Fig. 3.7]. If the energy deposition is sufficiently large, the superconducting magnet will quench, meaning it loses superconductivity (locally at first, and then this initial normal–conducting zone propagates to the rest of the magnet). In the case of a magnet quench it will take about 12 hours before normal LHC operation is restored [4]. If a that would cause a quench UFO is detected early enough, triggering a beam dump, it still takes about 3 hours to resume normal operation.

During LHC operation successful mitigation strategies are currently employed such that quenches are avoided, and such that unnecessary beam dumps are kept to a minimum [5]. In the future, however, the LHC is scheduled for an upgrade to increase the beam energy [6]. For higher beam energy, each UFO event will cause larger losses, because the individual beam–particles impact the UFO with more energy [7, Fig. 5.11]. This leads to the need for better understanding of the millisecond time–scale losses UFOs represent.

After analysis of a dedicated beam–induced quench test performed in 2011 [8], Bernhard *et al.* found that for transient losses on the millisecond time–scale, there is as much as a factor 4 difference between how much energy is actually necessary to quench a magnet and how much energy an electro–thermal model of the magnet predicts should be sufficient [9, Tab. V]; the magnets are more resilient against quenches than assumed. The model (see Ref. [10]) used to predict the energy necessary to quench simulates a single strand of the magnet cable cooled by He II in contact with the strand surface, and subjects the strand to the losses measured during the quench test. Helium cooling is accounted for by using a steady state Kapitza heat transfer relation at the interface between the strand and surrounding helium. This approach is typical of magnet stability modelling [11, 12].

Finding this discrepancy between simulated and observed behaviour lead to the interest in measuring the temperature response of a heater cooled by confined helium during millisecond time–scale losses. Section 2 expands on both theory and background from previous experimental work. An important shortcoming of current understanding is that the standard Kapitza surface heat transfer model was developed for steady state heating into large volumes of helium and we need to ensure its validity for use during transient heating into a confined volume of helium. There is also very little published data available from millisecond time–scale measurements of heat transfer to confined volumes, and our work will help fill this knowledge gap.

The measurement campaign presented in this paper revolves around two main time–profiles for applied heating power; 1) we start with a slow pulse that reaches peak power after about 9 ms, with a long tail, lasting a total of 400 to 500 ms. This helps assess the validity of using the Kapitza surface heat transfer expression in the confined channel helium volume. 2) to approximate UFO events we use fast pulses that deliver peak power after around 100 µs, that last a total of 800 to 1000 µs. We also apply steps to the heater, which reach their steady state power within about 100 µs as a means to compare closed channel and open bath test results.

The open bath test results are discussed in–depth in a separate publication (Ref. [13]). For convenience, when we refer to the open bath paper, which shares many similarities in the setup and measurement procedure, we will refer to it as the Open Bath Paper.

2 Theory and Background

In this paper we we consider heat transfer from a narrow rectangular heater strip exposed on one side to helium along its entire length. The helium is confined to a shallow channel. Heat transfer across the heater–helium interface is governed by the Kapitza heat transfer expression in Equation (1), which was first proposed by Claudet and Seyfert [14, Eq. 1];

$$Q_\mathrm{K} = a_\mathrm{K}\ (T_\mathrm{s}^{n_\mathrm{K}} - T_\mathrm{ref}^{n_\mathrm{K}})\,, \tag{1}$$

where Q_K is the Kapitza heat flux, T_s is the temperature of the heater at the heater–helium interface, T_ref is a reference temperature equal to that of the helium in the channel, and a_K and n_K are two fit parameters. In our Open Bath Paper we determine the Kapitza parameters for our stainless steel heater strip to be $a_\mathrm{K} = 1316.8\ \mathrm{W\,m^{-2}\,K^{-n_K}}$ and $n_\mathrm{K} = 2.528$. For convenience, when we refer to the surface temperature of the heater, we always mean the temperature at the interface between heater and helium, T_s.

Heat transfer to He II in the Kapitza regime involves the transmission of thermal phonons across the heater–helium interface [15, Sec. 7.5][16, Chap. 23]. The dominant phonon wavelength excited in the helium are approximately $\lambda = h v_\mathrm{He}/3.8 k_\mathrm{B}\ T$, where h is the Planck constant, v_He the speed of sound in helium, k_B is the Boltzmann constant, and T is the helium temperature [17, p. 168]. For temperatures between 1.9 K and T_λ (= 2.165 K), taking the speed of sound to be around 200 $\mathrm{m\,s^{-1}}$, we get a phonon wavelength on the order of 1 nm. Compared with the channel we use, of 120 µm depth, a phonon transmitted across the heater–helium interface will not distinguish the channel from an open bath. As such, we expect the Kapitza expression to hold, at least for steady state, also in the confined geometry.

Katerberg and Anderson verified that the measured Kapitza resistance between He II and a copper heater remained the same when measured during steady applied heat or during oscillating heating power [18]. Their fastest heating was generated by a sinusoidal 600 Hz current applied to the heater, leading to a peak in applied heating power every half–cycle, or 830 µs. They did not find conclusive evidence of a frequency dependence of the Kapitza resistance, though, as they point out, above about 1.6 K their data is not reproducible, and there seems to be a weak tendency for the Kapitza resistance to be lower for higher frequency. From this, we expect the Kapitza expression to certainly be valid for the applied heating that peaks after 9 ms, but it is not clear if it remains valid down to heating that peaks after just 100 µs.

2.1 Millisecond Time–Scale Data

Transient heat transfer experiments in He II tend to fall into three main categories;

1. Tests designed to assess the time it takes before onset of film boiling after subjecting a heater submerged in an open bath to a very strong heat flux, usually in excess of 100 $\mathrm{kW\,m^{-2}}$, depending on the bath temperature (see the Open Bath Paper for detailed discussion [13]). The time–scale of these measurements are often on the order of 100 µs or less, but they do not consider the time during which the heater warms up, and how the Kapitza expression may describe this time window.

2. Tests designed to assess propagation of second sound waves in He II (Ref. [19] discusses several such tests). The applied heating power densities of such tests well in excess of 100 $\mathrm{kW\,m^{-2}}$ and at time–scales on the order of 10 to 100 µs. The behaviour of the heater exciting these pulses is generally not considered.

3. Tests designed to assess lower heat fluxes propagating along a channel of He II [20–24]. While the applied heating power densities of such tests are often in the range of a few tens of $\mathrm{kW\,m^{-2}}$, the transient data, if at all available, is usually on the 0.1 s time–scale or slower, because heat propagation along even relatively short channels of He II is quite slow.

So, there is a gap in available data; for applied heating power density on the order of 1 to 100 $\mathrm{kW\,m^{-2}}$, there are no published results nn the millisecond time–scale that considers both helium and heater behaviour.

2.2 Heat Transfer in Confined Helium Geometries

Several experiments have been done in the past mapping out the steady state heat transfer characteristics of helium in varying sorts of confined geometries. Warren and Caspi measured the heater surface temperature of a cylindrical heater exposed on one side to a He II filled gap of varying thickness[25]; Chen and Van Sciver built a rectangular channel 127 mm long and 12.7 mm wide, measuring the heater surface and channel helium temperatures for varying channel depths and angles of inclination[26]; Kobayashi *et al.* built a short channel, open on either end to a large bath of He II, where they measured the heater surface temperature, the channel helium temperature immediately adjacent to the heater, and the temperature of the helium adjacent to the wall opposite the heater[27]; Granieri conducted a large study of steady state heat transfer in Rutherford cables of the type used in the LHC main dipoles[28, Chap. 3].

They all find steady state results roughly characterised by four regimes;

1. Below a small critical heat flux Q_λ, for which the helium temperature remains below T_λ, no thermal gradients are observed within the confined volume. Heat is applied to the confined helium according to the Kapitza regime, and it is transferred out of the helium by the Gorter–Mellink regime (see Section 2.3);
2. Between Q_λ and an intermediate heat flux Q_{NucBoil}, relatively poor heat transfer takes place between the heater and the helium, and most of the applied heat is transferred by conduction through the solids in the setup, rather than to the helium itself. This is recognised as a natural convection–like regime;
3. Between Q_{NucBoil} and a higher Q_{FilmBoil}, strong heat transfer from heater to helium takes place, identified as the nucleate boiling regime. The presence of this regime appears to depend not only on the channel orientation, but also the helium bath temperature. Near T_λ, the regime is seen regardless of channel orientation, while at 1.9 K it is hardly noticeable in some horizontal channels;
4. Above Q_{FilmBoil}, film boiling develops fully, and, like for the natural convection regime, only poor heater to helium heat transfer takes place.

While these critical heat fluxes are defined for steady state heating, which we are not investigating, we expect to see evidence of the transition into natural convection for tests where we heat the channel helium up to T_λ.

2.2.1 Transient Heat Transfer to a Channel

Okamura *et al.* measured transient temperatures in a 170 mm long, 7 mm wide channel of varying depth, open on either end, subject to steps in applied heating power density[29]. Their steady state results are not entirely in line with the expected four regimes; in particular there is no clear natural convection regime separating a low–heat flux Kapitza regime from a high–heat flux nucleate boiling regime. Furthermore, when their channel is horizontal, with the heater facing upwards, there is no nucleate boiling regime clearly present. However, they show transient measurements on the 0.1 second time scale. The key result is that the final steady state for $T_{\mathrm{channel}} < T_\lambda$ appears to need on the order of 3 to 5 seconds to be established.

Their results also show behaviour analogous to that seen in open baths or long channels heated from one end; for an applied heating power density larger than Q_λ, there is a finite life–time during which strong Kapitza cooling persists before the confined helium volume reaches T_λ, and there is a heat transfer regime change.

2.3 Heat Transfer in Helium

Above T_λ, in a horizontal channel filled with He I, where we neglect convective effects, the thermal conductivity of the helium is rather low, and comparable to that of an insulating material like Eccobond®, for instance. Below T_λ, however, the effective thermal conductivity of the same channel, now filled with He II, becomes more akin to, or even higher than, that of high–purity copper. The high effective thermal conductivity of He II is due to the Gorter–Mellink mutual friction regime. There exists also a laminar regime in He II. The Gorter–Mellink regime is dominant under two main conditions; 1) turbulence must be fully developed; and 2) there must be zero net mass flow of He II. Vinen made the early key contributions to understanding of turbulence in He II, finding that for an applied heating power density Q_{app}, it takes,

$$\tau = a Q_{\mathrm{app}}{}^{-3/2}, \tag{2}$$

seconds to develop turbulence, where a is a geometry–dependent fit parameter [21]. Chase found that in channels with obstructing orifices the time to develop turbulence becomes essentially zero, giving $a = 0$, while a is otherwise on the order of $100\ \mathrm{ks\,W^{3/2}\,m^{-3}}$ around 1.9 K, falling towards zero as the temperature approaches T_λ[22].

There isn't a neat criterion to assess whether or not the zero–net–mass flow condition is met. Heat transfer in He II is associated with fluid flow, and is described by Landau's two–fluid model[30]. Zero net mass flow means, in the two–fluid picture, that the normal–fluid component momentum flux $\rho_{\mathrm{n}}\vec{v}_{\mathrm{n}}$ exactly balances the superfluid component momentum flux $\rho_{\mathrm{s}}\vec{v}_{\mathrm{s}}$. In our work, we assume the zero–net–mass flow (counter–flow) condition to be met at all times, meaning we assume the Gorter–Mellink regime is always dominant.

In the Gorter–Mellink regime, the local helium heat flux Q_{GM} is given as;

$$Q_{\mathrm{GM}} = \left[-f^{-1}(T)\nabla T\right]^{1/m}, \tag{3}$$

where f^{-1} is the thermal conductivity function of He II (where we use that proposed by Sato *et al.* [31]), and m is an exponent originally found by Gorter and Mellink to be 3[20], while Sato *et al.* later propose $m = 3.4$[32] (which we use herein).

Using this, a modified heat equation is obtained from Fourier's law of cooling to express an effective thermal conductivity from Equation 3;

$$\rho(T)C_{\mathrm{p}}(T)\frac{\partial T}{\partial t} = \nabla\left\{\left[-f^{-1}(T)\frac{1}{|\nabla T|^{n-1}}\right]^{1/n}\nabla T\right\}, \tag{4}$$

where C_{p} is the specific heat capacity. This assumes that Equation 3, which, strictly speaking, is a steady state expression, also applies under transient conditions.

Seyfert *et al.* used this kind of approach to model heat transfer in an annular channel[33]. Okamura *et al.* did the same for He II in a pipe subject to slowly varying applied heating power[34]. Fuzier and Van Sciver modified Equation (4) to account for forced flow of He II in a pipe heated at one end, and found good agreement in the limiting cases of; 1) large mass flow, where thermal convection dominated heat transfer; and 2) low mass flow, where Gorter–Mellink counterflow dominates heat transfer[35][36, Sec. 5].

Helium material properties We take helium material properties from Arp *et al.* [37]. We use their data to build cubic spline interpolation functions between 1.7 and 100 K.

3 Setup

Most of the experimental setup was described in the Open Bath Paper, and here we will only point out the key differences. Figure 1 shows a diagram of the experimental sample placed in the cryostat. The Bottom Plate is the same plate as the downwards facing heater in the Open Bath Paper, corresponding to the `D`–sensors in the paper. The Top Plate is used to confine the helium to a 120 µm deep channel along the heater strip. The two PEEK plates are kept apart by Kapton tape laid along either long–side of the channel, and 16 aluminium bolts (eight per side) clamp the two plates together. Sensors measuring the heater temperature are labelled `H`, while those measuring the channel helium temperature are labelled `C`.

The dark blue rectangles at either end of the channel in the figure represent the Eccobond® through which pin–holes are made. The pin–holes have, roughly, a half–circular cross section, with their origins at the middle of the 3.1 mm wide channel groove in the Top Plate. Their cross section is $3.405 \cdot 10^{-8}$ m^2, or 9.15% of the channel cross section. They are 4 mm long, and along their bottoms they are exposed to the bare heater strip. The pin–holes limit the channel length to 150 mm.

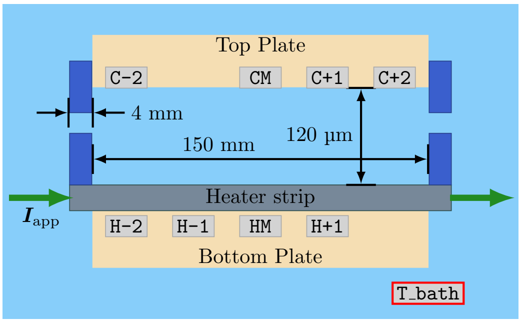

Figure 1: Diagram of the closed channel setup used for experiments. `H` sensors measure the heater temperature, and `C` sensors measure the channel helium temperature. `T_bath` is the reference probe. The channel is 150 mm long and 120 µm deep. It is 3.1 mm wide, while the heater is 3 mm wide. The pin–holes at either end are 4 mm long.

Figure 2 represents the region around the helium channel sensors. The assembly is essentially the same as for the heater sensors, described in the Open Bath Paper, but there is no Kapton or steel in the Top Plate, and the sensors have been turned so that the sensitive zirconium oxynitride film faces the helium to ensure the fastest possible thermal response time. The labels in the figure refer to the following;

- **(1)** Glass–fibre filled PEEK;
- **(2)** Eccobond® epoxy used to fill in holes, as well as seal the sample to prevent helium to escape through the crack where the two PEEK plates mate;
- **(3)** Copper sensor leads, attached by manufacturer;
- **(4)** GE 7031 varnish used to attach Cernox® sensors in recesses in the Top Plate;
- **(5)** Cernox® sapphire sensor substrate. Note that the sensors are not entirely flush with the PEEK surface in order to make sure the EPO–TEK beads could not touch the heater strip during testing of the assembly and final mounting;
- **(6)** EPO–TEK H20E silver filled epoxy used by Lake Shore Cryotronics to attach leads to sensor body;
- **(A)** Soldering point joining the sensor leads to larger external lead attachments, acting as thermal anchoring for the Cernox® sensors.

Note that unlike for the Bottom Plate, where the sensor is embedded within a stack of materials under the heater strip, the sensors on the channel side are mounted so their sensitive part is in direct contact with the helium. This means that the helium sensor temperature measurements do not need a post–processing step to account for a material stack like we do for the heater sensors. Analysis done in this paper uses the same modelling approach for the heater sensors as that used when discussing open bath measurements in our Open Bath Paper. The dimensions we use as a reference for the material stack under the heater strip are the same as well; 50 µm of stainless steel for the heater strip, 35 µm of varnish used to attach the heater sensor to the heater strip, 200 µm of sapphire representing the bulk of the Cernox® sensor, 20 µm of EPO–TEK used to attach the copper leads to the sensors, and 20 mm of copper for the leads that run to the back of the sample. Material parameters are discussed in Appendix A in our Open Bath Paper.

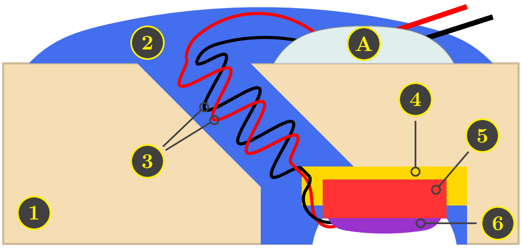

Figure 2: Schematic representation of the region around the Cernox® temperature sensors of the Top Plate, sensing the channel helium temperature. Label (1): Glass–fibre filled PEEK. (2) Eccobond®. (3): copper sensor lead wires. (4): GE 7031 varnish. (5): sapphire sensor substrate. (6): EPO–TEK H20E epoxy. (A): Soldering point where thin sensor leads join larger sensor lead attachments.

3.1 Calibration

The Cernox® sensors are calibrated in–situ against the reference probe in the same way as was done in the Open Bath Paper. The total estimated measurement uncertainty for the closed channel tests presented here is given in Table 1.

Table 1: Estimated measurement uncertainty ΔT.

Range, [K]			$\pm\Delta T$, [mK]
1.8	—	T_λ	5
T_λ	—	2.3	19
2.3	—	3	7
3	—	4	13
4	—	6	8
6	—	20	15

Instrumentation There are no differences in instrumentation from that used in the Open Bath Paper, save for two added measurement channels. One is for the extra temperature sensor, as we here have eight in total, rather than seven, and the other added channel is for a synchronisation measurement where the temperature data acquisition system senses the triggering signal to the powering circuit that delivers current to the heater strip. The temperature sensor data acquisition frequency is 20 kHz per sensor/channel.

Post–processing of transient measurements In order to obtain the transient temperature data from our measurements, we compensate for the presence of a filtering capacitor on the Cernox® sensor current excitation sources. This method is described in our Open Bath Paper.

3.2 Sealing the Helium Channel

After bolting the two PEEK plates together to confine the helium near the heater strip to the desired channel dimensions, we sealed all remaining gaps, except for the pin–holes, with Eccobond®, in order to ensure the helium was only in direct thermal contact with the bath through the two pin–holes. Figure 3 shows a photograph of the setup after Eccobond® sealing.

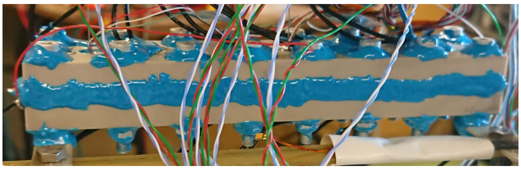

Figure 3: Photograph of setup after sealing gaps with Eccobond® to ensure no continuous helium channels exist between the channel and the outside bath, aside from the pin–holes.

Between the two PEEK plates we placed a strip of Kapton tape on either side of the channel. This serves two purposes; 1) the tapes act as a spacer to give the desired channel depth of 120 µm, and 2) the Kapton tapes cover the 16 bolt holes, and the aluminium bolts pass through the tape. So, after tightening the bolts, the layer of tape helps provide a seal to ensure the volumes between the bolt–hole walls and the bolts themselves are completely isolated from the helium in the channel.

3.3 Measurement Procedure

For our heating tests we use three different types of applied heating power densities;

- Steps that reach flat top power after about 100 µs. Applied heating power density reaches 970 $\mathrm{W\,m^{-2}}$.
- Slow RLC–like pulses that reach peak power after around 9 ms, lasting a total of 400 to 500 ms. Peak applied heating power density reaches 4300 $\mathrm{W\,m^{-2}}$.
- Fast RLC–like pulses that reach peak power after around 100 µs, lasting a total of 800 to 1000 µs. Peak applied heating power density reaches 130 $\mathrm{kW\,m^{-2}}$.

To generate the RLC–like pulses we use the circuit shown in Figure 4. The circuit components R_{pulse}, L, and C are used to shape the pulse. For slow pulses we use $C = 40$ mF, $L = 8.5$ mH, and $R_{\text{pulse}} = 3.8\ \Omega$. For fast pulses we use $C = 160$ µF, $L = 93$ µH, and R_{pulse}

= 1.3 Ω. We connect the heater strip power leads to the Terminal, and use the transistor $T2$ to release the energy stored in the capacitor by switching the gate signal $G2$. This switching is what triggers the heater strip data acquisitions system to log data.

R_{bypass}, $T2$, and the diode lets us keep the power supply on between tests and avoid any backwards energy flow from the capacitor during the pulse discharge.

The shape of the fast pulses is chosen to be similar to the transient UFO–losses seen in the LHC, while the slow pulses represent a transient that helps determine the region of validity of our modelling efforts.

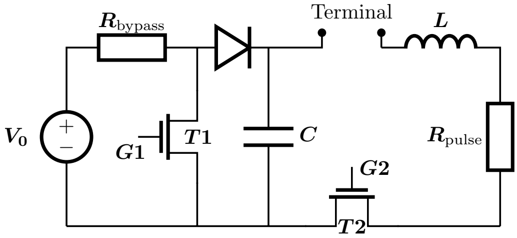

Figure 4: Circuit used to generate the slow and fast RLC–like heating pulses. R_{pulse}, L, and C are used to shape the pulse. The transistor T2 releases energy into the heater strip upon switching G2.

The heater strip, which is the same as the downwards facing heater from the Open Bath Paper, has a resistance of 0.458 Ω, and to represent the heating power developed in the strip, we use the applied heating power density calculated from the measured heater strip voltage;

$$Q_{\text{app}} = \frac{{V_{\text{meas}}}^2}{R_{\text{strip}}} \frac{d_{\text{strip}}}{v_{\text{strip}}}, \tag{5}$$

with V_{meas} the measured voltage, $R_{\text{strip}} = 0.458$ Ω, $d_{\text{strip}} = 50$ µm, and $v_{\text{strip}} = 150$ mm × 3 mm × 50 µm, the total volume of the heater strip.

The helium–wetted area of the heater strip is 150 mm × 3 mm. The helium in the 4 mm long pin–holes also contact the heater.

4 Slow Pulses in Applied Heating Power Density

Figure 5 shows a representative measurement of the thermal transient during the first 50 ms of a slow–pulse test in the closed channel. The bath temperature during the test was 1.9 K.

During the transient, all sensor temperatures on the heater remain close to each other, reaching about 2 K after 10 ms, and 2.03 K after 50 ms. The temperature variation between heater sensors is about ±5 mK after 50 ms, which is comparable to the estimated measurement uncertainty from Table 1. The kink in slope during the temperature rise coincides with the peak in the applied heating power density.

The temperatures in the channel are essentially indistinguishable during the entire test, meaning the helium in the channel heats up uniformly, reaching 1.996 K after 50 ms. The temperature variation between sensors is about ±2 mK. Despite the pin–holes at either end of the channel, a thermal gradient along the channel is not expected. As a simple estimate, we consider the cooling power of one pin–hole where the channel end is at 1.996 K, and the bath end at 1.9 K. We assume the pin–hole helium behaves according to the Gorter–Mellink heat transfer regime (see Section 2.3 for background and Section 6 for discussion of such a modelling approach to our setup). At 1.95 K, the thermal conductivity function of He II (in Equation 3) is $f^{-1} = 6.25 \cdot 10^{14}\ \text{W}^{3.4}\,\text{m}^{-5.8}\,\text{K}^{-1}$. At 4 mm length, $\Delta T/\Delta x = 24\ \text{K}\,\text{m}^{-1}$. The heat flux through a pin–hole is then 57 $\text{kW}\,\text{m}^{-2}$. With a pin–hole cross section of $3.41 \cdot 10^{-8}\ \text{m}^2$, the cooling power from two pin holes becomes 3.9 mW. The applied heating power peaks around 167 mW, or nearly two orders of magnitude above the pin–hole cooling power. For all our tests, the pin–hole cooling only matters during the long thermal relaxation time after no more energy is supplied to the heater strip.

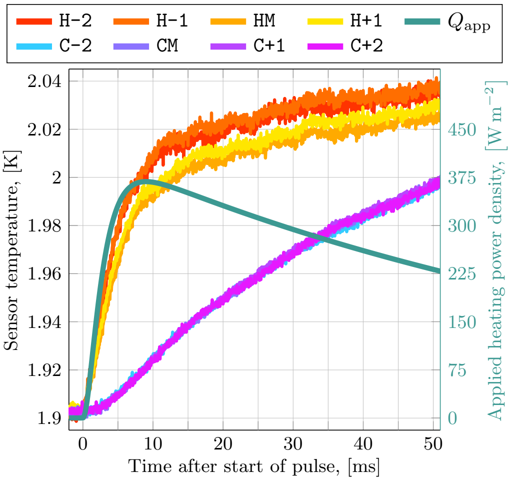

Figure 5: Representative measurement results during the first 60 ms of a slow–pulse test with peak applied heating power density 370 $\text{W}\,\text{m}^{-2}$. The initial bath temperature was 1.9 K, and it did not change during the test.

4.1 Simulation Using Measured Helium Temperature as T_{ref}

Figure 6 shows the same test as Figure 5, but includes a simulation like the one we used in the Open Bath Paper, namely the time–dependent heat equation with the

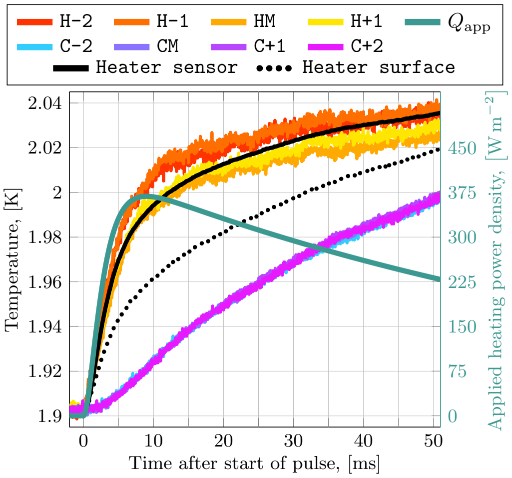

Figure 6: Same slow–pulse test as that shown in Figure 5, together with the result of a simulation that models only the material stack. The helium wetted surface of the heater is cooled by the Kapitza expression using the steady state Kapitza parameters found in our Open Bath Paper; $a_{\mathrm{K}} = 1316.8\ \mathrm{W\,m^{-2}\,K^{-n_K}}$ and $n_{\mathrm{K}} = 2.528$.

Kapitza expression (Equation (1)) used as a boundary condition at the surface of the heater.

The solid black curve shows the simulated temperature in the sensor location, and should be compared with the measured heater sensor temperatures. In the simulation shown we have taken the average of the measured helium temperatures, and use this as the reference temperature in the Kapitza expression. This means we do not simulate any helium behaviour.

For the simulation, we have used the steady state Kapitza parameters determined in our Open Bath Paper; $a_{\mathrm{K}} = 1316.8\ \mathrm{W\,m^{-2}\,K^{-n_K}}$, and $n_{\mathrm{K}} = 2.528$. In all plots that show a single test with simulation results, `Heater sensor` refers to the simulated temperature at the location of the sensitive part of the Cernox® sensor within the simulated domain. `Heater surface` refers to the simulated temperature at the Kapitza interface on the heater side.

The simulated sensor temperature is in excellent agreement with measurements. This means, so long as the helium temperature behaviour is known, and the losses are at least as slow as these pulses (reaching peak power after around 9 ms), the Kapitza heat transfer expression can be expected to capture the thermal behaviour of the system. This result is also a confirmation that even though the Kapitza expression was developed for a situation where the reference temperature was taken far from the heater, it describes the heat transfer also in a shallow channel where the helium is decidedly not far from the heater.

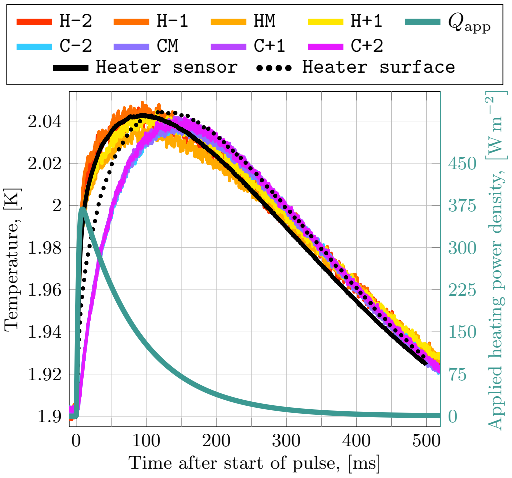

Figure 7: Same simulation result as that in Figure 6, showing the measurement and simulation result up to 500 ms.

4.1.1 Long Time Scale

In fact, the simulation shown in Figure 6 can be extended to the entire slow pulse, and the result, shown in Figure 7, remains in agreement with the measured heater sensor temperatures all the way up to between 150 and 200 ms after turning on the pulse. The small deviation between measurement and simulation that arises on this very long time scale could stem from the real geometry being three–dimensional, while we simulate it as a simplified one–dimensional geometry, neglecting, for instance, the impact of the PEEK plates themselves.

During the entire test we see the measured temperatures, both on the heater and channel side, remain nearly uniform, with the heater sensor temperatures peaking after about 90 ms at about 2.04 K. The channel helium temperatures continue rising for another 50 ms after this, as heat keeps transferring from the heater to the helium. The channel temperatures peak at about 2.038 K. The simulation result, with the heater surface temperature rising above the sensor temperature after about 100 ms, shows that during the slow relaxation back to the bath temperature, heat transfer along the sensor leads contributes more to cooling than cooling to helium. Since the measured sensor temperatures are above the simulation result at long time scales, it seems our simplified model slightly overestimates the heat flux along the sensor leads. Note that the discrepancy between simulation and measurement is no more than 6 mK, which is just a little more than the estimated measurement uncertainty.

4.1.2 Short Time Scale

Figure 8 shows the same simulation result as in figures 6 and 7, highlighting the first 12 ms.

All temperatures, both simulated and measured, rise smoothly from their initial values. The heater sensors rise roughly linearly between 1 and 4 ms, corresponding to the region where the applied heating power density rises linearly. After this, the slope tapers off, both due to the pulse nearing its peak, and because the heat capacity of the materials in the stack rises as the temperature grows. The helium channel temperatures start rising very slowly at first, since the heat transfer to the channel depends on the surface temperature of the heater. It then settles into a linear rise starting around 6 ms. From the simulation we see that the linear region in the measured helium temperatures corresponds to the heater surface temperature having reached a point where the temperature difference between heater and helium is roughly constant, so a nearly steady heat flux crosses the heater–helium interface. This time window also corresponds to the region where the applied heat pulse remains nearly constant around 360 W m^{-2} between about 6 and 13 ms.

We conclude that the relatively simple one–dimensional material stack model, with the Kapitza expression as the boundary condition representing helium cooling, using the measured channel helium temperature as modelling input, allows for simulation of the transient response to a slow pulse with excellent accuracy all the way from the start of this particular pulse up to around 150 ms.

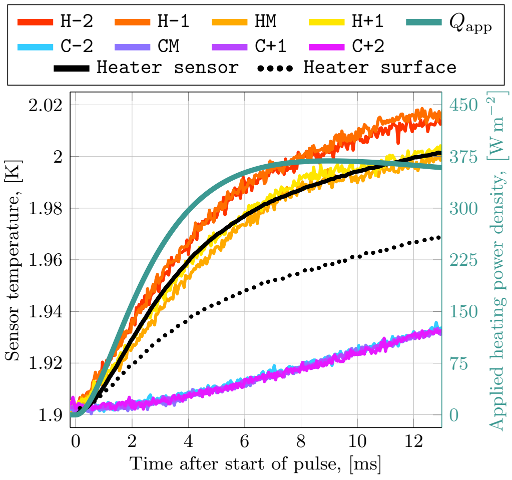

Figure 8: Same simulation result as that in Figure 6, showing the measurement and simulation result up to 13 ms.

4.2 Increasing Peak Power

Figure 9 shows measured and simulated temperatures for four successively larger slow pulses. The measured temperatures are represented as the average temperature among the four heater or four channel mounted sensors at each point in time. The average heater sensor temperatures are shown in green hues, while channel temperatures are shown in blues. The dashed curves in purple hues are the applied heating power density for each pulse. The solid curves in greens are the simulated temperatures at the heater sensor location based on the same kind of simulation presented in Section 4.1 using the plotted applied heating power densities.

For the weakest pulse that peaks at 1.07 kW m^{-2}, the average channel temperature reaches 1.965 K after 10 ms, with a variation around this average of ±5 mK. The average heater sensor temperature has risen to 2.170 K, with a variation of ±20 mK. For the strongest pulse that peaks at 4.34 kW m^{-2}, the average channel temperature reaches 2.113 K, with a variation of ±13 mK. The average heater sensor temperature reaches 2.700 K, with a variation of ±65 mK.

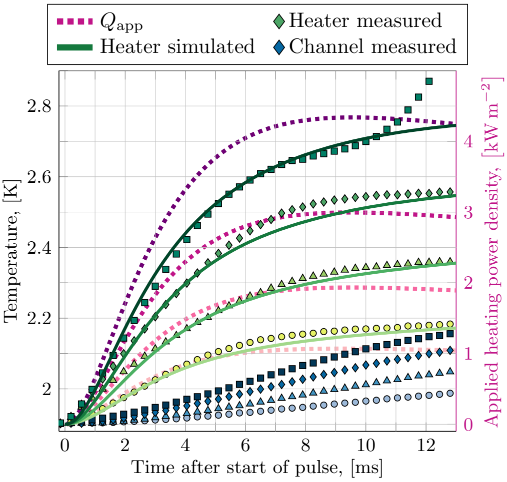

Figure 9: Measurement and simulation results for four successively larger slow pulses with peak applied heating power densities of 1.07, 1.93, 3.00, and 4.34 kW m^{-2}. The peaks all occur after between 9.2 and 9.5 ms. Curves of measured temperature data are the average of the four sensors on either the heater or the channel side respectively. Only every seventh data point is plotted. Dashed curves in pink and purple hues are the applied heating power densities: Qapp. Symbols in green hues are heater sensor measurement data: Heater measured. Symbols in blue hues are channel sensor measurement data: Channel measured. Solid curves in green hues are the simulated heater sensor results: Heater simulated.

After 10 ms for the largest pulse, the channel temperature approaches T_λ, and rather than flatten out, the slope of the heater sensor temperature increases. The heat transfer characteristics at the helium–heater interface completely change once He II transitions to He I. Rather than heat being transmitted by the highly efficient Kapitza conductance into superfluid helium, a natural convection heat transfer regime takes over. The applied heating power still needs to cross the interface, but for the less efficient convection regime, the heater temperature must rise considerably to transfer the same power. It is this regime change that is seen as the rapid temperature rise starting at 10 ms.

All slow–pulse tests with peak applied heating power densities above 0.68 kW m^{-2} see helium in the channel reach, and eventually go above, T_λ. We never see the channel temperature go above 4.2 K, however, even for the largest peak applied heating power density (peak at 4.34 kW m^{-2}). Note that the simulations in Figure 9 do not include any attempt at modelling the details of the regime change.

From the excellent agreement between simulation results and measured heater sensor temperatures, it is clear that using the Kapitza heat transfer expression as a boundary condition in transient modelling works well across a wide range of slow–pulse amplitudes, so long as the helium temperature to use as reference in the Kapitza expression is known. We expect the modelling to work also in open bath situations for these kinds of pulses, where the helium temperature does not change during the loss event.

During the simulations shown in Figure 9 we also estimate the fraction of applied heating power that flows backwards to the bath along the sensor leads of the heater sensors rather than forwards across the heater–helium interface (Kapitza interface). At the very start of the pulse, no heat flows across the Kapitza interface, since the heater temperature must first rise appreciably above the helium temperature. So, during the first 20 µs, most of the applied heat flows backwards. After this time, a larger and larger fraction is transferred across the Kapitza interface, until after around 200 µs, the heat flow fractions have stabilised to where only about 8% flows backwards. This fraction slowly decays, remaining above about 6% during the time window shown in the figure. From the steady state measurements in the Open Bath Paper we found the heat leaks backwards represent about 2 to 3% of the input power, so during the transient it is to be expected that somewhat more energy flows into the material stack to heat it up.

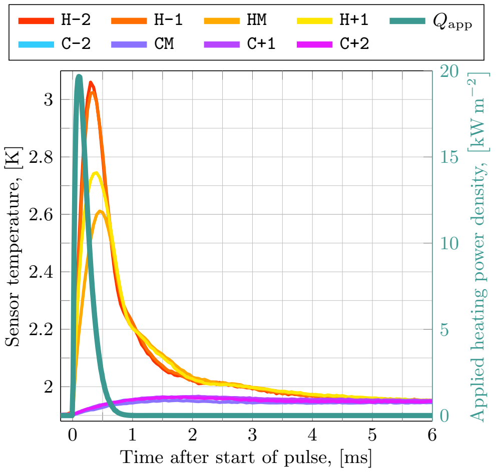

(a) Focus on heater sensors during the first 6 ms of the test.

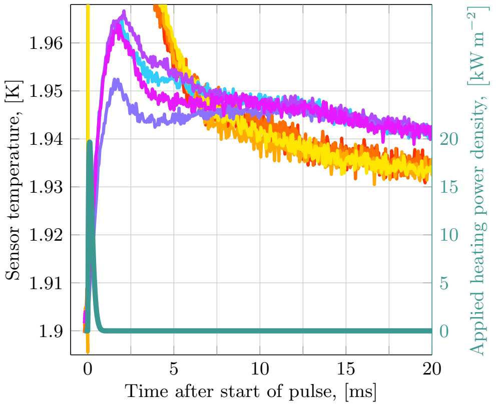

(b) Focus on channel sensors during the first 20 ms of the test.

Figure 10: Measurements from a fast–pulse test. Peak applied heating power density is 19.7 kW m^{-2}, 100 µs after the start of the pulse. Initial temperature was 1.9 K, and no bath temperature change was seen during the test.

5 Fast Pulses in Applied Heating Power Density

Figure 10 shows measured temperatures during a fast–pulse test that reached a peak in applied heating power density of 19.7 kW m^{-2} after 100 µs, with Figure 10a highlighting the heater sensors, and Figure 10b the channel sensors and the early stages of the thermal relaxation to bath temperature.

The larger applied heating power density means that although the fraction of heat flow backwards through the material stack is similar to that seen during slow–pulse tests, the absolute heat flow is larger. This in turn helps explain the larger variation between heater sensor peak temperatures during the test; there are variations in the region around the heater sensors (as discussed in the Open Bath Paper), and for a larger heat flow, these geometrical variations cause larger thermal gradients.

The peak heater sensor temperatures occur after between 300 and 450 µs, with `H-2` and `H-1` being faster, while `HM` is slowest. Recall that the data acquisition frequency is 20 kHz, so each measurement point is 50 µs apart. The faster sensors also reach the higher temperatures, consistent with there being slightly more material to heat up between the heater strip and the sensor itself, which reduces the peak temperature during a finite energy pulse such as this. Note that, with a single exception, all sensors have their peak temperatures happen before the applied heating power density has fallen to 15%

of its amplitude. The exception is the `HM` sensor during the strongest fast pulse, which has its peak temperature when the applied heating power density is about 2% of its amplitude.

The channel helium heats up much slower than the heater strip; this is because heat transferred into the helium must first build up in the heater in order to establish the necessary temperature difference across the Kapitza interface before then heating the helium. This, of course, requires time to develop due to the heat capacity of the heater strip steel. Note that helium temperatures start rising immediately, meaning heat transfer across the interface, though it takes time to fully develop, influences the energy distribution among the regions of the system right away.

Helium temperatures peak roughly at the same time, 1.7 ms after the start of the pulse, and only the middle channel sensor appears to behave differently from the others, showing a peak temperature about 13 mK below the other three channel sensors. After between 5 and 7.5 ms, the heater sensor temperature falls below the channel temperature. After 10 ms an equilibrium is established, with a quasi–stable temperature difference between the heater and channel sensors. After this time, the two groups of sensors show no significant internal variation, and they slowly relax to the bath temperature over about 150 ms. The temperature difference between the two groups slowly narrows until all temperatures end up at 1.9 K. During this slow relaxation the heater surface and the channel helium are in thermal equilibrium, with only a very small heat flow across the interface as heat leaks out of the channel helium.

Note that the complicated state between the peak helium temperature and the point where the smooth thermal relaxation sets in grows longer for stronger pulses. As the peak applied heating power density goes above about 36 $\mathrm{kW\,m^{-2}}$ the state lasts until 20 ms after the start of the pulse. By 54.1 $\mathrm{kW\,m^{-2}}$, it lasts till 30 ms, while for the strongest pulse, at 128.9 $\mathrm{kW\,m^{-2}}$, it lasts until 300 ms after the pulse. The time at which the heater sensor temperatures fall enough to reach the channel temperatures is consistently never longer than 10 ms.

During the entire fast pulse shown, the total energy developed in the heater strip is about 2.65 $\mathrm{mJ\,cm^{-3}}$. For a simple estimate, we assume all this energy goes into heating only the stainless steel heater strip. The heater strip volume is about $2.25{\cdot}10^{-8}$ $\mathrm{m^3}$, and at 2.7 K, its heat capacity is 79550 $\mathrm{J\,m^{-3}\,K^{-1}}$. For the given energy input, the heater temperature would rise to 3.4 K. On the channel side, we have about $5.58 \cdot 10^{-8}$ $\mathrm{m^3}$ of helium, which at 1.95 K has a heat capacity around 660 000 $\mathrm{J\,m^{-3}\,K^{-1}}$. Assuming the energy developed in the heater strip at some point in time is all contained in the helium, its temperature should rise to about 1.972 K, just 10 to 20 mK above the measured peak helium temperatures. These two simple estimates, that do not consider heat transfer from the heater to the helium, heat leaks to the materials below the heater, or heat flow out of the helium, are clearly in line with the observed values.

5.1 Large Fast Pulses

Figure 11 shows four successively larger fast–pulse tests, focusing on the first 3 ms. The measurement data is represented by the average temperature for each group of sensors; heater (green hues) and channel (blue hues) respectively. Table 2 summarises the features of the figure. As from Figure 10, during these stronger fast–pulse tests, sensors `H-2` and `H-1` give very similar results, with peak temperatures at the upper end of the variation given in Table 2, while `HM` has both the lowest amplitude and latest time of peak. This remains consistent with the thermal path between heater and sensor being somewhat longer for this sensor than the others. The times of peak heater sensor temperature are consistently around 350 µs, sensor `HM` being the outlier.

On the channel side, the peak temperatures always happen after around 2.1 ms, with no clear tendency for one particular sensor to deviate from the others. Furthermore, the peak helium channel temperatures remain very similar for all pulses. We observe no clear consistency in which sensor measures the lowest peak, though the middle channel sensor gives the lowest temperature in about half the fast–pulse tests.

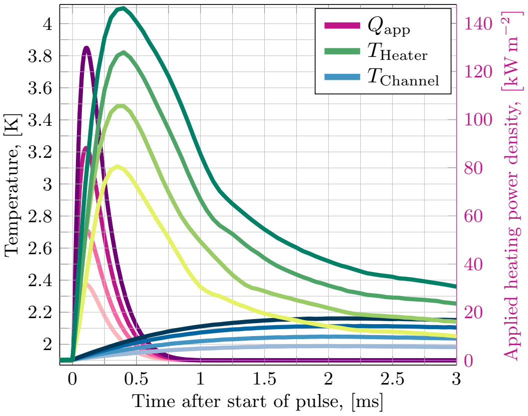

Figure 11: Measurement of four successively larger fast pulses with peak applied heating power densities of 31.5, 54.1, 88.2, and 129.8 $\mathrm{kW\,m^{-2}}$. The peaks all occur after between 100 and 110 µs. Curves of measured temperature data are the average of the four sensors on either the heater or the channel side respectively.

Note that up until the strongest pulses, with peak applied heating power densities above about 100 $\mathrm{kW\,m^{-2}}$, the temperature variation within the channel remains around ±7.5 mK, which is only barely larger than the measurement uncertainty of about ±5 mK. This means the channel maintains the 120 µm depth evenly along

Table 2: Summary of fast–pulse test from Figure 11. Q_{app} is here the peak value during each test. T^*_{heater} and T^*_{channel} are the peak values from the figure, while ΔT_{heater} and $\Delta T_{\text{channel}}$ are the variations around the peak value. τ^*_{heater} and τ^*_{channel} are the time of peak temperature, while $\Delta\tau_{\text{heater}}$ and $\Delta\tau_{\text{channel}}$ are the variations around this time.

Q_{app}	31.5	54.1	88.2	129.8	$\mathrm{kW\,m^{-2}}$
T^*_{heater}	3.109	3.486	3.822	4.096	K
ΔT_{heater}	+280 −250	+370 −450	+480 −610	+610 −640	mK
τ^*_{heater}	350	400	400	400	µs
$\Delta\tau_{\text{heater}}$	+100 −50	+100 −50	+150 −50	+300 −50	µs
T^*_{channel}	1.989	2.048	2.114	2.161	K
$\Delta T_{\text{channel}}$	+7 −7	+6 −8	+4 −3	+10 −9	mK
τ^*_{channel}	2.0	1.95	2.15	2.15	ms
$\Delta\tau_{\text{channel}}$	+0.4 −0.3	+0.15 −0.05	+0.3 −0.0	+0.15 −0.05	ms

its length, otherwise we would see larger variation between the peak temperatures. A significant depth variation would mean the sensors touch effectively different volumes of helium, but these volumes are subject to very similar heat flows from the heater. This conclusion only holds if we can assume that regions of the channel about 30 mm apart (sensor–to–sensor distance) are effectively isolated from each other on the time–scale investigated here. To check this, we assume heat transfer within the channel helium behaves according to the Gorter–Mellink regime. For a worst–case scenario, we take the thermal conductivity function value in Equation (3) at its peak; $6.6 \cdot 10^{14}\ \mathrm{W^{3.4}\,m^{-5.8}\,K^{-1}}$. For the typical peak temperature variation of $\Delta T = 15$ mK, and a distance $\Delta x = 30$ mm, we get a heat flux of $18.6\ \mathrm{kW\,m^{-2}}$, meaning a total power of 6.92 mW. Consider a situation where this power flows from a 30 mm long section of the channel at 2.115 K to an adjacent section 15 mK cooler. Taking the heat capacity at 2.1 K as $1.1 \cdot 10^6\ \mathrm{J\,m^{-3}\,K^{-1}}$, and disregarding the temperature increase in the cooler section, it would take about 27 ms before the surplus energy in the hotter region is transferred to the colder one. This is an order of magnitude longer than the time–scale we are looking at. Considering also that the thermal conductivity function of helium falls quite rapidly once above about 1.95 K, while the heat capacity grows towards T_λ, it is safe to regard the helium channel as a set of isolated volumes on the time–scale of a few milliseconds.

For the strongest pulse we see the channel temperatures reach very close to T_λ. The calibration uncertainty is large enough that even the highest channel sensor temperature is not conclusively above T_λ. For the slow–pulse tests, we clearly see the heat transfer regime change in the heater sensor data as the channel reaches T_λ, but no such evidence is seen during fast pulses. An important difference is that for fast pulses the peak channel temperature happens well after the applied heating power density has settled back to zero, at which point the only driver for heat flow across the helium–heater interface is the energy stored in the heat capacity of the heater strip (and material stack behind it). We will revisit this question in Section 6.3.

5.2 Simulating Fast Pulses With Measured $\mathbf{T_{ref}}$

Figure 12 shows the same test as that in Figure 10 together with the result of a simulation like that successfully used on slow pulses in Section 4.1. While slow pulses could be simulated with excellent accuracy using the measured channel helium temperature, it is clear that fast pulses cannot. Comparing the measured heater sensor temperature curves to the solid black simulated sensor temperature we find that the simulated temperature rises significantly faster than the measured temperatures. This is seen also on the simulated heater surface temperature which represents the temperature of the heater at the Kapitza interface.

The simulated heater surface temperature peaks after 177 µs at 3.023 K and the simulated heater sensor temperature peaks after about 210 µs at 3.322 K. The measured heater sensor temperatures peak after around 350 µs, and about 0.5 K lower. For stronger pulses, the peak simulated sensor temperature occurs slightly later; for the strongest fast pulse the peak happens after 240 µs, which is still much sooner than the 400 µs seen in measurements. There is also a considerable difference in the peak temperature value in Figure 12, where the simulation reaches about 0.5 K higher than the average of the measured peak temperatures. At least some of this discrepancy can be explained by the variations in materials surrounding the sensor. We investigate the effect of dimensional and material parameter variation in Section 6.2.

The simulated thermal relaxation after the peak is also different from measurements; after around 0.8 ms both simulation and measurement transitions to a slower cooling trajectory, but measurements are still at around 2.3 K and remain higher than the simulated trajectory which has fallen to about 2.1 K before the clear slope change. The simulated transient predicts the heater surface temperature should reach the helium temperature after about 1 ms. This is very consistent between all tested fast pulses, with simulation of the strongest fast pulse taking till 1.2 ms. When the heater surface temperature is equal to the helium temperature, the Kapitza expression gives zero heat flux across the interface. However, the channel helium temperature keeps rising until 1.7 ms after the start of the pulse (rising until 2.1 ms for the strongest pulses). This is a clear sign that simply applying the steady state Kapitza boundary condition at the heater surface does not capture the real physics at this time–scale; if there were no heat transfer from the heater

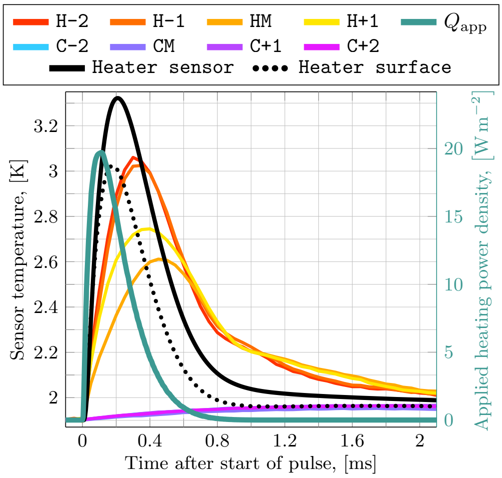

Figure 12: Same fast–pulse test as that shown in Figure 10, together with the result of a simulation that models only the material stack (exactly like that for slow pulses in Section 4.1), which uses the measured helium channel temperature as the reference in the Kapitza cooling boundary condition.

strip, the helium in the channel would not keep heating up.

6 Model the Channel Helium

To develop our modelling of the setup further, we introduce a simple model of the channel helium itself. To account for the pin–holes, we take our simulated domain to be one half of the channel, along its length, connected to one pin–hole at the right end. At the left end of the simulated domain, corresponding to the middle of the channel, we assume zero heat flow. The pin–hole is simulated along its 4 mm length, and we keep the right end, corresponding to the point where it touches the bath, at the bath temperature. Figure 13 shows a diagram of the boundary and interface nodes of the simulated domain.

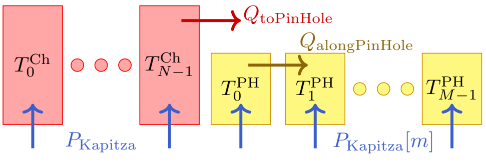

Figure 13: Diagram of channel and pin–hole nodes, and how they interface. There are N channel nodes, denoted by the "Ch" superscript, and M pin–hole nodes, denoted by the "PH" superscript. From the temperature distribution in the pin–hole we find $Q_{\text{alongPinHole}}$, and use this with the cross section of the pin–hole to determine $Q_{\text{toPinHole}}$. P_{Kapitza} denotes the volumetric heat flow into (or out of) the node from the heater strip. The index $[m]$ indicates that we use the pin–hole temperature at each node in the Kapitza expression.

The boundary and interface conditions are as follows;

- At channel node T_0^{Ch} we assume zero heat flux; we take the channel to be symmetrical around the middle.
- At pin–hole node T_{M-1}^{PH} we assume the helium temperature is equal to the bath temperature.
- At pin–hole node T_0^{PH} we assume the helium temperature is equal to the temperature of channel node T_{N-1}^{Ch}.
- At channel node T_{N-1}^{Ch} we let flow the heat flux $Q_{\text{toPinHole}}$. We find this heat flux from the estimated heat flux that flows between the two first pin–hole nodes, $Q_{\text{alongPinHole}}$, and scale this by the ratio between the pin–hole cross section and the channel cross section.
- At each node, a volumetric heat input/output P_{Kapitza} is found from the Kapitza expression, and either added as an energy source or subtracted as an energy sink.

In the simulated domain itself, we assume the Gorter–Mellink regime is always dominant, and discretise Equation (4), following a similar approach to Fuzier (see Eq. 5.22 in Ref. [36]). We obtain the following numerical scheme;

$$
\begin{aligned}
C_i \frac{T_i^{n+1} - T_i^n}{\Delta t} = {} & \frac{1}{2\Delta x}\left[\mathcal{A}_i \frac{T_{i+1}^{n+1} - T_i^{n+1}}{\Delta x} - \mathcal{B}_i \frac{T_i^{n+1} - T_{i-1}^{n+1}}{\Delta x}\right] \\
& + \frac{1}{2\Delta x}\left[\mathcal{A}_i \frac{T_{i+1}^{n} - T_i^{n}}{\Delta x} - \mathcal{B}_i \frac{T_i^{n} - T_{i-1}^{n}}{\Delta x}\right] \\
& + P_i^n
\end{aligned}
\tag{6}
$$

where C_i is the volumetric heat capacity of helium at node i; $T_i^n = T(x_i, t_n)$; Δx denotes the grid spacing in the x–direction; P_i^n is a time– and space–dependent volumetric heat source/sink, and;

$$
\begin{aligned}
\mathcal{A}_i &= \left(\frac{1}{f\left(\frac{1}{2}\left[T_i^n + T_{i+1}^n\right]\right)}\right)^{\frac{1}{m}} \left(\frac{\Delta x}{\left|T_{i+1}^n - T_i^n\right| + \epsilon}\right)^{\frac{m-1}{m}}, \\
\mathcal{B}_i &= \left(\frac{1}{f\left(\frac{1}{2}\left[T_i^n + T_{i-1}^n\right]\right)}\right)^{\frac{1}{m}} \left(\frac{\Delta x}{\left|T_i^n - T_{i-1}^n\right| + \epsilon}\right)^{\frac{m-1}{m}},
\end{aligned}
\tag{7}
$$

where ϵ is a small number, here $1 \cdot 10^{-8}$, to ensure numerical stability when the thermal gradient is very close to zero, and $m = 3.4$.

The heater strip runs along the bottom of both the channel and the pin–holes, and to simulate the heating of the channel/pin–hole we use the same material stack simulation as that in sections 4.1 and 5.2. The key difference is that now, instead of using the measured helium temperature as input to the Kapitza boundary condition on the heater surface of the material stack we use the simulated channel helium temperature. To simplify the simulation load we run only a single material stack simulation, getting only a single heater surface temperature, and use this to find the total volumetric energy flow into/out of each node of the channel/pin–hole helium. This simplification works well because the heat flux out of the pin–hole, cooling the channel, is not large enough to cause any meaningful thermal gradient along the length of the channel.

To assess the validity of this model, we test it on the slow pulse for which we know the simulation works well when using the measured helium temperature. Figure 14 shows a comparison between this new simulation approach, that also simulates the helium, and the previous simulation approach where we used the measured channel helium temperature. The solid grey curve is the same as the result shown in Figure 8, plotted up to 20 ms. The black dotted curve is the simulated heater sensor temperature from the new approach, while the black dash–dot–dotted curve is the helium temperature from the new approach.

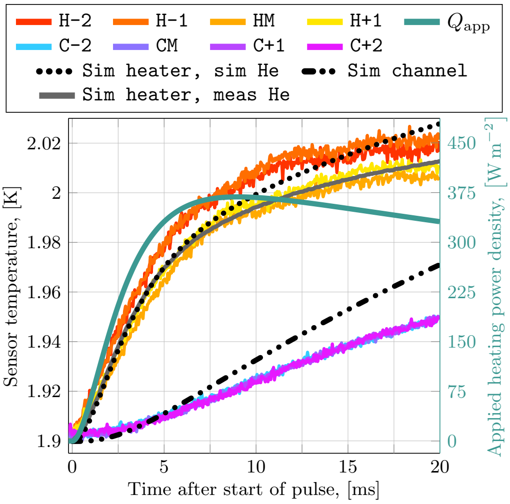

Figure 14: Slow–pulse test with the simulation result also shown in Figure 8, plotted until 20 ms, together with the simulation result that includes simulation of channel and pin–hole helium. `Sim heater, sim He` denotes the simulated heater sensor temperature from the new approach, and `Sim channel` denotes the simulated channel temperature. `Sim heater, meas He` is the old simulation result obtained by using the measured helium channel temperature. Note that the initial temperature of the two simulations differ by about 2.5 mK.

Looking at the simulated heater temperature, we see there is no difference between the two results before around 5 ms, and only after around 10 ms do the trajectories clearly deviate. The simulated helium temperature, however, appears to follow a different trajectory than the measured channel temperature immediately, though even after 5 ms it is still within the estimated calibration uncertainty of ±5 mK. That the deviation between the two simulation approaches only becomes clear around 10 ms is expected; the Kapitza expression, with the n_K exponent on both the heater and helium temperatures, gives very similar heat flux values for helium temperatures within a few millikelvin of each other. After 5 ms, the simulated heater surface temperature from both simulation approaches is about 1.943 K, with the new approach that also simulates the helium being on a slightly steeper trajectory. The measured helium temperature is around 1.9095 K, while the simulated helium temperature is 1.911 K. The Kapitza expression, using $a_\text{K} = 1316.8\ \text{W}\,\text{m}^{-2}\,\text{K}^{-n_\text{K}}$ and $n_\text{K} = 2.528$, gives 304 $\text{W}\,\text{m}^{-2}$ for the lower, measured helium temperature, and 290 $\text{W}\,\text{m}^{-2}$ for the higher, simulated helium temperature. This means the Kapitza cooling heat flux is only 5% larger with the measured helium temperature.

The reason the simulated helium temperature deviates from the measured temperature is more involved, but also expected; we make the channel by pressing two PEEK plates together with a total 16 aluminium bolts. While having so many bolts means the the clamping force is distributed along the plates, the joining of separate parts, necessarily, leaves a gap where the two plates meet. We have placed Kapton tape between the two plates, which helps form a better seal nearest the bolts where the clamping force is greatest. There will still remain small gaps from the manufacturing tolerances of parts which will be filled with helium; some of these gaps will be in contact with the channel helium. This additional helium will, of course, serve to increase the effective heat capacity of the channel. In addition to this, we do not account for heat transfer paths going from the channel helium out to the bath through the PEEK that surrounds it. We conclude that neglecting these parasitic cooling effects is valid until 5 ms.

6.1 Fast Pulses With Helium Simulation

Figure 15 shows the result of the new simulation approach compared with the measurements from the same fas–pulse test shown back in Figure 10. The solid black curve is the simulated heater sensor temperature (which should be compared with the measured temperatures). The dotted black curve is the simulated heater surface temperature. The dash–dot–dotted black curve is the simulated helium temperature.

From Subfigure 15a, the simulated heater sensor temperature is not substantially different from the result obtained by using the measured helium temperature (seen in Figure 12). The peak temperature is 3.322 K after 209 µs with both simulation approaches. The simulated heater surface temperatures, however, differ a little; this new simulation gives the peak simulated heater surface temperature after 179 µs at 3.025 K, which is 2 µs after and 2 mK above the simulation that used the measured

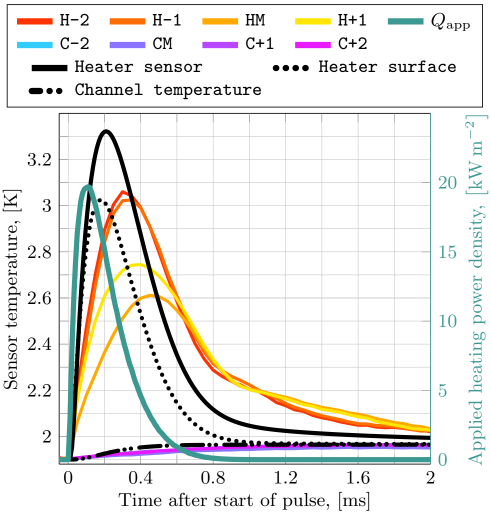

(a) Focus on heater sensors during the first 2 ms of the test.

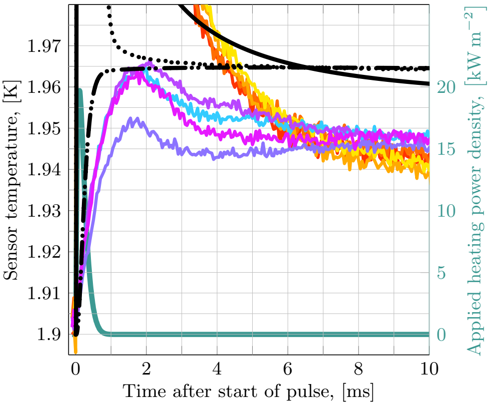

(b) Focus on channel sensors during the first 10 ms of the test.

Figure 15: Measurement from the same fast–pulse test shown in Figure 10, together with simulation results that include the channel helium connected to a pin–hole.

helium temperature for the Kapitza boundary condition. While not a meaningful difference in terms of our measurement uncertainties, this result is consistent with the different heat flux at the Kapitza interface when looking at the simulated helium temperature in Subfigure 15b. It rises faster than the measured temperature, meaning that the Kapitza heat flux will be slightly lower during this simulation, which in turn means slightly less effective cooling, leading to the higher peak temperature at a later time.

In Subfigure 15b we see the simulated helium temperature stabilise at 1.964 K after about 1 ms. The measured helium temperatures have a peak around 1.961 K (from the average of the four temperatures), but it takes till 1.7 ms before it happens. So, on the one hand, we can accurately simulate the peak helium temperature value, confirming that the channel helium is isolated from the parasitic cooling effects that eventually causes the slow–pulse simulation deviation around 5 ms in Figure 14. On the other hand, the rate of heat transfer to the helium is clearly not captured correctly by applying the steady state Kapitza expression, even if it gives the correct total energy transfer.

Since we do not consider the parasitic cooling effects, and since the pin–holes provide so little cooling power relative to the volume of the channel, the simulated helium temperature only very slowly decays compared with the measured values. Also, the simulated helium temperature keeps rising until around 6.5 ms where the simulated heater surface temperature has cooled down to that of the helium, at which point no significant heat transfer across the Kapitza interface takes place. This crossing point happens at the same time for both simulation and measurement, and we see the match all the way up to peak applied heating power densities around 100 kW m^{-2}. For larger pulses than this, the simulated helium temperature reaches T_λ, and we look more into this in Section 6.3.

6.2 Slowing Down the Simulated Transient

We now have a model of our system that can accurately simulate the temperature development for a slow pulse up to 5 ms. Furthermore, in situations where the helium temperature is known, the heater/material stack part of our modelling setup is essentially accurate for the entire duration of a slow pulse. That same model, with or without simulation of the helium, does not work satisfactorily for fast pulses. This corresponds qualitatively to the observations of UFOs in the LHC; the magnet needs more energy to reach the temperature at which it quenches as compared with a model of the magnet that works well for steady state losses. So, at the millisecond time–scale, processes not yet accounted for in the simple model lead to improved cooling performance that prevents magnets from quenching, and we can clearly see this effect in the slower–than–expected heater and helium temperature rises.

Can we explain the measured results by simply changing parameters within the model as we have implemented it? The following discussion compares the fast–pulse test in Figure 15 with simulations using various parameters. The results are general to all fast pulses regarding the key metrics of time and amplitude of peak.

6.2.1 Parameter Space From Open Bath Tests

In our Open Bath Paper we found a parameter space comprised of the steady state Kapitza parameter variation and uncertainty in dimensions of the various material layers in the material stack used for transient simulations.

Within this space, we could successfully simulate the temperature development of all sensors from about 1 ms after a step in applied heating power density. Between the step and the first millisecond, we saw that the measured temperature rise is slower than simulations. This same parameter space cannot explain the closed channel behaviour. By using $a_{\mathrm{K}} = 1213.6\ \mathrm{W\,m^{-2}\,K^{-n_K}}$, $n_{\mathrm{K}} = 2.86$, 41 µm of varnish between the heater strip and the Cernox® sensor, 10 µm of EPO–TEK for the sensor lead attachments, and 18 mm of copper leads, which represents the lowest temperature curve within the parameter space, we get a simulated sensor temperature that has a peak temperature value of 2.92 K after 210 µs for the same fast–pulse test as that shown in Figure 15. This temperature amplitude is about 120 mK below the two sensors `H-2` and `H-1`. The average sensor temperature measurement for this test has a peak temperature of 2.845 K after 350 µs. So, while the simulated temperature amplitude is better with the parameter changes, they still lead to a peak around 150 µs sooner than measurements.

So, within the estimated geometrical parameter space, we can get the right temperature amplitude for sensors `H-2` and `H-1`, but not the other two heater sensors. But the time of the simulated peak is always at least 100 µs too early.

6.2.2 Variation in Material Parameters

We do not get significant improvement even after allowing material parameter variation of ±20% on both thermal conductivity and heat capacity of the materials in the stack. ±20% represents a pessimistic assumption of the measurement uncertainty of material data found in literature (see Appendix A in the Open Bath Paper). Higher heat capacity, of course, slow down the simulated temperature response. Lowering the thermal conductivity of the varnish between the sensor and heater lowers the temperature amplitude, and increasing the steel thermal conductivity also lowers it. A simulation with $1213.6\ \mathrm{W\,m^{-2}\,K^{-n_K}}$ and $n_{\mathrm{K}} = 2.86$, 41 µm of varnish, 10 µm of EPO–TEK, and 18 mm of copper leads, where we also increase the thermal conductivity of steel by 20%, lower that of varnish by 20% and increase all heat capacities of the materials in the stack by 20% gives a peak simulated sensor temperature of 2.700 K, which is 45 mK below sensor `H+1`, but the peak is only slowed till 215 µs, much too fast.

Furthermore, none of these changes do anything to change the simulated helium temperature rise significantly. With a higher heat capacity of steel, it takes slightly longer before the Kapitza heat transfer builds up, but even with a 20% increase, the time at which the helium reaches the stable temperature seen in Subfigure 15b remains about 1 ms.

6.2.3 Thermal Boundary Resistance

In our model of the material stack, we have not so far considered the possible effect of thermal contact resistance between the solids. In particular, a thermal boundary resistance between the heater strip and the varnish layer, or between the varnish layer and the Cernox® sensor would help slow down the temperature rise and the amplitude of the simulated temperature response of the sensors. To assess the effect of such a thermal resistance we include a layer of material between the heater strip and the varnish that has an effective thermal conductivity of just 1% that of the varnish itself. This leads to a simulated sensor temperature peak of just 2.474 K, which is below even that of sensor `HM`, but it still happens after only 240 µs, much too soon compared with the measured transient. And, again, this change to the model does not alter the response of the helium.

6.2.4 Thermal Gradient Across the Channel

Since the pin–holes have such a small cooling effect on the channel, a reasonable change to the helium modelling is to instead simulate a channel domain upwards, across the channel, to see if the slow helium sensor response could be due to the time it takes heat to propagate from the helium adjacent to the heater to the helium near the sensor 120 µm away. For this kind of simulation we disregard the pin–holes completely, and use the heat flux from the Kapitza expression as a Neumann boundary condition at the heater–adjacent node of the channel helium. At the sensor–adjacent node we assume zero heat flux. With these boundary conditions we implement Equation (6) in the same way we do when simulating helium along the channel length.

We find only a negligible thermal gradient across the channel depth; on the order of 5 µK between the heater–adjacent and sensor–adjacent helium. This is essentially independent of which helium node we use as the reference temperature for the Kapitza expression. So, with the Gorter–Mellink heat transfer regime we cannot explain the slow helium temperature rise. Note that if the Gorter–Mellink regime is not dominant, it would be because it has not yet had time to develop fully, meaning the laminar heat transfer regime still matters, which transfers heat even better than the Gorter–Mellink regime, leading to even smaller thermal gradients across the channel.

6.2.5 Inter–Plate Helium

A final avenue we have looked at is to try and include the inter–plate helium that is trapped between the two PEEK plates after bolting shut and sealing with Eccobond®. This enters the realm of speculation, because we do not have reliable estimates for how wide this inter–plate gap is. We have flatness measurements of the PEEK plates when they are not under tension from the bolts which indicates there is a maximum gap–length of 50 µm. After applying the considerable clamping force of the 16 aluminium bolts the resulting gap is certainly not that large. However, if we assume the inter–plate gap, filled with helium, is uniformly 10 µm along the entire length of the channel, and that it runs uninterrupted all the way out to the bolt–holes about 6.5 mm from the edge of the channel, we can define a similar decomposed domain for the inter–plate helium as we do for the pin–holes. This does not yield a significantly slower simulated helium temperature response. However, it does result in a weak tendency of the helium temperature to fall after reaching the same peak temperature as that found for a channel alone. This is because now we allow for some heat to flow out of the channel region, along this extra helium volume.

Extending the speculative added helium domain even further, to include the helium trapped between the aluminium bolts and the PEEK wall of the hole, we can obtain a simulated helium temperature decays more similarly to the measured values, since there is now effectively even more helium into which heat from the channel can be siphoned off. It does not significantly slow down the initial temperature rise however.

Insofar as an inter–plate gap filled with helium exists, it is unlikely that it can be approximated as a continuous channel of even depth along the entire mating region of the two PEEK plates. Furthermore, that the helium around the aluminium bolts should be in direct contact with this hypothetical inter–plate helium is effectively precluded by the fact that where the aluminium bolts clamp down on the two plates, there is also the largest clamping force, meaning the volumes are completely sealed off.

6.3 Regime Change During Tests

For the strongest applied heating power densities, across all three time–dependent profiles, we see the helium temperature approach and, for some tests, go above T_λ. In order to expand the simulation framework to also include these high–power tests, we must implement some form of regime change once T_λ is reached.

In the helium domain, when a node goes above T_λ we change the effective thermal conductivity to that of stationary He I. This change is done in the thermal conductivity coefficients $\mathcal{A}$ and $\mathcal{B}$ in Equation (7).

For the heater–helium interface heat transfer, which is no longer governed by the Kapitza expression from Equation (1) when the helium temperature has gone above T_λ, we use a natural convection regime;

$$Q_{\text{interface}} = Q_{\text{NatConv}} = a_{\text{NatConv}}(T_{\text{s}} - T_{\text{ref}}), \tag{8}$$

where a_{NatConv} is the natural convection surface heat transfer coefficient.

During the relevant time–windows of the high–power tests we see no sign of nucleate boiling or the onset of film boiling, which would be accompanied with chaotic channel temperature measurements as the helium is perturbed by bubbles arising at the heater surface.

Our main interest is not the natural convection heat transfer regime itself, so we only need an order–of–magnitude value for this coefficient. Open bath experiments by Dorey [38], and Mori and Ogata [39], indicate it should be in the range 200 to 5000 $\mathrm{W\,m^{-2}\,K^{-1}}$. We use $a_{\text{NatConv}} = 1000\ \mathrm{W\,m^{-2}\,K^{-1}}$.

6.3.1 Strongest Fast Pulse

The strongest fast pulses we have tested are, from our simulations of the channel helium, predicted to see the phase transition to He I in the channel, with an associated change in heat transfer regime at the heater surface. Since such a regime change is a feature of many models applied to LHC magnets, we look into the strongest fast–pulse test from our measurement campaign. Figure 16 shows this test together with a simulation where the helium is considered along the length of channel, connected to a pin–hole. For helium above T_λ we assume the thermal conductivity of stationary He I; the channel is horizontal, so we do not expect any lateral convection currents to carry heat.

After about 0.56 ms, the simulated channel temperature reaches T_λ, seen as a kink in the dash–dot–dotted curve in Subfigure 16b. This is the time we change from Kapitza interface heat transfer to natural convection (Equation (8)), and where we take the helium thermal conductivity to be that of He I. This heat transfer regime moves much less heat that Kapitza for the same temperature difference between the heater and helium, and therefore, in Subfigure 16a, the heater surface temperature shoots up. Immediately before the regime change, the heat flux across the interface, from the Kapitza expression, is 15.2 $\mathrm{kW\,m^{-2}}$. After the regime change, the heat flux drops to 1.0 $\mathrm{kW\,m^{-2}}$. Energy is still supplied to the heater strip from the external source, contributing to the temperature increase. However, the largest contribution comes from redistribution of the energy already in the heater strip and material stack; during the time between the peak simulated heater temperature and the transition out of the Kapitza regime there is a large thermal gradient across the 50 µm thickness of the heater strip, with the bottom of the heater (nearest the sensor) being the hottest point in the simulated domain. This thermal gradient exists in the heater to push the Kapitza heat flux at the interface. When this heat flux suddenly drops to nearly zero, the energy stored in the heater must redistribute itself. This redistribution is seen as the brief period around 0.7 ms where the simulated sensor temperature remains nearly steady at 3.75 K.

As mentioned in Section 5.1, the measured channel temperatures, for sensors `C-2` and `CM` briefly peak above T_λ, though not enough to be beyond the estimated uncertainty range. Looking at the very clear simulated heater sensor feature associated with a heat transfer regime

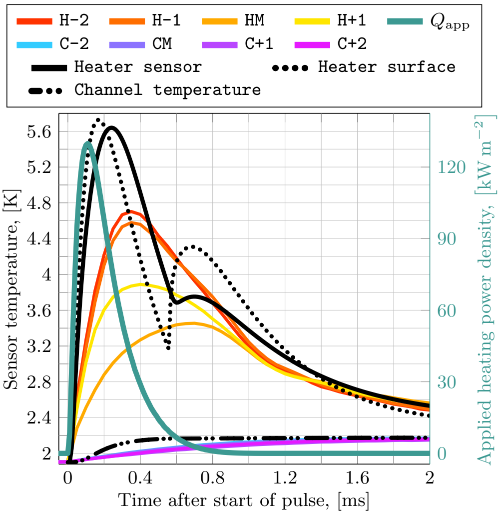

(a) Focus on heater sensors during the first 2 ms of the test.

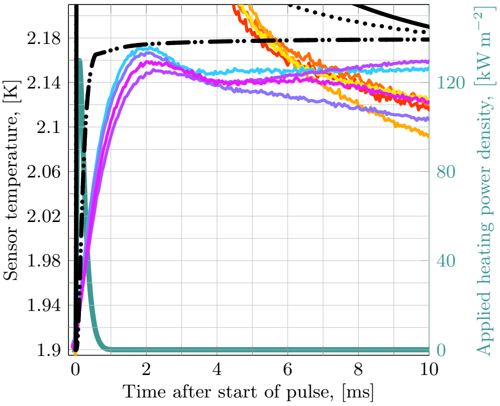

(b) Focus on channel sensors during the first 10 ms of the test.

Figure 16: Measurement from the strongest fast–pulse test shown in Figure 11, together with simulation results that include the channel helium connected to a pin–hole.

change it appears no such transition actually took place during the test, or, if it did, the Kapitza regime recovered fast enough that we could not observe the excursion.

Note that the apparent agreement between simulation and measurement after around 2 ms in Subfigure 16a depends on the choice of a_{NatConv} in Equation (8), and using $1000\ \mathrm{W\,m^{-2}\,K^{-1}}$ does not lead to such agreement for the three weaker fast pulses where the simulations also predict helium temperatures above T_λ. This is, of course, because the natural convection heat transfer coefficient depends on helium temperature, heater temperature, whether the helium flow near the heater is turbulent or laminar, and the confinement of the channel must also play a role, as it changes how the helium flows near the heater as compared with the open bath case for which data is available.

7 Comparing Tests

7.1 Open Bath and Closed Channel Steps

Figure 17 shows two tests; Open bath curves refer to a test of a step to $905\ \mathrm{W\,m^{-2}}$ applied to the heater strip cooled by an open bath (test performed as part of the measurement campaign for our Open Bath Paper), while Closed channel curves refer to a test of a step to $903\ \mathrm{W\,m^{-2}}$ applied to the heater strip cooled by the closed channel helium. The sensors whose temperatures are plotted are physically the same sensors (called `D-2` and `DM` in the Open Bath Paper). The channel temperature is represented by the average temperature of the four channel sensors.

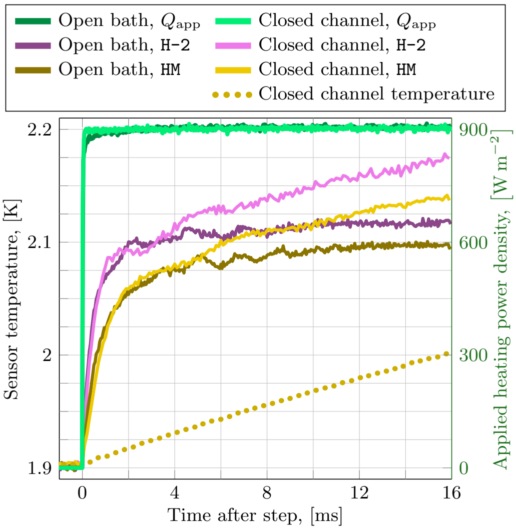

Figure 17: Comparison of step tests that reach around $900\ \mathrm{W\,m^{-2}}$ done in the open bath and closed channel configurations.

During the first 4 ms there is no distinction between the open bath and closed channel results. That there would be some time window during which no difference is seen makes intuitive sense; heat transferred into the helium from the surface of the heater strip would not immediately know about the helium being confined. There must be some form of time delay, such as a thermal diffusion time, associated with heat transfer within helium, and before the propagating temperature reaches the roof of the channel, the Kapitza interface sees the same as if exposed to an open bath. The question is how long does it take for this information to influence the system. The measurements clearly say around 4 ms from the heater sensor temperatures. The channel temperature measurement, on the other hand, starts rising almost immediately after the step, which is in line with our simulation result that shows no significant thermal gradient across the depth of the channel. Of course, we found some small thermal delay stemming from the material stack that separates the heater surface from the heater sensors, but even within the large parameter space we have tested, this cannot account for more than a few tens of microseconds at most, and certainly not several milliseconds.

The closed channel temperature rise follows a roughly linear trajectory starting at $t = 0$, growing by about $6\ \mathrm{mK\,ms^{-1}}$. The temperature growth rate of the closed channel heater sensors after their departure from the open bath results is about $5\ \mathrm{mK\,ms^{-1}}$. That they are not identical is no surprise, since the Kapitza heat transfer expression depends non–linearly on the helium temperature. It is, however, not clear why the closed channel heater temperatures do not appear to grow at all according to the helium temperature during the first 4 ms. By that time, the channel helium temperature has reached 1.93 K. Again, 4 ms is much longer than the effective thermal diffusion time through the material stack between the heater surface and the Cernox® sensors.

A similar comparison between identical steps to $546\ \mathrm{W\,m^{-2}}$ show that the open bath heater sensors have an initial rise time around half a millisecond faster than the closed channel equivalent. This is still significantly slower than relevant simulations. The time when the closed channel temperatures start deviating from the open bath ones is still around 4 ms, however.

This all points towards there being some property of the Kapitza heat transfer, apparent only at this millisecond time–scale, that does not depend intimately on the helium temperature near the interface. Another possibility is that for simulation of heat transfer at this time–scale, the two–fluid nature of He II cannot be simplified to the Gorter–Mellink heat transfer relation. From our simulations of heat transfer where we use the measured helium temperature as the reference for Kapitza cooling (Section 5.2), which isolates the Kapitza interface by using known helium behaviour, we still did not find the right heater behaviour. So not having the right heat transfer relations within the helium is not the only issue. Finally, our model of the region surrounding the heater sensors is simplified to only one dimension, which leaves the small possibility that the real three–dimensional geometry would need to be considered for sufficient accuracy. The main material we neglect when simplifying like this is PEEK, which is essentially a thermal insulator, especially when we consider only the first few milliseconds.

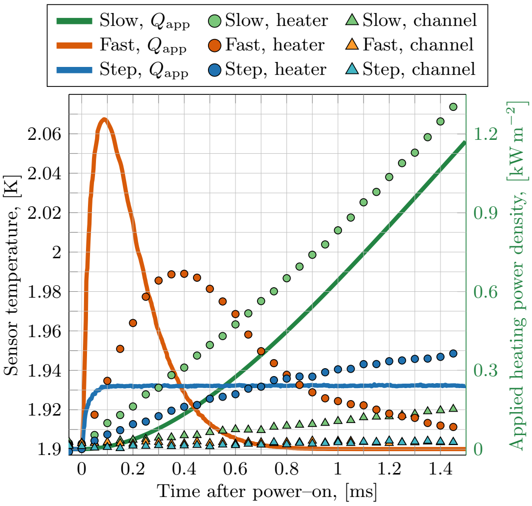

Figure 18: Comparison of three transient tests that have deposited roughly the same amount of energy in the heater strip after 1 ms. Each temperature curve is the average temperature of the four sensors that comprise the group (heater or channel).

7.2 Tests With Similar Energy Deposition

Figure 18 shows the first 1.5 ms of three different applied heating power density profiles that, after 1 ms have delivered roughly the same amount of energy into the heater strip. The slow pulse has delivered 0.113 mJ, the fast pulse 0.153 mJ, and the step 0.111 mJ.

The most important observation is that the helium temperature rise during the first millisecond of the slow–pulse test has clearly risen above the initial temperature by about 9 mK, which is almost twice the estimated calibration uncertainty. The fast–pulse and step tests, on the other hand, after having deposited at least that same amount of energy in the heater strip, see the helium temperature rise by no more than 2 mK which is less than half the calibration uncertainty.

This means that the time–structure of the energy deposition is of fundamental importance to the way energy is distributed between the two main parts of the system; heater and helium. Recall, for the slow pulse shown in the figure, we can very accurately simulate the entire time window shown, including the simulation of the channel helium. That same simulation approach predicts that the channel helium should rise about 3 mK over the first 1 ms. This is quite similar to the measured rise. However, the simulated heater sensor temperature is faster than the measured temperature, overestimating the Kapitza heat transfer during the first 0.5 ms. For the fast pulse, simulations give a very different helium behaviour than that seen; the simulated helium temperature rise, like seen before, reaches a flat top value after 1 ms that is 4 mK above the initial temperature, while the measured helium temperature only grows by 1 to 2 mK within this time. Note that the simulation gives a helium temperature rise of 3.5 mK after just 0.5 ms. The fast–pulse energy deposition is larger than that of the other two tests in the comparison, so the temperature after 1 ms should have been higher than just 1 to 2 mK if all the energy entered the helium. The measured helium temperature rises slowly to a peak about 2 to 3 mK above initial temperature after 8 ms.

So, for energy depositions that happen on the sub–millisecond time–scale, like fast pulses, an effect we have not accounted for in our modelling, that does not appear to be relevant at longer time–scales, leads to a channel helium temperature rise that is much slower than anticipated. The helium heats up from the heater strip, so the effect must also impact the heat transfer from heater to helium.

The strongest step performed reached $Q_{\text{app}} = 1.02\ \text{kW}\,\text{m}^{-2}$ after about 100 µs. It delivered 0.154 mJ of energy during the first 330 µs of the test. This is the same amount of energy as that delivered during the entire fast–pulse test shown in Figure 18. During these 330 µs, the heater sensor temperatures are indistinguishable between the two tests. Furthermore, the channel temperature rise during the first 330 µs of the step test is about 4 mK, while the simulated helium temperature rise is about 3 mK. So, it is only for the fast–pulse tests that it appears the energy transfer into helium is wrong when using the steady state Kapitza expression.

The models used to predict quench levels of LHC magnets incorporate the same physics we have implemented here, except for the internal heat transfer within helium, which is neglected for quench level estimates. In light of the underestimated LHC magnet quench levels during UFO events, we confirm that both heater and helium temperatures remain lower than expected during our controlled experiments. Since all attempts at variations of parameters in our model fail to explain the slower temperature response, on both the heater and helium side, it appears the use of the steady state Kapitza heat transfer expression could be invalid at the UFO time–scale.

8 Conclusion

To investigate superfluid–helium cooling of a heater subject to time–dependent heating on the millisecond time–scale, as relevant to UFO events in the LHC, we built an experimental setup consisting of a heater and a confined volume of He II cooling the heater from one side. The setup was previously validated in open bath experiments, where we found steady state Kapitza parameters for the stainless steel heater strip we use. Our setup measures the temperature of the heater strip and the channel helium.

We develop a heat transfer model based on the time–dependent heat equation together with the steady state Kapitza heat transfer expression as a cooling boundary condition at the heater–helium interface. We validate the model against measurements where the heater strip is subjected to a slow pulse in heating power that peaks after 9 ms and lasts for a total of 400 to 500 ms. When using the measured helium channel temperature as the reference temperature in the Kapitza heat transfer expression, we can accurately simulate the first 150 ms of such a pulse.

We expand this model to include the helium volume by considering a one–dimensional helium domain along the heater connected to a pin–hole at one end. We assume heat transfer within helium always adheres to the fully turbulent Gorter–Mellink regime. With this extension of the model, we can accurately simulate the first 5 ms of slow pulses in heating power. The deviations after this are tied to parasitic cooling effects in the helium stemming from the setup being built as two parts pressed together to form the helium channel.

For fast, UFO–like pulses, which deliver peak power after 100 µs and last for less than 1 ms in total, we consistently find that both the heater and the channel helium temperatures rise more slowly than what is predicted by the heat transfer model we validated for slow pulses. The slower temperature rise cannot be explained by material parameter variations, changes in the dimensions of material layers in the model, addition of a thermal boundary resistance between the heater and the sensor, a thermal gradient in the helium across the depth of the channel, or the effect of adding a hypothetical volume of helium between the two PEEK mounting plates.

Comparing slow–pulse, fast–pulse, and step tests that deliver the same amount of energy to the heater strip after 1 ms, we find that for the UFO–like fast–pulse energy deposition, the expected helium temperature rise, as predicted by our modelling, is higher and happens sooner than what we see in the measurements. The simulated helium temperature rise from the other two energy deposition profiles is in line with measurement. There must, therefore, be a missing, but important effect, not accounted for in our model.

Since fast–pulse simulations using the measured helium temperature in the Kapitza cooling expression do not give heater temperatures that agree with measurements, the missing effect is not isolated to the helium alone. As only the Kapitza interface influence both the heater and helium domains simultaneously, this points towards the steady state Kapitza heat transfer expression not being valid at the UFO event time–scale.

References

[1] T Baer et al. “UFOs in the LHC after LS1”. In: (2012), 5 p. DOI: `10.5170/CERN-2012-006.294`. URL: `http://cds.cern.ch/record/1493018`.

[2] Giulia Papotti, Markus Albert, Bernhard Auchmann, Eva Barbara Holzer, Matti Kalliokoski, and Anton Lechner. “Macroparticle-Induced Losses During 6.5 TeV LHC Operation”. In: CERN–ACC–2016–249 (2016), TUPMW023. 4 p. DOI: `10.18429/JACoW-IPAC2016-TUPMW023`.

[3] Scott M. Rowan. “LHC main dipole magnet circuits: sustaining near–nominal beam energies”. PhD thesis. 2016. URL: `http://cds.cern.ch/record/2229989`.

[4] A. Apollonio, B. Auchmann, L. Ponce, C. Roderick, R. Schmidt, M. Solfaroli, B. Todd, D. Wollmann, and M. Zerlauth. “2015 availability summary”. In: *6th Evian Workshop on LHC beam operation.* CERN, 2016, pp. 19–28.

[5] B Auchmann, J Ghini, L Grob, G Iadarola, A Lechner, and G Papotti. “How to survive a UFO attack”. In: (2016). 6th Evian Workshop on LHC beam operation, pp. 81–86. URL: `http://cds.cern.ch/record/2294520`.

[6] Frank Zimmermann et al. *HE-LHC: The High-Energy Large Hadron Collider: Future Circular Collider Conceptual Design Report Volume 4. Future Circular Collider.* Tech. rep. Geneva: CERN, 2018. DOI: `10.1140/epjst/e2019-900088-6`. URL: `https://cds.cern.ch/record/2651305`.

[7] Tobias Baer. “Very Fast Losses of the Circulating LHC Beam, their Mitigation and Machine Protection”. 2013. URL: `https://cds.cern.ch/record/1637966`.

[8] A. Priebe, J. Steckert, A. Verweij, et al. “Beam-induced Quench Test of a LHC Main Quadrupole”. In: *Conf. Proc. C* 110904 (2011). Ed. by Christine Petit-Jean-Genaz, pp. 2388–2390. URL: `http://accelconf.web.cern.ch/AccelConf/IPAC2011/papers/WEPC172.pdf`.

[9] B. Auchmann et al. “Testing beam–induced quench levels of LHC superconducting magnets”. In: *Phys. Rev. ST Accel. Beams* 18 (6 June 2015), p. 061002. DOI: `10.1103/PhysRevSTAB.18.061002`.

[10] A. Verweij. *QP3: User’s Manual.* CERN. 2008. URL: `https://edms.cern.ch/document/1150045/1`.

[11] A. Verweij. *CUDI: User’s Manual.* CERN. 2007. URL: `http://cern-verweij.web.cern.ch/Manual%20CUDI%20v13.doc`.

[12] Marco Breschi, Enrico Felcini, Francesca Breccia, P. P. Granieri, Eleonora Bergonzoni, Alessandro Bevilacqua, Pietro Galassi, Tiemo Winkler, and Luca Bottura. “Modeling of Beam Loss Induced Quenches in the LHC Main Dipole Magnets”. In: *IEEE Transactions on Applied Superconductivity* 29.5 (2019), pp. 1–7. DOI: `10.1109/TASC.2019.2906636`.

[13] J. B. Ghini, B. Auchmann, and B. Baudouy. *Millisecond Time-Scale Measurements of Heat Transfer to Open Bath of He II.* To be published. 2022.

[14] G. Claudet and P. Seyfert. “Bath cooling with subcooled superfluid helium”. In: *Advances in Cryogenic Engineering 27* (1981), pp. 441–449.

[15] S. W. Van Sciver. *Helium Cryogenics.* International Cryogenics Monograph Series. Springer New York, 2012. ISBN: 978–1–4419–9978–8.

[16] I. M. Khalatnikov. *An Introduction to the Theory of Superfluidity.* Ed. by David Pines. Trans. Russian by Pierre C. Hohenberg. Advanced Book Classics. Russian printing in 1965. Westview Press, 2000.

[17] Tsuneyoshi Nakayama. “Chapter 3: Kapitza Thermal Boundary Resistance and Interactions of Helium Quasiparticles with Surfaces”. In: ed. by D.F. Brewer. Vol. 12. Progress in Low Temperature Physics. Elsevier, 1989, pp. 115–194. DOI: `10.1016/S0079-6417(08)60042-6`.

[18] J. A. Katerberg and A. C. Anderson. “Comparison of steady-state and second-sound measurements of the Kapitza resistance”. In: *Journal of Low Temperature Physics* 42.1 (1981), pp. 165–176. DOI: `10.1007/BF00116702`.

[19] S.K. Nemirovskii and A.N. Tsoi. “Transient thermal and hydrodynamic processes in superfluid helium”. In: *Cryogenics* 29.10 (1989), pp. 985–994. ISSN: 0011–2275. DOI: `10.1016/0011-2275(89)90246-4`.

[20] C.J. Gorter and J.H. Mellink. “On the irreversible processes in liquid helium II”. In: *Physica* 15.3 (1949), pp. 285–304. ISSN: 0031–8914. DOI: `10.1016/0031-8914(49)90105-6`.

[21] W. F. Vinen. “Mutual friction in a heat current in liquid helium II. II. Experiments on transient effects”. In: *Proceedings of the Royal Society of London. Series A. Mathematical and Physical Sciences* 240.1220 (1957). Communicated by David Shoenberg, pp. 128–143. DOI: `10.1098/rspa.1957.0072`.

[22] C. E. Chase. “Thermal Conduction in Liquid Helium II. II. Effects of Channel Geometry”. In: *Phys. Rev.* 131 (5 Sept. 1963), pp. 1898–1903. DOI: `10.1103/PhysRev.131.1898`.

[23] S.W. Van Sciver. “Transient heat transport in He II”. In: *Cryogenics* 19.7 (1979), pp. 385–392. ISSN: 0011–2275. DOI: `10.1016/0011-2275(79)90120-6`.

[24] A. Vitrano, R. Bruce, and B. Baudouy. “Transient Conjugate Heat Transfer Numerical Simulation in Superfluid Helium”. In: *IOP Conference Series: Materials Science and Engineering* 755 (2020), p. 012068. DOI: `10.1088/1757-899x/755/1/012068`.

[25] R. P. Warren and S. Caspi. “Measurements of heat transfer to helium II at atmospheric pressure in a confined geometry”. In: *Presented at the Cryogenic Engineering Conference, San Diego CA, USA.* 1981. URL: `https://escholarship.org/uc/item/2gg9z5zh`.

[26] Z. Chen and S.W. Van Sciver. “Channel heat transfer in He II — steady state orientation dependence”. In: *Cryogenics* 27.11 (1987), pp. 635–640. ISSN: 0011–2275. DOI: `10.1016/0011-2275(87)90086-5`.

[27] H. Kobayashi, Y. Fujimura, T. Murata, and M. Sakata. “Heat transfer through subcooled He I layer from distributed heat source in a pressurized He II channel”. In: *Cryogenics* 37.12 (1997), pp. 851–855. ISSN: 0011–2275. DOI: `10.1016/S0011-2275(97)00145-8`.

[28] Pier Paolo Granieri. “Heat transfer between the superconducting cables of the LHC accelerator magnets and the superfluid helium bath”. Presented 29 Aug 2012. Apr. 2012. URL: `https://cds.cern.ch/record/1479179`.

[29] T. Okamura, T. Suzuki, N. Seki, and S. Kabashima. "Heat transport in He II channel with phase transition". In: *Cryogenics* 34.3 (1994), pp. 187–193. ISSN: 0011–2275. DOI: `10.1016/0011-2275(94)90168-6`.

[30] L. Landau. "Theory of the Superfluidity of Helium II". In: *Physical Review* 60 (4 1941), pp. 356–358. DOI: `10.1103/PhysRev.60.356`.

[31] A. Sato, M. Maeda, and Y. Kamioka. "Chapter 201 - Normalized representation for steady state heat transport in a channel containing He II covering pressure range up to 1.5 MPa". In: *Proceedings of the Twentieth International Cryogenic Engineering Conference (ICEC 20)*. Ed. by Liang Zhang, Liangzhen Lin, and Guobang Chen. Oxford: Elsevier Science, 2005, pp. 849–852. ISBN: 978–0–0804–4559–5. DOI: `10.1016/B978-008044559-5/50204-0`.

[32] A. Sato, M. Maeda, T. Dantsuka, M. Yuyama, and Y. Kamioka. "Temperature Dependence of the Gorter–Mellink Exponent m Measured in a Channel Containing He II". In: *AIP Conference Proceedings* 823.1 (2006), pp. 387–392. DOI: `10.1063/1.2202439`.

[33] P. Seyfert, J. Lafferranderie, and G. Claudet. "Time dependent heat transport in subcooled superfluid helium". In: *Cryogenics* 22.8 (1982), pp. 401–408. ISSN: 0011–2275. DOI: `10.1016/0011-2275(82)90084-4`.

[34] T. Okamura, Y. Yoshizawa, A. Sato, K. Ishito, S. Kabashima, and S. Shioda. "Time dependent heat transfer in pressurized superfluid helium". In: *Cryogenics* 29.11 (1989), pp. 1070–1074. ISSN: 0011–2275. DOI: `10.1016/0011-2275(89)90263-4`.

[35] S. Fuzier and S.W. Van Sciver. "Experimental measurements and modeling of transient heat transfer in forced flow of He II at high velocities". In: *Cryogenics* 48.3 (2008), pp. 130–137. ISSN: 0011–2275. DOI: `10.1016/j.cryogenics.2008.02.004`.

[36] Sylvie Fuzier. "Heat Transfer and Pressure Drop in Forced Flow Helium II at High Reynolds Numbers". PhD thesis. Florida State University, 2004.

[37] V. D. Arp, R. D. McCarty, and Friend D. G. *Thermophysical properties of Helium-4 from 0. 8 to 1500 K with pressures to 2000 MPa.* Tech. rep. NIST Technical Note 1334 (revised). National Institute of Standards and Technology, 1989. URL: `https://nvlpubs.nist.gov/nistpubs/Legacy/TN/nbstechnicalnote1334.pdf`.

[38] A.P. Dorey. "Heat transfer at low temperatures". In: *Cryogenics* 5.3 (1965), pp. 146–151. ISSN: 0011–2275. DOI: `10.1016/0011-2275(65)90008-1`.

[39] Hideaki Mori and Hisanao Ogata. "Natural Convection Heat Transfer to Liquid Helium in a High Centrifugal Acceleration Field". In: *JSME International Journal Series B* 37.1 (1994), pp. 109–115. DOI: `10.1299/jsmeb.37.109`.

ISBN 978-82-326-5302-7 (printed ver.)
ISBN 978-82-326-6765-9 (electronic ver.)
ISSN 1503-8181 (printed ver.)
ISSN 2703-8084 (online ver.)

NTNU
Norwegian University of
Science and Technology